

# Liquid Crystal Dielectric Image Lines for Integrated Reconfigurable Millimeter-Wave Beamsteering Applications

Am Fachbereich Elektrotechnik und Informationstechnik  
der Technischen Universität Darmstadt  
zur Erlangung des akademischen Grades eines  
Doktor-Ingenieurs (Dr.-Ing.)  
genehmigte

## Dissertation

von

M. Sc.

**David Henning Tesmer,**

geboren am 29.01.1992  
in Kassel, Deutschland

Referent: Prof. Dr.-Ing. Rolf Jakoby  
Korreferent: Prof. Dr.-Ing. Martin Vossiek

Tag der Einreichung: 28. Februar 2023  
Tag der mündlichen Prüfung: 01. Juni 2023

D17  
Darmstadt 2023

Tesmer, Henning: Liquid Crystal Dielectric Image Lines for Integrated Reconfigurable Millimeter-Wave Beamsteering Applications  
Darmstadt, Technische Universität Darmstadt  
Jahr der Veröffentlichung der Dissertation auf TUPrints: 2023  
URN: urn:nbn:de:tuda-tuprints-243417  
Tag der mündlichen Prüfung: 01. Juni 2023  
Veröffentlicht unter CC BY-SA 4.0 International  
<https://tuprints.ulb.tu-darmstadt.de/id/eprint/24341>

# Erklärungen laut Promotionsordnung

## **§ 8 Abs. 1 lit. c PromO**

Ich versichere hiermit, dass die elektronische Version meiner Dissertation mit der schriftlichen Version übereinstimmt.

## **§ 8 Abs. 1 lit. d PromO**

Ich versichere hiermit, dass zu einem vorherigen Zeitpunkt noch keine Promotion versucht wurde. In diesem Fall sind nähere Angaben über Zeitpunkt, Hochschule, Dissertationsthema und Ergebnis dieses Versuchs mitzuteilen.

## **§ 9 Abs. 1 PromO**

Ich versichere hiermit, dass die vorliegende Dissertation selbstständig und nur unter Verwendung der angegebenen Quellen verfasst wurde.

## **§ 9 Abs. 2 PromO**

Die Arbeit hat bisher noch nicht zu Prüfungszwecken gedient.

Darmstadt, 28. Februar 2023

---



# Acknowledgements

This dissertation presents the research results obtained during my time at the Institute of Microwave Engineering and Photonics (IMP) at Technische Universität Darmstadt. In this section, I would like to acknowledge the persons who supported me during my pursuit of the doctorate degree.

First, I want to sincerely thank my supervisor, Prof. Dr.-Ing. Rolf Jakoby, for his kind continuous support throughout the past years. The trust and freedom he provided during my time as a doctorate student shaped me both professionally and personally. He always had an open ear to any issue arising, and his experience helped me to view circumstances, problems and opportunities from a different perspective.

I am very grateful for my colleagues at the institute, who provided a productive and kind working environment. In particular, I want to thank Dr.-Ing. Ersin Polat, with whom I had many talks about theoretic and practical problems, and with which I had the joy of sharing an office. Similarly, I thank Dongwei Wang, Pranroy Agrawal, Stipo Matic, Jesús Sanchez-Pastor, Robin Neuder and Dr-Ing. Martin Schüßler for fruitful discussions, kind advice, and many conversations about topics beyond the day-to-day business. The IMP band, including Dr.-Ing. Ersin Polat, Pranroy Agrawal and Dr.-Ing. Martin Schüßler, was an after-work activity I enjoyed a lot. From the sometimes tiring rehearsals, to photo shoots and Christmas performances, it was a time I never want to miss.

Special thanks go to Andreas Semrad and Peter Kießlich from the institute's workshop. Without their helping hands a lot of the work presented in this dissertation would not have been possible. Similarly, I would like to thank Maria Kaiser, Elenore Titow and Nicole Neurohr for their support regarding IT, formalities and literally anything else that could come up.

I enjoyed working with students, and thank them for helping me to try out different approaches and ideas.

Last, I want to sincerely thank my wife Laura for her support during the ups and downs throughout my time at the institute. Without her, the outcome of this dissertation would have been for sure different.



# Abstract

This work investigates the capabilities and performance of liquid crystal based dielectric image lines as a basis for reconfigurable millimeter-wave components and their use for beam-steerable antennas. The components, which are operated at W-band (75 GHz to 110 GHz), are designed, manufactured and characterized. The dielectric image line topology is well suited to combine the advantages of fully dielectric waveguides with the integrated character of commercial devices. Especially, the integration of liquid crystal can be easily achieved, and does not require modifying the printed circuit board on which the dielectric image line is placed.

As a basis for the components, suitable materials are analyzed first, before an adaptive measurement setup is introduced. Two modes of the dielectric image line are of particular interest in this dissertation: the fundamental  $E_{11}^y$ -mode and the orthogonally polarized higher-order  $E_{11}^x$ -mode. The first components are liquid crystal phase shifters of low permittivity ( $\epsilon_r = 2.53$ ). In the fundamental mode, a low profile, a maximum figure-of-merit of  $136^\circ \text{dB}^{-1}$ , response times of 6 s to 9 s and linear performance in a temperature range from  $-10^\circ$  to  $80^\circ$  are achieved. With the orthogonally polarized mode, a higher figure-of-merit of  $188^\circ \text{dB}^{-1}$  is obtained at the cost of higher response times. Utilizing a special design, the electrodes can be employed directly on the dielectric. This results in fast switch-on response times in the range of milliseconds, which is the fastest time obtained with dielectric waveguides up to today. This high decrease in switch-on response time represents a 99% and 97% improvement when compared to a fully dielectric liquid crystal phase shifter and a classic electrode placement besides the dielectric image line, respectively.

On the basis of the phase shifters, reconfigurable antennas are investigated in the dielectric image line topology. With broadband rod antennas,  $1 \times 4$  array demonstrators are realized. By utilizing multimode-interference for the first time in the dielectric image line topology at millimeter-waves, compact power dividers are realized. Combining the array with the aforementioned phase shifters leads to the first liquid crystal dielectric image line rod antenna phased array. It shows gain of 17 dBi to 18 dBi and has a beam steering range of  $\pm 10^\circ$ . As a less complex and more narrowband alternative, a liquid crystal leaky wave antenna is introduced, too. By allowing the bias electrodes to contribute to the radiation characteristics, a simple antenna is realized, with a gain of 15 dBi, capable of scanning  $10^\circ$  by applying only one bias voltage.

Furthermore, novel additive manufacturing techniques are evaluated to allow automated fabrication of the investigated components. An innovative guiding mechanism, which enables the combination of liquid crystal with high permittivity materials ( $\epsilon_r = 9$ ), is introduced as a means of enabling smaller components.





# Kurzfassung

In dieser Arbeit werden dielektrische Spiegelleitungen bezüglich ihrer Tauglichkeit und Performanz für flüssigkristallbasierte Millimeterwellenkomponenten, insbesondere im Hinblick auf strahlschwenkende Antennen, untersucht. Dabei werden die im W-Band (75 GHz bis 110 GHz) betriebenen Komponenten konzipiert, hergestellt und charakterisiert. Die dielektrische Spiegelleitungstopologie ist besonders geeignet um die Vorteile dielektrischer Leitungen in einer integrierten Umgebung, wie sie beispielsweise auf kommerziellen Leiterplatten zugegen ist, umzusetzen. Besonders die Integration von Flüssigkristallen kann bei dielektrischen Wellenleitern einfach umgesetzt werden, sodass eine Platine keinerlei sondergefertigte Kavitäten oder spezielle Materialien aufweisen muss.

Als Grundlage aller weiteren Entwicklungsschritte werden zunächst geeignete Materialien für die dielektrischen Spiegelleitungen selbst untersucht und ein adaptiver Messaufbau eingeführt. Besonderes Augenmerk wird auf zwei Modentypen, der  $E_{11}^y$  Grundmode und der orthogonal zum dieser polarisierten  $E_{11}^x$  Mode, gelegt. Für alle weiteren Untersuchungen bilden Flüssigkristall-Phasenschieber von niedriger Permittivität ( $\epsilon_r = 2.53$ ) die Grundlage. Der Demonstrator in der Grundmode weist ein geringes Profil auf und es wird eine maximale Phasenschiebergüte von  $136^\circ \text{dB}^{-1}$  neben Schaltzeiten von 6 s bis 9 s erreicht. Messungen über einen Temperaturbereich von  $-10^\circ \text{C}$  bis  $80^\circ \text{C}$  bestätigen ein lineares Verhalten des Bauteils. In der orthogonal polarisierten Mode kann eine höhere Phasenschiebergüte von bis zu  $188^\circ \text{dB}^{-1}$  erreicht werden, allerdings auf Kosten der Schaltzeit. Durch ein spezielles Layout können die Elektroden auch direkt auf das Dielektrikum aufgebracht werden. Dieser Schritt erlaubt es erstmals in dielektrischen Flüssigkristallkomponenten Einschaltgeschwindigkeiten im Millisekundenbereich zu erreichen. Die Geschwindigkeitserhöhung liegt im Vergleich zu volldielektrischen Vergleichskomponenten bei 99% und zum ursprünglich in dieser Arbeit eingeführten Elektrodennetzwerk bei 97%.

Um strahlschwenkende Antennen zu realisieren, werden aufgrund der Erkenntnisse zu den Phasenschiebern zunächst breitbandige Spiegelleitungs-Stabantennenarrays untersucht.  $1 \times 4$  Demonstratoren werden hergestellt, wobei zum ersten Mal Multimode-Interferenz in der Spiegelleitungstopologie im Millimeterwellenbereich verwendet wird, um eine kompakte Leistungsteilung zu erreichen. Das resultierende *phased array* weist einen Antennengewinn von 17 dBi bis 18 dBi in einem Strahlschwenkbereich von  $\pm 10^\circ$  auf und stellt das erste flüssigkristallgesteuerte Spiegelleitungsarray seiner Art dar.

Um die Komplexität der Ansteuerungselektronik zu reduzieren, wird ebenfalls eine flüssigkristallbasierte Leckwellenantenne untersucht. Durch simultane Verwendung

## *Abstract*

der Ansteuerungselektroden als Abstrahlelemente kann eine Antenne von geringer Komplexität realisiert werden, die einen Antennengewinn von 15 dBi aufweist, und mit nur einer Steuerspannung eine Strahlschwenkung von  $10^\circ$  erreicht.

Zusätzlich werden zum Ende dieser Arbeit additive Herstellungsverfahren evaluiert, um die vorgestellten Konzepte industriell fertigen zu können. Dabei ist besonders ein innovativer Ansatz, der es erlaubt Flüssigkristall mit Materialien deutlich höherer Permittivität ( $\epsilon_r = 9$ ) zu kombinieren, hervorzuheben.

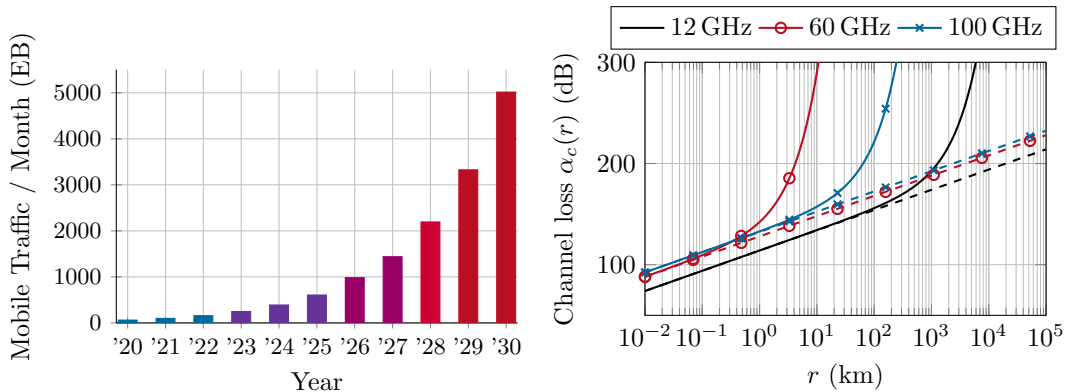
# Contents

<b>Abstract</b>	<b>iii</b>
<b>1. Introduction</b>	<b>1</b>
<b>2. Fundamentals of Liquid Crystal</b>	<b>7</b>
2.1. Nematic Liquid Crystal . . . . .	9
2.2. Magnetic and Electric Properties . . . . .	11
2.3. Bias Schemes . . . . .	12
2.4. Characteristic Properties for Microwave Applications . . . . .	15
<b>3. Dielectric Image Lines</b>	<b>19</b>
3.1. Waveguide Topology . . . . .	20
3.1.1. Operating Modes . . . . .	23
3.1.2. Loss Mechanisms . . . . .	25
3.2. Material Selection and Characterization . . . . .	32
3.3. Excitation of Dielectric Image Lines . . . . .	38
<b>4. Liquid Crystal Dielectric Image Line Phase Shifters</b>	<b>43</b>
4.1. LC-Phase Shifter in $E_{11}^y$ -Mode . . . . .	44
4.1.1. Design . . . . .	44
4.1.2. Fabrication and Microwave Characterization . . . . .	49
4.1.3. Temperature Characterization . . . . .	52
4.1.4. Electrode Integration for Fast Switch-On Response Times . . . . .	56
4.2. LC-Phase Shifter in $E_{11}^x$ -Mode . . . . .	63
4.2.1. Design . . . . .	63
4.2.2. Fabrication and Microwave Characterization . . . . .	65
4.3. Comparison of both Phase Shifters . . . . .	67
<b>5. Beamsteering Liquid Crystal Dielectric Image Line Antennas</b>	<b>71</b>
5.1. Rod Antenna Arrays . . . . .	72
5.1.1. Single Antenna Elements in $E_{11}^y$ - and $E_{11}^x$ -Mode . . . . .	72
5.1.2. 1 x 4 Antenna Arrays . . . . .	76
5.1.3. 1x4 Phased Array in $E_{11}^y$ -Mode for Beamsteering . . . . .	84
5.2. Leaky Wave Antennas . . . . .	88
5.2.1. Operation Principle . . . . .	90
5.2.2. Unit Cell and Antenna Design . . . . .	92

<b>6. Towards Additively Manufactured Liquid Crystal Dielectric Image Line Components</b>	<b>105</b>
6.1. Material Extrusion for Low-Permittivity Components . . . . .	105
6.2. Stereolithography for High-Permittivity Components . . . . .	109
6.3. Comparison and Discussion . . . . .	115
<b>7. Conclusion and Outlook</b>	<b>117</b>
<b>A. Appendix</b>	<b>125</b>
A.1. Relation of $S$ - and $T$ -Matrix . . . . .	125
A.2. Extracted Permittivity and Permeability of an Empty Sample with the NRW Method . . . . .	125
A.3. Schematics of Waveguide Transitions . . . . .	125
A.4. Mode Conversion in the $E_{11}^x$ -Mode LC Phase Shifter . . . . .	128
A.5. Antenna Measurement Setups . . . . .	128
A.6. Leaky Wave Antennas . . . . .	130
A.6.1. Frequency Scanning Rexolite LWA in $E_{11}^y$ -Mode . . . . .	130
A.6.2. LWA in $E_{11}^x$ -Mode . . . . .	131
<b>B. Acronyms</b>	<b>135</b>
<b>Bibliography</b>	<b>137</b>

# 1. Introduction

In today's society, there is a steady and ever rising demand for higher data rates. Especially wireless services, networks and applications have to satisfy the necessary requirements for the Internet of Things, machine-to-machine (M2M) networks, ultra-high definition video services, high resolution radar, and high-precision remote sensors. As visible in Fig. 1.1 (a), the global mobile traffic is estimated to exponentially increase and to surpass 5000 Exa( $10^{18}$ )Byte in 2030 [ITU15b]. To achieve high data rates, higher absolute bandwidth needs to be provided. With the sub-6 GHz spectrum getting increasingly crowded, the frequency of operation for many services is steadily raised, such as in the establishing 5th generation mobile communications standard (5G), or emerging WLAN standards, which utilize frequencies up to V-band (40 GHz to 75 GHz) [IEE12; Rap+13]. Nonetheless, no stagnation of the global mobile traffic is expected (Fig. 1.1 (a)). To cope with this exponential growth, even higher frequencies have to be considered, and frequencies in the millimeter-wave(mmW)-regime (30 GHz to 300 GHz) have to be more commonly used [Rap+13; MA15]. The drawback of increasing frequency of operation in the mmW-regime is the free-space loss  $\alpha_{fs}$ , which is linked to the frequency by  $\alpha_{fs} \propto f^2$ . In addition, attenuation caused by the excitation of molecular resonances, mainly of oxygen and water molecules, is contributing to the total loss of wireless electromagnetic (EM) propagation. The course of free-space loss and total loss by adding



(a) Mobile traffic per year, including M2M traffic, (b) Free-space loss (dashed) and combination of free-space loss with atmospheric attenuation (solid).

Figure 1.1: (a) Estimated development of mobile traffic in ExaByte [ITU15b] and (b) encountered channel loss at 12 GHz, 60 GHz, and 100 GHz [ITU15a].

## 1. Introduction

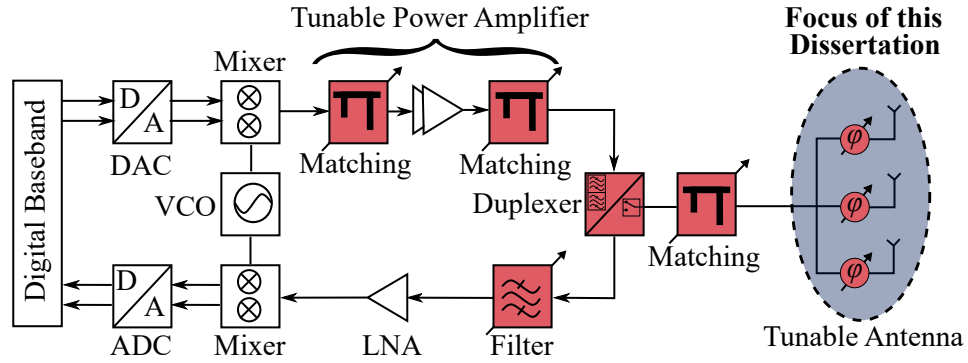


Figure 1.2: Block diagram of a reconfigurable RF-frontend, based on [Fer+22]. Tunable blocks are shaded in red. The focus of this dissertation, reconfigurable antennas and phase shifters, is highlighted with a shaded ellipse.

atmospheric attenuation is visualized in Fig. 1.1 (b). As distinct frequency windows of low molecular attenuation exist, those frequencies are of particular interest for wireless services. The W-band (75 GHz to 110 GHz) belongs to one of those windows, visible in less attenuation at 100 GHz than at 60 GHz in Fig. 1.1 (b). Representative applications in W-band are automotive radar or radiometric applications. In order to compensate the high free space loss, the output power of a transmitter can be increased. Since power is a limited and costly resource, and components which either provide such powers or have to operate at high power levels can be rather expensive, high gain antennas are preferred for loss compensation. However, since increasing gain is linked to decreasing half-power beam width, it is crucial to align transmitter and receiver, even in (semi-)static scenarios. Hence, misalignment due to deliberate movement, or undesired drift, has to be compensated by beam steering antennas. To avoid mechanically turning an antenna, which requires a motor with high maintenance, electrical means of beam steering offer a cheap, lightweight and almost maintenance-free alternative, which is enabled by reconfigurable materials and technologies. Besides antennas, filters and matching networks need to be reconfigurable in modern systems, e.g. for channel selection. Fig. 1.2 shows a block-diagram of a completely reconfigurable radio-frequency (RF) frontend. In this work, the main focus is put on reconfigurable transmission lines and antennas. A key property for reconfigurable devices is tunability, which can be achieved in various ways:

- **Semiconductors**

Silicon-based complementary metal-oxide-semiconductors (CMOS) are a well-established technology, which enable fast response times, and high tuning resolution. Their main drawback is low broadband linearity, high power consumption, and increased loss at frequencies of 100 GHz and beyond [Fer+22].

- **Microelectromechanical Systems**

These small electrically controlled mechanical components offer fast tuning

speed (microseconds) with low power consumption [Fer+22]. Due to the advancement in technology, feature sizes comparable to frequencies of up to 750 GHz are reported [FB17]. Since they can be manufactured by extremely durable materials, a high amount of switching cycles can be achieved [Rah+21]. However, they can break, wear out or become blocked, which makes maintenance in non-accessible, autonomous scenarios the main challenge of this technology.

- **Functional Materials**

The EM properties of functional materials can be controlled by external electric or magnetic bias fields. The response of these materials to the external bias can have different molecular or atomistic origins. Functional materials mostly used in RF-applications are:

- Ferrites:

These materials are magnetically tunable. An example for such a material is yttrium iron garnet. While good results can be achieved, the main drawback lies in purely magnetically controlled tunability and operation frequencies in the lower GHz range [Ge+22]. In order to apply an electrically controlled magnetic bias field, a constant current is necessary, and hence power consumption is high.

- Ferroelectrica:

Tuning relies on displacing a (charged) atom in a crystal lattice by means of an external electric field, which changes the polarization of the material. The most prominent example for a material in RF-applications is barium strontium titanate, which shows good linearity and power consumption. Since its loss increases drastically at high frequencies, it is usually used below 10 GHz [Bao+08].

- Liquid Crystal (LC):

Depending on the orientation of molecules with respect to the RF-polarization, the macroscopic permittivity changes. Since the molecules' orientation can be controlled by external magnetic/electric bias fields, tuning is enabled by an arrangement of magnets/electrodes. The main issue of this tuning mechanism is its speed (milliseconds to minutes), since mechanical forces act against realignment of the molecules, and the liquid material state. The material is of low loss, and can be used from 10 GHz up to the THz-regime [Wei+13; JGW20; WFS21].

In this dissertation, LC is used to investigate tunable components, since it shows high potential for use at high frequencies and offers continuous, fully electric control of its permittivity. Therefore, the concepts shown in this dissertation can also be extended to higher frequencies.

Besides increased free-space loss, the loss of wave guiding structures increases with frequency as well. Especially metallic planar waveguides become lossy at W-band,

## 1. Introduction

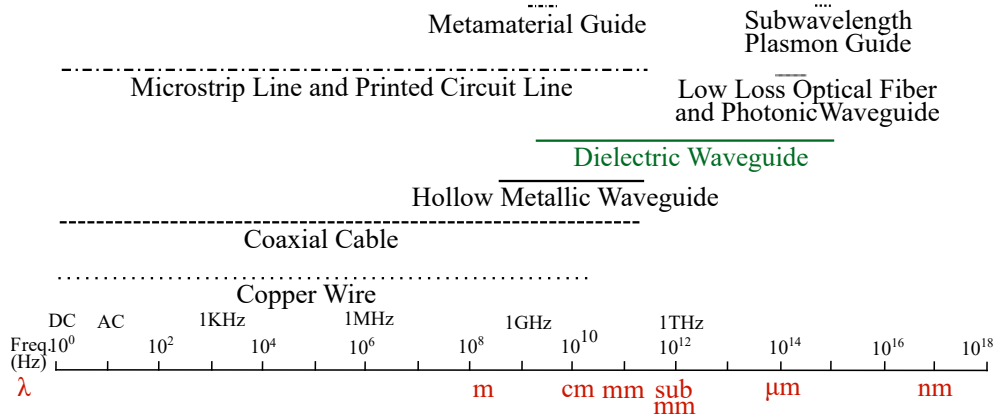


Figure 1.3: Different waveguide topologies and their spectral regions, based on [YS08].

mostly due to high metallic loss and surface roughness of the metal. Fig. 1.3 shows the utilizable range of several waveguide technologies. As an alternative, hollow waveguides can be used up to 300 GHz. They have low loss, but they are enclosed, rigid waveguides, which makes LC integration a very challenging task [Jos+13; Jos+15a], and are not very compatible to integrated planar circuits. Recently, dielectric waveguides (DWGs) have been of renewed focus at mmWs. Being a well-established technology in optics, they offer a very low-loss alternative to the conventional waveguide structures, and can serve as a good interconnect between individual chips at mmW [Dis+19; Wit+20]. The biggest challenge of DWGs is their open waveguide topology, which requires either shielding or cladding material, and their rather low compatibility to planar structures. In fact, low profiles are often key requirements in commercial applications.

A possible candidate for linking quasi-optical, dielectric approaches with the conventional planar electronics is the dielectric image line (DIL). Ever since its introduction in the 1950s [Kin52; Wil59], it has not been in the focus of industrial applications, even though it had been continuously researched during the 1970s [Ito76; WRG77; Sol79a]. With today's rapidly advancing technology, a re-assessment of its use in mmW applications is necessary, and [WS20] is an example for a recently published first guide to DIL design, based on the knowledge gained in the 1970s. Besides their general compatibility to printed circuit boards (PCBs), advantages of DWGs can be utilized in the DIL topology. Therefore, concepts like photonic crystal waveguides, discrete soldered components, multilayer PCB approaches, monolithic integrated circuits and artificially created dielectrics can co-exist on one PCB. LC has been recently combined with DWGs and showed overall good results [Ree20; Pol+20b; JGW20; Fer+22], with their main advantage being low loss. However, these approaches have been lacking the perspective of integration to larger systems, and especially their long response time is a drawback. The DIL topology allows either to reduce the profile of the dielectric waveguide in its fundamental mode ( $E_{11}^y$ ), or to



emulate a fully dielectric waveguide, by using a higher order mode and an increased cross-section of the DIL. The possibilities and capabilities of the DIL topology for cost-efficient tunable RF-frontends is investigated in this dissertation.

Chapter 2 serves as an introduction to LC. Its general EM and mechanical properties are covered and different compounds for microwave applications are compared.

The DIL topology is introduced in Chapter 3, and sources of loss are investigated by simulations and measurements. Two main modes of operation, the fundamental  $E_{11}^y$ -mode and the higher order, orthogonally polarized  $E_{11}^x$ -mode, are of particular interest, since they offer different advantages and many components in the following chapters are designed for either one of them. Different materials, which have to be compatible to the LC's permittivity range, are characterized, also covering adhesives, which are necessary for mounting the DIL on a metallic ground plane. The waveguide transitions used throughout this dissertation for all measurements are introduced and assessed in terms of loss, such that the measured components can be evaluated without the transitions lowering their performance.

Chapter 4 covers reconfigurable LC-DILs. These phase shifters are investigated in terms of the effect of LC integration, bias electrode design and performance. A higher focus is set on the  $E_{11}^y$ -mode in this chapter, and the corresponding LC-DIL is characterized for both temperature change and improved switch-on response time. The end of this chapter is formed by a comparison of  $E_{11}^y$ - and  $E_{11}^x$ -mode phase shifters, and their performance compared to various LC-phase shifters around 100 GHz.

Reconfigurable DIL-LC antennas are discussed in Chapter 5. Based on the results of Chapter 3, non-reconfigurable rod antenna arrays and leaky wave demonstrators are investigated first, followed by their integration with the reconfigurable lines presented in Chapter 4. The tunable rod antenna array and leaky wave antenna (LWA) operate in  $E_{11}^y$ -mode. Each of the introduced tunable antennas is compared to other LC-based antennas of similar working principle.

Chapter 6 shows the advancements towards low-cost, low-complexity realization of the introduced demonstrators from the previous chapters via additive manufacturing. Besides low-permittivity-based demonstrators, a new concept for combining low permittivity LC with high permittivity alumina is introduced and verified by a demonstrator in  $E_{11}^x$ -mode.

In Chapter 7, the results of this dissertation are summarized, and conclusions are drawn. With support from the results of Chapter 6, future trends, improvements and fields of studies are identified. Since the DIL is a cost-efficient, low-complexity topology, mass-producible, inexpensive (tunable) RF-frontends can ease the pressure of the rapidly increasing growth of demand for broadband wireless components.



## 2. Fundamentals of Liquid Crystal

The discovery of LC reaches back to the late 19th century. Friedrich Reinitzer first reported colorful changes when heating or cooling cholesteryl-benzoate. In addition, he found that cholesteryl-benzoate showed two different kinds of melting points [Rei88]. In between these two melting points, he observed the substance as a cloudy liquid. One year later, in 1889, Otto Lehmann first used the term "liquid crystal" in order to describe the observed behavior [Leh89]. Without any technical application, this phenomenon was not pursued with high academic effort. This changed with the beginning of the 1960s, when the optical birefringence of LC-mixtures gained increased interest. The accompanied research effort led to the nowadays well-established liquid crystal displays which are a core asset in every household, office, and portable electronics.

With the change to a new millennium, LC gained first research interest for microwave applications [LML93; WLJ02; Mul+04]. Due to its anisotropy in permittivity, LC can be used as a tunable material, which is essential for electronically reconfigurable microwave components such as phase shifters and filters. After first successful realizations of reconfigurable demonstrators at frequencies below 40 GHz, e.g. by [Mue+05; Goe+09; Gae+09; FBJ12; Jos+15a; Jos+15b; Pra+15; Wan+22a], companies, such as ALCAN Systems, Kymeta Corporation or NexTenna, are in the process of implementing LC-based antennas and systems at these frequencies. Nowadays, more and more effort is put into reconfigurable components at higher frequencies, starting at around 60 GHz, and beyond [Jos+18; Pol+20a; NIH18; Sun+20; Lan+20]. This is due to the increased demand for reconfigurable devices at these frequencies and the beneficial material properties of LC, which can remain very stable, even up to THz frequencies [Wei+13], while low power consumption can be ensured.

The term "liquid crystal" describes a special phase of matter, showing both characteristics of a liquid and of a crystal. One or more of these so-called mesophases can exist in between a strictly ordered crystalline structure, where each molecule is fixed both in position and orientation, and an isotropic liquid, where molecules may move and rotate arbitrarily. Hence, LC shows in its special mesophase(s) a certain degree of positional and/or orientational order of molecules, while movement of molecules is still possible. LC-compounds which solely change their phase by temperature are called thermotropic LCs, where a stepwise melting process through different mesophases with their corresponding degrees of order are present [New04]. If the determination of the LC phase is depending on the concentration of a solvent, they are called lyotropic LCs [Ste04]. Thermotropic LC can be further divided into groups

## 2. Fundamentals of Liquid Crystal

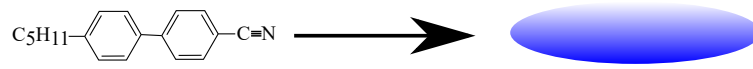


Figure 2.1: Chemical structure of an exemplary LC-molecule K15/5CB [YW06] (left), and the rod-shape used to represent calamitic LC-molecules in general throughout this dissertation (right).

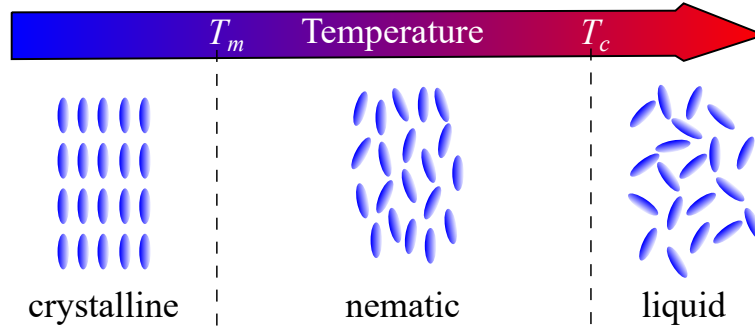


Figure 2.2: Schematic of thermotropic nematic calamitic LC. The crystalline phase transitions to the nematic phase at temperature  $T_m$  (melting point), which changes to the liquid phase at  $T_c$  (clearing point). The temperature increases from left to right.

determined by the molecular structure of an LC-molecule. The two most prominent groups are calamitic LCs, with rod-like molecules, and discotic LCs, which show disk-like molecules. LCs used in the microwave regime usually belong to the first category. Fig. 2.1 shows the chemical structure of an exemplary calamitic LC-molecule, 5CB, and a rod-shape representation, which is used throughout this dissertation to represent any LC-molecule for simplicity reasons. Fig. 2.2 depicts the different phases of a thermotropic calamitic LC in dependence of temperature. Calamitic LC-compounds can further be distinguished by the type of order present in the LC mesophase. The two most simple LC phases are the nematic phase and the smectic phase. In the nematic phase, the molecules maintain a preferred orientational order, but they can flow and reposition. In contrast, the smectic LC phase adds to the orientational order of nematic LC an additional positional order of molecules, since the molecules' centers of mass are arranged in layers. This work solely utilizes thermotropic nematic calamitic LCs.

In the remainder of this chapter an introduction to nematic liquid crystal, and how to describe its properties with respect to the molecule alignment, is given. Furthermore, due to the anisotropy arising from the rod-like molecule shape, magnetic and electric properties of nematic LC are reviewed, before control of the molecules' orientation with means of bias fields is presented. The end of this chapter is formed

by relevant properties of LC for mmW-applications.

## 2.1. Nematic Liquid Crystal

Nematic calamitic LC-molecules tend to align their long major molecule axis parallel to each other. Due to this behavior, caused by intermolecular forces, the temporal and spatial average macroscopic direction of molecules in a unit volume can be described by a unit vector  $\vec{n}$ , called the director.  $\vec{n}$  is defined to show the overall direction of the long molecule axis, since the short axes of nematic LC are usually uniaxial [YW06]. Even though nematic LC-molecules show polarity, a macroscopic influence on the director is not observed, and hence  $\vec{n} = -\vec{n}$ . Fig. 2.3 displays the relation of an individual molecule and its orientation, represented by  $\vec{a}$ , to the director  $\vec{n}$ . The deviation of  $\vec{a}$  to  $\vec{n}$  can be described by the azimuthal angle  $\Phi$ , and the polar angle  $\Theta$ , if  $\vec{n}$  is chosen such that it coincides with the  $z$ -axis. The probability that  $\vec{a}$  points towards the direction defined by  $\Theta$  and  $\Phi$  can be described by the orientational distribution function  $f(\Theta, \Phi)$ , where the probability of a molecule being oriented within  $\Theta + d\Theta$  and  $\Phi + d\Phi$  is  $f(\Theta, \Phi) \cdot \sin \Theta d\Theta d\Phi$  [YW06]. In the isotropic phase, each molecule points to an arbitrary direction. Hence, since there is equal probability for each direction of  $\vec{a}$ ,  $f(\Theta, \Phi) = \text{const.}$ . In addition, since nematic LCs are uniaxial, there is no preferred orientation of the short minor axes, eliminating dependency of  $\Phi$ , leading to  $f(\Theta, \Phi) = f(\Theta)$  [YW06]. A maximum for  $f(\Theta)$  is obtained if  $\Theta = 0, \pi$  (coinciding with  $\vec{n}$ ), and its minimum if the molecule's long axis is orthogonal to  $\vec{n}$ , i.e.  $\Theta = \pi/2, 3/2\pi$ .

The order parameter  $S$  serves as a measure to quantify the degree of orientational order present in an LC volume. It is given by the average value of the second-order Legendre polynomial [CH97]:

$$S = \langle P_2(\cos \Theta) \rangle = \left\langle \frac{3}{2} \cos^2 \Theta - \frac{1}{2} \right\rangle = \frac{\int_0^\pi f(\Theta) \left( \frac{3}{2} \cos^2 \Theta - \frac{1}{2} \right) \sin \Theta d\Theta}{\int_0^\pi f(\Theta) \sin \Theta d\Theta}. \quad (2.1)$$

In the case of equal alignment of each molecule with respect to  $\vec{n}$ , i.e.  $\Theta = 0$ ,  $S = 1$ .

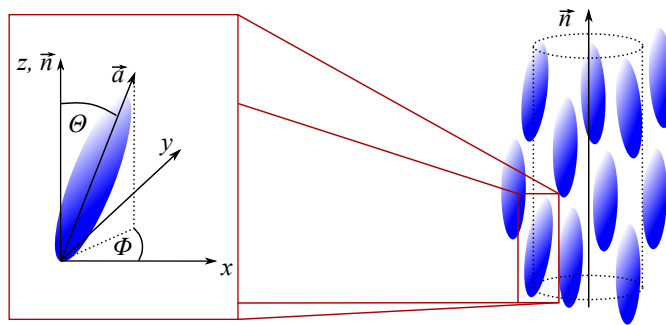


Figure 2.3: Orientation  $\vec{a}$  of a single molecule with respect to the director  $\vec{n}$  along the  $z$ -axis (left), which is part of the dashed unit volume on the right.

## 2. Fundamentals of Liquid Crystal

In the state of the least order, the isotropic phase, all molecules point with equal probability in each direction, hence,  $f(\Theta) = \text{const.}$ , and therefore,  $S = 0$  [CH97; YW06].  $S$  may also take negative values, if all molecules' long axes are perpendicular to the director [YW06]. In the nematic phase  $0 < S < 1$  holds. In order to describe  $S$  in dependence of temperature for thermotropic LC, a single molecule potential  $V$  can be used, which also considers intermolecular forces, e.g. van der Waals interactions

$$V(\Theta) = -\nu S \left( \frac{3}{2} \cos^2 \Theta - \frac{1}{2} \right), \quad (2.2)$$

where  $\nu$  is an orientational interaction constant [YW06; MS60]. The potential has a minimum when the molecule is oriented along  $\vec{n}$ , and its strength is directly proportional to  $S$ , and it is the same for parallel or antiparallel alignment to  $\vec{n}$ . With the single molecule partition function

$$Z = \int_0^\pi e^{-V(\Theta)/k_B T} \sin \Theta d\Theta, \quad (2.3)$$

where  $k_B$  denotes the Boltzmann constant, the probability of the molecule orienting along polar angle  $\Theta$  is:

$$f(\Theta) = \frac{e^{-V(\Theta)/k_B T}}{Z}. \quad (2.4)$$

Hence, solving Eqn. (2.4) for  $S$ , contained in  $V(\Theta)$ , yields:

$$S = \frac{1}{Z} \int_0^\pi P_2(\cos \Theta) e^{\nu S P_2(\Theta)/k_B T} \sin \Theta d\Theta. \quad (2.5)$$

From Eqn. (2.5),  $S$  can be determined numerically. A typical qualitative course of  $S$  in dependence of  $T$  is sketched in Fig. 2.4. As discussed,  $S = 1$  and  $S = 0$  in the crystalline and isotropic phase, respectively. At the transition to and from the nematic mesophase, a discontinuity of the function is present. The dependency of  $S$  on temperature is clearly visible in the nematic phase, where variations are typically between  $0.8 \geq S \geq 0.3$  [CH97]. This loss of order is directly observable in the temperature-dependent behavior of LC-components, which is also shown in

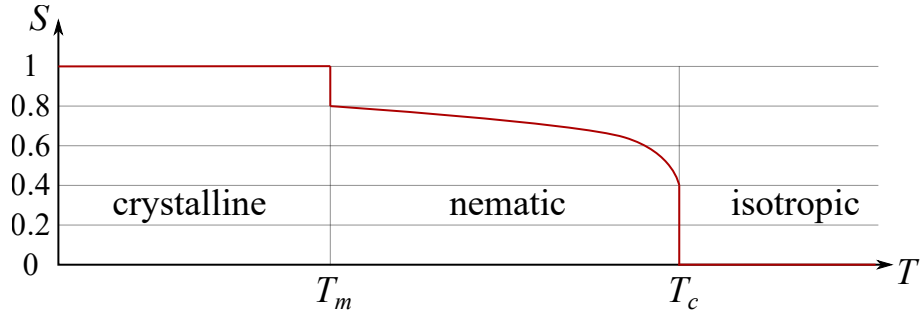


Figure 2.4: Schematic course of  $S$  in dependence of  $T$ , based on [Gae15].

Chapter 4. The quantitative behavior of the order parameter can also be obtained by the empirical formula [YW06]

$$S = \left(1 - \frac{0.98T}{T_c}\right)^{0.22}. \quad (2.6)$$

## 2.2. Magnetic and Electric Properties

Due to their molecule shape, LCs are diamagnetic and dielectric materials. Hence, external magnetic or electric bias fields induce a magnetic or electric dipole moment, resulting in a magnetization  $\vec{M}$  or a polarization  $\vec{P}$ . Due to high similarities regarding magnetic and electric properties, both are simultaneously elaborated in this section. Since inducing field and resulting magnetization/polarization do not necessarily need to be aligned, a tensor representation is necessary. The generalized expressions for magnetization and polarization can be written as

$$\vec{M} = \frac{\vec{B}}{\mu_0} - \vec{H} = \frac{1}{\mu} \vec{\chi}_m \vec{B} \quad (2.7) \quad \vec{P} = \vec{D} - \varepsilon_0 \vec{E} = \varepsilon_0 \vec{\chi}_e \vec{E}, \quad (2.8)$$

where the magnetic permeability  $\mu = \mu_0 \mu_r$  is the product of magnetic constant  $\mu_0$  and relative permeability  $\mu_r$ ,  $\varepsilon_0$  is the vacuum permittivity, and  $\vec{\chi}_m$  and  $\vec{\chi}_e$  are the magnetic and electric susceptibility tensor, respectively. In the simplest case, by assuming the director is pointing in  $z$ -direction, the tensors can be represented by a diagonal matrix:

$$\vec{\chi}_m = \begin{pmatrix} \chi_{m,\perp} & 0 & 0 \\ 0 & \chi_{m,\perp} & 0 \\ 0 & 0 & \chi_{m,\parallel} \end{pmatrix} \quad (2.9) \quad \vec{\chi}_e = \begin{pmatrix} \chi_{e,\perp} & 0 & 0 \\ 0 & \chi_{e,\perp} & 0 \\ 0 & 0 & \chi_{e,\parallel} \end{pmatrix}. \quad (2.10)$$

Here, the entries with a parallel ( $\parallel$ ) or perpendicular ( $\perp$ ) subscript represent the susceptibility when the field is parallel or perpendicular to the director. If the director is not aligned in  $z$ -axis the simple representation in the equations above can be transformed by coordinate transformation utilizing a rotational matrix  $\mathbf{R}$  [YW06]. With  $\vec{1}$  being the unit tensor and

$$\vec{B} = \mu_0(\vec{H} + \vec{M}) = \mu_0 \underbrace{(\vec{1} + \vec{\chi}_m)}_{\vec{\mu}_r} \vec{H} \quad (2.11) \quad \vec{D} = \varepsilon_0 \vec{E} + \vec{P} = \varepsilon_0 \underbrace{(\vec{1} + \vec{\chi}_e)}_{\vec{\varepsilon}_r} \vec{E} \quad (2.12)$$

## 2. Fundamentals of Liquid Crystal

a direct link from susceptibilities to the anisotropy of LC can be established. The maximum anisotropy of nematic LC is therefore given by the difference in magnetic permeability or dielectric permittivity as [Ste04]

$$\Delta\mu = \mu_{\parallel} - \mu_{\perp} \quad (2.13) \quad \Delta\varepsilon = \varepsilon_{\parallel} - \varepsilon_{\perp}. \quad (2.14)$$

Since mostly the difference in relative permittivity or permeability is of concern, the expressions  $\Delta\mu_r = \mu_{r,\parallel} - \mu_{r,\perp}$  and  $\Delta\varepsilon_r = \varepsilon_{r,\parallel} - \varepsilon_{r,\perp}$  are more applicable throughout this dissertation, and are therefore preferably used. The magnetic anisotropy is in general much smaller than the dielectric anisotropy. The former is usually in the range of  $10^{-6}$ , while the latter is 6 orders of magnitudes higher [Ste04; CH97]. Depending on the LC-compound and the frequency of operation, typical values in the mmW-regime are  $0.7 \leq \Delta\varepsilon_r \leq 1.1$ . Due to the small magnetic anisotropy,  $\mu_r \approx 1$  for any molecular orientation. However, strong bias magnets can still be utilized in order to change the orientation of the molecules, and hence change the effective permittivity of the LC volume. This concept is often used in laboratory environments to arrange the LC-molecules in a desired orientation, as described in the next section.

### 2.3. Bias Schemes

In order to utilize the dielectric anisotropy of LC for mmW-applications, the alignment of molecules with respect to an RF-field needs to be controlled. Applying a bias field directly influences the preferred orientation of the LC-molecules with respect to the bias field lines. The alignment of the director can be described if the energy density of a unit volume in presence of a bias field is considered [Ste04]. Magnetic and electric energy density are:

$$f_{mag} = -\frac{1}{2}\vec{B} \cdot \vec{H} = -\frac{1}{2}\mu_0\mu_{r,\perp}\vec{H}^2 - \frac{1}{2}\mu_0\Delta\mu_r(\vec{n} \cdot \vec{H})^2 \quad (2.15)$$

$$f_{el} = -\frac{1}{2}\vec{D} \cdot \vec{E} = -\frac{1}{2}\varepsilon_0\varepsilon_{r,\perp}\vec{E}^2 - \frac{1}{2}\varepsilon_0\Delta\varepsilon_r(\vec{n} \cdot \vec{E})^2. \quad (2.16)$$

The energy is minimized if director  $\vec{n}$  and the corresponding field are aligned in case of positive anisotropies,  $\Delta\mu, \Delta\varepsilon > 0$ , which means that the molecules will align parallel to the applied bias field lines. If the anisotropy is negative, the molecules align perpendicular to the field lines. In this dissertation, the LC-compounds show positive anisotropy only. Besides the pure electric and magnetic energy density, various other aspects, such as boundary conditions of a finite cavity, which cause mechanical forces on the molecules, affect the director along the LC cavity. Usually, the resulting deformation of the director occurs over a distance much larger (several  $\mu\text{m}$ ) than the molecular size (several nm) [Jos18; YW06]. Hence, this deformation can be described by continuum theory, similar to the elastic theory of solids [Fra58; Ose33; Zoc33]. The energy  $W$  in a volume of LC is dependent on the elastic, electric



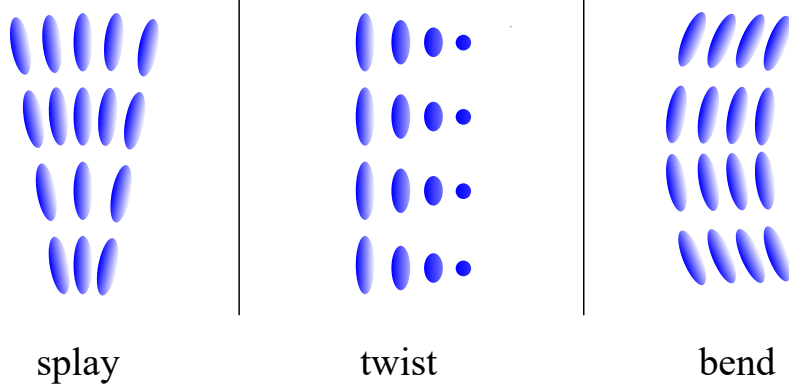


Figure 2.5: Schematics of two-dimensional elastic deformations of LC.

and magnetic properties, and can be obtained by integrating over the corresponding energy densities in the volume of the LC cavity:

$$W = \iiint_V f dV = \iiint_V (f_{elast} + f_{el} + f_{mag}) dV. \quad (2.17)$$

The premise for the application of the continuum theory is that the molecules are only allowed to rotate in fixed positions. The LC-molecules tend to align themselves parallel to each other, such that the molecule potential  $V$  (Eqn. (2.2)) is lowest for each molecule. Hence, in order to achieve an elastic deformation, energy has to be introduced to this system, e.g. by bias fields or mechanical boundary conditions. Having covered the magnetic and electric energy density in Eqns. (2.15) and (2.16), the elastic energy density needs to be attended. There are three possible elastic deformations, namely splay, twist and bend. They are illustrated in Fig. 2.5. The contribution of each of these deformations to the elastic energy density, also referred to as Frank-Oseen energy density is [Ste04]

$$f_{elast} = f_{splay} + f_{twist} + f_{bend} = \frac{1}{2}K_1(\nabla \cdot \vec{n})^2 + \frac{1}{2}K_2(\vec{n} \cdot \nabla \times \vec{n})^2 + \frac{1}{2}K_3(\vec{n} \times \nabla \times \vec{n})^2, \quad (2.18)$$

where  $K_1$ ,  $K_2$  and  $K_3$  are elastic constants different for each LC-compound, and dependent on temperature and order parameter  $S$ . If the surface is big compared to the LC volume, a surface term  $\frac{1}{2}(K_2 + K_4)\nabla \cdot ((\vec{n} \cdot \nabla)\vec{n} - (\nabla \cdot \vec{n})\vec{n})$  has to be added to Eqn. (2.18). In this dissertation, only big volumes compared to the surface are present, which is why this term is omitted. Following Eqns. (2.15), (2.16) and (2.18), the orientation of LC can be achieved in three different ways:

- **Mechanical:** By structuring the surface of the cavity, specific surface anchoring of the molecules is created [YW06], most commonly aligned parallel to the surface. Usually, this is achieved by means of a polyimide film on a carrier substrate which is mechanically rubbed in one direction. This causes grooves in which the LC-molecules align in parallel [Tak+05]. This technique is only feasible for low cavity heights below 100  $\mu\text{m}$ .

## 2. Fundamentals of Liquid Crystal

- **Electrical:** Electrodes of different potential are used to create an electric field in the LC cavity. As shown above, the molecules align in parallel to the applied field.
- **Magnetical:** The electrodes of electrical bias can be interchanged with magnets. Similar to the electric case, the molecules align in parallel to the applied magnetic bias field.

In this dissertation, only the latter two are used, since we are dealing with volumetric structures with cavities higher than 100  $\mu\text{m}$ . In addition, a hybrid electro-magnetic bias, which was first suggested by [LML93], is also applied in this dissertation. As mostly electric bias is used for continuously tunable microwave LC-devices, this form of bias is addressed in this section. It is best understood with the example of a parallel-plate capacitor, shown in Fig. 2.6. Throughout the following formulas, only the splay deformation is considered. If the other deformations are of concern, the elastic constant  $K_1$  has to be exchanged for the corresponding elastic constant of interest. Assuming an infinitely wide parallel-plate capacitor with plate distance  $h_{LC}$ , the voltage necessary to form an equilibrium between the elastic forces and the electric forces, known as the threshold voltage  $V_{th}$ , is [Ste04]

$$V_{th} = \pi \sqrt{\frac{K_1}{\varepsilon_0 \Delta \varepsilon_r}}. \quad (2.19)$$

Below this voltage no change in orientation of the molecules can be achieved by the resulting weak electric field. They remain in their original orientation, in case of Fig. 2.6 tangential to the metallic plates of the capacitor. If the bias voltage  $V_b$  is increased beyond  $V_{th}$ , the so-called Fredericksz Transition sets in, and the molecules

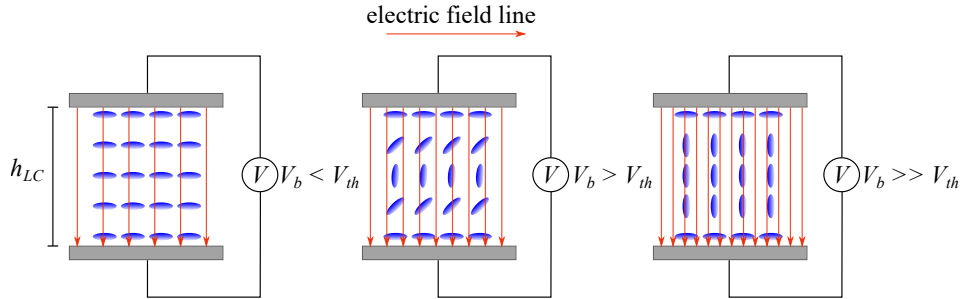


Figure 2.6: Representation of the Fredericksz Transition in a parallel-plate capacitor. A pre-orientation of the molecules tangential to the capacitor plates, e.g. by an alignment layer, is assumed. The orientation of the molecules is influenced by the field strength, i.e. the bias voltage between the capacitor plates. If the voltage is below  $V_{th}$ , no change in molecular alignment can be achieved (left). By surpassing  $V_{th}$ , the molecules start to align along the field lines due to higher field strength (middle), until nearly perfect alignment of the molecules and the field lines is achieved (right).

## 2.4. Characteristic Properties for Microwave Applications

start to align their long axis weakly along the field lines. The stronger the voltage, the more the molecules are aligned along the field lines, until the molecules are perfectly aligned. Depending on the field strength, and therefore on the voltage, the molecules undergo their transition to their final orientation with different response times. Especially mechanical attributes, such as the elastic constants and rotational viscosity  $\gamma_{rot}$  are playing a key role for this time, and are different for each LC-compound. Considering these aspects, the switch-on response time is [YW06]

$$\tau_{on} = \frac{\gamma_{rot}}{\varepsilon_0 \Delta \varepsilon_r (E^2 - E_{th}^2)} = \frac{\gamma_{rot} h_{LC}^2}{K_1 \pi^2 (V_b^2 / V_{th}^2 - 1)}. \quad (2.20)$$

On the other hand, if the voltage is dropped to zero and no field forces the molecules to a specific alignment, they are returning to the lowest energetic state, which is their initial state. This switch-off response time is again depending on the mechanical properties of the LC, and is similar to Eqn. (2.20) with the electric field contribution dropped:

$$\tau_{off} = \frac{\gamma_{rot} h_{LC}^2}{K_1 \pi^2}. \quad (2.21)$$

It can be observed that, besides material parameters and  $V_b$ ,  $h_{LC}$  has high impact on the response times, since it affects both switch-on and switch-off response time in a quadratic manner. If high LC cavities have to be employed, the much slower switch-off response time can be overcome by employing more than two electrodes. In the simplest case, a second pair of electrodes is added to the right and left of a cavity. Therefore, both alignments are actively achieved, and there is no reliance on passive re-alignment. The second pair of electrodes can also be replaced by permanent magnets, forcing the molecules back to their pre-alignment when the bias voltage is released.

Similar relations are true for purely magnetic bias with permanent magnets. This form of bias is solely used for proof-of-concept and characterization purposes, due to lack of easy reconfiguration. Replacing the electrodes of the capacitor in Fig. 2.6 by permanent magnets, threshold field strength  $H_{th}$  and the corresponding switch-on response time is given by [Ste04]

$$H_{th} = \frac{\pi}{h_{LC}} \sqrt{\frac{K_1}{\Delta \chi_m}} \quad (2.22)$$

and

$$\tau_{on,mag} = \frac{\gamma_{rot}}{\Delta \chi_m (H^2 - H_{th}^2)} = \frac{\gamma_{rot}}{\Delta \chi_m H^2 - K_1 \pi^2 / h_{LC}^2}. \quad (2.23)$$

## 2.4. Characteristic Properties for Microwave Applications

In microwave applications, several properties of LC-compounds are of special interest. For highest possible continuous tuning, the anisotropy of the relative permittivity  $\Delta \varepsilon_r$  at the frequency of operation is desired to be high.  $\Delta \varepsilon_r$  can vary greatly

## 2. Fundamentals of Liquid Crystal

in dependence of frequency. While comparably high values of  $\Delta\varepsilon_r$  can be present at 1 kHz, the frequency usually used for biasing, it reduces in general at higher frequencies. Since all bias fields are static or operate at low frequencies, these values are paramount for the control of LC orientation, and therefore its interaction with microwaves. The material tunability of an LC-compound has been introduced as [Fer+22]

$$\tau_{LC} = \frac{\varepsilon_{r,\parallel} - \varepsilon_{r,\perp}}{\varepsilon_{r,\parallel}} = \frac{\Delta\varepsilon_r}{\varepsilon_{r,\parallel}}. \quad (2.24)$$

Besides the desire for a high material tunability at mmW-frequencies, the material loss, described by the loss tangent ( $\tan \delta$ ) of the LC-compound in each alignment state, is crucial for the performance of any RF-component. The relation of tunability and the maximal, orientation-dependent, loss of the mixture results in the material quality factor

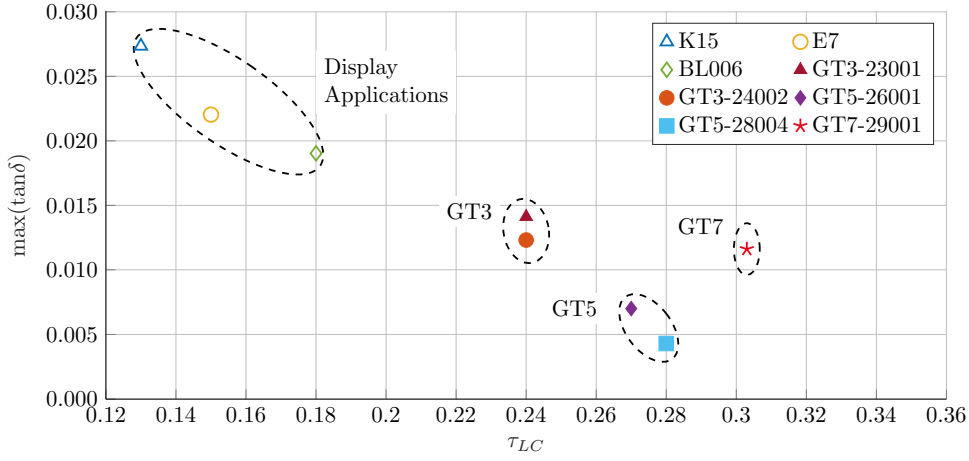
$$\eta_{LC} = \frac{\tau_{LC}}{\max(\tan \delta)}, \quad (2.25)$$

with  $\tan \delta = \frac{\text{Im}(\varepsilon_r)}{\text{Re}(\varepsilon_r)}$ . In order to obtain these parameters, different material characterization techniques have been employed at different frequencies [Göll10; Kar14; Wei17; ZFB18; Pol+19a; Yu+19]. On the one hand, broadband measurements cover a wider frequency range, but are less precise in parameter acquisition. On the other hand, resonant methods are very precise, but their realization at frequencies beyond 60 GHz is challenging due to the constraints of physical size. A comprehensive overview of material parameters obtained by resonant and broadband methods is given in [ZFB18]. While first demonstrations of tuneable microwave components were conducted with LC-compounds designed for display applications, development of mixtures tailored to the micro- and millimeterwave regime started in the last decade. Table 2.1 serves as a direct comparison of the parameters of LCs for display

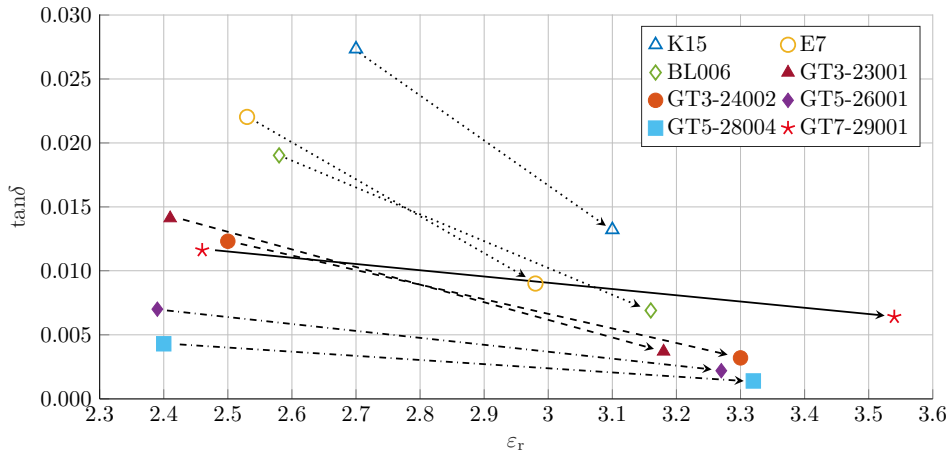
Table 2.1.: Characteristic parameters of different LC-mixtures [FW17; WFS21]. All values are given at room temperature of 20 °C.

		<i>Display</i>		<i>Microwave</i>	
	<b>Mixture</b>	<b>E7</b>	<b>BL006</b>	<b>GT3-23001</b>	<b>GT7-29001</b>
19 GHz (appli- cation)	$\varepsilon_{r,\perp}$	2.53	2.58	2.41	2.46
	$\varepsilon_{r,\parallel}$	2.98	3.16	3.18	3.53
	$\tan \delta_{r,\perp}$	0.022	0.0191	0.0141	0.0116
	$\tan \delta_{\parallel}$	0.009	0.0069	0.0037	0.0064
	$\tau_{LC}$	0.15	0.184	0.244	0.303
1 kHz (bias)	$\varepsilon_{r,\perp}$	5.2	5.2	4.0	4.6
	$\varepsilon_{r,\parallel}$	19.5	22.3	8	26.7
	$\Delta\varepsilon_r$	14.3	17.1	4.0	22.1
	$\gamma_{rot}$ (mPas)	254	569	727	307
	$T_C$ (°C)	58.0	118.5	173.5	124

## 2.4. Characteristic Properties for Microwave Applications



(a) Maximum loss tangent versus tunability.



(b) Loss tangent versus relative permittivity in dependence of molecular alignment. The beginning of the arrow marks the perpendicular alignment ( $\epsilon_{r,\perp}$ ), and the arrow tip indicates the parallel alignment ( $\epsilon_{r,\parallel}$ ). The arrow line style differs for each group (e.g. GT3 and GT5) shown in (a).

Figure 2.7: Comparison of different LC-compounds for display applications and those tailored specifically for microwave applications by Merck KGaA, Darmstadt, Germany, at 19 GHz. Graphics based on [Fer+22], data from [Fer+22; FW17; ZFB18; WFS21].

## 2. Fundamentals of Liquid Crystal

applications compared to LCs for microwave applications. Especially Merck KGaA, Darmstadt, Germany, is commercializing LC for microwave applications in their licriOn™ series. GT3-23001 and GT7-29001 are especially tailored for microwave applications. The difference in the performance parameters of LC for display applications, and the different generations of Merck’s specific microwave LCs is visualized in Fig. 2.7. While tuneability in general increased, the material loss at 19 GHz steadily decreased. The increased tuneability of GT7 is paid for by increased material loss, when compared to GT5 mixtures. However, GT5 suffered from high  $\gamma_{rot}$ , which leads to slow response times. Moreover, less deviation in  $\tan \delta$  is present with each iteration of the GT-variants (Fig. 2.7 (b)), such that different alignments states of LC are less susceptible to differences in loss. In this dissertation, mostly GT7-29001 is used in simulations and measurements. It shows stable material properties, which are decreasing slightly with frequency and temperature [Pol23], as Tab 2.2 and Fig. 2.8 indicate. The development of new microwave LC-compounds is an ongoing trend [FW17; WFS21], and innovative concepts are investigated to influence the behavior of these compounds. In [Lan+20; BKG16] first experimental results of mixtures of LC and graphene or microfibers are reported. The stable material properties of LC up to THz-frequencies [Wei+13] are very promising for translating the concepts introduced in this dissertation to applications at higher frequencies.

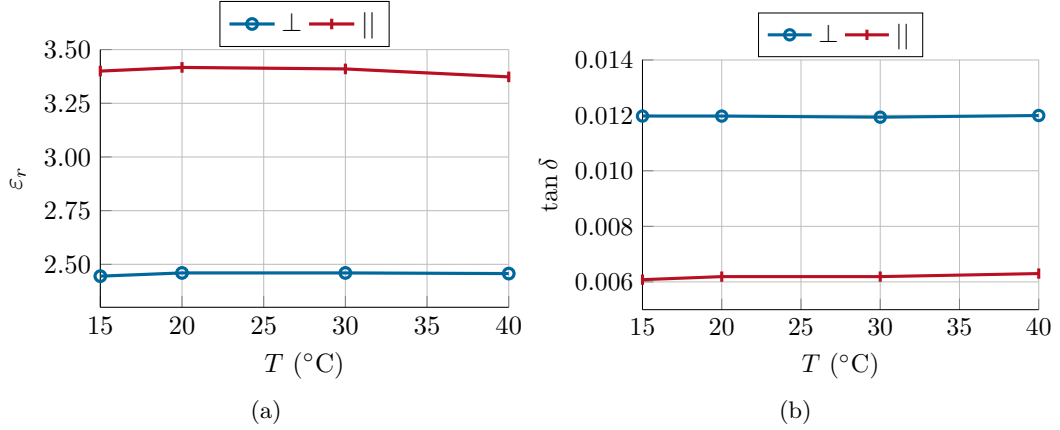


Figure 2.8: Permittivity and loss tangent of GT7-29001 at 60 GHz for different temperatures [Pol23].

Table 2.2.: Characteristic parameters of LC-mixture GT7-29001 at 19 GHz and 60 GHz. All values are given at room temperature of 20 °C.

$f$ (GHz)	$\epsilon_{r,\perp}$	$\epsilon_{r,\parallel}$	$\tan \delta_{\perp}$	$\tan \delta_{\parallel}$	$\tau_{LC}$	$\eta_{LC}$	Reference
19	2.46	3.53	0.0116	0.0064	0.303	26.13	Merck KGaA
60	2.46	3.42	0.0119	0.0062	0.281	23.59	[Pol23]

### 3. Dielectric Image Lines

Dielectric image lines (DILs) were proposed in the 1950s for the micro- and millimeter wave range, first by King and Wiltse with a semicircular cross-section [Kin52; KS58; Wil59]. Being a rather unsuccessful topology, mostly due to the fact that mmW-technology was not very advanced at this time, it took more than 10 years until new approaches were undertaken. Knox and Toullos [KT70; Kno76] reshaped the cross-section to a rectangular one in 1970. This redesign came at a time of refreshed interest in mmW-frequencies for technical applications, and results from the thriving, well-developed optical circuit design were incorporated in Knox's and Toullos' research. Several proposals on waveguide theory, wave launchers [Ito76; Sol79b], couplers [MIM75; Ito76], filters [Ito77; SI78; Sol79b; SW85] and antennas [Ito77; WRG77; Sol79b] followed in the 70s and 80s [WS20]. Various fabrication approaches, such as gluing, clamping, casting, or photolithographic and thick film processes were investigated and compared [Sol76; Hei75]. Tests were mostly conducted at frequencies from 20 GHz to 40 GHz, but the DIL circuits stood no chance compared to the rapidly advancing planar technologies, such as microstrip or coplanar waveguides, which are more compatible to discrete components.

With the ever-increasing frequency of operation as a means to produce high absolute bandwidths, future communication standards strive for operating frequencies above 100 GHz. Hence, the increasing conductor loss of planar circuits is becoming a bigger problem. In the search for low-loss alternatives, dielectric waveguides and their close relative, the DIL, are becoming relevant for researchers again [PW06b; DH11; JLR12; DH13; Xin+17; WS20]. Especially results covering DIL-antennas [PW06a; PW07; Wu+12; Xin+17; PBA17; PBA18] are of renewed interest. Fully dielectric waveguides (DWGs) have been successfully combined with LC in recent years [Ree+17b; Ree+17a; Jos+18; Pol+20b]. However, these first designs are of rather unique topologies which are hard to integrate into conventional systems. Besides the topology itself, the bias network, necessary to control the LC, is rather bulky in these first demonstrators, and results in long switch-on response times.

In contrast to DWGs, the DIL is compatible to conventional PCB layouts, utilizing their top metallization as the ground plane. This allows more compact design when aiming for LC integration. The insertion of LC into a DIL demands usually for a low-permittivity dielectric to be used as the hosting material, which is why the main focus in this dissertation is on those low-permittivity dielectrics. Low-permittivity dielectrics are beneficial for antenna applications, but result in larger physical size. A new concept on how to circumvent this restriction is presented in Chapter 6.

This chapter serves as an introduction to the DIL topology and its different modes of operation, linked to different distributions of metallic and dielectric loss. After

### 3. Dielectric Image Lines

covering the fundamentals, the material selection and the waveguide transitions used throughout this dissertation are introduced. As an example on how to interpret the theoretical results obtained in the first sections of this chapter, DIL crossovers are investigated at the end of the chapter.

## 3.1. Waveguide Topology

This dissertation focuses solely on rectangular cross-sections, since they offer a clear distinction between orthogonal modes, which will play an important role throughout the following chapters. In addition, manufacturing a rectangular cross-section with subtractive methods such as milling is of low complexity. The DIL topology is explained best by comparing it to its fully dielectric counterpart. Fig. 3.1 displays the cross-section of a DWG next to its equivalent DIL. By introducing a metallic half-space, a DIL can represent a DWG of twice its height, since the metallic half-space produces an image of the field distribution above it. This phenomenon can be described by the well-known image theory, which is extensively used e.g. when describing fields of antennas above a ground plane [Bal05]. Throughout the establishment of DILs, different approaches for the description of the field distribution of DILs have been developed [Goe69; Mar69; KT70; SW78]. They are showing very similar results, with main differences occurring in cases where the EM wave is only weakly guided by the waveguide [YS08; WS20]. In this section, the approximate approach of Knox and Toullos [KT70] is briefly revised in order to describe the field and propagation properties of DILs. This approach is closely related to Marcatili's theory of an open DWG [Mar69], which was the first to provide an approximation yielding largely good results for both the electromagnetic fields and the propagation coefficients. Fig. 3.2 displays the nature of the approach. The space around the DIL of height  $h$  and width  $w$  is first divided into different field areas ① to ⑤. In line with Marcatili's approach, the field in area ⑤ is considered to be negligibly small, thus no coupling between area ② and ③ via ⑤ is assumed. Area ④ is the ground

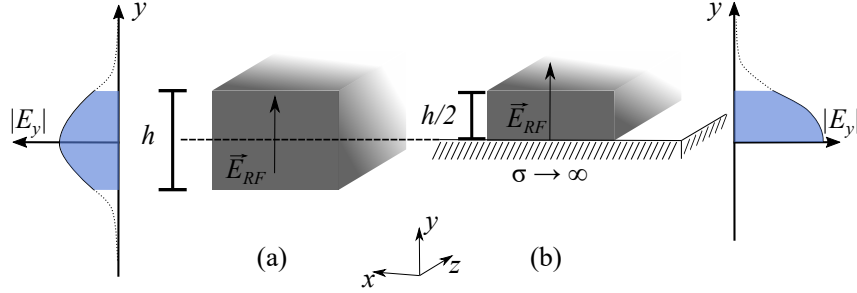


Figure 3.1: (a) Fully dielectric waveguide of quadratic cross-section and (b) its dielectric image line counterpart, with corresponding qualitative field distributions. The field confined in the dielectric is shaded in blue and the evanescent components are indicated with dotted lines.



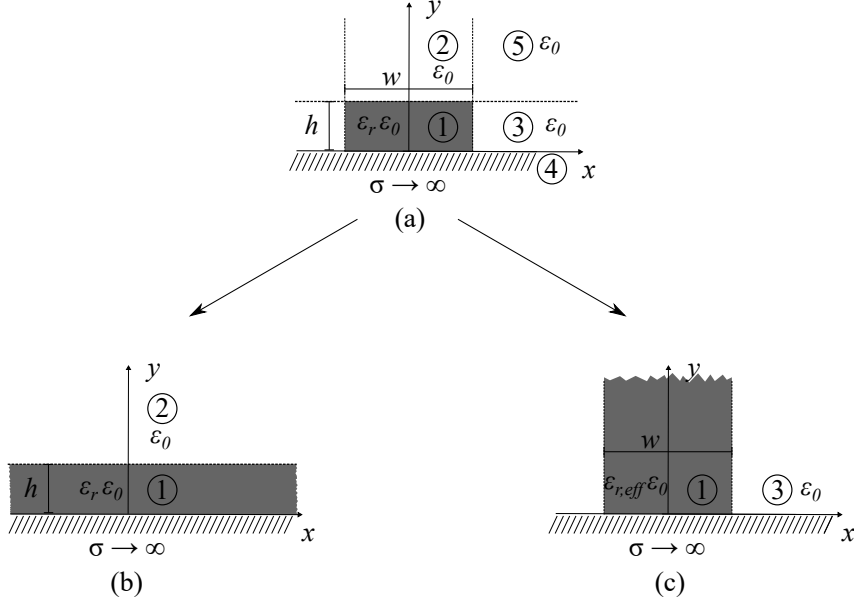


Figure 3.2: Decomposition of the DIL for analysis according to [KT70]. (a) Cross-section of a DIL with corresponding field regions ① to ⑤. (b) Slab waveguide of infinite width and (c) narrow, infinitely high DIL with effective permittivity  $\epsilon_{r,eff}$ .

plane, assumed as perfectly conducting. The wave equations derived from Maxwell's equations for the structure in Fig. 3.2 (a) are

$$\frac{\partial^2 H_\nu}{\partial x^2} + \frac{\partial^2 H_\nu}{\partial y^2} + \frac{\partial^2 H_\nu}{\partial z^2} + \omega^2 \epsilon_0 \epsilon_{r,\nu} \mu_0 H_\nu = 0, \quad (3.1)$$

$$\frac{\partial^2 E_\nu}{\partial x^2} + \frac{\partial^2 E_\nu}{\partial y^2} + \frac{\partial^2 E_\nu}{\partial z^2} + \omega^2 \epsilon_0 \epsilon_{r,\nu} \mu_0 E_\nu = 0. \quad (3.2)$$

In the equations above, it is assumed that the electromagnetic wave propagates along  $z$ -direction, described by  $e^{j\beta_z z}$ , with  $\beta_z$  being the phase coefficient.  $\nu = 1, \dots, 5$  represents the corresponding field regions. The analysis starts with the decomposition of the structure in Fig. 3.2 (a) to the dielectric slab shown in Fig. 3.2 (b). It extends infinitely in  $x$ - and  $z$ -direction, but is of finite height  $h$ . Hence, only field regions ① and ② are present. In its fundamental mode, the main field components in the transverse plane are the  $E_y$  and  $H_x$  components, and the  $E_x$  and  $H_y$  components are negligibly small. Due to the infinite extension in  $x$ , there is no dependency on this coordinate. The  $H_x$ -components in region ① and ② can be set up as

$$H_{x1} = A_1 \cos(k_y y) e^{-j\beta_z z}, \quad (3.3)$$

$$H_{x2} = A_2 e^{k_{y0} y} e^{-j\beta_z z}, \quad (3.4)$$

with the arbitrary constants  $A_1, A_2$ .  $k_y, k_{y0}$  represent the wave numbers inside the dielectric and outside, respectively. In region ② the field decays in an evanescent

### 3. Dielectric Image Lines

manner. The cosine dependency in region ① is necessary to satisfy the boundary condition for the  $E_y$  component in region ① at the ground plane ( $y = 0$ ), and hence:

$$E_{y1} = -A_1 \frac{\beta_z}{\omega \varepsilon_0 \varepsilon_r} \cos(k_y y) e^{-j\beta_z z}, \quad (3.5)$$

$$E_{y2} = -A_2 \frac{\beta_z}{\omega \varepsilon_0} e^{-k_{y0} y} e^{-j\beta_z z}, \quad (3.6)$$

$$E_{z1} = -jA_1 \frac{k_y}{\omega \varepsilon_0 \varepsilon_r} \sin(k_y y) e^{-j\beta_z z}, \quad (3.7)$$

$$E_{z2} = -jA_2 \frac{k_{y0}}{\omega \varepsilon_0} e^{-k_{y0} y} e^{-j\beta_z z}. \quad (3.8)$$

After applying the boundary condition at  $y = h$  and mathematical simplifications the relation of the wave numbers in  $y$  becomes [WS20]

$$k_y h = n \frac{\pi}{2} - \arctan \frac{k_y}{\varepsilon_r k_{y0}}, \quad n = 1, 3, 5, \dots, \quad (3.9)$$

in which  $k_{y0}$  can be replaced by  $k_{y0} = \sqrt{\omega^2 \varepsilon_0 \mu_0 (\varepsilon_r - 1) - k_y^2}$ , yielding  $k_y$ .

This result is now used to calculate the second decomposition, the narrow and high DIL in Fig. 3.2 (c). Instead of using the relative permittivity  $\varepsilon_r$  for this analysis, the effective dielectric constant

$$\varepsilon_{r,eff} = \varepsilon_r - \frac{k_y^2}{k_0^2} \quad (3.10)$$

is employed to describe the structure, which is the main difference to Marcatili's approach. In the analysis of the narrow and infinitely high DIL, similar assumptions as in the case of the slab waveguide are made: fields are independent of the  $y$ -coordinate, and dominant fields are  $H_x$ ,  $H_z$ , and  $E_y$ , which have to be distinguished between regions ① and ③. Following this approach, we similarly find

$$k_x w = n \frac{\pi}{2} - \arctan \frac{k_x}{k_{x0}}, \quad n = 0, 1, 2, 3, \dots, \quad (3.11)$$

which can be used to determine  $k_x$  with the help of  $k_{x0} = \sqrt{\omega^2 \varepsilon_0 \mu_0 \varepsilon_{r,eff} - k_x^2}$ . With these results at hand we can conclude the phase coefficient  $\beta_z$  of the line to be

$$\beta_z = \sqrt{\omega^2 \varepsilon_0 \varepsilon_{r,eff} \mu_0 - k_x^2}. \quad (3.12)$$

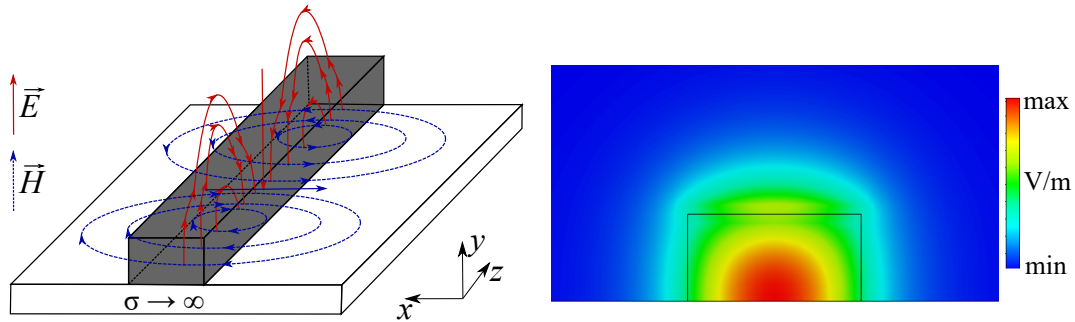
Therefore,  $\beta_z$  depends on the physical parameters  $\varepsilon_r$ ,  $w$  and  $h$ . With modern 3D simulation tools, the cross-section of a DIL with fixed permittivity can be fine-tuned such that a desirable number of modes is reached, and further investigations e.g. on radiation loss at bends etc. can be conducted. In this dissertation, CST Studio Suite is used for these simulations, and results are shown in the following sections.

### 3.1.1. Operating Modes

Due to the boundary condition for the tangential electric field at the ground plane  $E_{\text{tan}} = 0$ , certain mode configurations in DILs cannot exist, which are supported in a fully dielectric waveguide. The nature of modes in a DWG/DIL are hybrid, i.e. neither pure TE- nor TM-modes, since both E- and H-field show components in the direction of propagation. They are generally labelled as HE-modes, but a more precise way to describe a specific mode is the  $E_{nm}^y$  and  $E_{nm}^x$  nomenclature. Assuming the propagation in  $z$ -direction,  $n$  and  $m$  are the mode numbers in  $x$ - and  $y$ -direction, and the superscript  $x$  or  $y$  show the dominant polarization of the  $E$ -field, neglecting the field component in  $z$ -direction. Fig. 3.3 displays the field distribution of the hybrid fundamental  $E_{11}^y$ -mode. The coordinate system in Fig. 3.3 will be the corresponding coordinate system for all DIL components investigated in this dissertation. Especially, two field configurations are of main interest:

1. The dominant  $E_{11}^y$ -mode
2. The higher-order  $E_{11}^x$ -mode, orthogonally polarized to the  $E_{11}^y$ -mode.

The field distribution of these two modes and their relation to a DWG are visualized in Fig. 3.4. The  $E_{11}^y$ -mode is always the dominant mode of any DIL. As sketched in Fig. 3.4, the modes supported by a DIL are dependent on its cross-section. Furthermore, shown in the previous section, frequency and permittivity of the DIL have to be considered. Hence, generalized dispersion diagrams utilize the normalized frequency  $B = 4fh\sqrt{\varepsilon_r - 1}/c_0$  in order to take account of the various dependencies. Regardless, in this section mostly the influence of one parameter on the dispersion characteristics are shown, while the others are fixed. Therefore, the following dispersion diagrams are always plotted specifically versus  $f$  or  $h$ . The corresponding



(a) Electric and magnetic field lines along a DIL. (b) Average  $E$ -field at 110 GHz at the DIL's cross-section, simulated with CST Studio Suite.

Figure 3.3: (a) Field distribution of the  $E_{11}^y$ -mode and (b) its average  $E$ -field strength along the cross-section of the waveguide. The dielectric is of permittivity  $\varepsilon_r = 2.53$  and has a cross-section of  $0.9 \text{ mm} \times 1.8 \text{ mm}$ .

### 3. Dielectric Image Lines

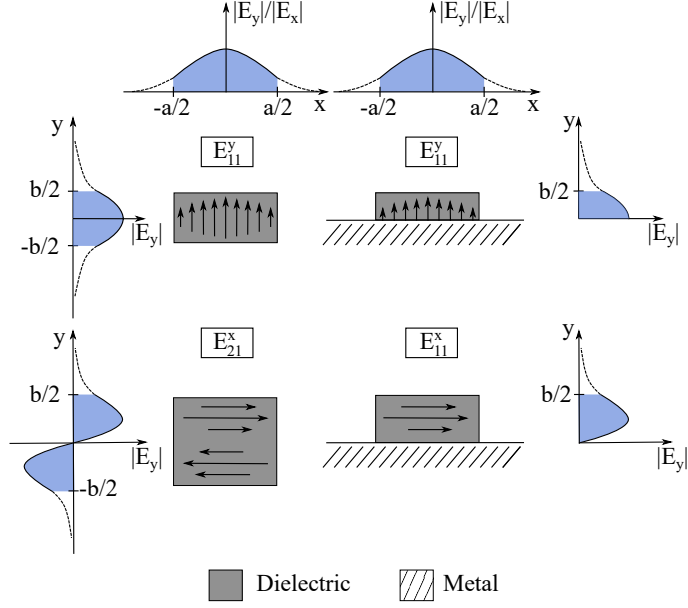


Figure 3.4: Field distribution for the two main DIL modes (right) and their counterpart in DWG topology (left).

propagation constant  $\beta_z$ , is usually normalized to  $\Delta = (\beta_z^2 - k_0^2)/(k_1^2 - k_0^2)$ , with  $k_0 = 2\pi f\sqrt{\mu_0\varepsilon_0}$  and  $k_1 = 2\pi f\sqrt{\mu_0\mu_r\varepsilon_0\varepsilon_r}$  being the wave numbers in free space and the DIL's material, respectively. Applying this normalization means that with increasing  $B$ ,  $\Delta$  increases towards 1 (wave fully guided in the material of the DIL). Below cutoff  $\Delta = 0$  (wave fully guided in free space). Fig. 3.5 shows a dispersion diagram in W-band for a DIL with cross-section  $h \times w = 0.9 \text{ mm} \times 1.8 \text{ mm}$ , composed of different dielectrics. It is evident that at low permittivity, a small increase of 0.33 in  $\varepsilon_r$  from Rogers RT5880 to C-LEC Plastics Rexolite 1422 already results in higher  $\Delta$ , while at high permittivity, an increase in relative permittivity  $\varepsilon_r$  by 3.1 from Premix PPE650 to Alumina does not significantly change the dispersion characteristics of the well-guided mode.

Since most work in this dissertation is done on the basis of Rexolite 1422, Fig. 3.6 shows specifically the properties of a DIL composed of this material. Especially when changing the height  $h$  of the DIL, while keeping  $w = 1.8 \text{ mm}$ , the cut-on of the higher-order modes can be controlled. Fig. 3.6 (a) shows true single mode operation is obtained at 95 GHz with  $h \leq 0.9 \text{ mm}$ . For larger  $h$ , the orthogonally polarized  $E_{11}^x$ -mode may propagate as well. The  $E_{21}^y$ -mode starts to propagate at  $h \approx 1.2 \text{ mm}$ , but is due to the small fixed width  $w$  not increasing rapidly in  $\Delta$ , and therefore extremely weak bound to the DIL. With proper waveguide transitions at the DILs' ends, the  $E_{11}^x$ -mode and the  $E_{11}^y$ -mode can be effectively suppressed (see Section 3.3). When considering broadband behavior (Fig. 3.6 (b)), we observe the natural shift in cut-on frequency towards lower values with increasing  $h$ . Two distinct values,  $h = 0.9 \text{ mm}$

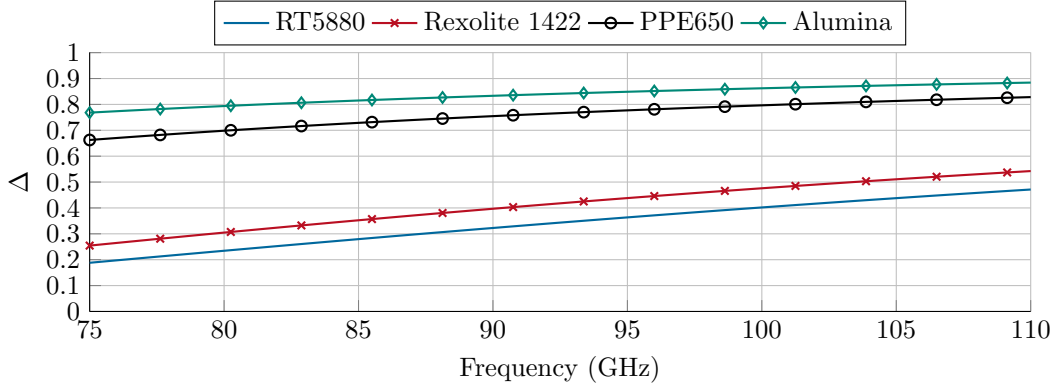
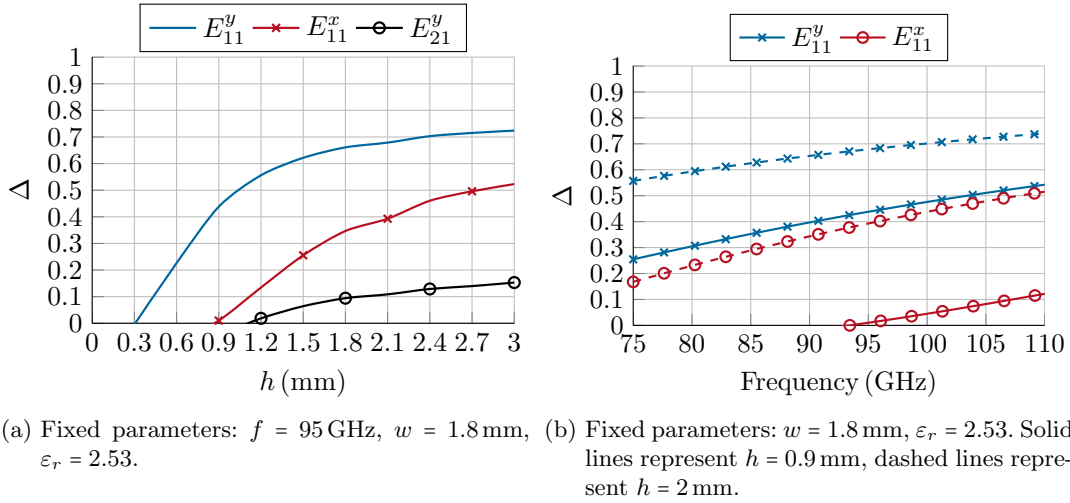


Figure 3.5: Dispersion diagram of the  $E_{11}^y$ -mode of a DIL composed of different materials, but with fixed cross-section  $0.9 \text{ mm} \times 1.8 \text{ mm}$ . The corresponding permittivities are:  $\varepsilon_{r,\text{RT}} = 2.2$ ,  $\varepsilon_{r,\text{Rex}} = 2.53$ ,  $\varepsilon_{r,\text{PPE}} = 6.5$ , and  $\varepsilon_{r,\text{Alu}} = 9.6$ .



(a) Fixed parameters:  $f = 95 \text{ GHz}$ ,  $w = 1.8 \text{ mm}$ ,  $\varepsilon_r = 2.53$ . (b) Fixed parameters:  $w = 1.8 \text{ mm}$ ,  $\varepsilon_r = 2.53$ . Solid lines represent  $h = 0.9 \text{ mm}$ , dashed lines represent  $h = 2 \text{ mm}$ .

Figure 3.6: Dispersion diagrams of a DIL consisting of Rexolite 1422. (a) first three modes at  $95 \text{ GHz}$  in dependence of height  $h$ , (b) first two modes at  $h = 0.9 \text{ mm}$  and  $h = 2 \text{ mm}$  in dependence of frequency.

and  $h = 2 \text{ mm}$ , have been selected for this plot, since they are used in this dissertation for operation in  $E_{11}^y$ - and  $E_{11}^x$ -mode, respectively. Their similarity in  $\Delta$  at the given heights serves as a basis of a fair comparison of two DIL-LC phase shifters in  $E_{11}^y$ - and  $E_{11}^x$ -mode, respectively, presented in Chapter 4.

### 3.1.2. Loss Mechanisms

Besides the inherent loss given by the dissipation factor  $\tan \delta$  of the DIL's dielectric, two main sources of loss are present with DILs. They are radiation loss, caused by

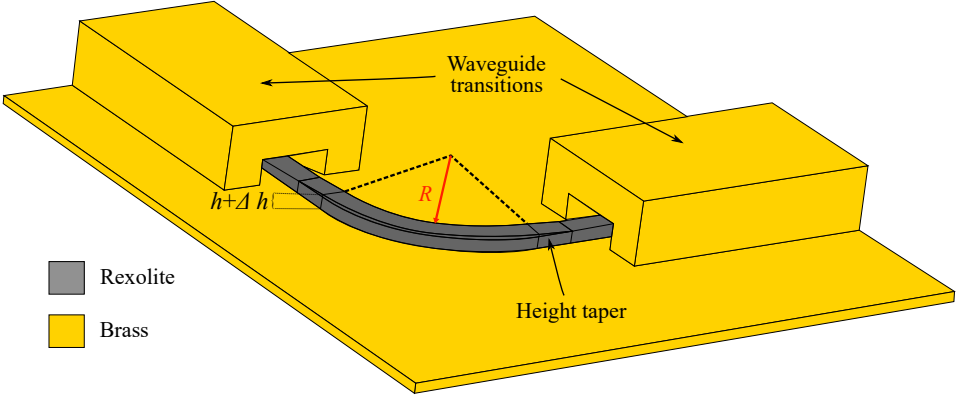
### 3. Dielectric Image Lines

discontinuities both of the dielectric or the ground plane, and metallic loss, introduced by the ground plane of finite conductivity and non-zero surface roughness. This ohmic loss is very dependent on the mode of operation the DIL is designed to operate in.

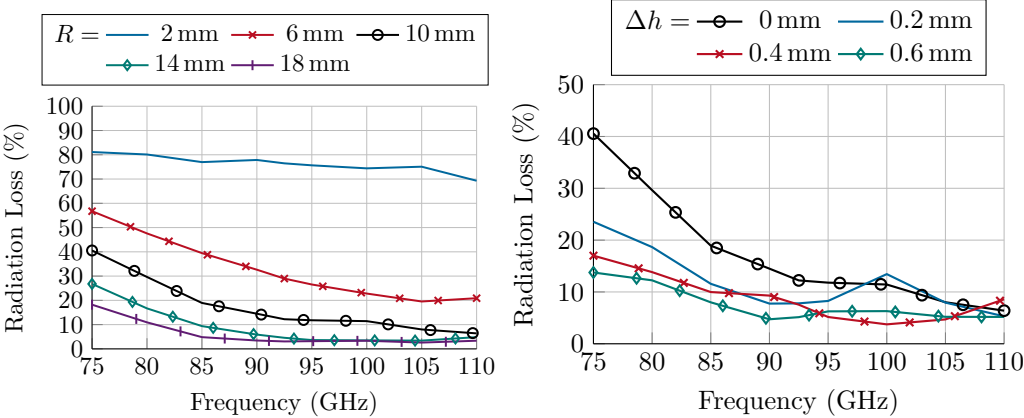
#### Radiation Loss

Radiation loss is obtained at any discontinuity of the DIL. This can include abrupt changes in the DIL's cross-section, obstacles in the form of metallic or dielectric structures besides or on top of the DIL, structures in the ground plane, and bends of the waveguide. Structures besides, above or below the DIL are usually desired features used to form antennas [Ito77; SW85; PB17; Xin+17; PBA18], which is covered in more detail in Chapter 5. Abrupt changes in the DIL's cross-section can be avoided by tapering smoothly from one cross-section to the other. Radiation at bends is usually non-desirable, and needs to be prevented.

Fig. 3.7 depicts the simulation setup and resulting radiation loss of a DIL in  $E_{11}^y$ -mode with a cross-section of  $0.9\text{ mm} \times 1.8\text{ mm}$ , composed of Rexolite 1422, for different bending radii and heights of a  $90^\circ$  bend. The waveguide transitions are described in detail in Section 3.3. The radiation loss is high for small bends and decreases with frequency as the effective cross-section of the DIL increases with frequency. A simple way to reduce radiation loss at these bends is by tapering the DIL to a higher height  $h$  at the bends, thus increasing  $\Delta$  in the DIL forming the curvature (Fig. 3.6 (a)). This effect is shown for different additional height  $\Delta h$  in Fig. 3.7 (c). In order to add this extra height without radiation loss due to the discontinuity in height, a 3 mm long taper is used, shown in Fig. 3.7 (a). Especially at lower frequencies, where the slope of  $\Delta$  is higher, the benefit from an increased height is stronger. Adding  $\Delta h = 0.4\text{ mm}$  can decrease radiation loss by more than 40% at 75 GHz, and remains about 5% lower at frequencies higher than 90 GHz. From a different perspective, a significant reduction in  $R$  can be achieved adding  $\Delta h$ : the same radiation properties of  $R = 18\text{ mm}$  and  $\Delta h = 0\text{ mm}$ , can be maintained with  $R = 10\text{ mm}$  and  $\Delta h = 0.4\text{ mm}$ , hence  $R$  can be reduced by 44.5%, which is a high advantage for integrated applications. The necessary increase in height by 31% can be seen as a minor absolute increase, if the initial dimensions of the DIL are small enough. The high reduction in radiation loss outweighs additional dielectric loss stemming from the larger cross-section of the DIL: the dielectric loss contribution with respect to the total power fed to the system is only increasing by less than 1%. Low loss materials, such as Rexolite 1422 or Alumina, are hence preferable for this approach. For industrial applications, mass-manufacturing constraints, e.g. substrate height, need to be circumvented. Additive manufacturing can avoid this restriction of fixed substrate heights, and the radiation loss at bends could be efficiently reduced in a customizable manner.



(a) Simulation setup including waveguide transitions.



(b) Fixed cross-section  $w \times h = 0.9 \text{ mm} \times 1.8 \text{ mm}$  and different  $R$ .

(c)  $R = 10 \text{ mm}$  and increased  $h$  by  $\Delta h$

Figure 3.7: Radiation loss at bends of a Rexolite-DIL. (a) Simulation setup in CST Microwave Studio Suite. Radiation loss with (b) different bending radius  $R$  with same height, and (c) increased height at the curvature by  $\Delta h$  with a fixed bending radius of  $R = 10 \text{ mm}$ . The radiation loss is given as the percentage of the relation of radiated power with respect to the total power fed to the system. The slightly higher radiation loss in (c) at 100 GHz with  $\Delta h = 0.2 \text{ mm}$  compared to  $\Delta h = 0 \text{ mm}$  is due to reflections at the waveguide transition at this frequency, which leads to a weak resonance.

### Surface Roughness

In practical applications, the conductivity  $\sigma$  of the ground plane is not infinitely high, as assumed during the previous derivation of the propagation constant. In particular, besides the inherent  $\sigma$  of the material of ground plane, its roughness is of high importance. Similar to metallic planar waveguides, a high surface roughness deteriorates the attenuation coefficient of the waveguides. This effect is of increasing impact with higher frequency or higher permittivity, since the skin-depth reduces with decreasing wavelength. Hence, the surface quality of the ground plane material is directly related to the absolute loss of any component characterized in this dissertation.

In order to get insights of this effect in practice, surface roughness is investigated both simulatively and practically in this section, for both  $E_{11}^y$ - and  $E_{11}^x$ -mode. In order to extract the attenuation coefficient  $\alpha$  of the DILs, a multi-line approach is used [Tak+09; DSV18a]. The block diagram of the approach is given in Fig. 3.8. Both simulation and measurement are conducted with respect to reference plane A, hence including waveguide transitions. In practice, a vector network analyzer (VNA) from Keysight, combined with Anritsu 3740A-EW mixer modules with WR10 waveguide extensions, is connected to the waveguide transitions. With the multi-line measurement of two lines with different lengths  $l_1$  and  $l_2$ , reference plane A can be shifted to reference plane B. As visible in Fig. 3.8 the measurable S-parameters consist of the concatenation of the scattering matrices of the line  $S_X$ , and the two waveguide transitions,  $S_A$  and  $S_B$ . For an easy manipulation of concatenated S-matrices, the transfer matrix  $T$  is commonly used, and the relation between S- and T-matrix can be found in the appendix A.1. With T-matrices we can easily write

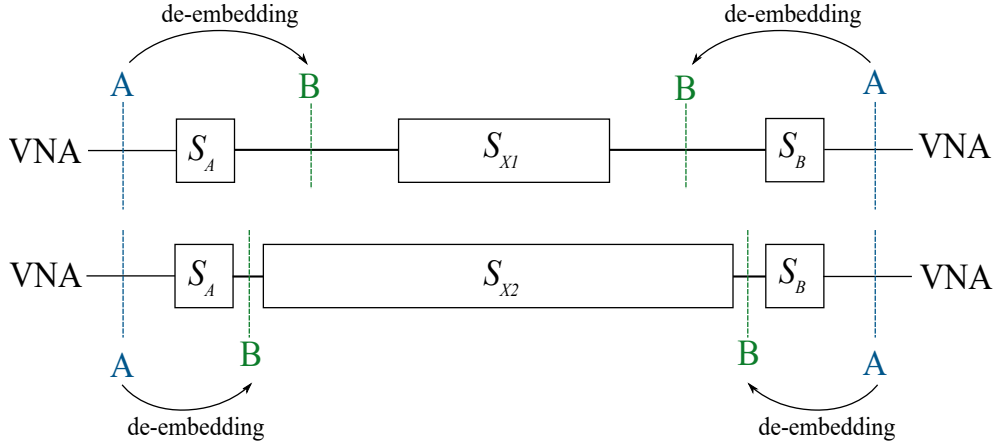


Figure 3.8: Block diagram of the multi-line method used for obtaining the line attenuation coefficient  $\alpha$ .  $S_A$  and  $S_B$  denote the scattering matrices of the waveguide transitions,  $S_{X1}$  and  $S_{X2}$  are the scattering matrices of the DIL with length  $l_1$  and  $l_2$ , respectively.



the total transfer matrices of both measurements,  $T_{M1}$  and  $T_{M2}$  as:

$$T_{M1} = T_A \cdot T_{X1} \cdot T_B, \quad (3.13)$$

$$T_{M2} = T_A \cdot T_{X2} \cdot T_B. \quad (3.14)$$

Inverting  $T_{M2}$  and multiplying it with  $T_{M1}$  leads to

$$T_{M1} \cdot T_{M2}^{-1} = T_A \cdot T_{X1} \cdot T_{X2}^{-1} \cdot T_A^{-1}. \quad (3.15)$$

The transfer matrix of a perfectly matched transmission line, as which  $T_{X1}$  and  $T_{X2}$  are modeled, is

$$T_X = \begin{pmatrix} e^{-j\gamma l} & 0 \\ 0 & e^{j\gamma l} \end{pmatrix}, \quad (3.16)$$

with  $l$  being the length of the line section. Hence, Eqn. (3.15) becomes

$$T_{M1} \cdot T_{M2}^{-1} = T_A \cdot \begin{pmatrix} e^{j\gamma \Delta l} & 0 \\ 0 & e^{-j\gamma \Delta l} \end{pmatrix} \cdot T_A^{-1}, \quad (3.17)$$

where  $\Delta l = l_2 - l_1$  denotes the length difference of the two line sections. The form  $B = C^{-1} \cdot A \cdot C$  of Eqn. (3.17) evokes  $\text{eig}(B) = \text{eig}(A)$  [Fis13], and leads to

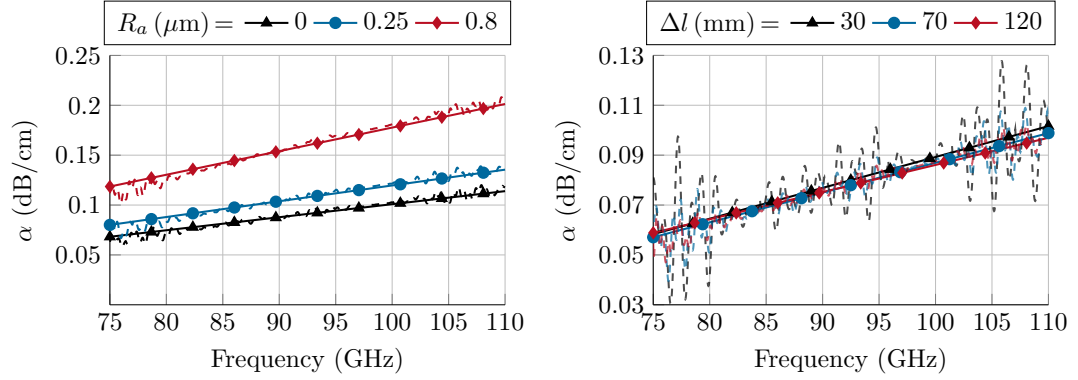
$$\text{eig}(T_{M1} \cdot T_{M2}^{-1}) = \begin{pmatrix} e^{j\gamma \Delta l} \\ e^{-j\gamma \Delta l} \end{pmatrix}. \quad (3.18)$$

Therefore, the attenuation coefficient  $\alpha$  and phase coefficient  $\beta$  can be determined from the set of measured S-parameters and their corresponding  $T$ -matrix by

$$\gamma = \frac{\ln(\text{eig}(T_{M1} \cdot T_{M2}^{-1}))}{\Delta l} = \alpha + j\beta. \quad (3.19)$$

Our main interest lies specifically in the attenuation coefficient  $\alpha$ , and its behavior with increasing surface roughness. Fig. 3.9 (a) shows the simulated attenuation constant of a Rexolite DIL ( $w \times h = 0.9 \text{ mm} \times 1.8 \text{ mm}$ ) in  $E_{11}^y$ -mode for different root-mean-square (RMS) values of the ground plane's surface roughness profile  $R_a$ , using the two line lengths  $l_1 = 30 \text{ mm}$  and  $l_2 = 150 \text{ mm}$ . The resulting length difference  $\Delta l = 120 \text{ mm}$  is chosen as a trade-off between a feasible maximum length for verification in measurement, and ripple reduction of the raw  $\alpha$ , which influences the resulting fit, as shown in Fig. 3.9 (b). In Fig. 3.10 the extracted  $\alpha$  from both simulation and measurement are compared. In practice, the ground planes are inspected using a Veeco Dektak 6M Stylus Profilometer, and the RMS of the surface roughness is found to be  $\text{RMS}_{meas} \approx 0.8 \mu\text{m}$ . The quality of the different ground planes cannot be assured to be exactly equally polished, hence a slight deviation in surface roughness is always present, which can slightly alter the measured  $\alpha$  and lead to larger ripples. Nonetheless, a high agreement regarding slope and value of  $\alpha$  is obtained. Higher values of the measurement can stem from slightly higher material loss, and stronger ripples due to sensitivity to loss and the inherent assumption in

### 3. Dielectric Image Lines



(a) Increase of the attenuation coefficient  $\alpha$  with higher surface roughness.  $\Delta l = 120$  mm. (b) Ripple reduction for more accurate linear fits of the attenuation coefficient  $\alpha$  with increasing  $\Delta l$ , with a surface roughness of RMS = 0  $\mu\text{m}$ .

Figure 3.9: Simulation results of the attenuation coefficient  $\alpha$  of a DIL (Rexolite,  $w \times h = 0.9 \text{ mm} \times 1.8 \text{ mm}$ ) in  $E_{11}^y$ -mode. Dashed lines are raw values of the extracted  $\alpha$ , according to Eqn. (3.19), solid lines represent a linear fit to the data.

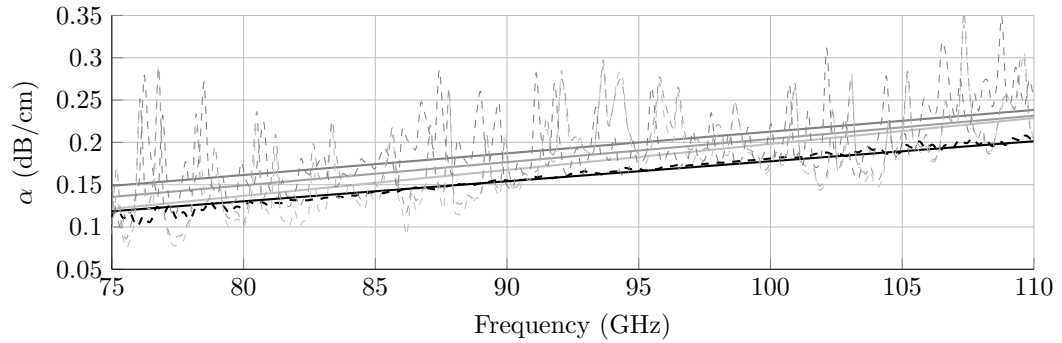


Figure 3.10: Simulated (black) and measured (shades of gray) attenuation coefficient  $\alpha$  of a DIL (Rexolite,  $w \times h = 0.9 \text{ mm} \times 1.8 \text{ mm}$ ) in  $E_{11}^y$ -mode. The raw data is dashed, the fitted data is solid. Simulation data assumes a surface roughness of RMS = 0.8  $\mu\text{m}$ .

the mathematical approach that the waveguide transitions, represented by  $S_A$  and  $S_B$ , are in both measurements *exactly* identical.

The same parameters ( $l_1 = 30 \text{ mm}$ ,  $l_2 = 150 \text{ mm}$  and  $\Delta l = 120 \text{ mm}$ ) are used for examining a Rexolite DIL ( $w \times h = 1.8 \text{ mm} \times 2 \text{ mm}$ ) in  $E_{11}^x$ -mode. Fig. 3.11 displays a comparison of simulations and one representative measurement, which shows high agreement between measurement and simulation. Note the reduced  $y$ -range in Fig. 3.11. A direct comparison of simulated  $\alpha$  for  $E_{11}^y$ - and  $E_{11}^x$ -mode, shown in Fig. 3.12 reveals that the  $E_{11}^x$ -mode is less sensitive to rough surfaces. This is due to its field distribution, which is close to zero at the ground plane. The fundamental

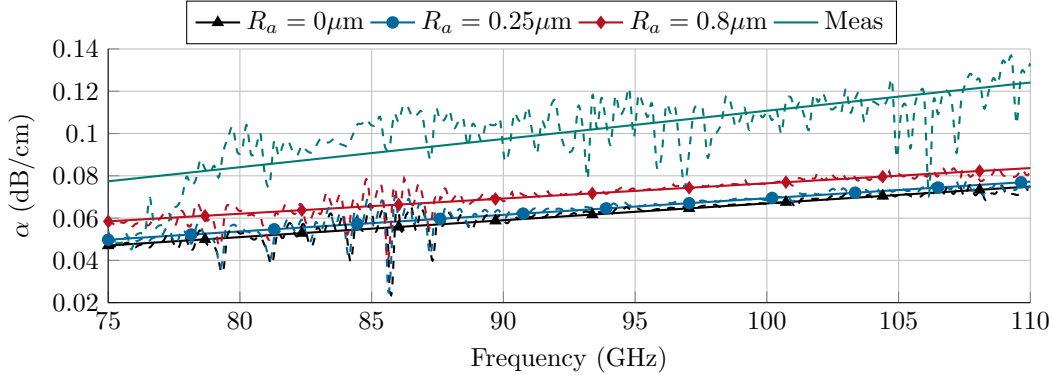


Figure 3.11: Simulated attenuation coefficient  $\alpha$  versus frequency for the  $E_{11}^x$ -mode with different surface roughness of the ground plane compared to a representative measurement of a DIL (Rexolite,  $w \times h = 1.8 \text{ mm} \times 2 \text{ mm}$ ). The raw data is dashed, the fitted data is solid.

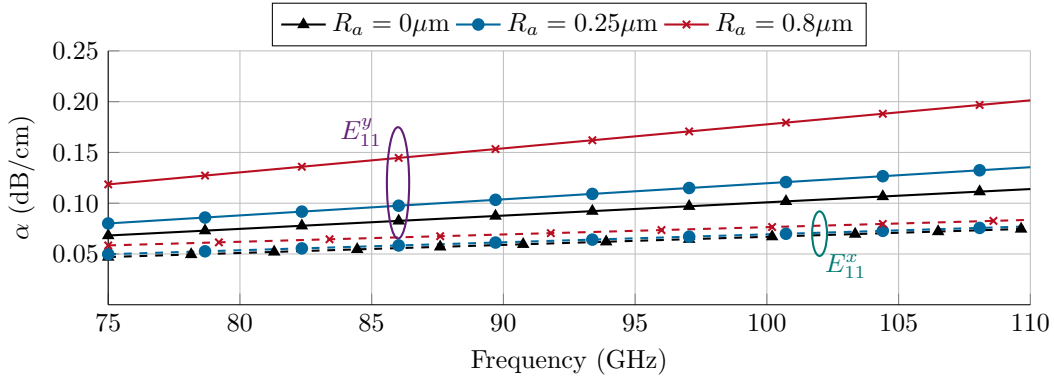


Figure 3.12: Simulated attenuation coefficient  $\alpha$  versus frequency for the  $E_{11}^y$ - (solid) and  $E_{11}^x$ -mode (dashed) with different surface roughness of the ground plane, with accordingly different cross-sections.

mode is more susceptible to surface roughness and shows overall higher attenuation. Nonetheless, the fundamental mode is in many applications still preferable, as it requires the lowest DIL cross-section, and mode conversion is not an issue. Regardless, Fig. 3.12 highly suggests that integrated solutions should rely on the  $E_{11}^x$ -mode when transitioning to higher frequencies than covered in this dissertation. In addition, as shown in Chapter 4, more aspects than the attenuation coefficient  $\alpha$  of the underlying DIL component have to be taken into account, when utilizing LC in DIL environments.

## 3.2. Material Selection and Characterization

As discussed in the previous sections, the choice of the material the DIL is composed of is defining its size, loss, and, in case of this dissertation, its compatibility for hosting LC. Hence, the dielectric properties, namely relative permittivity and  $\tan \delta$ , are of substantial interest when designing DIL circuitry, capable of LC-hosting. The common core-cladding principle ( $\epsilon_{r,core} > \epsilon_{r,cladding}$ ) needs to be respected when adding an LC-core to the DIL, and hence, the choice of relative permittivity is limited to maximally  $\epsilon_r \approx 3$ , even if in Chapter 6 first efforts are undertaken to circumvent this classical restriction. The loss of the dielectric should be as low as possible, such that little power is dissipated throughout the DIL component. Besides the properties of the used dielectric, those of additional materials, such as adhesives necessary to mount the DIL on the ground plane, are essential to know.

There are numerous methods which can be used to investigate materials regarding their RF-characteristics. They can be grouped into two methods: resonant and non-resonant approaches. Resonant characterization requires a resonator, either formed by the dielectric itself [Hir+96; Jim+19] or by a hosting cavity [COT99]. They are very precise in the parameters they extract. However, a disadvantage is that they provide information only for a narrowband frequency range. In order to achieve broadband results, non-resonant methods, e.g. transmission line based methods or free-space methods can be used [NR70; SRD90; BPM06]. The trade-off of broadband methods is that they allow for the estimation of  $\epsilon_r$  in a wide range of frequencies, but its  $\tan \delta$  resolution is limited. In this dissertation, an additional constraint is added, since besides solid dielectrics, adhesives and 3D-printed materials are investigated. As the latter two are materials which have to cure, it can not be allowed that they deform during production of the samples. Especially when dealing with glue, it is challenging to create a well-defined sample without any holding structure. At the frequencies of interest around 100 GHz, hollow waveguide resonators become very small and filling glue without perturbing the resonator itself bears many risks. Hence, resonant methods are not pursued in this dissertation. Instead, a hollow waveguide-based approach is used, where a thin waveguide shim, which hosts the material under test (MUT), is inserted into the waveguide. Especially for glue and 3D-printed materials, where manufacturing technologies may not meet the demanded precision of standalone samples yet, this approach helps to create a defined sample. Parts of the MUT which exceed the holding structure can be mechanically or chemically removed.

In order to analyze the properties of the corresponding materials used in this dissertation, the Nicolson-Ross-Weir (NRW) method is used [NR70; Wei74]. The NRW approach is transmission-line-based, and utilizes both transmissive and reflective behavior of the MUT, in order to obtain its relative permittivity  $\epsilon_r$ , permeability  $\mu_r$  and loss tangent. The following pages briefly revise the algorithm of the modified NRW technique [Rot+16; PRB11; SNS18] and introduce the measurement setup. Fig. 3.13 illustrates the measurement principle with a rectangular waveguide. A sample of known thickness  $d$  is inserted into the waveguide. In practice, this can be

### 3.2. Material Selection and Characterization

achieved by clamping a waveguide shim, filled with the MUT, in between two hollow waveguides. A VNA, connected to Anritsu 3740A-EW mixer modules with WR10 waveguide extensions, is calibrated to the surface of the shim, and provides both  $S_{11}$  and  $S_{21}$ . These parameters are directly linked to the transmission and reflection coefficients introduced by the MUT

$$S_{11} = \Gamma \frac{1 - T^2}{1 - \Gamma^2 T^2} \quad (3.20)$$

$$S_{21} = T \frac{1 - \Gamma^2}{1 - \Gamma^2 T^2}. \quad (3.21)$$

$\Gamma$  denotes the reflection coefficient present by the difference in characteristic impedance of the air-filled waveguide to the one filled with the MUT, and  $T$  represents the transmission coefficient of the finite MUT sample with thickness  $d$ :

$$\Gamma = \frac{Z - Z_0}{Z + Z_0} \quad (3.22)$$

$$T = \exp(-\gamma d). \quad (3.23)$$

With the help of

$$K = \frac{S_{11}^2 - S_{21}^2 + 1}{2S_{11}} \quad (3.24)$$

transmission and reflection coefficient can be computed by the measured S-parameters

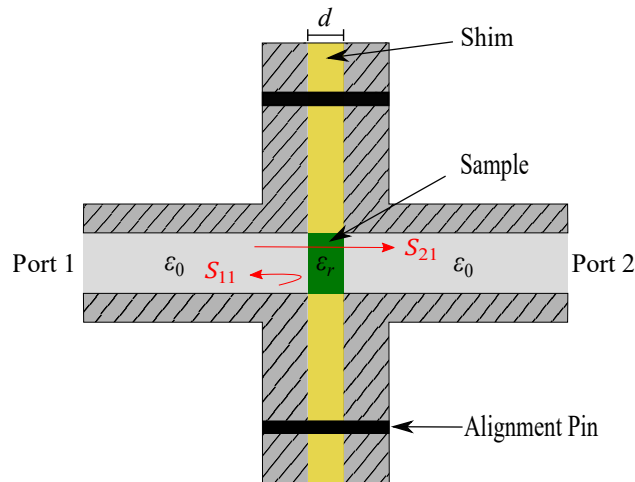


Figure 3.13: Cross-sectional view of the NRW approach with a hollow waveguide [Tes+21b] (CC BY 4.0). The sample is held in place by a waveguide shim.

### 3. Dielectric Image Lines

via

$$\Gamma = K \pm \sqrt{K^2 - 1} \quad (3.25)$$

$$T = \frac{S_{11} + S_{21} - \Gamma}{1 - (S_{11} + S_{21}) \cdot \Gamma}. \quad (3.26)$$

The sign in Eqn. (3.25) has to be chosen such that  $|\Gamma| \leq 1$  in order to fulfill a passive material. By rearranging Eqn. (3.22) to  $Z/Z_0 = (1 + \Gamma)/(1 - \Gamma)$ , and inserting the corresponding impedances

$$Z = j \frac{\omega \mu_r \mu_0}{\gamma} \quad (3.27)$$

$$Z_0 = j \frac{\omega \mu_0}{\gamma_0}, \quad (3.28)$$

where  $\omega$  denotes the angular frequency of operation, and

$$\gamma = j \frac{2\pi}{\lambda_0} \sqrt{\varepsilon_r \mu_r - \left(\frac{\lambda_0}{\lambda_c}\right)^2} \quad (3.29)$$

$$\gamma_0 = j \frac{2\pi}{\lambda_0} \sqrt{1 - \left(\frac{\lambda_0}{\lambda_c}\right)^2}, \quad (3.30)$$

where  $\lambda_0$  and  $\lambda_c$  are the free-space and cutoff wavelength of the waveguide, respectively,  $\mu_r$  of the MUT can be obtained by

$$\mu_r = \frac{\lambda_{0g}}{\Lambda} \cdot \frac{1 + \Gamma}{1 - \Gamma}, \quad (3.31)$$

with

$$\lambda_{0g} = \frac{\lambda_0}{\sqrt{1 - \left(\frac{\lambda_0}{\lambda_c}\right)^2}}, \quad \Lambda = \frac{\lambda_0}{\sqrt{\varepsilon_r \mu_r - \left(\frac{\lambda_0}{\lambda_c}\right)^2}}. \quad (3.32)$$

The relative permittivity can be obtained by solving Eqn. (3.31) for

$$\varepsilon_r = \frac{\lambda_0^2}{\mu_r} \left( \frac{1}{\Lambda^2} + \frac{1}{\lambda_c^2} \right). \quad (3.33)$$

Following [SNS18; LMT11], ambiguity can be circumvented with

$$\Lambda = \frac{-j2\pi d}{\ln(T)} = \frac{-j2\pi d}{\ln(|T|) + j \arg(T + 2\pi m)}, \quad (3.34)$$

where the integer  $m$  has to be different from zero if the sample size approaches  $d \approx m\lambda_g/2$ , in order to avoid discontinuities in the extracted  $\varepsilon_r$  and  $\mu_r$ .

Using the procedure described above, different dielectrics and adhesives have been analyzed, which are summarized in Table 3.1, grouped by their different material types. The measurement setup and a microscopic picture of a sample of a

### 3.2. Material Selection and Characterization

Table 3.1.: Materials investigated using the NRW method. They are grouped by their material types: solids, adhesives and 3D-printables.

	Material	Description
Solids	Teflon	Polytetrafluoroethylene (PTFE), fluorocarbon solid
	Premix PPE300	Polyphenylene ether (PPE), thermoplastic
	Rexolite 1422	Cross-linked polystyrene, thermoplastic
Adhesives	Rexolite Adhesive 12517	Rexolite 1422 specific adhesive
	Pattex Plastix	Superglue
	Norland Optical Adhesive 81	UV glue
	QuickStick 135 Mounting Wax	Wafer Mounting Wax
3D-Printables	Zeonex RS420	Cyclo Olefin Polymer (COC)
	Creamelt COC	Cyclo Olefin Polymer (COC)
	Topas Blend	Custom blend of Cyclo Olefin Polymer (COC)

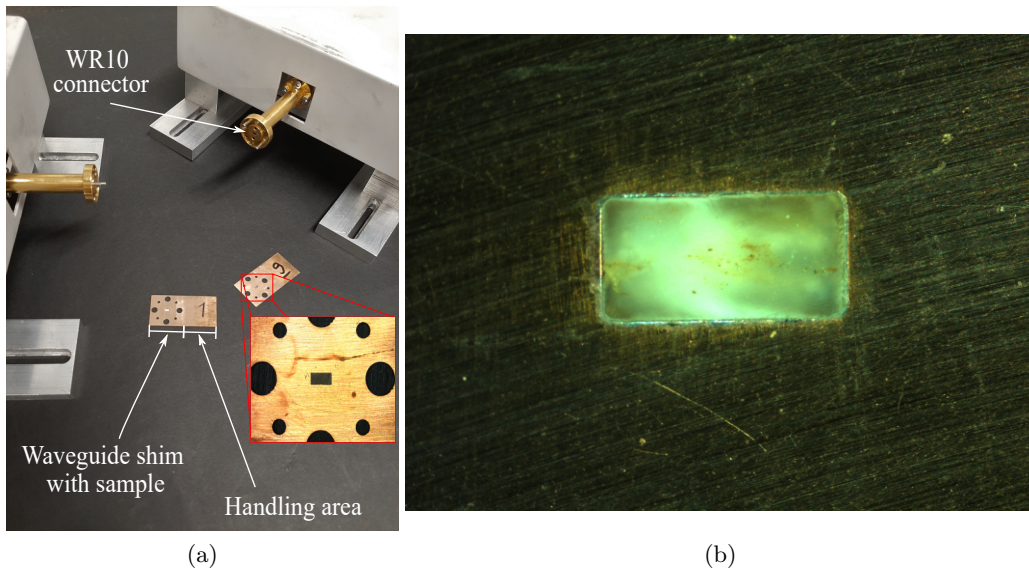


Figure 3.14: (a) Measurement setup of the NRW method and (b) microscopic view of Zeonex RS420 in the sample holder [Tes+21b] (CC BY 4.0).

### 3. Dielectric Image Lines

3D-printable MUT is shown in Fig. 3.14. The sample holders are laser-cut from  $d = 0.4$  mm thick Tombak sheets, including the WR10 waveguide segment for the MUT and the necessary through-holes for screws and dowels. The holders are filled with the MUTs given in Table 3.1. In case of the solids, the MUT is cut to fit the size of the WR10 waveguide ( $1.27 \text{ mm} \times 2.54 \text{ mm}$ ) and are mechanically squeezed into the window. Solids show the highest potential for errors, especially in  $\tan \delta$ , due to the possibility of air gaps between sample and waveguide wall arising from the assembly procedure. In contrast, the adhesives and 3D-printable MUTs are filled in their viscose state into the sample holder and cure in it, thus air gaps are inherently prevented. Therefore, the approach is well suited for materials which have to cure in any way. In case of the adhesives, it can take several filling steps before a suitable sample is created, since the glue loses volume due to evaporation of contained solvents. Fig. 3.15 shows the extracted permittivity and loss tangent of the analyzed materials.

In terms of permittivity, all MUTs show low permittivity, which is necessary for a possible combination with LC ( $2.4 \leq \varepsilon_{r,LC} \leq 3.6$ ). Teflon (PTFE) serves as a reference material to verify the extracted parameters, but is not well suited as a DIL material. This is mostly because it is very soft, which makes it hard to machine precise DIL structures. Most importantly, however, is the fact that glue does not adhere well to PTFE [Jos18]. Other widely used low-permittivity dielectrics for mmW-frequencies, such as high-density polyethylene (HDPE) ( $\varepsilon_r = 2.3$ ,  $\tan \delta = 3.1 \cdot 10^{-4}$  at  $f = 160 \text{ GHz}$ ) [Ata+13; Lam96] show the same issues as PTFE. Hence, those materials are not considered. From the remaining dielectrics which are promising candidates for the DIL material, especially Rexolite 1422, Zeonex RS420, and Creamelt COC have promising permittivity values between 2.3 and 2.6. However, for long periods of time during this dissertation, the 3D-printable materials were still showing adhesion problems to the ground plane, when aiming for a direct manufacturing process without glue. Therefore, Rexolite 1422 is mostly used throughout this dissertation. It can be simply and precisely processed by computer numeric control (CNC) milling [Jos18; Ree20]. This fabrication approach demands the use of adhesives, which are investigated side-by-side with the solids and the additives. The relative permittivity of the considered adhesives ranges from approximately 2.5 to 3.2. It is important that the adhesive has a permittivity close to the used dielectric, in order to avoid layers of different permittivity, especially when operating the DIL in the  $E_{11}^y$  mode. Hence, Rexolite glue obviously is preferable in the scenario of a Rexolite DIL, followed by superglue, mounting wax and optical adhesive.

Furthermore, the loss of the DIL's dielectric and potential adhesive is a crucial factor for the DIL's performance. At this point, it is essential to highlight again that, due to the broadband characteristic of the NRW method, the material loss is very sensitive to noise and can not be extracted very precisely [Kha+12; Cos+17]. Hence, the presented material loss should be examined with this circumstance in mind. Over-estimated loss can be observed at all materials from 75 GHz to 85 GHz. This is due to a slight deviation in the extracted  $\mu_r$  in this frequency range, see Fig. A.1 in the appendix. Nonetheless, a clear relation of the materials to each other



### 3.2. Material Selection and Characterization

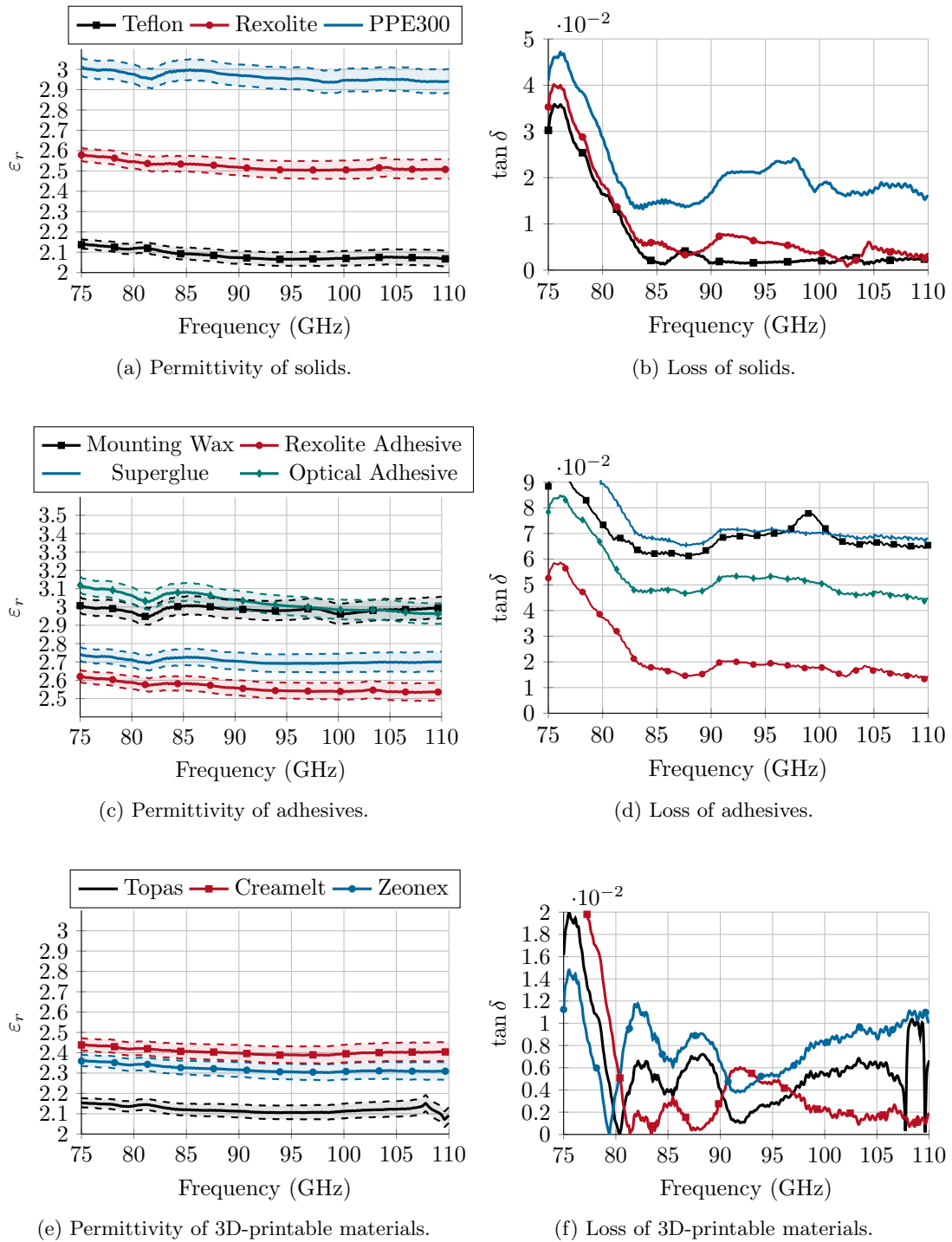


Figure 3.15: Permittivity (left) and corresponding loss tangent (right) extracted by the NRW method, smoothed and with independently scaled  $y$ -axis range. Colored areas between dashed lines are included for an uncertainty in sample size thickness  $d$  by  $\pm 10 \mu\text{m}$  ( $\pm 2.5\%$ ). The plots are grouped as follows: top - solids, middle - adhesives, and bottom - 3D-printable materials.

### 3. Dielectric Image Lines

in terms of loss can be well determined, and hence, promising materials can be separated from less favorable materials. This makes the presented approach an attractive method for testing customized blends and newly developed 3D-printable RF-materials with comparable low effort. After pre-selecting promising materials with the NRW method, the extra effort of manufacturing highly precise samples of the desired material can be invested to achieve narrowband characterizations of loss by using a resonant method.

The solid, classical dielectrics show a clear difference in loss, with Teflon and Rexolite being the favorable options when compared to PPE300. The materials which can be additively manufactured are very similar in loss, and close to the behavior of Rexolite. Hence, they could all be promising materials for tunable LC-DIL components. The adhesives clearly differ in loss. Wafer mounting wax and superglue show high  $\tan\delta$  when compared to Rexolite adhesive. The optical adhesive performs not as well as Rexolite adhesive, but can be used as an alternative. Consequently, during the course of this dissertation, Rexolite glue is mostly used. However, it was found that Rexolite adhesive provides lower adhesion to the ground plane than the optical adhesive. Hence, in scenarios outside the lab, where mechanical forces or environmental circumstances have to be considered, optical adhesive should be preferred.

### 3.3. Excitation of Dielectric Image Lines

Excitation of DWGs and DILs can be realized by different approaches [SRI81; GWD82; PDK96; TLC00; Hof+03; Ric07; YS08; DH12; XCZ13; PB15; DSV18a; Wit+20; WS20]. In most cases, the excitation is performed by a transition from one waveguide topology to the dielectric topology. In this dissertation, measurements are conducted with Keysight PNA using the aforementioned 3740A-EW W-band mixer modules, which have WR10 rectangular waveguide (RWG) output ports. When transitioning from an RWG to a dielectric structure, horn transitions are most efficient [YS08], since the polarization of the  $TE_{10}$  mode in the RWG can be used to excite to the  $E^y$  or  $E^x$  mode in the dielectric waveguide. When using these transitions, the dielectric is inserted into the RWG, which has a horn flare at its end to avoid parasitic radiation. The DWG inside the RWG is usually tapered for better matching [Ric07; YS08; Jos18; Ree20; WS20].

Following this approach, WR10-to-DIL transitions were designed in this dissertation. Since they are a crucial part of all following measurements, their layout and operation principle is described first, before the properties of the manufactured transitions is thoroughly investigated. Fig. 3.16 shows the layout of the transition from WR10 to a Rexolite-DIL in  $E_{11}^y$ -mode. In section A, the DIL is tapered such that smooth coupling from RWG to the dielectric is ensured. The DIL is already at its final height  $h = 0.9$  mm. In section B, the RWG is filled completely by the dielectric. In order to remain at the same cut-off frequency, the width of this section is reduced, hence the DIL has a cross-section of  $1.6 \text{ mm} \times 0.9 \text{ mm}$  at this point. In addition, a small Rexolite pin is used to keep the dielectric securely in place. The horn-like

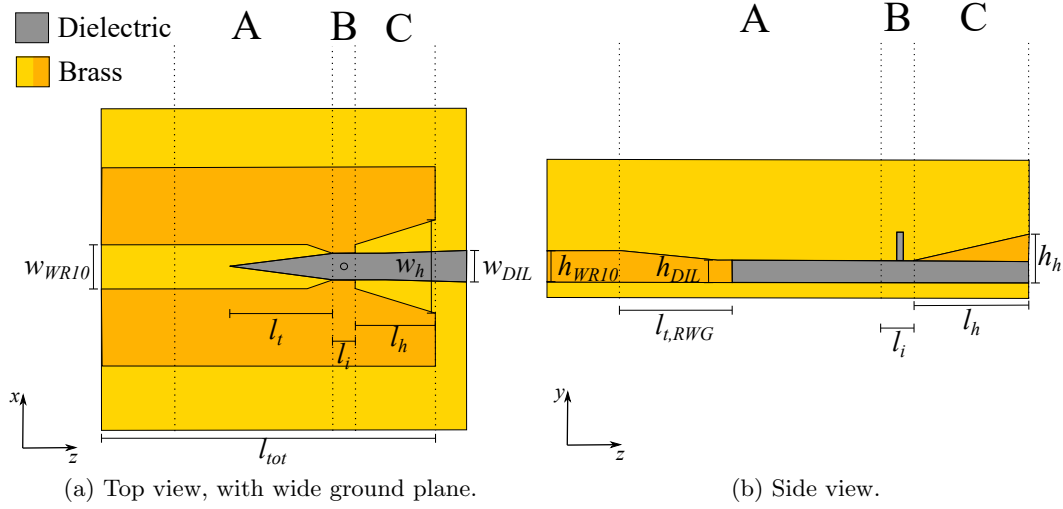


Figure 3.16: Schematic of the transition for  $E_{11}^y$ -mode. The taper dimensions have been optimized with CST Studio Suite to reduce radiation loss and minimize reflections in the RWG. The most important dimensions are:  $w_{WR10} = 2.54$  mm,  $h_{WR10} = 1.27$  mm,  $h_{DIL} = 0.9$  mm,  $l_{t,RWG} = 4$  mm,  $l_t = 6$  mm,  $l_i = 1$  mm,  $l_h = 4.7$  mm,  $w_h = 5.5$  mm,  $h_h = 1.9$  mm,  $w_{DIL} = 1.8$  mm, and  $l_{tot} = 19.5$  mm.

section C accomplishes both reduced radiation loss and allows tapering the DIL to its full width  $w = 1.8$  mm. In order to achieve a design which allows the excitation of different components on different ground planes in practice, a split-block design with three parts is used in this dissertation:

- top part with the RWG structure in it and parts of the flange
- ground plane with dielectric component/structure on it
- bottom part with parts of the flange

Fig. 3.17(a) shows these three parts for a simple line structure. They are milled from brass using CNC milling. Technical drawings of the parts are included in the appendix (Fig. A.2). The modular design allows connecting different DIL structures of any shape to the measurement equipment, if they have a feed of same or similar permittivity and cross-section as the  $E_{11}^y$  Rexolite DIL.

The transition to the orthogonal  $E_{11}^x$ -mode is in its principle of operation identical to the one to the  $E_{11}^y$ -mode. In order to achieve the desired polarization parallel to the ground plane, the WR10 waveguide needs to be rotated by  $90^\circ$ , so that its long side is perpendicular to the ground plane. Accordingly, sections A to C are similar as shown in Fig. 3.16, but individually optimized for the increased cross-section of

### 3. Dielectric Image Lines

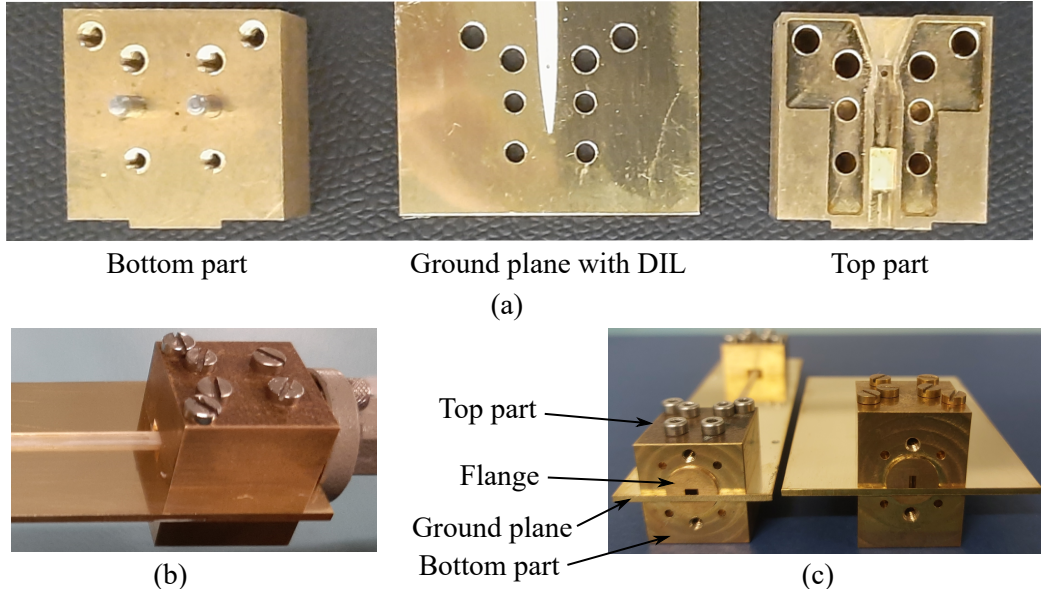
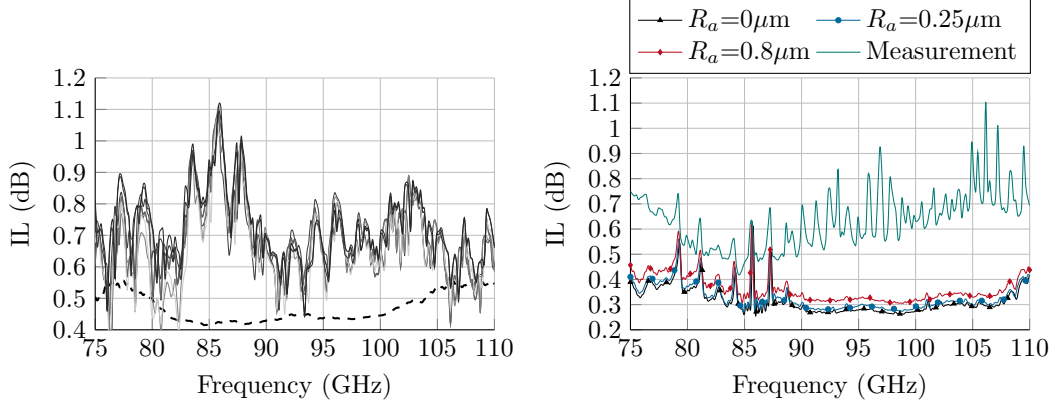


Figure 3.17: Fabricated transitions to Rexolite DIL structures. (a) Disassembled parts: bottom part with threads and pin dowels, ground plane with through holes and DIL structure on it and top part with through holes and the RWG layout. (b) Assembled transition which feeds a line structure and is connected by a flange to a WR10 waveguide on the right. (c) View on the WR10 end of the  $E_{11}^y$  transition with a two-port structure on the ground plane (left) and on the  $E_{11}^x$  transition with a one-port structure on a wide ground plane (right).

1.8 mm×2 mm. Its detailed dimensions can be found in Fig. A.3 in the appendix. Both manufactured transitions are shown in Fig. 3.17 (c). Using the multi-line method from Section 3.1.2, the total loss of the transitions can be determined in simulations and measurement: with the attenuation coefficient  $\alpha$  at hand, the total absolute insertion loss  $IL_{line}$  of a line section of length  $l$  can be calculated. The total insertion loss  $IL_{tot}$  of the back-to-back structure, connected by the line, is also known. Hence,  $IL_{transition} = \frac{1}{2}(IL_{tot} - IL_{line})$  can be used to calculate the insertion loss caused by one transition. This aids in evaluating the phase shifters that will be connected to the transitions in Chapter 4 as an individual component. This approach is necessary since a TRL (thru-reflect-line) or SOLT (short-open-line-thru) calibration cannot be realized, due to radiation at an "open"/"short". Fig. 3.18 depicts the loss per transition for  $E_{11}^y$ - and  $E_{11}^x$ -transition in simulation and measurement. We observe a higher IL in measurements than in simulation. Since the extracted IL is noisy, the difference in IL is evaluated using mean values of simulated and measured data. In this way, a conservative estimate of the additional IL is obtained, since high peaks are neglected. In  $E_{11}^y$ -mode the average measured IL is 0.69 dB, and therefore 0.22 dB higher than the simulated average IL of one transition (0.47 dB). The transition

### 3.3. Excitation of Dielectric Image Lines



(a) Simulation ( $R_a = 0.8 \mu\text{m}$ , dashed) and multiple measurements (solid) of one  $E_{11}^y$  transition. (b) Simulation of different roughness and measurement of one  $E_{11}^x$  transition.

Figure 3.18: Extracted IL per waveguide transition. (a) Simulation of the  $E_{11}^y$ -mode and multiple measurements. (b) Measurement of the  $E_{11}^x$ -mode and multiple simulations with different  $R_a$ .

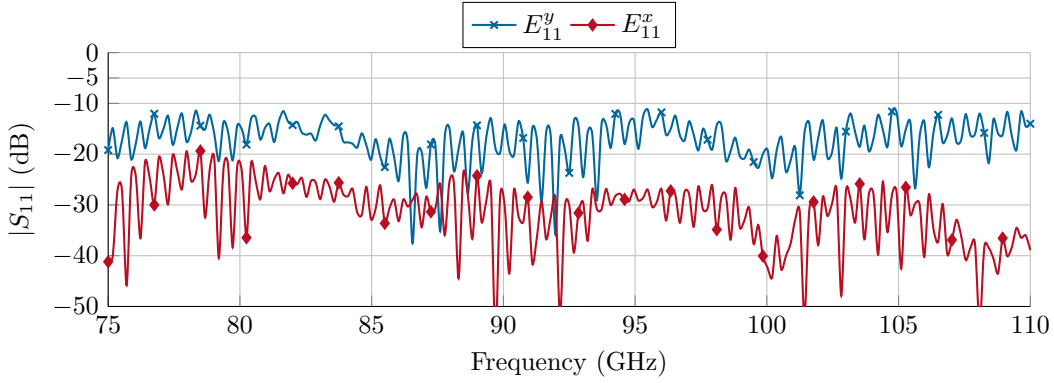


Figure 3.19: Measured  $|S_{11}|$  of a  $l = 150 \text{ mm}$  long Rexolite  $E_{11}^y$  and  $E_{11}^x$  DILs connected to the corresponding transitions.

of the  $E_{11}^x$ -mode's average measured IL is 0.27 dB higher (measurement: 0.64 dB, simulation 0.36 dB). Since in two-port measurements two transitions contribute to the total IL, we can conclude that two transitions contribute with an absolute loss of 1.37 dB and 1.27 dB to measurements of  $E_{11}^y$ - and in  $E_{11}^x$ -components, respectively. In both cases, this is about 0.5 dB more than the simulation predicts. Additional loss can stem from slightly higher material loss and manufacturing tolerances, which lead to higher propagation and radiation loss of the transition. Good matching is obtained for both transitions, as Fig. 3.19 shows, with the  $E_{11}^x$  transition achieving better results than the  $E_{11}^y$  transition, owed to the different position of the cutting planes in the corresponding split-block designs.



## 4. Liquid Crystal Dielectric Image Line Phase Shifters

Tunable phase shifters are essential components for tunable RF-systems, especially for phased arrays. Many types of phase shifters, such as loaded line [Atw85; RB00; Göl10], switched/delay line [LD19], and reflection [Isk+16] phase shifters exist. At upper mmW-frequencies, delay line phase shifters are mostly used. They belong to the true delay line phase shifters, which show a frequency dependent phase shift, in contrast to true phase shift phase shifters, which show constant phase shift at all frequencies [RL01]. LC based phase shifters belong to passive delay line phase shifters. In addition, LC-phase shifters are analogue phase shifters which can continuously change their phase shift, opposed to digital phase shifters which show discrete phase shifts. At V- and W-band, multiple dielectric LC-phase shifters have been realized [Pol+20b]. Even though they can not be easily integrated to conventional systems and require high bias voltages, they have proven to be of very low loss and are suitable for e.g. antennas in the same topology [Jos18; Ree20].

When a delay line LC-phase shifter is tuned, its effective permittivity changes. This leads to a change in propagation constant  $\beta$ , and hence the electrical length of the delay line changes. The maximum possible phase shift  $\Delta\varphi$  in degree is obtained by the difference in propagation constants  $\Delta\beta$ , and the phase shifter length  $l_{PS}$ :

$$\Delta\varphi = \varphi_{\parallel} - \varphi_{\perp} = \left( \Delta\beta \cdot \frac{\pi}{180^\circ} \right) \cdot l_{PS} = \left( \frac{360^\circ \cdot f}{c_0} \cdot (\sqrt{\varepsilon_{r,\text{eff},\parallel}} - \sqrt{\varepsilon_{r,\text{eff},\perp}}) \right) \cdot l_{PS}. \quad (4.1)$$

The subscripts  $\perp$  and  $\parallel$  describe the orientation of the LC-molecules with respect to the RF-polarization. In order to quantize the efficiency of (LC) phase shifters, different aspects have to be taken into account. The most common way to characterize a phase shifter is by the figure-of-merit (FoM), which relates maximum phase shift  $\Delta\varphi$  and maximum insertion loss IL of the component at any bias state [Fer+22]:

$$\text{FoM} = \frac{\Delta\varphi_{\text{max}}}{\text{IL}_{\text{max}}}. \quad (4.2)$$

The FoM is a frequency dependent parameter, since phase shift and IL vary with frequency. In addition, the steering efficiency  $\tau$  is used to emphasize the phase shift and physical length of the phase shifter:

$$\tau = \frac{\Delta\varphi}{l_{PS}}. \quad (4.3)$$

While these two parameters are most common, the response times, as well as necessary bias voltage/power have to be taken into account. As stated in the introduction,

#### 4. Liquid Crystal Dielectric Image Line Phase Shifters

fully dielectric phase shifters may show high FoM, but lack fast response times or feasibility for integration to conventional topologies.

This chapter covers two LC-DIL phase shifters, one for the  $E_{11}^y$ -mode and one for the  $E_{11}^x$ -mode. More focus is put on the  $E_{11}^y$ -mode phase shifter, as most investigations in this dissertation are based on it. However, as demonstrated in Chapter 3, the  $E_{11}^x$ -mode can be of increased interest for frequencies beyond 110 GHz, and is therefore compared to the  $E_{11}^y$ -mode phase shifter.

### 4.1. LC-Phase Shifter in $E_{11}^y$ -Mode

The  $E_{11}^y$ -mode is best suited for the first analysis of an LC-DIL phase shifter, since it is the fundamental mode. In the following, the  $E_{11}^y$ -mode DIL which hosts the LC is always of cross-section  $1.8 \text{ mm} \times 0.9 \text{ mm}$ , in accordance to all observations and results obtained in Chapter 3.

#### 4.1.1. Design

In order to change the effective permittivity of the DIL, an LC core needs to be inserted into the line. Since the LC core differs in permittivity of the DIL's dielectric (LC:  $2.46 \leq \varepsilon_r \leq 3.53$ , Rexolite:  $\varepsilon_r = 2.53$ ), the core needs to be tapered to mitigate reflections and radiation loss. First demonstrators use a trench of LC, which is open at its top. Fig. 4.1 shows the simulation model, and  $|S_{11}|$  in dependence of the taper length  $l_{\text{taper}}$  of a DIL with LC section. Especially in perpendicular orientation, mismatch and radiation loss occur due to the difference in permittivity of DIL and LC, which is why this particular case is shown in Fig. 4.1 (b). A feasible taper length

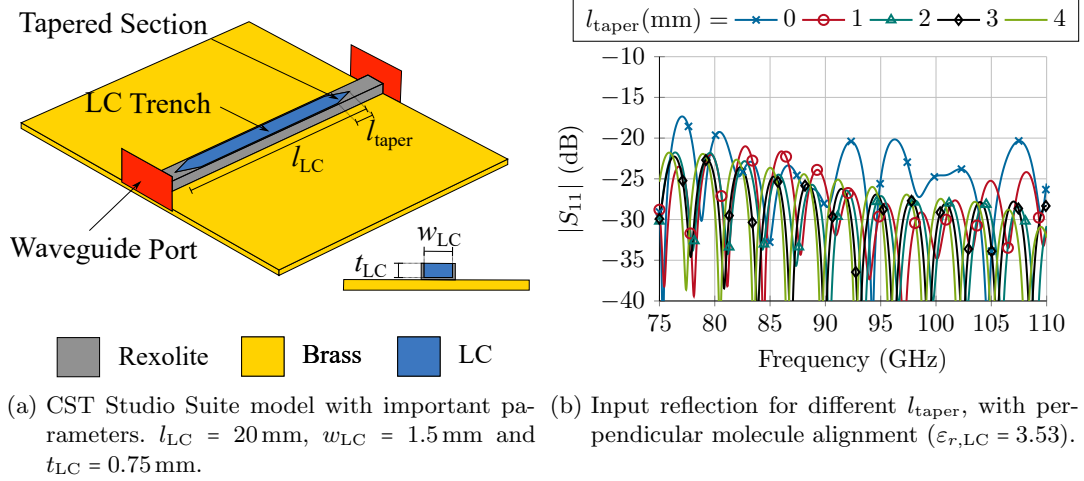
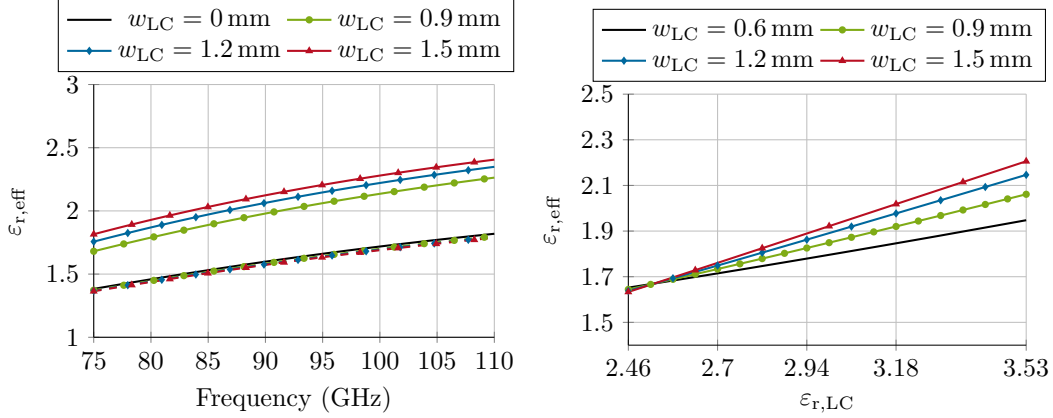


Figure 4.1: (a) Simulation model and (b) input reflection for different  $l_{\text{taper}}$ . Good matching is achieved with  $l_{\text{taper}} = 2 \text{ mm}$ , but radiation loss can be further mitigated when increasing  $l_{\text{taper}}$  to  $3 \text{ mm}$ .



#### 4.1. LC-Phase Shifter in $E_{11}^y$ -Mode



(a) Effective permittivity of a LC-DIL in dependence of  $w_{\text{LC}}$  with  $\epsilon_{r,\text{LC}} = 3.53$  (solid) and  $\epsilon_{r,\text{LC}} = 2.46$  (dashed). (b) Effective permittivity of a LC-DIL at 95 GHz in dependence of  $w_{\text{LC}}$  and  $\epsilon_{r,\text{LC}}$ .

Figure 4.2: Influence of  $w_{\text{LC}}$  on  $\epsilon_{r,\text{eff}}$  of the LC-DIL (a) over frequency, and (b) at 95 GHz.

of 3 mm is chosen for all following designs, to ensure minimal reflections at the shortest length. It reduces radiation loss by 32% at 95 GHz when compared to a non-tapered structure. The width  $w_{\text{LC}}$  and depth  $t_{\text{LC}}$  of the LC cavity directly affect the realizable phase shift. In the  $E_{11}^y$  mode, the field strength is at its maximum at the ground plane. Therefore,  $t_{\text{LC}}$  needs to be as high as possible, such that only a thin Rexolite layer exists between LC and ground plane. In order to be mechanically stable, the maximum depth is  $t_{\text{LC}} = 0.75$  mm. This leaves a layer of 150  $\mu\text{m}$  at the bottom of the LC trench, which is still thick enough such that no friction from low mechanical stress occurs. The width  $w_{\text{LC}}$  of the trench directly translates to the realized effective permittivity of the phase shifter, depending on the molecules' alignment, and, therefore, to the achievable differential phase shift. Keeping  $t_{\text{LC}} = 0.75$  mm at its mechanically stable minimum, the effect of different trench width  $w_{\text{LC}}$  on the effective permittivity of the LC-DIL is shown in Fig. 4.2 (a). The LC's lowest permittivity is close to the value of the Rexolite's permittivity. Hence, in this state of molecule alignment,  $w_{\text{LC}}$  does only negligibly impact the overall effective permittivity  $\epsilon_{r,\text{eff}}$  of the structure. In high permittivity, however, the effect is visibly higher with increasing  $w_{\text{LC}}$ . This effect is represented by the slope of the curves in Fig. 4.2 (b), where  $w_{\text{LC}}$  and the LC's permittivity are varied at a fixed frequency of 95 GHz. As a consequence, the change of  $\epsilon_{r,\text{eff}}$  of the phase shifter is highly sensitive to changes in the value of the high permittivity state. Therefore, if the maximum permittivity is not reached, e.g. by non-ideal biasing, the impact can be high on the performance of the phase shifter. This effect is quantified in Fig. 4.3 (a):

at  $w_{\text{LC}} = 1.5$  mm, slight deviations in maximum permittivity in the parallel state can lead to significant reduction in the achievable  $\Delta\epsilon_r$ . At  $\epsilon_{r,\text{LC}} = 3.41$  and  $\epsilon_{r,\text{LC}} = 3.17$ , which corresponds to a reduction of 3.4% and 10% from the maximum value

#### 4. Liquid Crystal Dielectric Image Line Phase Shifters

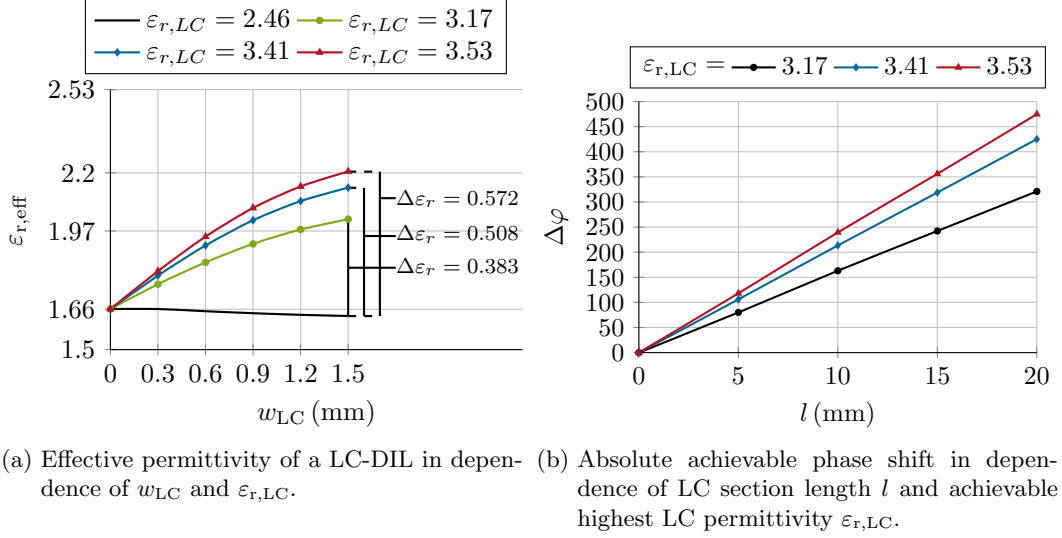


Figure 4.3: Influence of the achievable maximum LC permittivity  $\epsilon_{r,\text{LC}}$  on (a) the achievable anisotropy  $\Delta\epsilon_r$ , and on (b) the absolute phase shift  $\Delta\varphi$ , both at 95 GHz.

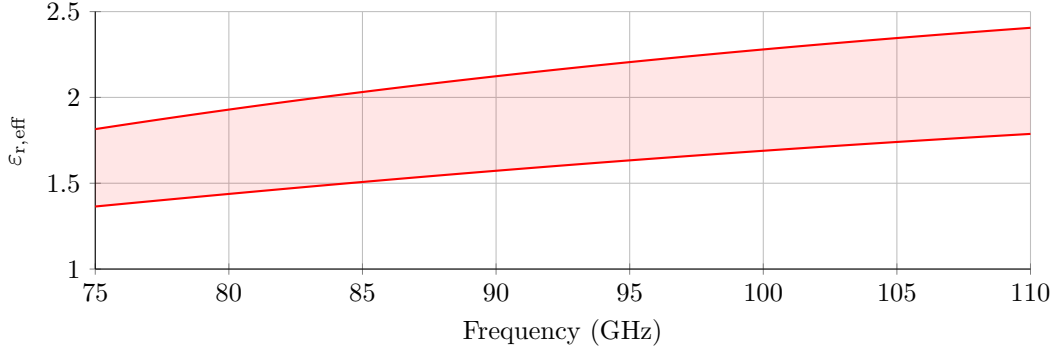


Figure 4.4: Tuneable range of  $\epsilon_{r,\text{eff}}$  with the final dimensions of  $w_{\text{LC}} = 1.5$  mm and  $t_{\text{LC}} = 0.75$  mm.

$\epsilon_{r,\text{LC}} = 3.53$ , respectively, the maximum achievable  $\Delta\epsilon_r$  is reduced by 11% and 32%, respectively. This effect is translated to an absolute difference in differential phase shift, which deviates significantly with increasing length  $l$  of the phase shifter, see Fig. 4.3 (b). As we aim for highest  $\Delta\varphi$ , the widest, mechanically stable  $w_{\text{LC}} = 1.5$  mm is chosen, together with  $t_{\text{LC}} = 0.75$  mm. Hence, the side and bottom walls of the trench have a thickness of 150  $\mu\text{m}$ , each. This leads to a range of  $\epsilon_{r,\text{eff}}$  which is displayed in Fig. 4.4. For direct comparison to a measurement, the waveguide ports in Fig. 4.1 (a) are replaced by the waveguide transitions designed in the previous chapter. In addition, an electrode arrangement is set up, such that both LC-molecule alignments can be electrically controlled. The full simulation setup is

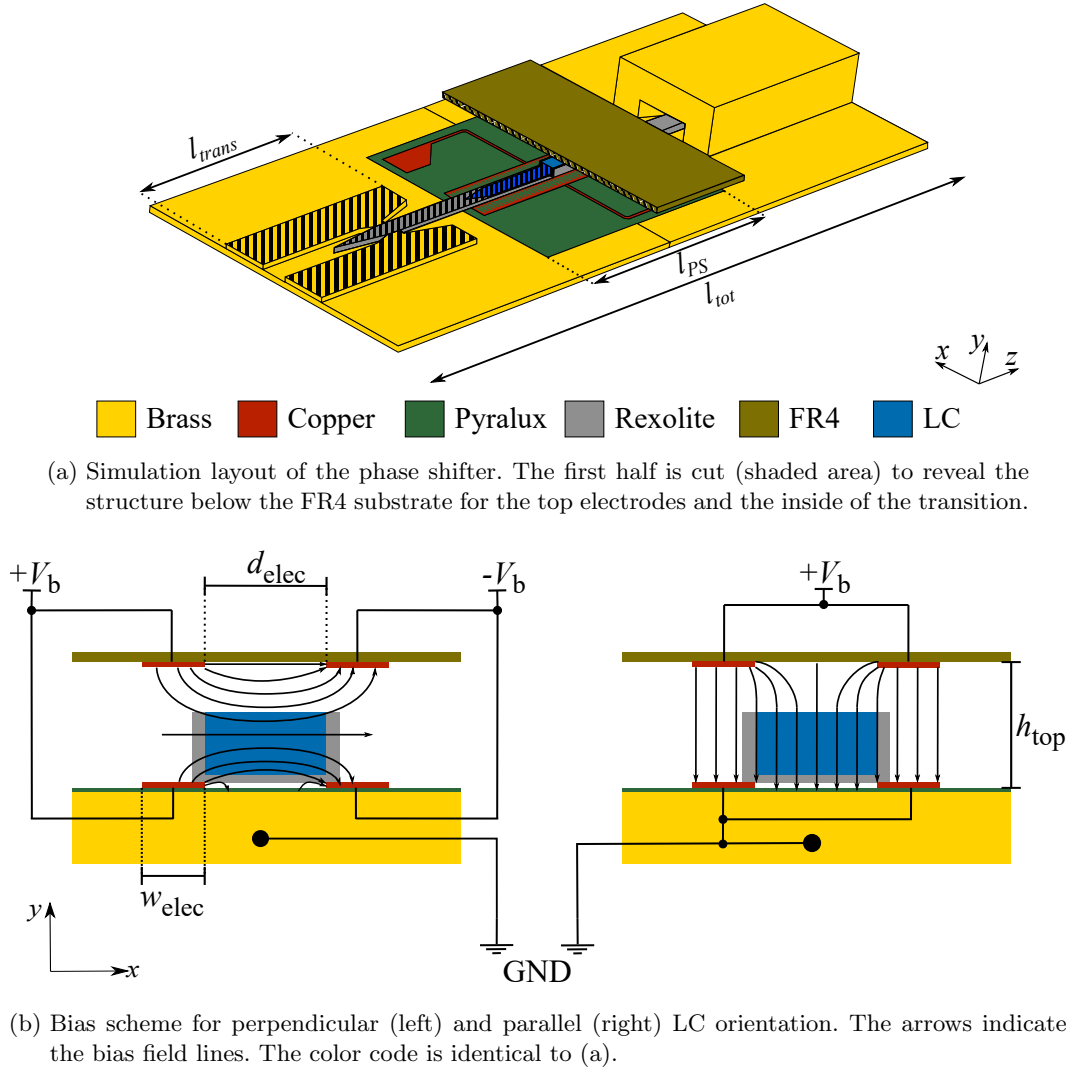


Figure 4.5: Simulation model (top) and bias scheme of the  $E_{11}^y$ -mode phase shifter (bottom).

shown in Fig. 4.5.

All corresponding final dimensions from Fig. 4.1 and Fig. 4.5 are given in Table 4.1. In order to bias the LC cavity, the electrode must be designed to mitigate two

Table 4.1.: Most important dimensions of the  $E_{11}^y$ -mode DIL phase shifter.

Parameter	$l_{LC}$	$w_{LC}$	$t_{LC}$	$l_{taper}$	$l_{PS}$	$l_{trans}$	$l_{tot}$	$d_{elec}$	$w_{elec}$	$h_{top}$
Value (mm)	21	1.5	0.75	3	23	19.5	67	1.25	1.8	1.9

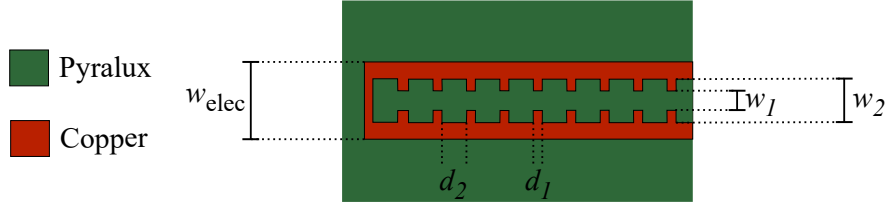
#### 4. Liquid Crystal Dielectric Image Line Phase Shifters

problems:

1. Bias field distortion due to the ground plane, mainly in perpendicular alignment.
2. Suppression of parasitic modes, which may arise in the bottom electrodes' substrate.

The ground plane is an image plane, which enables the image line topology. However, its fundamental properties hold true for (quasi-)static bias fields as well, i.e. the field distribution of the bias electrodes can be deduced by placing virtual image electrodes below the ground plane. Hence, a simple electrode setup such as utilized in [Ree20] which frames the waveguide is not possible and the electrode network is more related to hollow waveguide designs. Wide, flat bottom electrodes are necessary, which are in line with the desire of an integrated design. The  $18\ \mu\text{m}$  thick top electrodes, which are processed on a common FR4 substrate, need to be placed with a distance  $d_{\text{elec}}$  from the ground plane, such that they do not disturb the evanescent field of the DIL, and such that they provide a bias field distribution within the LC cavity, which is orthogonal to the RF-polarization. In order to provide the latter, top and bottom electrodes need to be sufficiently far away from each other. This distance was simulatively determined to  $d_{\text{elec}} = 1.25\ \text{mm}$ . Nonetheless, a fully accurate perpendicular alignment cannot be achieved, as sketched in Fig. 4.5 (b). The top electrode FR4 substrate does not affect wave propagation, and is arbitrarily set to a thickness of  $500\ \mu\text{m}$ .

The second problem arises due to the strip-like structure of the bottom electrodes. They are  $9\ \mu\text{m}$  thick and processed on  $12\ \mu\text{m}$  DuPont Pyralux AC substrate ( $\epsilon_r = 3.7$ ,  $\tan \delta = 0.003$ , at 1 MHz [DuP]), such that the DIL is only marginally distanced from the ground plane. Still, undesired parasitic modes can be excited in the substrate between electrode and ground plane. With increasing substrate thickness, this phenomenon gets more pronounced, see Fig. 4.6 (c). Even though a substrate thickness of  $t_{\text{Subst}} = 30\ \mu\text{m}$  corresponds to 3.3% of the DIL's height, this thickness proves to be impractical. Hence, the bottom substrate should be as thin as possible. In practice, small discrepancies in this height can arise, especially since the bottom substrate needs to be mounted on the ground plane. As the formation of substrate modes is very sensitive to substrate thickness, a stepped-impedance structure is employed to suppress this formation further. The layout of the stepped-impedance structure is shown in Fig. 4.6 (a) where Babinet's principle was used to create an inverted stepped-impedance structure, such that the edges of top and bottom electrodes still coincide. The difference of an unstructured strip versus the stepped-impedance structure with  $t_{\text{Subst}} = 12\ \mu\text{m}$  is shown in Fig. 4.6 (b).



(a) Layout of the inverted stepped-impedance bottom electrode structure.

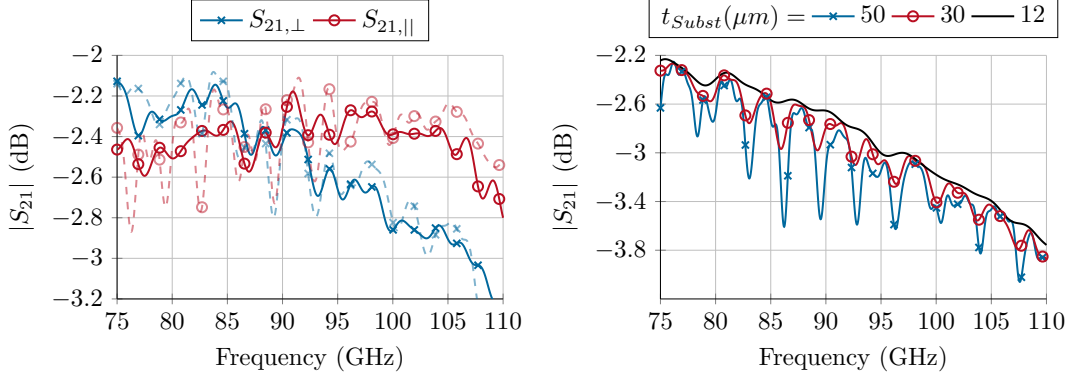
(b) Ripple reduction when employing a stepped impedance structure (solid) compared to non-structured electrodes (dashed). (c) Deterioration of  $|S_{21}|$  with increasing bottom substrate thickness  $t_{Subst}$ .

Figure 4.6: (a) Inverted stepped-impedance electrode structure and (b) its impact on the simulated  $|S_{21}|$  of the phase shifter compared to non-structured bottom electrodes. (c) Shows the high sensitivity on substrate thickness. The dimensions in mm are:  $w_{elec} = 1.8$ ,  $w_1 = 1.25$ ,  $d_1 = 1.25$ ,  $w_2 = 1.25$ ,  $d_2 = 1.25$ .

#### 4.1.2. Fabrication and Microwave Characterization

The Rexolite part of the phase shifter and its brass ground plane are milled by a Datron M10pro+ CNC milling machine at the precision mechanics workshop of TU Darmstadt. The waveguide transitions, also made by this workshop, are those introduced in Section 3.3. The ground plane is a 1.6 mm thick brass sheet. The bottom electrodes are photolithographically processed on 12  $\mu\text{m}$  thick Pyralux AC substrate, and the top electrodes are milled with a LPKF ProtoMat S100 rapid prototype circuit board plotter on 500  $\mu\text{m}$  thick FR4 substrate. The thickness of the bottom electrode substrate should be as thin as possible, but it needs to be mounted on the ground plane. Manually distributed glue results in uncontrolled height, which deteriorates the phase shifter's performance, as shown in Fig. 4.6 (c). Hence, a 1.5  $\mu\text{m}$  thin layer of MaN415 photoresist is spin-coated on the backside of the Pyralux substrate and used as glue, to minimize the total height of the bottom substrate. Together with the transitions, the DIL is placed on the ground plane with the bottom substrate. It is filled with LC using a micropipette, and the electrodes

#### 4. Liquid Crystal Dielectric Image Line Phase Shifters

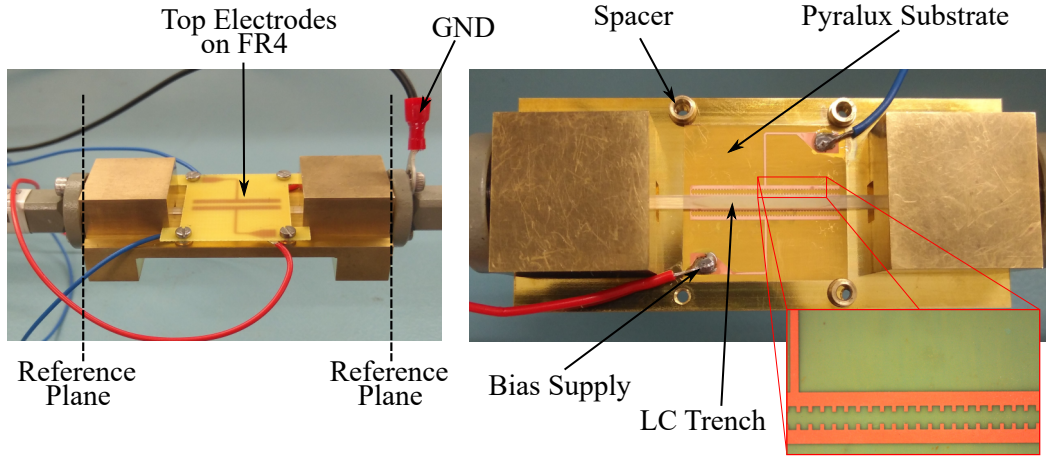
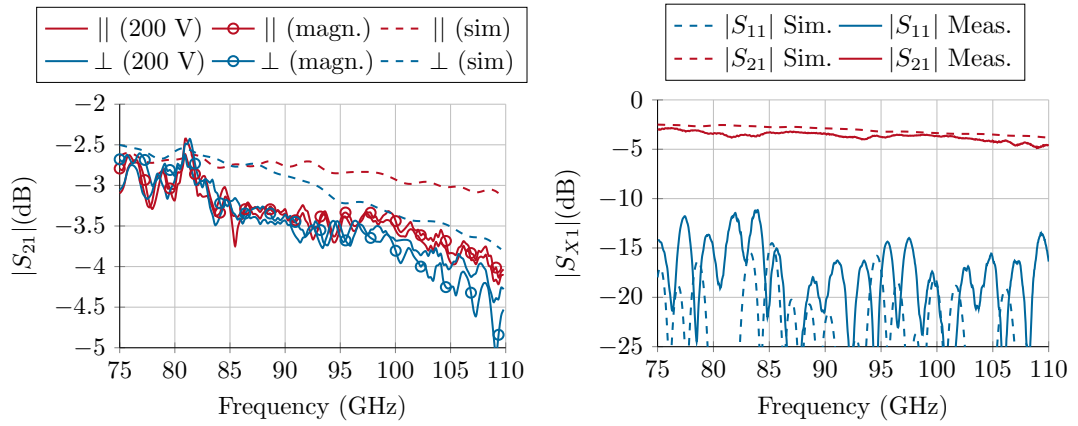


Figure 4.7: Photograph of the demonstrator in full assembly (left), and with the top electrodes removed to reveal the bottom electrode substrate, the LC section and a zoomed microscopic view of the bottom electrodes (right), based on [Tes+20a] © 2020 IEEE.



(a) Transmission of the phase shifter for different bias schemes. Magnetic bias is applied with assembled electrodes. (b) Simulation and measurement in most lossy configuration (perpendicular alignment).

Figure 4.8: Simulated and measured S-parameters of the realized  $E_{11}^y$ -mode phase shifter.

are connected to the voltage supply. The top electrode substrate is held in place by small spacers. The voltage source provides a 1 kHz rectangular bias signal with a peak-to-peak voltage of maximally  $V_{pp} = 200$  V. Fig. 4.7 shows the partly and fully assembled demonstrator, as well as a microscopic view of the stepped impedance bottom electrode. The S-parameters of the phase shifter are shown in Fig. 4.8. Different bias schemes show similar measurement results (Fig. 4.8 (a)). For magnetic

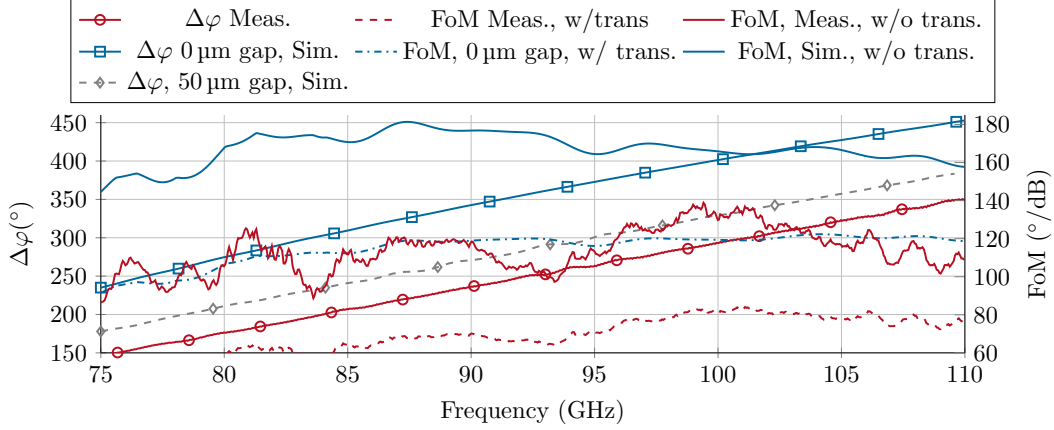
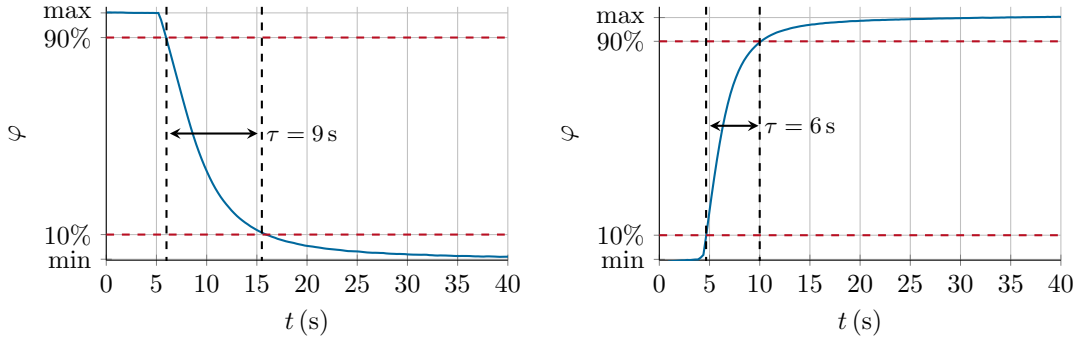


Figure 4.9: Measured differential phase shift  $\Delta\varphi$  and resulting FoM in comparison to simulations with different gap widths between DIL and ground plane. For simulations, an RMS of surface roughness for the ground plane of  $R_a = 0.8 \mu\text{m}$  is assumed.

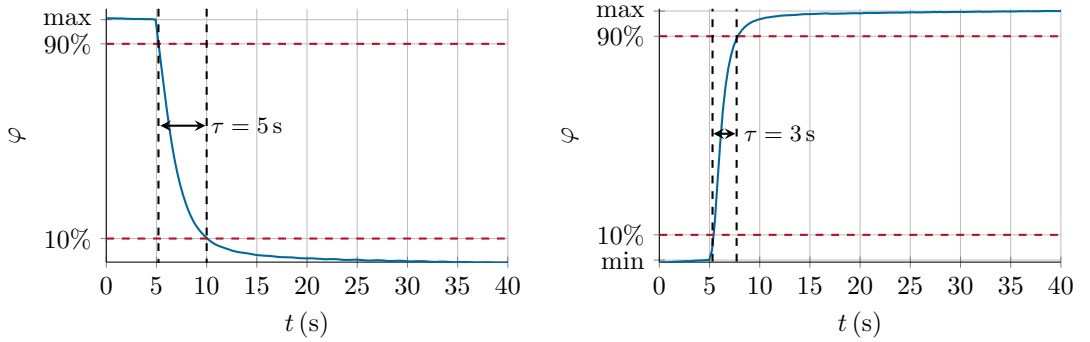
bias, permanent magnets which apply a magnetic flux density of  $B = 200 \text{ mT}$  are placed around the demonstrator to achieve the desired LC orientation. Good matching is achieved with  $|S_{11}| < -10 \text{ dB}$  in the entire W-Band, as Fig. 4.8 (b) indicates. Higher IL of up to 1 dB more than simulated is observed, which stems mostly from the higher loss of the transitions (see Section 3.3). The achieved phase shift  $\Delta\varphi$  and the resulting FoM are plotted in Fig. 4.9. About  $100^\circ$  less differential phase shift than simulated is obtained. A non-optimal electric bias field can contribute to this discrepancy. This can be quantified by comparing  $\Delta\varphi_{\text{el}}$  with electric bias to  $\Delta\varphi_{\text{mag}}$  with magnetic bias: the electric bias shows a maximum reduction in  $\Delta\varphi$  by up to  $50^\circ$ . Of similar importance is a small gap between bottom electrode substrate and DIL, which could not be excluded during measurements. Hence, Fig. 4.9 includes the loss in differential phase for a  $50 \mu\text{m}$  gap. This gap contributes to a reduction of  $\Delta\varphi$  by a constant offset of around  $65^\circ$ . With reduced  $\Delta\varphi$ , and slightly higher loss in practice, the measured FoM is smaller than simulated. The directly measured FoM ranges from  $50^\circ \text{ dB}^{-1}$  to  $84^\circ \text{ dB}^{-1}$  and reaches its maximum of  $84^\circ \text{ dB}^{-1}$  at 101 GHz. With knowledge of the transition's loss in practice, averaging  $0.687 \text{ dB}$  per transition (c.f. Section 3.3), the FoM of the standalone phase shifter can be estimated to range from  $93.57^\circ \text{ dB}^{-1}$  to  $136.91^\circ \text{ dB}^{-1}$  without transitions, which are good values for phase shifters in W-Band. The standalone FoM of the simulated phase shifter is included in Fig. 4.9, and reaches up to  $182^\circ \text{ dB}^{-1}$ , mostly because of the higher  $\Delta\varphi$ .

The high advantage of an LC-DIL phase shifter compared to a fully dielectric one manifests in its reduced response time, which is generally measured between the 90% and 10% value of the initial and final signal state. Those are shown in Fig. 4.10, for two different peak-to-peak voltages  $V_{pp}$  of the 1 kHz rectangular bias signal. Due to closer electrode spacing, a reduction of response time by up to 65%

#### 4. Liquid Crystal Dielectric Image Line Phase Shifters



(a) Response time from perpendicular to parallel state, with  $V_{pp} = 200$  V. (b) Response time from parallel to perpendicular state, with  $V_{pp} = 200$  V.



(c) Response time from perpendicular to parallel state, with  $V_{pp} = 300$  V. (d) Response time from parallel to perpendicular state, with  $V_{pp} = 300$  V.

Figure 4.10: Measured response times of the  $E_{11}^y$ -mode phase shifter for different peak-to-peak voltages  $V_{pp}$ , of the 1 kHz rectangular bias voltage. Phases are normalized to their maximum (perpendicular) to minimum (parallel) phase, and corresponding lines which mark the 90% or 10% threshold are included.

when compared to a fully dielectric demonstrator with same  $V_{pp} = 200$  V is achieved [Ree20; Tes+20a]. With higher  $V_{pp}$ , response times can be further reduced. A high voltage is mainly necessary for fast response times, since  $V_{pp} = 200$  V is sufficient to reach the maximum phase shift. Hence, an overshoot of bias voltage for a fast response time, followed by a lower voltage for maintaining the desired phase shift can be used in practical applications.

#### 4.1.3. Temperature Characterization

The performance of the  $E_{11}^y$ -mode phase shifter is also evaluated in dependence of temperature. In environments outside the lab, high temperature differences may arise, e.g. due to exposure to weather effects. For this evaluation, the phase shifter



is placed on a thicker ground plane, which has the bottom parts of the transition integrated in it. A PT100 temperature sensor is inserted into the thick ground plane, and monitors its temperature without interacting with the DIL. In order to heat or cool the ground plane, it is mounted on a copper block with fluidic channels. A Julabo FP50 Heating/Refrigerating Circulating Thermostat is used to heat or cool the copper block. With feedback from the sensor, a constant temperature can be achieved in the ground plane. In order to avoid moist or frost on the structure, it is enclosed by a transparent PVC box, in which a steady flow of nitrogen is present. For simplicity reasons, the electrodes are not included in this setup and LC control is performed by magnets. They rotate around the whole setup, and provide a magnetic flux density of  $B \approx 0.25$  T. The measurement setup is shown in Fig. 4.11. A temperature range from  $-10^\circ\text{C}$  to  $80^\circ\text{C}$  is covered. Lower temperatures could not be realized by the Julabo FP50 Thermostat, since the cooling liquid heats up during its way from the thermostat to the cooling block. Higher temperatures than  $80^\circ\text{C}$  cause the DIL to deform.

Measurement results are summarized in Fig. 4.12. While matching is not affected,  $|S_{21}|$  decreases with increasing temperature, regardless of alignment state. A maximum difference of 1.5 dB in parallel LC orientation, and 1.9 dB in perpendicular orientation is observed. It is most noticeable that with every temperature interval of  $10^\circ\text{C}$ , an almost constant decrease  $\Delta|S_{21}| \approx 0.2$  dB is measured. The characteristic curves of  $|S_{21}|$  remain almost in parallel for each temperature. Since GT-29001 is a thermotropic LC-mixture, its anisotropy decreases with temperature, as the order of molecules decreases. Hence, the achievable differential phase shift  $\Delta\varphi$  de-

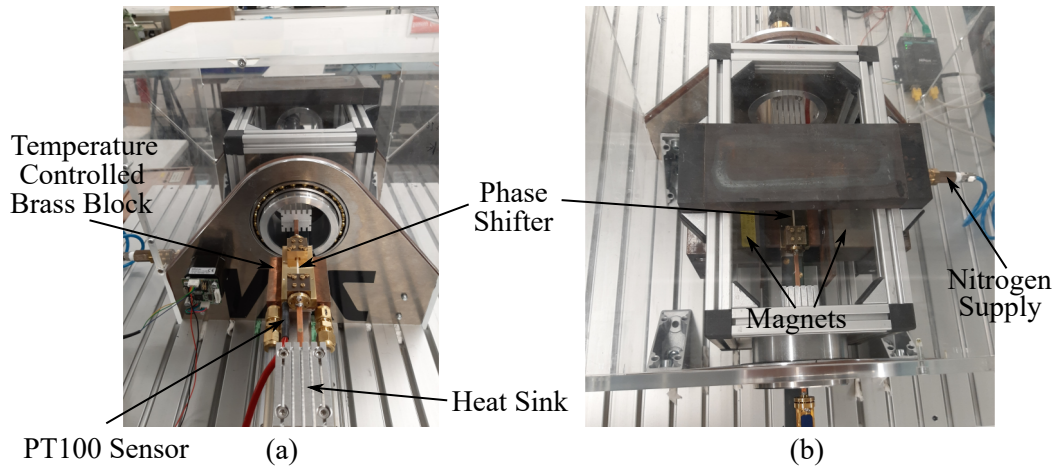


Figure 4.11: Measurement setup for temperature characterization. The setup in (a) is inserted into the arrangement of rotatable magnets, which are enclosed by a PVC box. (b) shows a top view of the inserted setup with magnets positioned for perpendicular LC alignment [Tes+21b] (CC BY 4.0).

#### 4. Liquid Crystal Dielectric Image Line Phase Shifters

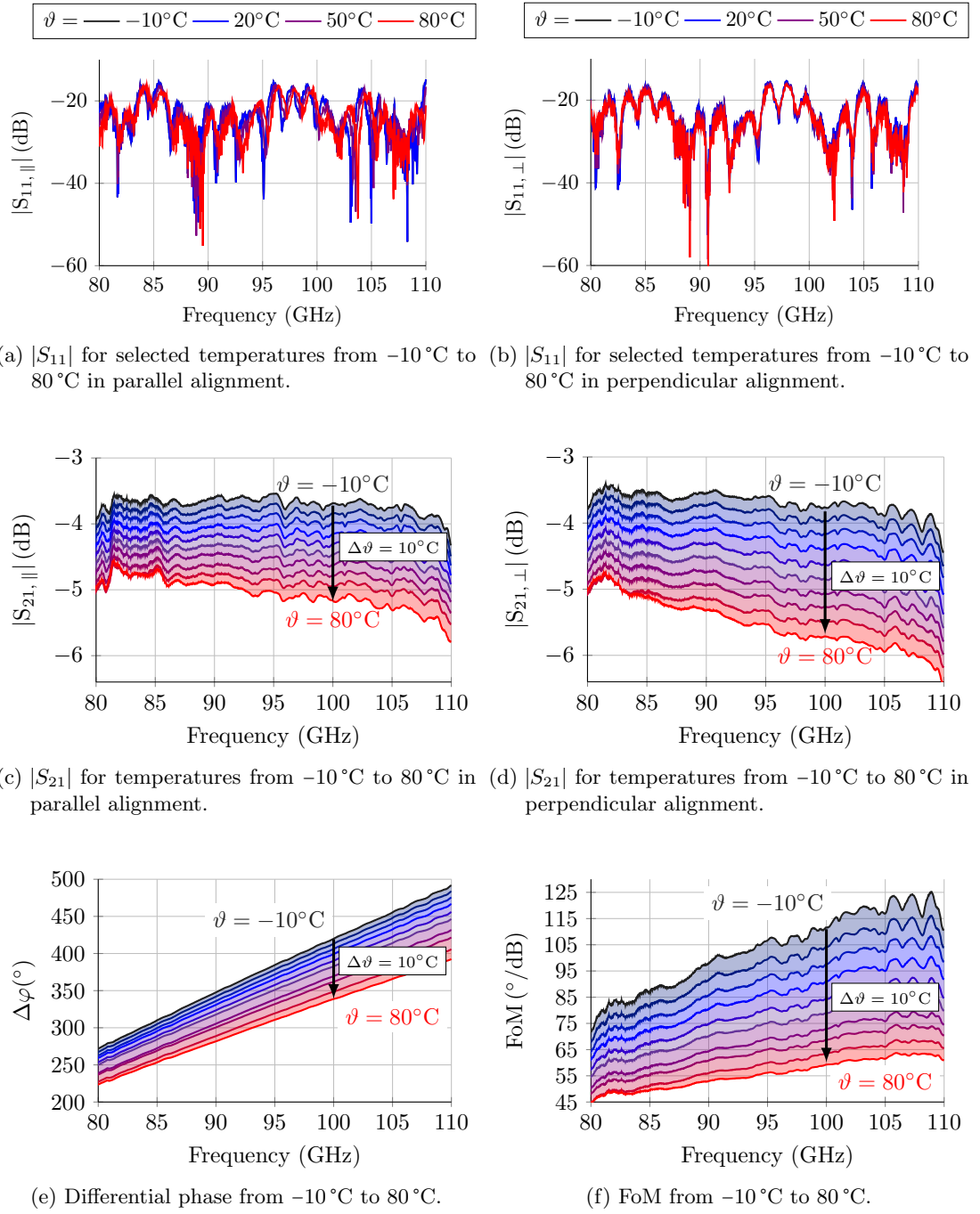


Figure 4.12: Temperature characterization of the phase shifter [Tes+21b] (CC BY 4.0). Since no significant change in  $|S_{11}|$  is present within the investigated temperature range, only selected temperatures are plotted in (a) and (b) for more clarity.

creases with the reduction of  $\Delta\varepsilon_r$ , caused by increasing temperature. Similar to the course of  $|S_{21}|$ ,  $\Delta\varphi$  decreases linearly for each frequency. However, due to the decreasing anisotropy, different slopes in  $\Delta\varphi$  are present when observing the behavior for the whole frequency range, as already shown in Section 4.1.1 (Fig. 4.3 (b)). In particular, we observe that the frequency  $f_{\Delta\varphi 360}$ , where  $\Delta\varphi = 360^\circ$ , shifts from  $f_{\Delta\varphi 360} = 91.7$  GHz to  $f_{\Delta\varphi 360} = 104$  GHz in the investigated temperature range from  $-10^\circ\text{C}$  to  $80^\circ\text{C}$ . At room temperature ( $\vartheta = 20^\circ\text{C}$ ),  $f_{\Delta\varphi 360} = 94$  GHz. This is at a lower frequency than in the measurement with electrodes ( $f_{\Delta\varphi 360} = 110$  GHz), due to three reasons: first, an air gap has been carefully avoided by using Rexolite adhesive. Second, no bottom electrode substrate is present in this setup. Third, magnetic bias is able to provide a non-distorted bias field distribution, since the field lines are not affected by the ground plane. The increased differential phase directly leads to a high FoM, depicted in Fig. 4.12 (f). The maximum FoM at 109 GHz ranges from  $126.6^\circ\text{dB}^{-1}$  to  $63.7^\circ\text{dB}^{-1}$  in the investigated temperature interval, and degrades by

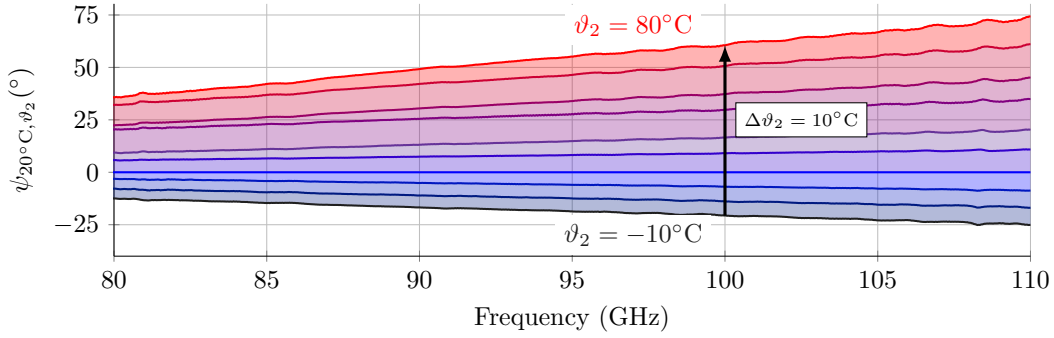
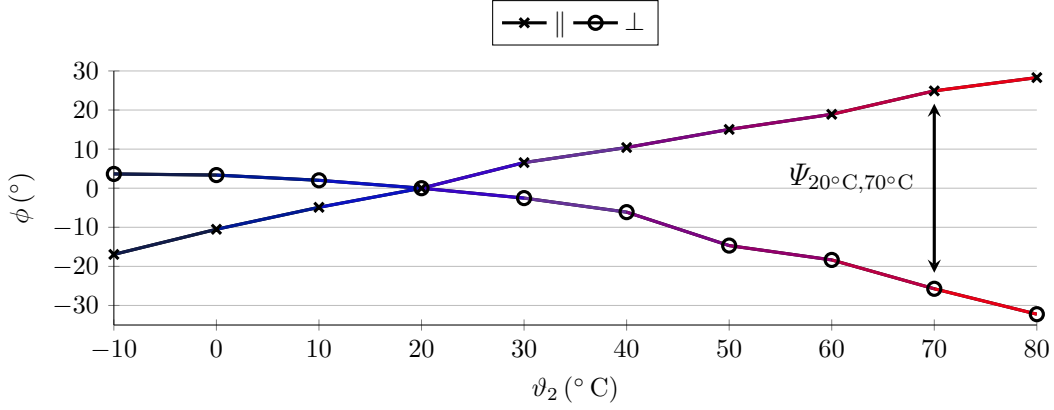

 (a) Course of  $\Psi_{20^\circ\text{C}, \vartheta_2}$  over frequency.

 (b)  $\phi$  at 100 GHz.

Figure 4.13: (a) Difference in  $\Delta\varphi$  and (b) its decomposition to change of phase in parallel or perpendicular molecule alignment. Both  $\Psi$  and  $\phi$  have reference temperature  $\vartheta_1 = 20^\circ\text{C}$  [Tes+21b] (CC BY 4.0).

#### 4. Liquid Crystal Dielectric Image Line Phase Shifters

2.5° dB<sup>-1</sup> to 8° dB<sup>-1</sup> per  $\Delta\vartheta = 10^\circ\text{C}$ . The FoM includes the loss of the waveguide transitions. As the differential phase resembles the utilizable anisotropy of the LC, it is worth investigating the behavior of  $\Delta\varphi$  further. The difference of  $\Delta\varphi$  at a fixed frequency between temperatures  $\vartheta_1$  and  $\vartheta_2$  is represented by

$$\Psi_{\vartheta_1, \vartheta_2} = \Delta\varphi_{\vartheta_1} - \Delta\varphi_{\vartheta_2}. \quad (4.4)$$

At 100 GHz  $\Psi_{-10^\circ\text{C}, 80^\circ\text{C}} = 80^\circ$ . It is most reasonable to set  $\vartheta_1 = 20^\circ\text{C}$  to show the discrepancy in differential phase shift compared to room temperature. The course of  $\Psi_{20^\circ\text{C}, \vartheta_2}$  versus frequency is shown in Fig. 4.13 (a). As expected, the discrepancies rise linearly with frequency and have different slopes for each  $\vartheta_2$ . While at  $\vartheta_2 = 30^\circ\text{C}$  the slope of  $\Psi$  is  $0.17^\circ\text{GHz}^{-1}$ , it rises to  $1.29^\circ\text{GHz}^{-1}$  at  $\vartheta_2 = 80^\circ\text{C}$ . To assess to which extent the change of anisotropy  $\Delta\varepsilon_r$  is dependent on molecule alignment, the raw phase in parallel and perpendicular alignment is compared to the reference phase at  $\vartheta_1 = 20^\circ\text{C}$ , for each temperature  $\vartheta_2$ . The deviation from the reference phase is denoted by

$$\phi = \varphi_{\vartheta_2} - \varphi_{\vartheta_1}. \quad (4.5)$$

$\phi$  is plotted in Fig. 4.13 (b) at 100 GHz. We observe that the parallel alignment is more affected by temperature change than the perpendicular alignment. The phase of both alignment states changes rather linearly, with slopes of  $0.55^\circ\text{K}^{-1}$  in parallel and  $0.4^\circ\text{K}^{-1}$  in perpendicular alignment. This higher dependency in parallel alignment is in agreement with the observation of [Pol23] (c.f. Fig. 2.8 (a)). The provided data indicate that a rather linear degradation of performance of an LC-DIL phase shifter can be expected in practice, when the ambient temperature increases. In practical applications, a more narrow frequency band is likely to be employed. In order to balance off reduced  $\Delta\varphi$  and degraded  $|S_{21}|$  with increasing temperature, the thermal conductivity of the metallic ground plane can be used to employ passive heat sinks, or active thermoelectric coolers.

##### 4.1.4. Electrode Integration for Fast Switch-On Response Times

Even though significant reduction in response time compared to fully dielectric LC-phase shifters has been demonstrated in the previous section, voltages of  $V_{pp} = 200\text{V}$  and response times in the range of seconds are limiting the field of applications for LC-DIL phase shifters. In order to reduce both, the electrode placement should be as close as possible to each other. The goal in this section is to put the electrode structure directly on the DIL without interfering with the propagating wave.

Usually, placement of any metallic structure on a DIL causes radiation loss. Hence, the goal is to minimize this radiation loss without affecting the mode of the propagating wave severely. The overall idea of the designs presented in this section follows a simple analogy: like linear polarizers, where one wave polarization is suppressed while the other remains untouched, an electrode structure which only affects one polarization while being "invisible" to the other one is pursued. Following this analogy, an  $E_{11}^y$ -mode LC-DIL phase shifter should not have electrodes which are long in

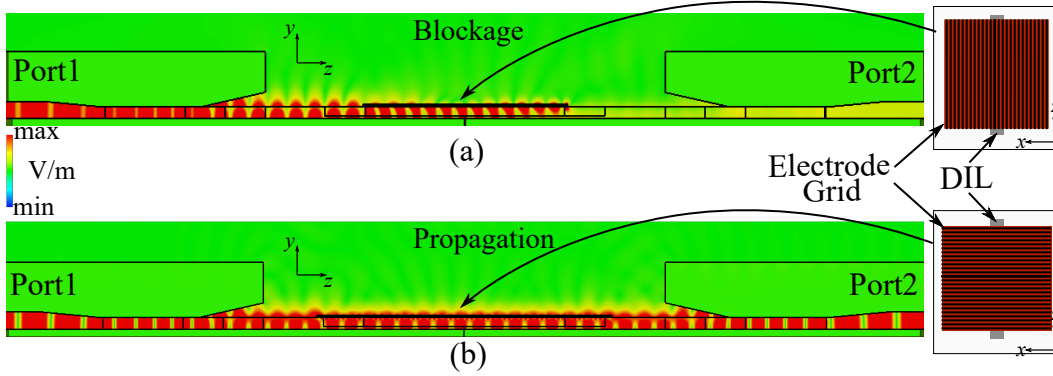


Figure 4.14: Absolute instantaneous electric field at 85 GHz at the longitudinal cross-section of the simulation setup. It includes the waveguide transitions at both ends, and a thin substrate with electrode strips, shown in a top-view on the right, which is put on the DIL in the center of the setup. (a) Electrode strips along propagation direction. (b) Electrode strips orthogonal to propagation direction.

$y$ -direction. Since this direction is normal to the ground plane, no electrode design will ever be long in  $y$ -direction. From the remaining two directions,  $x$  and  $z$ , there is one direction in which components of the  $E$ -field are present: due to the *hybrid* nature of the modes of DILs, there will always be components in the direction of propagation, i.e.  $z$ , and field lines reach from one point of the DIL to another point along the DIL. If a conducting connection between them exists, a current may flow. Hence, the main direction in which electrodes should extend to is orthogonal to  $y$  and  $z$ , i.e.  $x$ . First trials have been conducted by simulations. Fig. 4.14 shows the instantaneous field distribution of a Rexolite DIL in  $E_{11}^y$ -mode with a substrate, on which an electrode grid with different orientation is placed directly on the DIL. The electrodes grid is composed of strips of width  $w = 200 \mu\text{m}$ , thickness  $t = 12 \mu\text{m}$ , a distance  $d = 200 \mu\text{m}$  to each other, and go from one end of the substrate to the other one. The substrate is RO5880 ( $\epsilon_r = 2.2$ ,  $\tan \delta = 0.0009$ ) in one of its commercial standard thicknesses of  $t_{subst} = 0.127 \text{ mm}$ . In Fig. 4.14 (a), the strips are repeated in  $x$ -direction, i.e. their long side is along  $z$ , and leads to severe perturbations of the field distribution. In Fig. 4.14 (b), the repetition is in  $z$ , and the long side is along  $x$ , hence, the evanescent field of the DIL may pass unperturbed. Closer inspection reveals that transmission in the orthogonal case is only possible in certain, about 10 GHz wide frequency windows, according to Fig. 4.15 (a). Resonances within the structured section of the DIL cause band stops, and within these frequency regions no operation is possible. This layout has been fabricated to confirm simulations. Measurement results are shown in Fig. 4.15 (b) and (c), and highlight the sensitivity to small angular deviations  $\Delta\rho$  from perfect orthogonal alignment in practice. The DIL is milled from Rexolite 1422, and the electrode grid is etched on RO5880. The substrate is glued on top of the DIL with help of optical adhesive. Deviations by

#### 4. Liquid Crystal Dielectric Image Line Phase Shifters

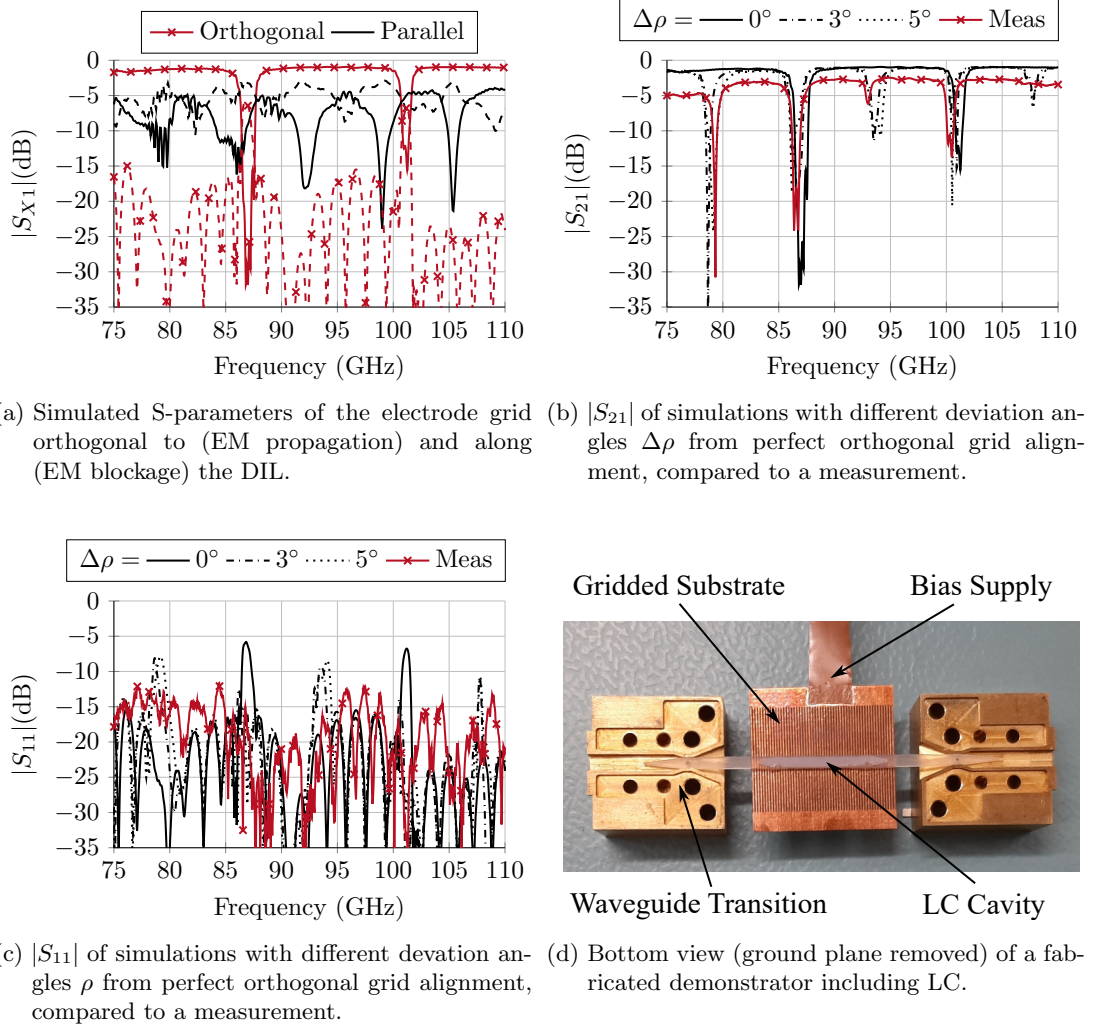


Figure 4.15: (a)-(c) Simulation and measurement data of a Rexolite DIL (no LC present) with an electrode grid, and (d) a picture of a demonstrator with LC cavity.

1.5 dB in  $|S_{21}|$  are present due to higher transition loss, and higher material loss than anticipated in simulations, e.g. by the RO5880 substrate or higher amounts of glue used in practice. Fig. 4.15 (d) depicts a demonstrator with an LC cavity. In order to fill the DIL with LC, two small filling holes are at the sides of the cavity, placed directly at the tips of its tapers. LC is filled with a syringe, and the holes are sealed with optical adhesive. The LC-DIL phase shifter is mounted on the ground plane with Rexolite adhesive. When using the grid with an LC cavity, and tuning the LC, the windows shift slightly, and higher insertion loss, stemming from the LC, is present, as shown in Fig. 4.16. Windows from 79 GHz to 84 GHz, from 87 GHz to 97 GHz, and from 101 GHz to 110 GHz can be utilized in all bias states. However,

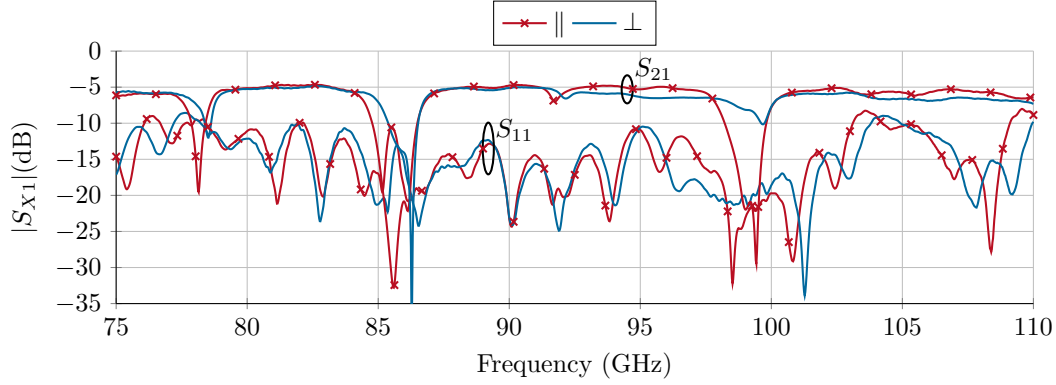


Figure 4.16: Measured S-parameters of an LC-DIL phase shifter with grid electrodes (c.f. Fig. 4.15 (d)) in parallel and perpendicular molecule alignment.

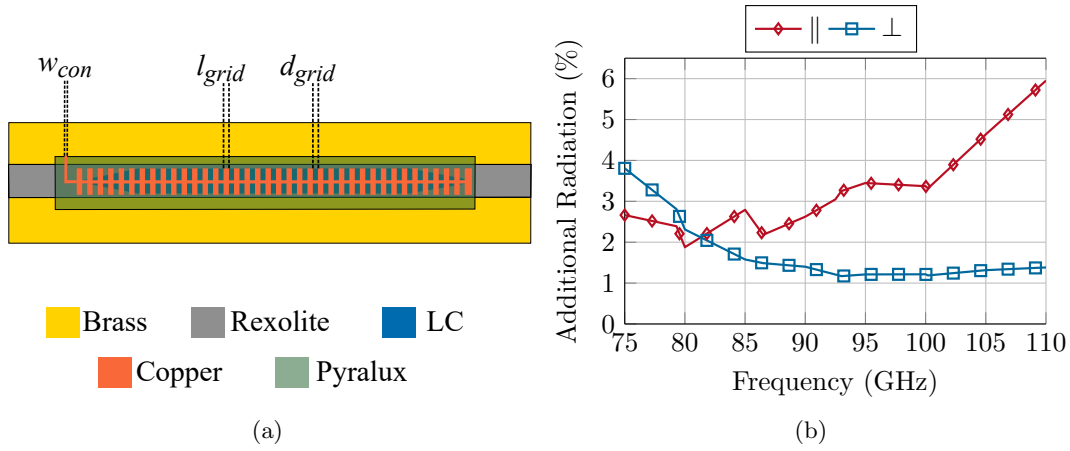


Figure 4.17: (a) Layout of the optimized electrode and (b) the additional radiation caused by it when compared to a simulated structure without electrodes.

due to the combined loss of LC and electrode substrate the phase shifter gets lossy. In addition,  $\Delta\varphi$  is mitigated and ranges from  $101.5^\circ$  to  $266^\circ$  in W-band. Hence, the FoM ranges from  $21^\circ \text{dB}^{-1}$  to  $39^\circ \text{dB}^{-1}$ , only. If taking account of the waveguide transitions, the FoM slightly improves to  $31.5^\circ \text{dB}^{-1}$  to  $48.8^\circ \text{dB}^{-1}$ . However, the switch-on response time can reach sub-second values for  $V_{pp} > 150 \text{ V}$ . In order to utilize the full W-band without the windowed characteristic and to mitigate effects of the substrate, the layout of the electrode is changed in two ways: first, the substrate is changed to  $12 \mu\text{m}$  thin Pyralux AC, and the layout of the electrode is revised. The main goal is to enable a structure which could be directly put on the DIL's top, e.g. by selective metallization. This means that the whole electrode structure should not exceed the width of the DIL. Optimizations are carried out with CST Microwave Studio Suite. The optimized electrode structure is shown in Fig. 4.17 (a). The grid

#### 4. Liquid Crystal Dielectric Image Line Phase Shifters

character is maintained with electrodes of width  $l_{grid} = 0.3$  mm which have a spacing of  $d_{grid} = 0.3$  mm. The reduced width of the electrodes helps to suppress modes and maintain a layout which could be metallized directly on the DIL. In order to bias the individual electrode strips, a  $100\ \mu\text{m}$  thin bias line connects them to each other. The thinner the line, the less its influence on the system. Due to manufacturing restrictions, this line could maximally be reduced to  $75\ \mu\text{m}$  when processed on Pyralux. In order to assess the structure's influence, and in particular the longitudinal bias line's influence on radiation, simulations with and without the electrode structure have been conducted. The additional radiation loss introduced by the electrode network is shown in Fig. 4.17 (b). From 80 GHz on, the additional radiation loss ranges from 1% to 2% in perpendicular molecule alignment and is below 4% for parallel alignment, before it starts to increase at 100 GHz. The realized demonstrator is shown in Fig. 4.18 (a). For simplicity reasons, the substrate is wider than necessary. Since the integrated electrode takes care of parallel alignment, perpendicular alignment is only achieved by the natural re-organization of the molecules after bias is released. This results in a non-optimal perpendicular alignment state. Perfect perpendicular alignment can be forced by employing a pair of magnets besides the DIL phase shifter, as shown in Fig. 4.18 (b). Their static magnetic field forces the molecules into perpendicular alignment. The electric field has therefore to surpass a threshold voltage, at which it becomes stronger than the magnetic field, to create parallel alignment. Due to the distance of the magnets to the DIL, they do not interfere with the structure and do not influence its performance. The S-parameters are given in Fig. 4.19 (a). Stop bands have been successfully removed, and similar performance is achieved in both, parallel and perpendicular molecule alignment. However, higher loss,  $|S_{21}| \approx -5$  dB, than anticipated in simulations is present. In this design, the filling holes have been moved from the side of the LC cavity taper to the bottom of it, since filling holes on the sides proved to be very impractical. The new position of the filling holes allow easy filling of LC, but since they are directly on the ground plane, where the E-field is maximal, the glue necessary for sealing can have bigger

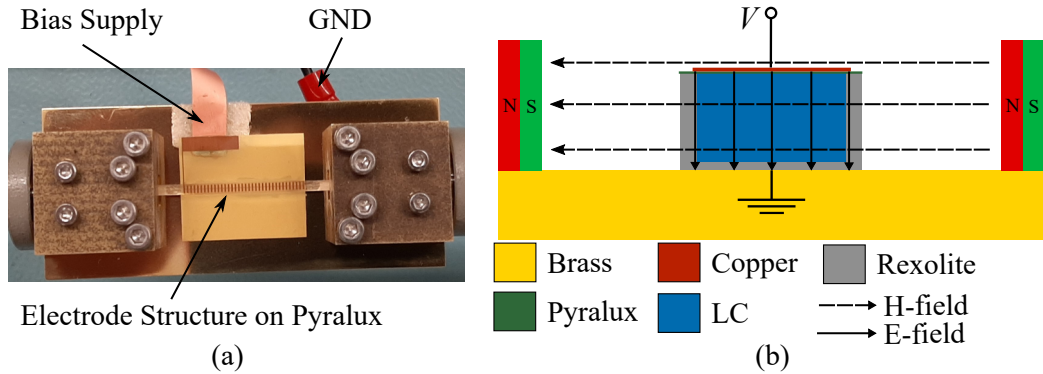
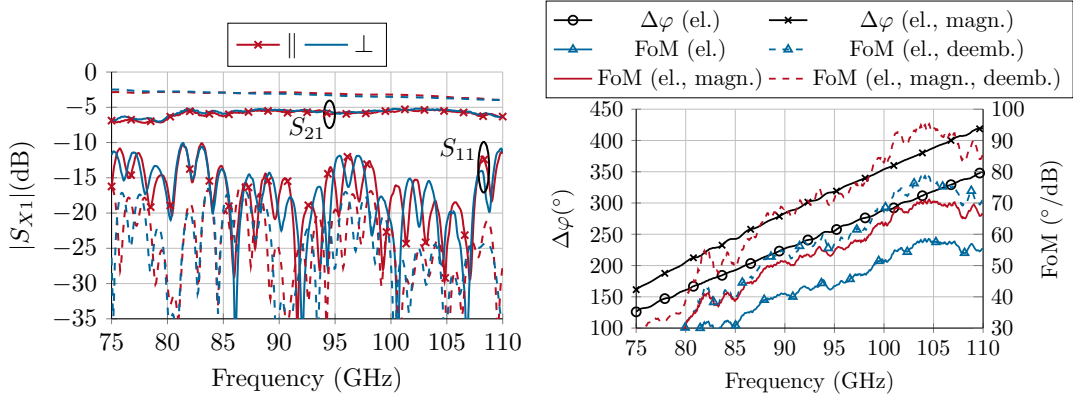


Figure 4.18: (a) Demonstrator with improved electrode design [Tes+22a] ©2022 IEEE and (b) hybrid bias scheme.

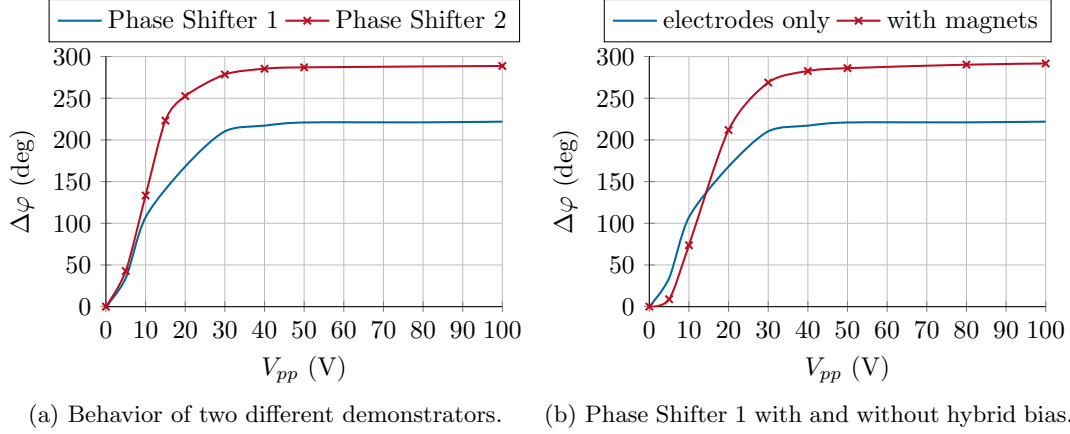


#### 4.1. LC-Phase Shifter in $E_{11}^y$ -Mode



(a) Measured (solid) versus simulated (dashed) S-parameters. (b)  $\Delta\varphi$  and resulting FoM (with and without magnets) of the phase shifter.

Figure 4.19: (a) S-parameters of the phase shifter with integrated electrode and (b) resulting  $\Delta\varphi$  and FoM with and without hybrid bias. Dashed lines in (b) indicate the deembedded FoM, which excludes transition loss.



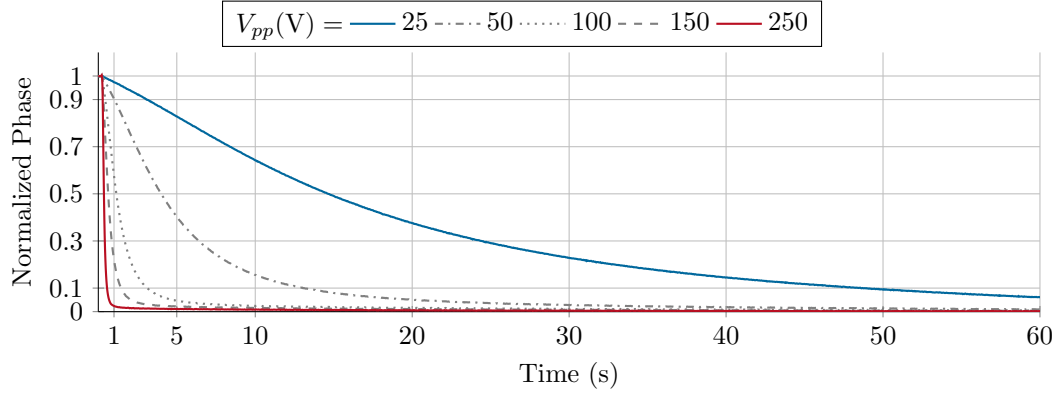
(a) Behavior of two different demonstrators. (b) Phase Shifter 1 with and without hybrid bias.

Figure 4.20: Necessary voltage  $V_{pp}$  for a certain differential phase shift  $\Delta\varphi$  at 100 GHz.

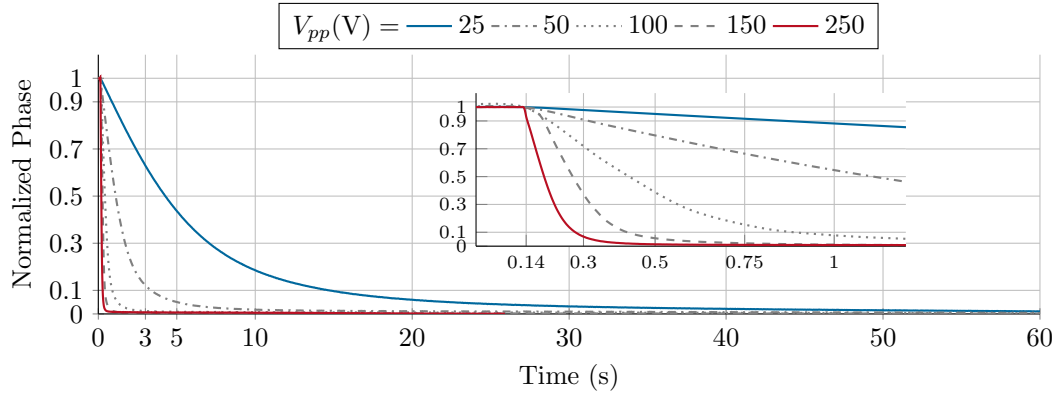
impact on the structure's loss.

The achieved differential phase shift and resulting FoM are presented in Fig. 4.19 (b). When excluding the transitions, the phase shifter with integrated electrodes can reach a maximum FoM of  $80^\circ \text{dB}^{-1}$ . When employing hybrid bias with magnets, which create a  $B = 70 \text{ mT}$  strong magnetic flux density at the LC cavity's position, higher  $\Delta\varphi$  can be achieved while leaving the S-parameters unchanged. As a result, the FoM increases, and reaches values of up to  $94^\circ \text{dB}^{-1}$  after deembedding. The main benefit from placing the electrodes directly on the DIL are lower voltages for a desired phase shift, and faster switch-on response times. The necessary voltage for biasing the demonstrator are shown in Fig. 4.20, for both pure electric and hybrid bias

#### 4. Liquid Crystal Dielectric Image Line Phase Shifters



(a) Switch-on response time for hybrid bias.



(b) Switch-on response time for electrical bias. Zoomed view on first second included.

Figure 4.21: Switch-on response times for (a) hybrid and (b) electric bias.

schemes. Fig. 4.20 (a) includes two curves for two individually realized phase shifters to highlight assembly tolerances, mainly caused by glue entering the sealing holes. As we can observe in Fig. 4.20 (b), the hybrid bias increases the necessary voltage for a desired phase shift slightly. Due to better perpendicular alignment, the maximum  $\Delta\varphi$  can be increased by about  $50^\circ$  at 100 GHz when employing magnets. Since only a small increase in  $V_{pp}$  is present with hybrid bias, it should be preferred, if space and resources can be allocated to this bias scheme. Fig. 4.21 shows the switch-on response time for hybrid and electric bias. With low voltages, long response times are necessary for reaching the desired signal state. Drastic decrease to the sub-second range is possible for  $V_{pp} > 150$  V. The fastest switch-on response time of 134 ms is realized for electric bias at  $V_{pp} = 250$  V. In hybrid bias, this response time doubles to 270 ms. These switch-on response times are significantly lower than in previous designs. A 99.2% decrease with respect to fully dielectric concepts (17 s, [Ree20]) and a 97.7% decrease with respect to the distanced layout from Section 4.1.1 has been achieved. Since Fig. 4.20 shows that lower voltages are necessary to keep a certain

phase shift, the concept of overshooting this necessary voltage for a quick response, and then stabilizing on the desired voltage, is the only way to achieve sub-second switch-on response time characteristics. In this section, only fast switch-on response time is covered. If the voltage is returned to zero, perpendicular molecule alignment is either achieved by natural re-alignment or by the magnetic bias field. These response times are at the current state at the range of seconds, but can be addressed by either stronger magnets, or experimental LC-mixtures [Lan+20].

## 4.2. LC-Phase Shifter in $E_{11}^x$ -Mode

The considerations for the  $E_{11}^y$ -mode phase shifter can be transcribed to the orthogonal  $E_{11}^x$ -mode. For this, the suitable cross-section of  $w \times h = 2 \text{ mm} \times 1.8 \text{ mm}$  (c.f. Section 3.1.1) is used for the Rexolite DIL in which the LC is incorporated.

### 4.2.1. Design

Similar considerations to the  $E_{11}^y$ -mode LC-phase shifter are taken into account when designing the  $E_{11}^x$ -mode LC-phase shifter. A  $t_{LC} = 1.55 \text{ mm}$  high LC cavity is inserted in the Rexolite body, which has a 3 mm long taper. As a result, a  $250 \mu\text{m}$  thick layer of Rexolite remains between LC and ground plane. Fig 4.22 (a) shows that the width  $w_{LC}$  of this cavity mainly affects  $\varepsilon_{r,eff}$  in parallel director alignments, similar to Fig. 4.2 (a). The effect of different  $w_{LC}$  is stronger, since the cavity has a higher  $t_{LC}$ . In Fig. 4.22 (b), the effect of different width at various  $\varepsilon_{r,LC}$  is shown. Compared to

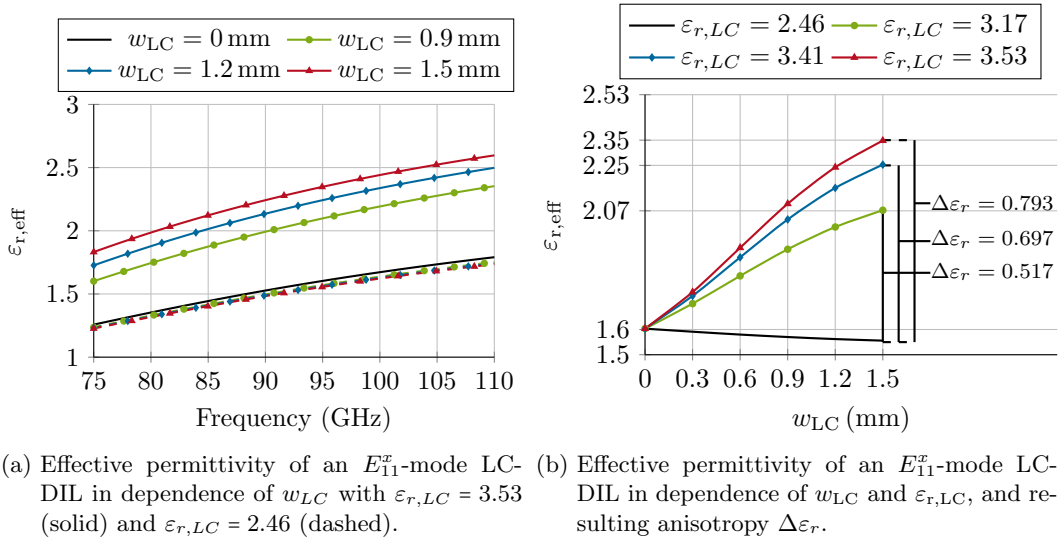


Figure 4.22: Influence of  $w_{LC}$  on  $\varepsilon_{r,eff}$  of the  $E_{11}^x$ -mode LC-DIL (a) over frequency and (b) consequences of the achievable maximum LC permittivity  $\varepsilon_{r,LC}$  on the achievable anisotropy  $\Delta\varepsilon_r$  at 95 GHz.

#### 4. Liquid Crystal Dielectric Image Line Phase Shifters

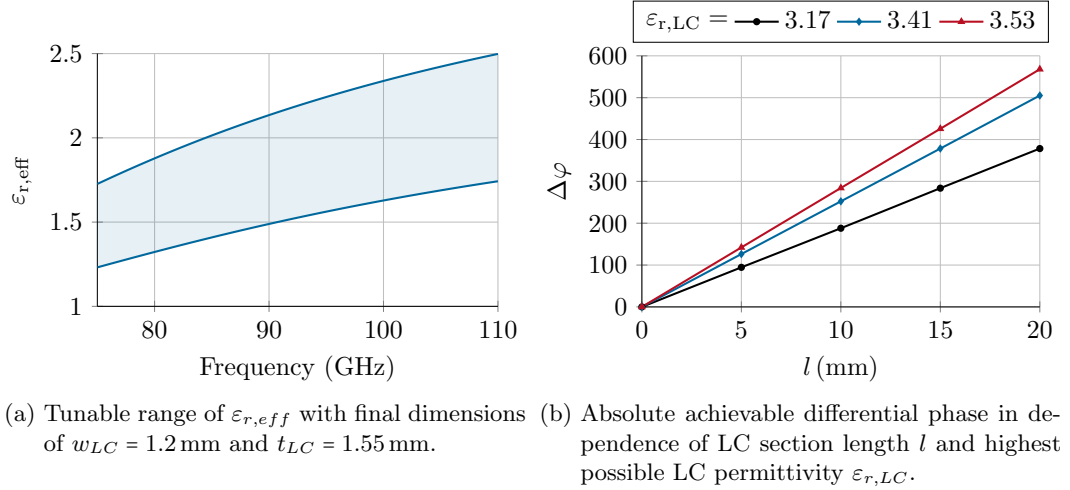


Figure 4.23: (a) Achievable range of  $\epsilon_{r,eff}$  with dimensions for the final design and (b) achievable  $\Delta\varphi$  at 95 GHz.

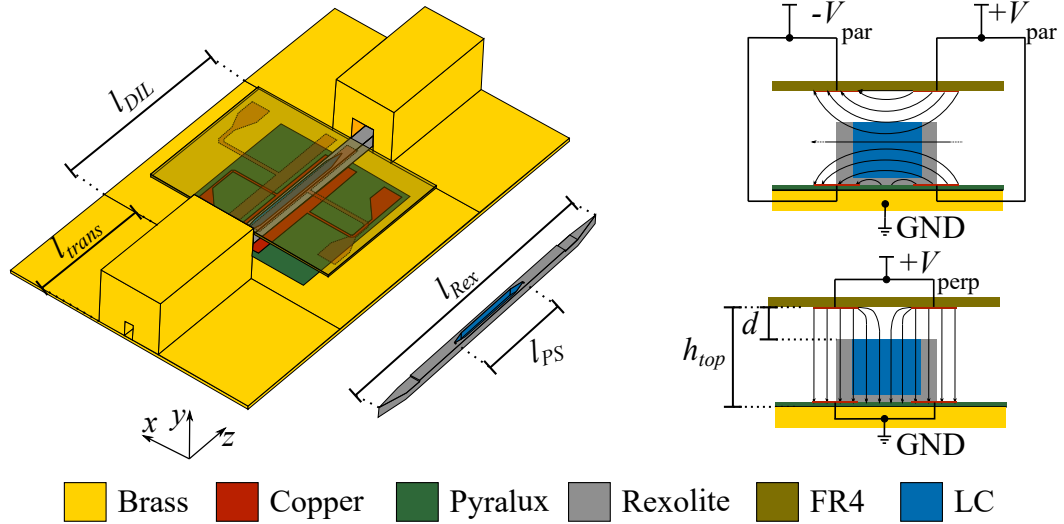


Figure 4.24: CST simulation model (left). The top electrode substrate is transparent to see the underlying LC-DIL phase shifter and bottom electrodes. The Rexolite structure with a cavity is displayed next to the simulation model with corresponding dimensions [Tes+20b] ©2020 IEEE. The bias states (right) are: top - parallel high permittivity, bottom - perpendicular low permittivity. Corresponding dimensions are in Table 4.2.

Fig. 4.3 (a), which covers this effect for the  $E_{11}^y$ -mode, we see that higher absolute  $\Delta\epsilon_r$  is present (e.g. 38% higher for  $w_{LC} = 1.5$  mm and  $\epsilon_{LC} = 3.53$ ). The resulting

Table 4.2.: Most important dimensions of the  $E_{11}^x$ -mode DIL phase shifter.

Parameter	$l_{PS}$	$w_{LC}$	$t_{LC}$	$l_{taper}$	$l_{DIL}$	$l_{trans}$	$l_{ReX}$	$h_{top}$	$w_{elec}$	$d$
Value (mm)	21	1.2	1.55	3	30	19.5	67	3.8	1.8	2

deterioration in  $\Delta\varepsilon_r$  if the high permittivity is not fully reached remains in the same range of percentile reduction, i.e. 12.2% and 35% when reducing from  $\Delta\varepsilon_r = 0.793$  to  $\Delta\varepsilon_r = 0.697$  and  $\Delta\varepsilon_r = 0.517$ , respectively. This larger absolute range of  $\Delta\varepsilon_r$  is mostly due to the different field distribution and the larger LC cavity. Hence, a higher drop in  $\Delta\varphi$  can be observed with decreasing  $\Delta\varepsilon_r$ , while a wider range of  $\varepsilon_{r,eff}$  can be theoretically covered by the  $E_{11}^x$ -mode phase shifter, as shown in Fig. 4.23. For maximum  $\Delta\varphi$ , the final width and depth of the LC cavity are  $w_{LC} = 1.2$  mm and  $t_{LC} = 1.55$  mm. The initial  $w_{LC} = 1.5$  mm proved to be unstable for the  $E_{11}^x$ -mode in measurements, which is shown in Fig. A.4 in the appendix. The layout of the full wave simulations of the phase shifter, together with its electrode network, is shown in Fig. 4.24. A distanced electrode setup is chosen for this demonstrator, and bias is similar to the  $E_{11}^y$ -mode phase shifter, with the only difference being that parallel and perpendicular alignment is switched, due to the different polarization of the  $E_{11}^x$ -mode. The most important parameters of the demonstrator are summarized in Table 4.2. Due to the larger cross-section in  $E_{11}^x$ -mode, the top electrodes have to have a larger distance  $h_{top}$  to the bottom electrodes. The main benefit compared to the  $E_{11}^y$ -mode is that no stepped impedance structure is necessary for the  $w_{elec} = 1.8$  mm wide bottom electrodes, and the bottom substrate thickness does not have a critical influence on the transmission of the phase shifter. This is due to the different field distribution, which has a minimum at the ground plane. Hence, the bottom electrodes are employed as simple metallic strips, such as the top electrodes.

#### 4.2.2. Fabrication and Microwave Characterization

All components are realized similarly to the  $E_{11}^y$ -mode phase shifter: the Rexolite DIL, and the brass components, are milled by a Datron M10pro+ CNC milling machine at the precision mechanics workshop of TU Darmstadt. The ground plane is a 1.6 mm thick brass sheet. The top electrodes are milled by a LPKF ProtoMat S100 rapid prototype circuit board plotter on a 1 mm thick FR4 substrate. The bottom electrodes are photolithographically processed on 12  $\mu$ m thin Pyralux AC substrate. This substrate is mounted on the ground plane with wafer mounting wax. All parts are assembled, and the LC is filled, before bias connections and the top electrode shield are placed on the demonstrator, which is shown in Fig. 4.25. A 1 kHz rectangular bias signal with peak-to-peak voltage  $V_{pp}$  is applied, and the corresponding obtained S-parameters are shown in Fig. 4.26 (a), for  $V_{pp} = 200$  V. Good matching of  $|S_{11}| < -20$  dB with a small exception from 79 GHz to 82 GHz is obtained, and IL ranges from 3.8 dB to 4.3 dB, with a deviation in  $|S_{21}|$  between simulation and measurement of 0.65 dB to 1.23 dB.  $\Delta\varphi$  and FoM are depicted in

#### 4. Liquid Crystal Dielectric Image Line Phase Shifters

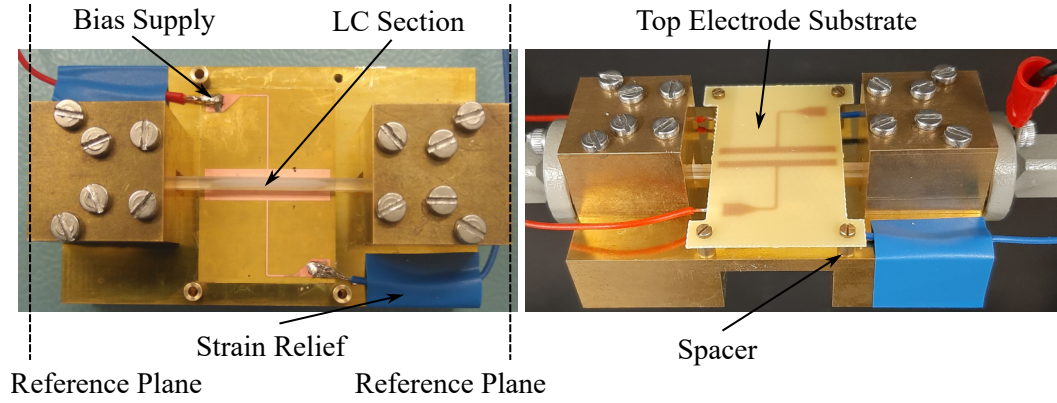
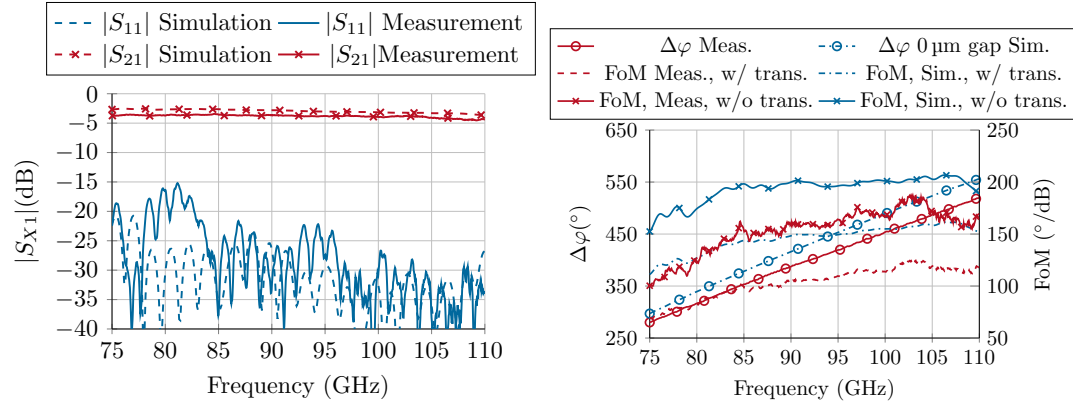


Figure 4.25: Demonstrator of the  $E_{11}^x$ -mode phase shifter. The non-structured bottom electrodes are visible on the left. On the right, the demonstrator is fully assembled with the top electrode substrate mounted above the phase shifter [Tes+20b] ©2020 IEEE.



(a) Simulation and measurement of S-parameters in most lossy configuration (perpendicular alignment). (b) Differential phase shift and FoM, including a simulation with a 100  $\mu\text{m}$  air gap between ground plane and phase shifter.

Figure 4.26: (a) S-parameters of the realized  $E_{11}^x$ -mode LC phase shifter, and (b) obtained  $\Delta\varphi$  and FoM. Simulations assume a RMS surface roughness of  $R_a = 0.8 \mu\text{m}$ .

Fig. 4.26 (b). A difference in  $\Delta\varphi$  is present, which increases with frequency. It is maximally  $40^\circ$  and therefore, much lower than in  $E_{11}^y$ -mode due to the mode being less susceptible to perturbation at the ground plane, such as air gaps: a fairly large air gap of 100  $\mu\text{m}$  does not affect the structure significantly, and affects  $\Delta\varphi$  by maximally  $20^\circ$ , as shown in [Tes+20b]. The deviation in  $\Delta\varphi$  can have its origin in imperfect bias field distributions, and slightly reduced  $\Delta\epsilon_r$  of the LC-mixture GT7-29001 at frequencies around W-band (c.f. Fig. 2.8). The FoM, including transition

### 4.3. Comparison of both Phase Shifters

loss, ranges from  $75^\circ \text{dB}^{-1}$  to  $124^\circ \text{dB}^{-1}$ . Without transition loss, the FoM ranges from  $100^\circ \text{dB}^{-1}$  to  $188^\circ \text{dB}^{-1}$ . The simulated FoM (excluding transition loss) reaches up to  $200^\circ \text{dB}^{-1}$ . Especially at frequencies around 103 GHz, where the measured IL is almost in agreement with the simulation, both simulated and measured FoM reach very similar values. The remaining difference is only due to the slightly reduced  $\Delta\varphi$  at these frequencies. The switch-on and switch-off response times of this phase shifter are both around 35 s long, with a bias of  $V_{pp} = 300 \text{ V}$ . This is about seven times longer than in  $E_{11}^y$ -mode. Hence, the potential of this phase shifter is more towards higher frequencies beyond 100 GHz. Since the overall cross-section of the phase shifter will reduce with frequency, faster response times can be achieved. With similar considerations about integrating electrodes for faster response time, the  $E_{11}^x$ -mode phase shifter can unfold its full potential at these higher frequencies, since the  $E_{11}^y$ -mode phase shifter increasingly suffers from metallic loss caused by surface roughness (c.f. Fig. 3.12).

### 4.3. Comparison of both Phase Shifters

In this chapter, two DIL LC-phase shifter demonstrators have been introduced. The main focus was on the  $E_{11}^y$ -mode phase shifter. Fig. 4.27 serves as a graphical reference in terms of tunability of  $\varepsilon_{r,\text{eff}}$ . The  $E_{11}^x$ -mode phase shifter covers a wider range of  $\varepsilon_{r,\text{eff}}$  compared to the  $E_{11}^y$ -mode phase shifter, which directly translates to higher  $\Delta\varphi$ . The  $E_{11}^y$ -mode phase shifter offers the smallest cross-section with a low height  $h$ , which enables faster response times and less voltage requirements. Response times of the first  $E_{11}^y$ -mode demonstrator are in the range of 3 s to 9 s (Section 4.1.1), which can be further decreased to the ms-range by employing electrode structures directly on the DIL (Section 4.1.4). However, high sensitivity in proper contact to the ground plane and strong interaction with potential bottom electrodes, or possible neighboring structures on the ground plane, have to be taken into account when

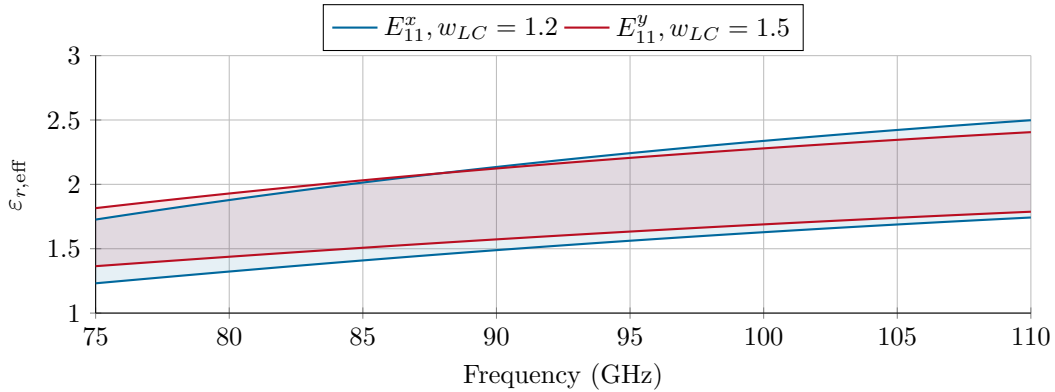


Figure 4.27: Tuneability range in  $\varepsilon_{eff}$  of the  $E_{11}^y$ - and  $E_{11}^x$ -mode phase shifter with the corresponding LC cavity width  $w_{LC}$  in mm.

#### 4. Liquid Crystal Dielectric Image Line Phase Shifters

employing an  $E_{11}^y$ -mode phase shifter. In addition, the  $E_{11}^y$ -mode is more susceptible to surface roughness (Section 3.1.2) and will therefore show higher loss when aiming for frequencies beyond 110 GHz. This problem can be circumvented with the  $E_{11}^x$ -mode phase shifter, where the modal field distribution has a minimum at the ground plane. Hence, no special care in the bottom electrode layout has to be taken, and hybrid DC/RF-structures could coexist closely when using an  $E_{11}^x$ -mode phase shifter. In addition, the  $E_{11}^x$ -mode phase shifter is naturally less susceptible to surface roughness. However, a DIL needs to have a larger cross-section to support the  $E_{11}^x$ -mode than a DIL in  $E_{11}^y$ -mode. In this dissertation, the  $E_{11}^x$ -mode DIL has a 55% larger cross-section than the  $E_{11}^y$ -mode DIL. The larger height directly translates to larger response times of up to 35 s and high bias voltages. In principle, electrode integration on top of a  $E_{11}^x$ -mode DIL is possible, but was not pursued during this dissertation. This principle is tested in an LWA (Section 5.2.2 and Appendix A.6.2). In general, LC-DIL phase shifters show good temperature stability between  $-10^\circ\text{C}$  and  $80^\circ\text{C}$  (Section 4.1.3). This behavior has been investigated in  $E_{11}^y$ -mode, but is expected to be similar in  $E_{11}^x$ -mode. Active or passive cooling on the ground plane can enhance the LC-DIL phase shifters during operation. A direct comparison between both phase shifters and to other LC-based phase shifters is shown in Table 4.3. The top half of Table 4.3 includes different LC-phase shifters in various non-dielectric-based topologies. Planar solutions can provide very fast switch-on response times and low  $V_{pp}$ . Due to high loss and very high sensitivity to fabrication tolerances, they are mostly not used towards 100 GHz. FoMs range to up to  $70^\circ\text{dB}^{-1}$  for planar phase shifters, and up to  $80^\circ\text{dB}^{-1}$  for all phase shifters covered in the upper half of Table 4.3. The second half of Table 4.3 includes dielectric-based LC-phase shifters. They usually show high  $\Delta\varphi$ , high FoMs beyond  $100^\circ\text{dB}^{-1}$ , and their bias circuits are never part of the waveguide topology. Hence, they do not require a bias-tee, but their electrodes need to be incorporated in their structure, which can cause difficulties in design. Due to their volumetric topology, higher bias voltages

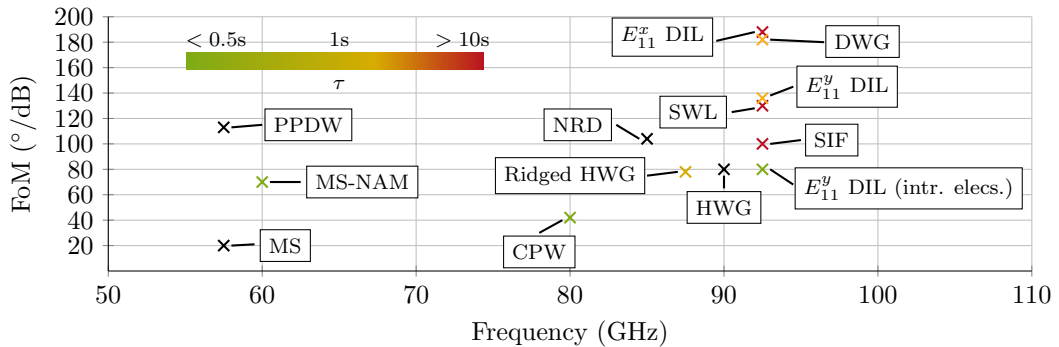


Figure 4.28: Comparison of different LC-phase shifters at frequencies beyond 50 GHz, with abbreviations according to Table 4.3. The response time is color-coded. If no data is available, the color is black.



### 4.3. Comparison of both Phase Shifters

and lower response time results. The PPDW, NRD, SIF and sWL are characterized *including* transition loss, since no data on this loss is present. Hence, the FoM of the standalone phase shifters is in general higher than given in Table 4.3. Parts of this table are graphically arranged in Fig. 4.28, which compares frequency of operation in relation to achievable FoM and switch-on response times.

#### 4. Liquid Crystal Dielectric Image Line Phase Shifters

Table 4.3.: Comparison of different LC-phase shifters at mmW, measured above 50 GHz. Dielectric waveguide topologies are in the lower part of the table. Abbreviations: MS - microstrip transmission line; HWG - hollow waveguide; MS-NAM - microstrip with narrow membrane; CPW - coplanar waveguide; PPDW - parallel-plate dielectric waveguide; NRD - non-radiating dielectric, SIF - step index fibre; sWL - sub-wavelength dielectric line.

	LC	$f$ (GHz)	$l/\lambda_{0,mid}$	$\Delta\varphi_{max}$ ( $^{\circ}$ )	$IL_{max}$ (dB)	FoM $_{max}$ ( $^{\circ}$ /dB)	$\eta_{max}$ ( $^{\circ}$ /mm)	$V_{pp,max}$ (V)	$\tau_{on}$ (s)	Ref.
MS	E7	50-65	1.43	260	20	20	34.76	11	-	[Bul+10]
	GT5-26001	80-110	13.62	130	2	80	3.02	magn.	-	[Jos+17]
MS-NAM	GT7-29001	5-67	0.8	120	3	70	33.33	10	0.003	[Wan+22a]
	Ridged HWG	65-110	8.7	600	10	78	20	30	1.5	[Mue+06]
CPW	-	65-95	1.46	180	4	42	18.6	30	0.002	[Fri+12]
PPDW	GT5-26001	50-75	7.91	330	4.8	113	10	300	-	[Ree+17a]
	GT5-26001	98-110	6.94	270	4.8	85	15	300	-	[Pol+19b]
SIF	GT5-26001	75-110	5.86	425	5.1	100	22.1	1.1k	> 60	[Ree+17b]
	sWL	75-110	10.19	860	7.5	130	27.3	200	17	[Ree+19a]
DWG	VMLC-2101	75-110	9.25	440	3.5	182	14.7	400	1.5	[Hu+22]
	GT7-29001	75-110	6.48	350	3.2	136	16.7	200	9	[Sect. 4.1.2]
$E_{11}^y$ -DIL	GT7-29001	75-110	6.48	350/420	3.8	80/94	16.7/21	50	0.134 / 0.270 @200V	[Sect. 4.1.4]
	$E_{11}^x$ -DIL	GT7-29001	75-110	480	3.7	188	22.7	200	35	[Sect. 4.2]

## 5. Beamsteering Liquid Crystal Dielectric Image Line Antennas

In this chapter, DIL antennas and their capability for LC-based beam steering are investigated. The W-band from 75 GHz to 110 GHz is considered, based on the results on DILs/LC-DILs from the previous two chapters.

In general, there is a large variety of possible antenna elements that can be used to form LC-based, beam steerable DIL antennas or antenna arrays: rods [PW06a; PBA17], resonators [Qur+17; AH18], and leaky-wave-based structures [SW85; PW07; PB17; PBA18] are the most common antenna element types. Lens antennas are usually not used in DIL topology [Wu+12; NIH18].

Rod antennas are simple broadband surface wave antenna elements, which are often used in fully dielectric topologies [GW12; Ree+18; DAH20]. They have been successfully combined with fully dielectric LC-waveguides [Ree20]. Since they are tapered waveguides, translating them to the DIL topology makes them compatible to the DIL phase shifters discussed in the previous chapter.

Resonators are of narrow bandwidth, and feeding from a purely DIL-based topology is possible, and is usually done by a serial feed, such as in [AKG09; JLR12; Xin+17]. Due to the high variance in resonator performance if each resonator is individually filled with LC, this antenna element type is not considered in this chapter.

Lens antennas are broadband and can provide significant gain. They are in general large in terms of wavelength, and often geometric optics is used to analyze them in an initial step. LC lens antennas have been investigated in V-band, both in parallel-plate waveguide and fully dielectric waveguide topology [Ree+19a; Tes+19b]. Large amounts of LC are required, and high voltages are necessary to steer the beam. Mainly, their size is the reason why they are not investigated in this dissertation.

Leaky wave antennas (LWAs) are composed of a radiative structure on or around a waveguide, which is fed in a serial manner. In their most compact form, they are created by a waveguide with perturbations, e.g. metallization on the DIL, grating in the ground plane, etc., in order to create radiation. Hence, fabrication of those antennas is usually of low complexity. LWAs are of low profile, can provide high directivity and radiation to broadside. As they scan their main lobe direction with frequency, the bandwidth at a particular radiation angle can be narrowband.

Two antenna types are investigated in this chapter: 1) rod antennas, due to their broadband characteristics and high compatibility to the phase shifters introduced in the previous chapter. Single DIL antenna elements are investigated first, and their difference to fully dielectric rod antennas is highlighted, before two array demonstrators, in  $E^y$ - and  $E^x$ -mode and with a fixed antenna pattern, are presented. This con-

## 5. Beamsteering Liquid Crystal Dielectric Image Line Antennas

cept is extended to a 1x4 phased array in  $E^y$ -mode by combining four phase shifters (Section 4.1.4) with the corresponding antenna elements. 2) LWAs are investigated in order to achieve broadside radiation with a low antenna profile. Here, the main focus is on the use of the radiator elements as an electrode simultaneously, such that the advantages of a quasi-planar component with low bias voltage is created. The main properties of LWAs are covered with the investigation of non-reconfigurable LWAs, before LC is integrated.

### 5.1. Rod Antenna Arrays

Rod antennas have often been used in fully dielectric setups [Pou+10; Fan+14; Riv+15; Ree+18; Tes+19a]. These antennas are created by tapering a dielectric waveguide, such that a smooth match from characteristic waveguide impedance to free space impedance is obtained. They radiate in the direction of propagation in the DWG, i.e. to end-fire. Their simple shape can be scaled easily by controlling the permittivity of the dielectric, and they are easy to adapt to different frequencies. DWG rod antennas are non-planar, and can be sensitive to mechanical stress. DWG rod antennas have been successfully combined with LC at W-band [Ree+19b; Pol+20a] to phased arrays. However, their main drawback are the phase shifters in DWG topology, which are bulky due to their electrode network, need high voltages and show slow response times. In addition, the electrodes between different phase shifters have to be shared by two neighboring phase shifters, hence tuning one phase shifter can influence the bias state on its neighbor element. Another challenge of LC-DWG rod antenna arrays is scalability. Due to the mentioned dependence on neighboring electrodes and the overall bulky setup, scaling to a high number of antenna elements is linked with significant effort, especially in the bias network.

#### 5.1.1. Single Antenna Elements in $E_{11}^y$ - and $E_{11}^x$ -Mode

A DWG rod antenna can be as easily transferred to the DIL topology as the corresponding waveguides: the cross-section is cut in half and the lower half is replaced by a metallic half-space. The ground plane provides mechanical stability, such that longer tapers with very small taper tips are still feasible in practice. However, taper type, relation of taper length  $l_t$  and ground plane length  $l_g$  have to be considered carefully in the DIL topology. Fig. 5.1 displays the models of the rod antennas used throughout this dissertation for both  $E_{11}^y$ - and  $E_{11}^x$ -mode. They are composed of Rexolite 1422 in order to be compatible with the structures discussed earlier in this dissertation. Width  $w$  and initial height  $h$  before tapering are determined by the waveguide dimensions of the corresponding mode, which are introduced in Chapter 3 and used for the phase shifter designs in Chapter 4. As with fully dielectric rod antennas,  $l_t$  mainly controls gain and half-power beam width (HPBW) of the antenna pattern [Vol07]. Gain rises, and HPBW decreases with increasing  $l_t$  before both start to saturate, and no significant change is obtained with further increase of  $l_t$ . The ground plane length  $l_g$  is most relevant for the elevation angle  $\theta$ . With

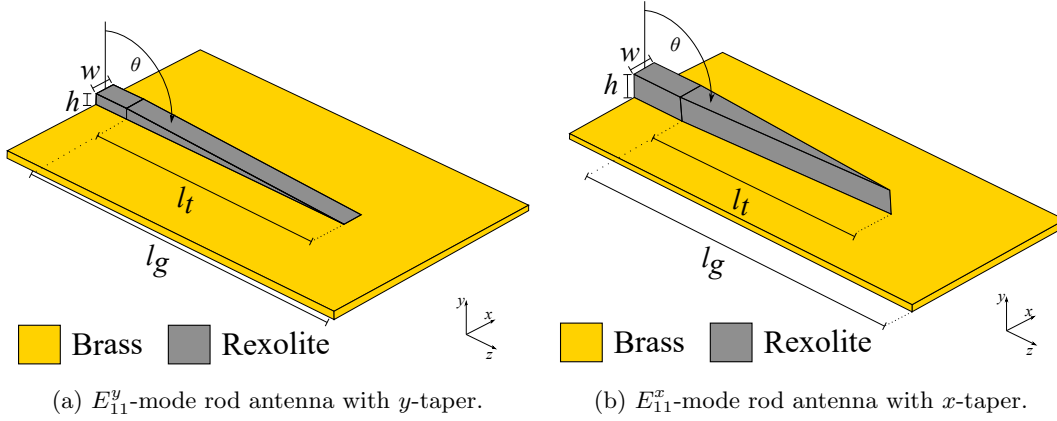


Figure 5.1: Rod antenna types used in this dissertation.

increasing  $l_g$ ,  $\theta$  (see Fig. 5.1) approaches  $90^\circ$ . This is intuitive, since an infinitely long ground plane would provide a perfect image of the system, i.e. a fully dielectric rod in free space. For highest gain with the shortest length,  $l_t$  has been simulatively determined to  $l_t = 21$  mm. In this simulation,  $l_g \gg l_t$  in order to ensure no parasitic effect of a short ground plane. The taper type has been investigated using CST Studio Suite, and it has been found that a taper parallel to E-polarization causes fewer ripples in the antenna pattern. Hence, all simulation results are with the corresponding taper types, as indicated in Fig. 5.1. For simulations, a waveguide transition is included, in order to represent measurements as precise as possible.

With  $l_t = 21$  mm fixed, Fig. 5.2 shows the simulated gain and sidelobe level (SLL) of both antennas for various  $l_g$ . It is found that, especially for  $E_{11}^y$ -mode,  $l_g = 31$  mm provides the best trade-off between gain, main lobe ripples, SLL, and stable  $\theta$  for all frequencies. The  $E_{11}^x$ -mode shows less sensitivity of  $l_g$ , and both antennas perform worst if the ground plane is terminated halfway through the taper length of the rod, i.e.  $10 \text{ mm} \leq l_g \leq 19 \text{ mm}$ . For comparison,  $l_g = 31$  mm is chosen to be the same for  $E^y$ - and  $E^x$ -mode, resulting in  $\theta_y \approx 75^\circ$  and  $\theta_x \approx 70^\circ$  in the entire frequency band, respectively. In principle, an end-fire antenna can be created by  $l_g \approx 0$  mm and if minor drawbacks in the pattern shape are accepted. Results for the  $E_y^{11}$ -mode can be found in the appendix A.5, but due to mechanical instability, this approach is not pursued in this dissertation. Fig. 5.3 shows the realized antenna elements, milled from Rexolite 1422, adhered with Rexolite adhesive on the ground plane, and fed by the waveguide transitions.

Since an elevation angle  $\theta \neq 90^\circ$  is present, the azimuth measurement has to be conducted at this angle. Hence, a tilted hollow waveguide section with the exact corresponding angle has been manufactured, such that the antenna is tilted on the turntable. More information of the measurement setup can be found in the appendix A.5. Fig. 5.4 depicts the magnitude of the measured S-parameters. Both antennas are matched with  $|S_{11}| < -10$  dB throughout W-band. The obtained radiation patterns are summarized in Fig. 5.5, and the frequency behavior of gain and SLL (in elevation

## 5. Beamsteering Liquid Crystal Dielectric Image Line Antennas

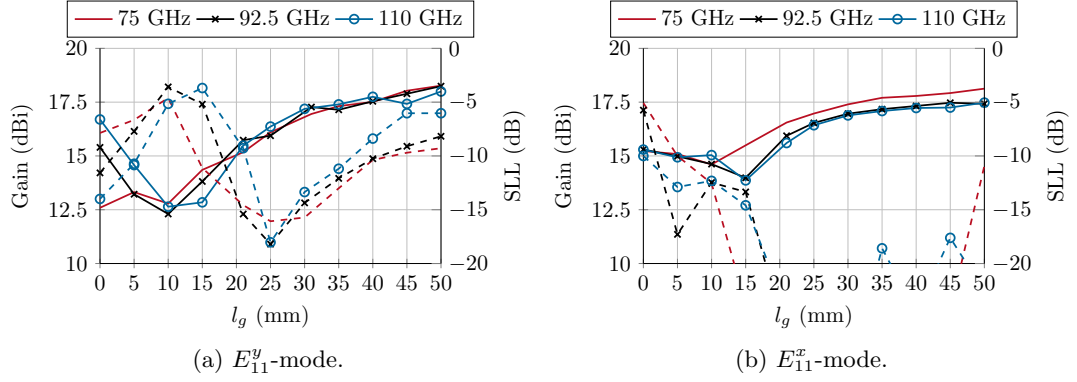


Figure 5.2: Simulated gain (solid) and SLL (dashed) for rods in both modes.

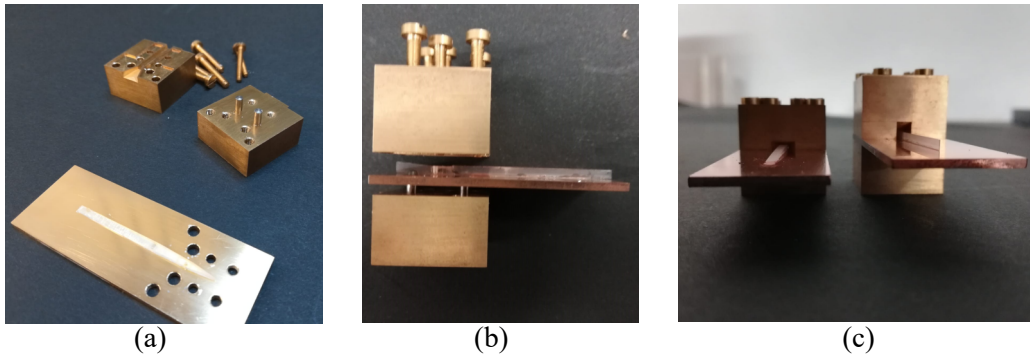


Figure 5.3: Manufactured antenna elements. (a)  $E_{11}^y$ -mode rod with split block transition, (b)  $E_{11}^x$ -mode rod directly before assembly, (c) both assembled demonstrators.

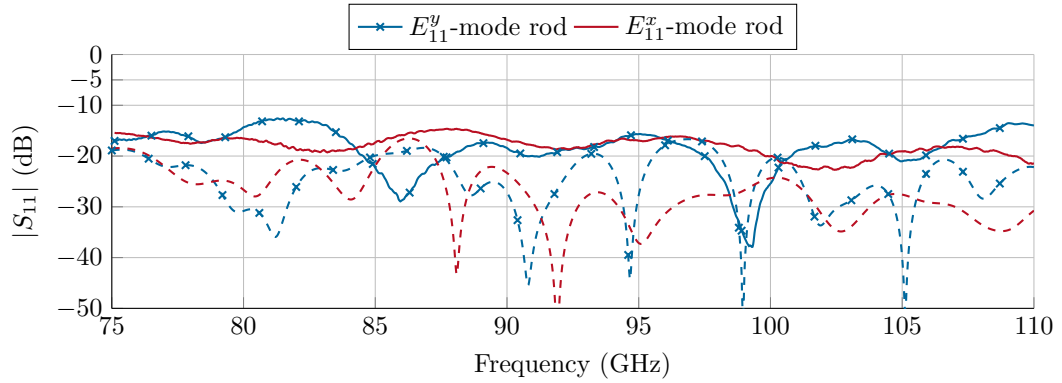


Figure 5.4: Simulated (dashed) and measured (solid)  $|S_{11}|$  of the rod antennas.

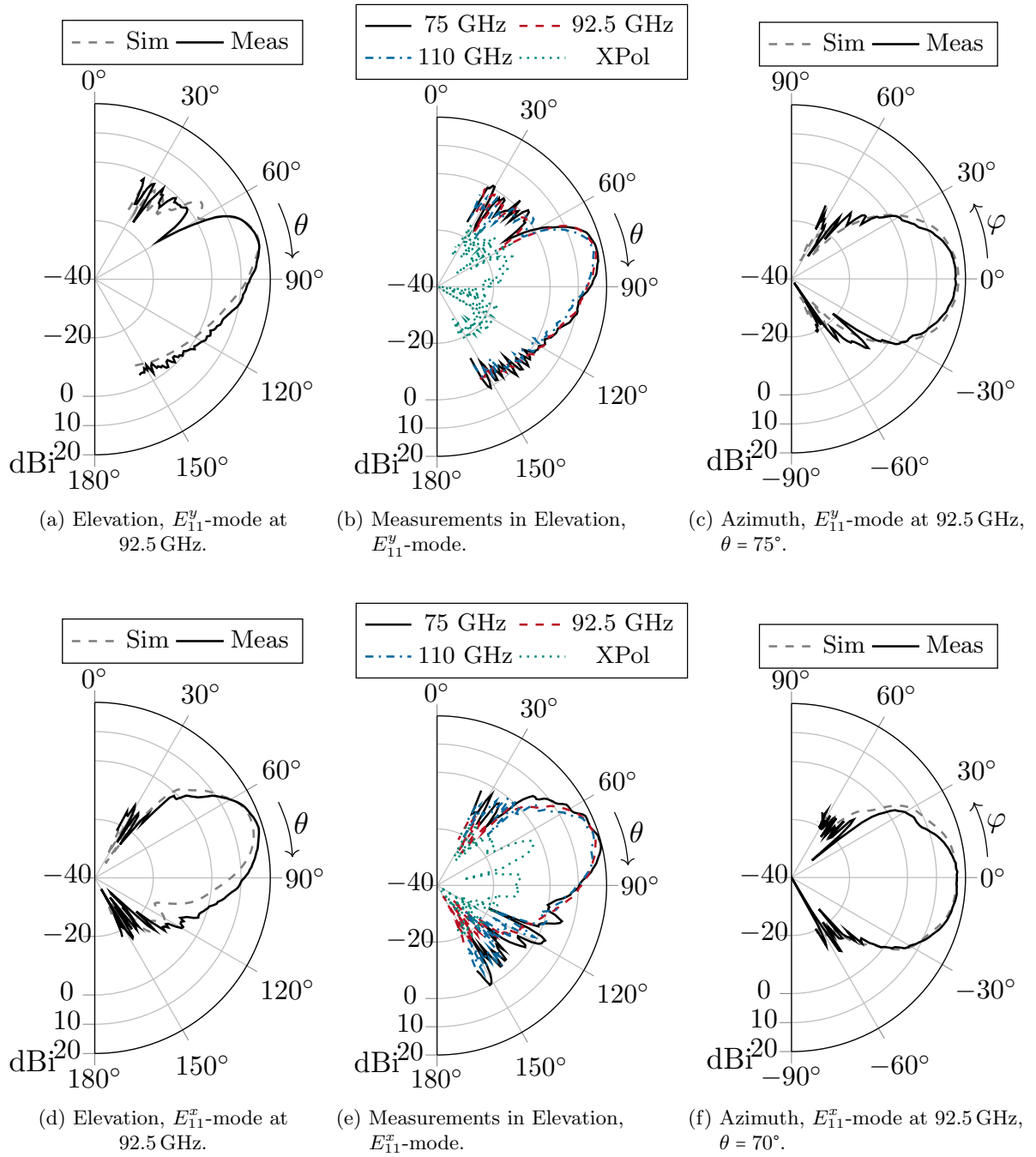


Figure 5.5: Simulated and measured far fields for rod antennas in (a) to (c)  $E_{11}^y$  mode, and in (d) to (f)  $E_{11}^x$  mode. Cross polarization is measured at 92.5 GHz.

## 5. Beamsteering Liquid Crystal Dielectric Image Line Antennas

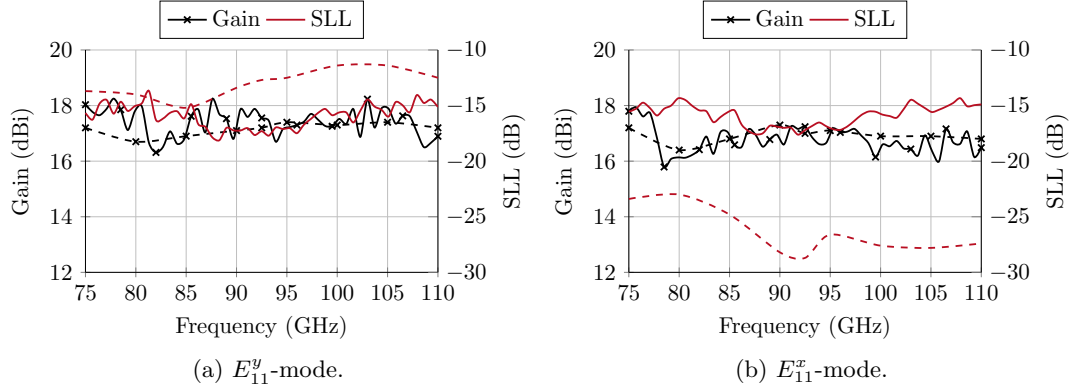


Figure 5.6: Simulated (dashed) versus measured (solid) course of gain and SLL in W-band for both antennas.

plane) is plotted in Fig. 5.6. Both antennas provide a gain of around 17 dBi, with a SLL better than  $-15$  dB. Simulation and measurement of the patterns coincide well in azimuth and elevation plane. In elevation, ripples at angles of  $\theta \approx 30^\circ$  or higher exist for both antenna elements. They stem from spurious radiation caused by the waveguide transitions and will be present at all antenna measurements in this dissertation.

Both antenna elements provide stable, broadband properties, and can therefore be employed for broadband arrays. The  $E_{11}^y$ -mode element radiates slightly more towards endfire and is well suited if a low profile is desired. It is more reliant on longer ground planes than the  $E^x$ -mode element, which is operating well even if  $l_g = l_t = 21$  mm (c.f. Fig. 5.2). Higher cross-polarization of  $-20$  dB is present with the  $E_{11}^x$ -mode element ( $E_{11}^y$ -mode:  $-35$  dB), since the fundamental, cross-polarized  $E_{11}^y$ -mode is supported by the  $E_{11}^x$ -mode waveguide structure.

### 5.1.2. 1 x 4 Antenna Arrays

With full knowledge on the element behavior, they can be combined to an array. In this dissertation,  $1 \times 4$  arrays are designed, manufactured and characterized as a proof-of-concept. In order to feed the elements, an easy way of power division is necessary. Serial feeds are possible [Che+09], but since they are frequency dependent, they are contradicting to the broadband nature of the antenna elements. Broadband corporate feeds can be realized by Y-branches [Jos18], but in order to reduce radiation loss, the branches become space consuming. Coupling structures [WS20] of adjacent DILs can reduce this space, but the necessary coupling length increases exponentially, both with frequency and distance between the lines. Broadband structures require the aspect ratio of the DIL's cross-section to be very small, which in turn leads to very high amounts of evanescent field components. Therefore, adjacent structures, such as packaging or other components, can influence the



coupler's performance. In addition, the complexity of the coupling network rises linearly with the number of output ports. A simple way to achieve power division in one step is multimode interference (MMI) [BBM94; SP95]. MMI has its origins in the optical regime, and has been successfully translated in 1D and 2D fully dielectric waveguide antennas at W-Band [RJJ16; Tes+19a]. Its principle is briefly revised on the following pages, before its adaptation to the DIL topology is presented. With the power divider at hand, the  $1 \times 4$  arrays can be easily designed.

MMI is often referred to as self-imaging. This is due to the  $N$ -fold repetition of an input field distribution at certain lengths of a multimode waveguide, with  $N$  being an arbitrary positive integer. The multimode waveguide is solely different from the single mode waveguide in its width  $w$ , i.e. it is extended in  $x$ -direction. By exciting the multimode waveguide with a single mode waveguide, the input field distribution at  $z = 0$ ,  $\Psi(x, 0)$ , can be represented as a superposition of all modes  $m$  with the modal field profile  $\psi_m(x)$  which are supported by the multimode waveguide

$$\Psi(x, 0) = \sum_m c_m \psi_m(x), \quad (5.1)$$

where  $c_m$  is an excitation coefficient for the  $m$ -th mode. Since all  $m$  modes propagate with different propagation constants  $\beta_m$  along the waveguide, an interference pattern arises along the direction of propagation ( $z$ -direction). Hence, when using the term "higher order mode" in this section, it always refers to higher order modes of the *same* polarization, i.e. modes only of type  $E^y$  or  $E^x$ , depending on the input field's type. If mode conversion, e.g. from type  $E^x$  to  $E^y$  takes place, the corresponding power will be lost, since no interference of the converted mode with the modes of the original polarization can take place. The composition of the field profile  $\Psi(x, z)$  in the multimode waveguide can be represented as

$$\Psi(x, z) = \sum_{m=0}^{M-1} c_m \psi_m(x) e^{j(\beta_0 - \beta_m)z}, \quad (5.2)$$

where  $M$  represents the maximum number of modes supported by the multimode waveguide, and  $\beta_m$  is the propagation constant of the  $m$ -th mode. Time dependency in the form of  $\exp(j\omega t)$  is omitted in the equation above and all following forms of this equation for the sake of simplicity. The difference  $\beta_0 - \beta_m$  can be approximated by the "beat length"  $L_\pi$ , which describes the length the two lowest order modes  $\beta_0$  and  $\beta_1$  have to travel such that a phase difference of  $\pi$  is reached [SP95]

$$L_\pi \approx \frac{4\sqrt{\varepsilon_r}W_e^2}{3\lambda_0}. \quad (5.3)$$

$\varepsilon_r$  represents the dielectric constant of the multimode waveguide,  $W_e$  is the waveguide's effective width which takes evanescent field components into account, and  $\lambda_0$  is the free space wavelength of the operation frequency. With  $L_\pi$ , the difference  $\beta_0 - \beta_m$  can be described as [BBM94]

$$\beta_0 - \beta_m \approx \frac{\pi m(m+2)}{3L_\pi}. \quad (5.4)$$

## 5. Beamsteering Liquid Crystal Dielectric Image Line Antennas

Hence, by plugging Eqn. (5.4) into Eqn. (5.2) we get

$$\Psi(x, z) = \sum_{m=0}^{M-1} c_m \psi_m(x) e^{j \frac{\pi m(m+2)}{3L\pi} z}. \quad (5.5)$$

Eqn. (5.5) shows that if the exponential becomes 1 or  $(-1)^m$ , we get the same (or mirrored) expression as in the feeding point (Eqn. (5.1)), hence an image of the input field distribution. In general, these self-images occur at  $z = 3L_\pi p$ , with  $p = 1, 2, 3, \dots$  since this is a periodic phenomenon. In between these distances, higher order self-images are formed in the form of multiple self-images along the width of the multimode waveguide. The particular length for an  $N$ -fold image is given by [SP95]

$$L_{p,N} = \frac{p}{N} 3L_\pi. \quad (5.6)$$

All  $N$  images have the same fraction  $1/\sqrt{N}$  of the original input power, when neglecting loss. For shortest components,  $p = 1$  throughout the rest of this dissertation, and explicit indexing of  $p$  is omitted. The feeding point affects Eqn. (5.6) with different factors [SP95]. The shortest distance is achieved when feeding at the exact middle of the width of the multimode waveguide, causing so-called symmetric interference. As the input field distribution forces a maximum in the middle of the multimode waveguide, the input field distribution can only be reassembled by odd modes ( $E_{11}^y, E_{31}^y, E_{51}^y, \dots$ ), i.e. modes which are not zero at the middle of the multimode waveguide. By this technique,  $L_N$  can be reduced by a factor of 4 to

$$L_N = \frac{3L_\pi}{4N}. \quad (5.7)$$

Fig. 5.7 shows an MMI pattern in  $E^y$ -mode, together with the distinctive lengths for  $N = 1, 2, 3, 4$  maxima. At shorter distances, higher order images can not be resolved.

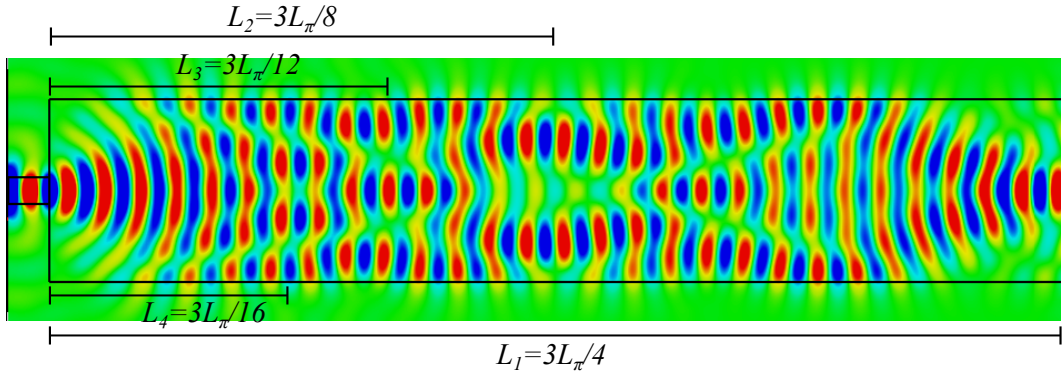


Figure 5.7: Instantaneous electric field distribution in an  $E^y$ -multimode DIL, consisting of Rexolite 1422, at 90 GHz, with the single mode feed positioned symmetrically on the left. Simulated with CST Microwave Studio Suite.

This can be circumvented by using a wider width of the multimode waveguide. Power division can be achieved by cutting the multimode waveguide at the desired  $L_N$ , and connecting single mode waveguides at the positions where the  $N$ -fold images form.

### MMI Dividers in $E_{11}^y$ - and $E_{11}^x$ -Mode

The MMI dividers are shown in Fig. 5.8. They are of the same width  $w_{\text{MMI}}$  for better comparability, and to ensure that output ports have the same spacing  $d = 3.1$  mm to each other. The design procedure uses initial lengths  $l_{\text{MMI}}$ , calculated with the equations in the previous section, and then fine-tunes them with CST Studio Suite, mostly to take account of the inclusion of loss, surface roughness and the blended multimode section at the input point. This blend is to reduce parasitic radiation due to the abrupt change in width between feeding waveguide and MMI section. Since a symmetric feed is used,  $S_{31}$  &  $S_{41}$ , and  $S_{21}$  &  $S_{51}$  behave identical, respectively. Hence, when investigating magnitude and phase relations, it is sufficient to compare e.g.  $S_{21}$  to  $S_{31}$ . Fig. 5.9 (a) shows the obtained power split between the two output port groups for their respective  $l_{\text{MMI}}$ . A difference in the course of  $|S_{X1}|$  exists between the two dividers, which is based on the difference in propagation constants of the corresponding modes. Hence, the optimum  $l_{\text{MMI}}$  is also different for both modes, and power split can differ due to the inclusion of loss in simulations. Both dividers are designed to show good power splits from 95 GHz to 105 GHz. When optimizing  $l_{\text{MMI}}$  for the results displayed in Fig. 5.9 (a), absolute power split and imbalance between the ports have to be considered. Taking both aspects into account, the final lengths have been determined to  $l_{\text{MMI},y} = 16.5$  mm and  $l_{\text{MMI},x} = 14.35$  mm. The  $E^y$ -MMI divider shows slightly increased imbalance, but better results at higher frequencies than the  $E^x$ -MMI divider. When inspecting Fig. 5.7, a phase difference  $\Delta\varphi$  between the four self-images at  $L_4$  can be observed.  $\Delta\varphi \approx 100^\circ$  in  $E^y$ -mode and  $\Delta\varphi \approx 85^\circ$

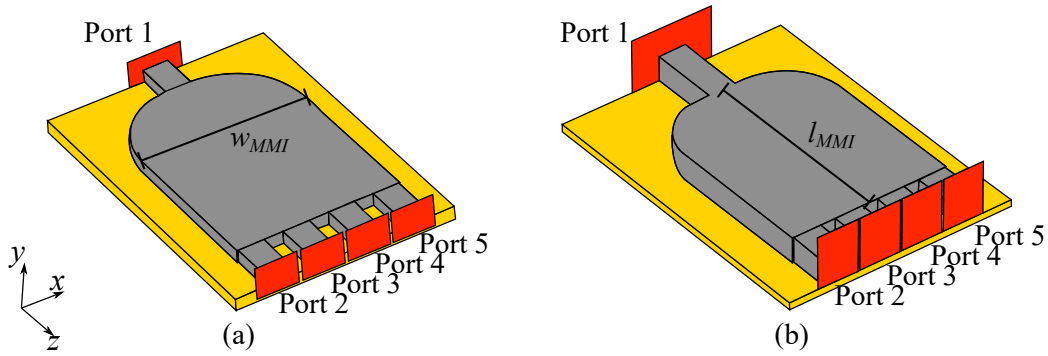
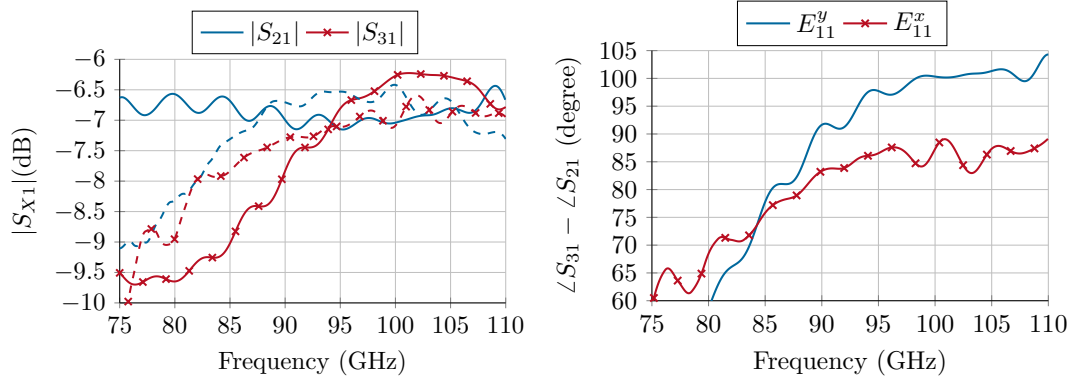


Figure 5.8: MMI divider models for simulations with CST Microwave Studio. (a)  $E^y$ -mode, with  $l_{\text{MMI}} = 16.5$  mm, (b)  $E^x$ -mode, with  $l_{\text{MMI}} = 14.35$  mm. Both dividers have the same width  $w_{\text{MMI}} = 11.5$  mm. The input port is Port 1.

## 5. Beamsteering Liquid Crystal Dielectric Image Line Antennas



(a) Output power levels of the  $E^y$ -MMI divider (solid), and the  $E^x$ -MMI divider (dashed). (b) Phase difference  $\Delta\varphi$  between the output ports.

Figure 5.9: Simulated S-parameters at W-band for both power dividers. (a) Magnitude of  $S_{21}$  and  $S_{31}$ , (b) phase difference between Port 2 and Port 3.

in  $E^x$ -mode for the operation frequency range from 95 GHz to 105 GHz with nearly equal power split. This difference is plotted in Fig. 5.9 (b) for both power dividers. Due to the higher discrepancy in  $|S_{21}|$  and  $|S_{31}|$  in  $E^y$ -mode, the corresponding  $\Delta\varphi$  has a steeper ascent before it settles for a stable value. When the dividers are to be used for an antenna array, the corresponding  $\Delta\varphi$  has to be compensated in order to achieve in-phase radiation. When comparing the  $E^y$ -MMI divider to a fully dielectric counterpart [RJJ16], similar values in phase can be observed, but the course of available output power at Port 2 and Port 3 is more flat in DIL topology, and therefore, about 1 dB more power is available at 105 GHz than in [RJJ16].

### 1x4 Arrays in $E_{11}^y$ - and $E_{11}^x$ -Mode With Fixed Antenna Patterns

The  $1 \times 4$  arrays are realized by connecting the individual antenna elements from Subsection 5.1.1 to the divider outputs. Due to the phase difference present at the different output ports, a phase compensation mechanism has to be employed, such that useful radiation characteristics can be achieved. In fully dielectric designs, the phase was mostly compensated by changing the taper length of the rod antenna elements [RJJ16; Tes+19a]. While showing usable results, this direct manipulation of taper length  $l_t$  changes the gain between the antenna elements by 1.5 dB, which is non-desirable. Furthermore, in [RJJ16; Tes+19a] the outer antenna elements have longer  $l_t$ , which results in higher gain for elements at the outer positions of the array. Besides this drawback, employing different  $l_t$  in DIL rod antenna arrays leads to different radiation angles  $\theta$  when keeping the ground plane length  $l_g$  fixed. Altering the length of the single mode output of the MMI divider before connecting the DIL rod antenna element has a similar effect on  $\theta$ , since the length of the output section needs to be rather long, and therefore, the affected antenna elements move closer to

the edge of the ground plane.

From Chapter 3, we know that the propagation constant can be increased by either applying a higher cross-section, or by changing the permittivity of the waveguide. Modifying the cross-section, e.g. the height, seems to be a very simple and feasible approach, but e.g. in  $E_{11}^x$ -mode, an additional height on the output waveguides of  $\Delta h = 0.4$  mm (+22%) only results in an additional phase delay of  $6.5^\circ \text{ mm}^{-1}$ . Therefore, the phase shift gained by this method is not large enough to compensate the phase difference of the output ports with reasonable size. Increasing the permittivity of the waveguide could be achieved with a dielectric core of different material, such as in [Tes+19b], but includes a second material different from the rest of the DIL structure. Additive manufacturing could incorporate this approach, but this option was not available at the time of this dissertation. Instead, the long, but constant taper length  $l_t$  is used for phase compensation: in both modes, the height of the DIL along  $l_t$  is slightly increased by  $\Delta h$  for the two central antenna elements, such that the propagating wave has a slightly higher  $\beta$  than in the neighboring elements. This approach is visualized in Fig. 5.10 (a) and changes neither  $\theta$ , nor affects the gain of the individual elements significantly. With the optimized additional  $\Delta h$ , gain is maximally changed by 0.2 dB, and the obtained SLL in azimuth is shown in Fig. 5.10 (b). An optimum of  $\Delta h = 0.15$  mm ( $E_{11}^y$ -mode) and  $\Delta h = 0.4$  mm ( $E_{11}^x$ -mode) is determined, and slightly better overall performance is obtained in  $E_{11}^y$ -mode. Fig. 5.11 depicts the realized demonstrators, which are both milled from Rexolite 1422 in one piece. Small Rexolite positioning pins are used with these demonstrators, in order to assure proper orientation on the ground plane. The position of the pins has been chosen such that they are in regions of the MMI dividers with very low field

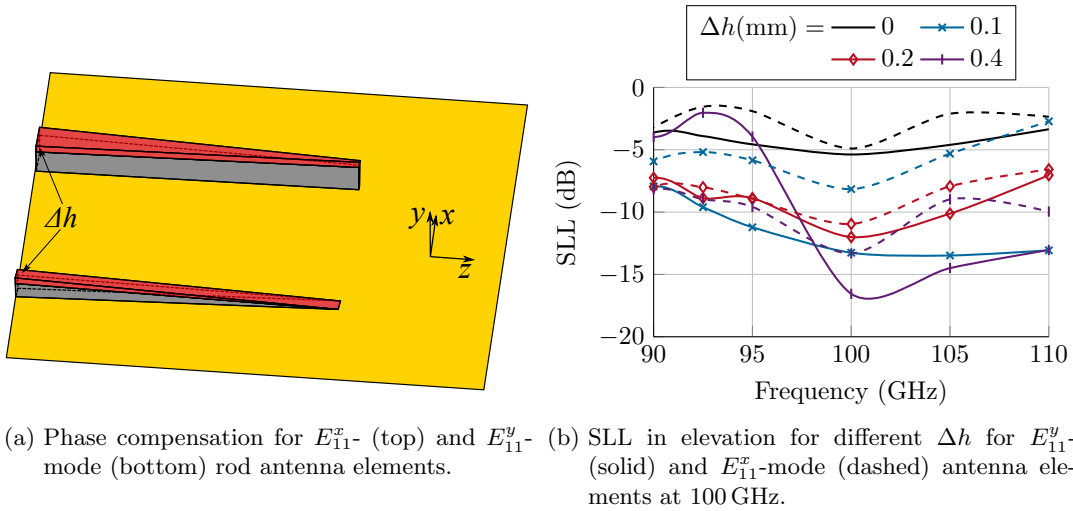


Figure 5.10: (a) Phase compensation by adding  $\Delta h$  to the rod antenna elements, shaded in red, and (b) resulting SLL of a  $1 \times 4$  array for different  $\Delta h$  added to the central two antenna elements.

## 5. Beamsteering Liquid Crystal Dielectric Image Line Antennas

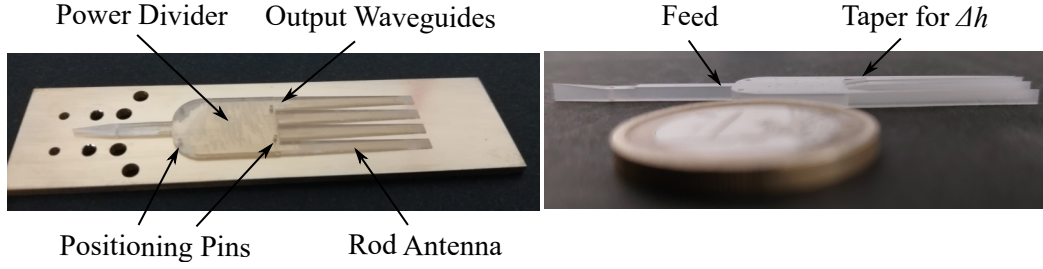
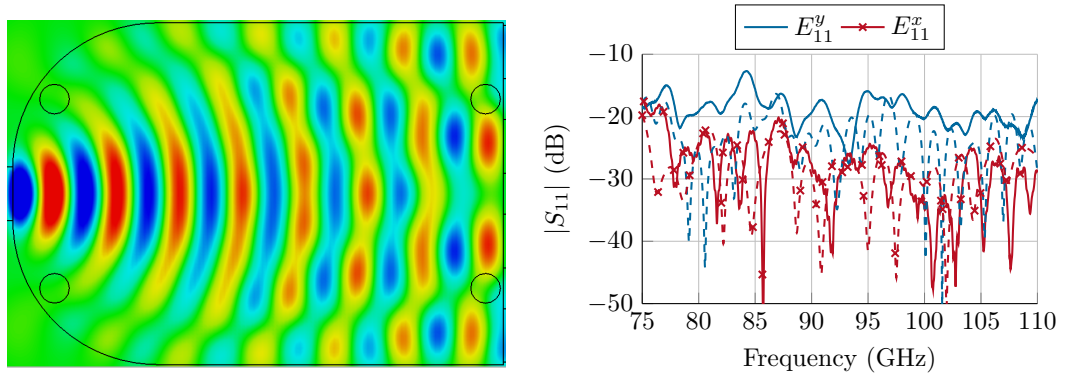


Figure 5.11: Manufactured demonstrators. Left:  $E_{11}^y$ -mode rod array, mounted on a ground plane [Tes+22c] ©2022 IEEE. Right:  $E_{11}^x$ -mode rod array with a 1 € coin for size reference. In order to reduce parasitic radiation, a small taper to  $\Delta h$  for the central antenna elements is employed.

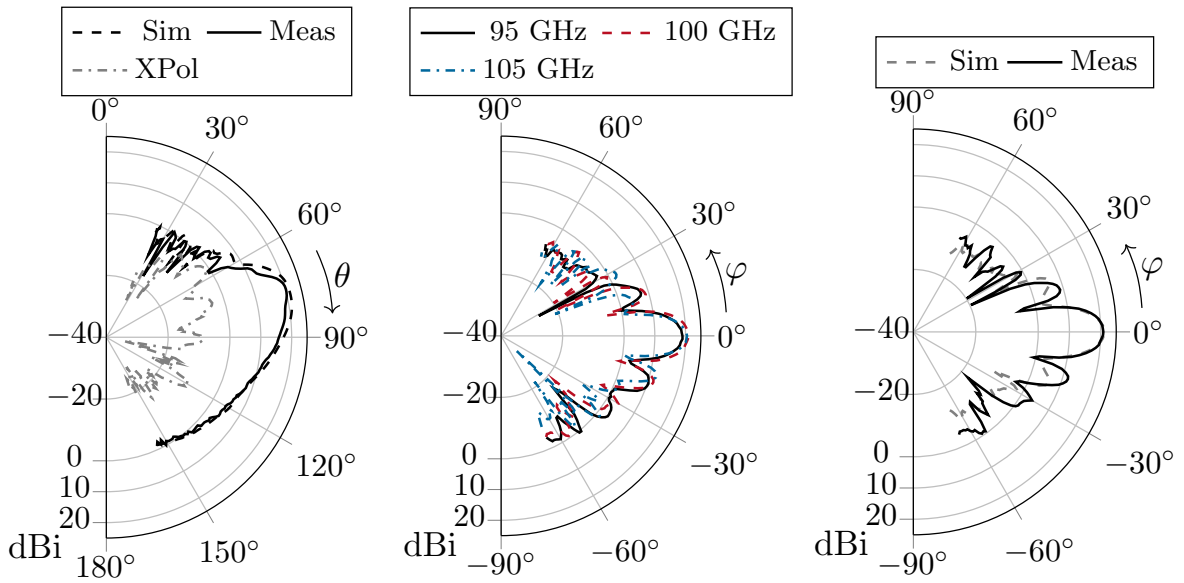


(a) Positioning pin locations (circles) in the  $E^y$ -MMI divider. (b) Simulated (dashed) and measured (solid) input reflection of both antenna arrays.

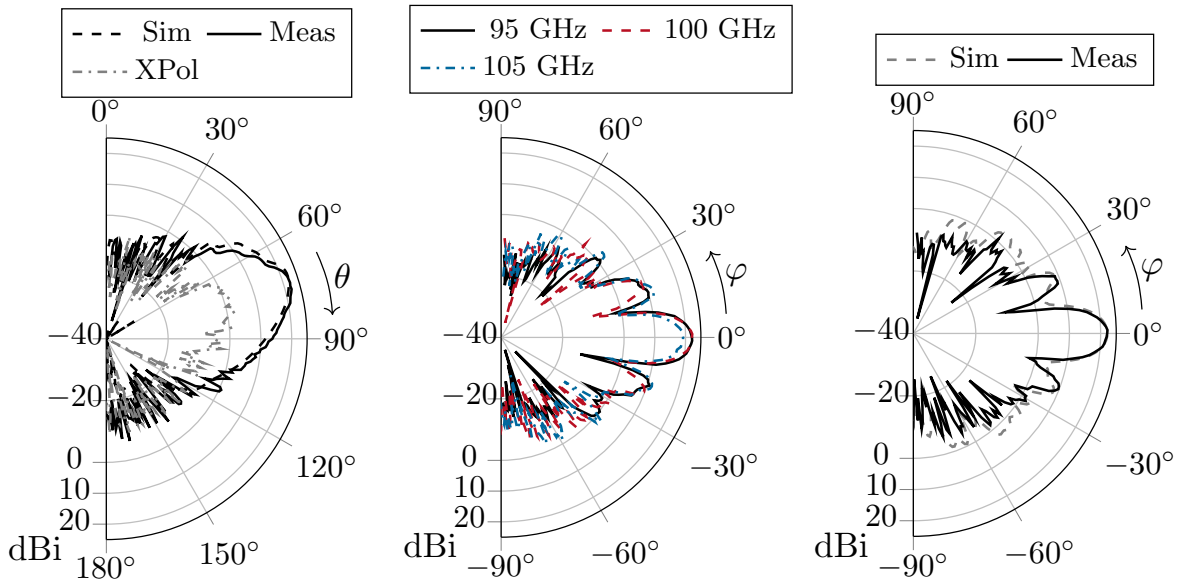
Figure 5.12: (a) Simulated instantaneous field distribution with positioning pin locations, and (b)  $|S_{11}|$  of the antenna arrays.

strength, see Fig. 5.12 (a). Fig. 5.12 (b) depicts the measured input reflection of both demonstrators, which is well below  $-10$  dB at all frequencies. The obtained antenna patterns are illustrated in Fig. 5.13. Good agreement of simulation and measurement is obtained. Gain and SLL are plotted in Fig. 5.14. The  $E_{11}^y$ -mode array demonstrator shows slightly unbalanced side lobes at  $\pm 16^\circ$ , which is frequency independent and due to fabrication tolerances. Maximum gain of 21 dBi and 23 dBi is obtained for  $E_{11}^y$ - and  $E_{11}^x$ -mode, respectively.

A direct comparison to different rod antenna arrays is given in Table 5.1. The DIL arrays are on par with voluminous two-dimensional dielectric arrays. Their slightly larger size in one dimension, due to the ground plane length, can be adapted according to space restrictions in practical applications. The main benefit of DIL antennas compared to HWG and DWG arrays lies in their quasi-planar, PCB-like nature. The total efficiency from the operation frequency of 90 GHz to 105 GHz is 97% to 72% (simulated: 95% to 92%) for the  $E_{11}^y$ -mode array. The  $E_{11}^x$ -mode array's



(a) Simulation and measurement of the  $E_{11}^y$ -mode array in Elevation at 100 GHz. (b) Measurements of the  $E_{11}^y$ -mode array in Azimuth,  $\theta = 75^\circ$ . (c) Simulation and measurement of the  $E_{11}^y$ -mode array in Azimuth at 92.5 GHz,  $\theta = 75^\circ$ .



(d) Simulation and measurement of the  $E_{11}^x$ -mode array in Elevation at 100 GHz. (e) Measurements of the  $E_{11}^x$ -mode array in Azimuth,  $\theta = 70^\circ$ . (f) Simulation and measurement of the  $E_{11}^y$ -mode array in Azimuth at 92.5 GHz,  $\theta = 70^\circ$ .

Figure 5.13: Simulated and measured far fields for the rod antenna arrays in (a) to (c)  $E_{11}^y$ -mode, and in (d) to (f)  $E_{11}^x$ -mode. Cross polarization is measured at 100 GHz.

## 5. Beamsteering Liquid Crystal Dielectric Image Line Antennas

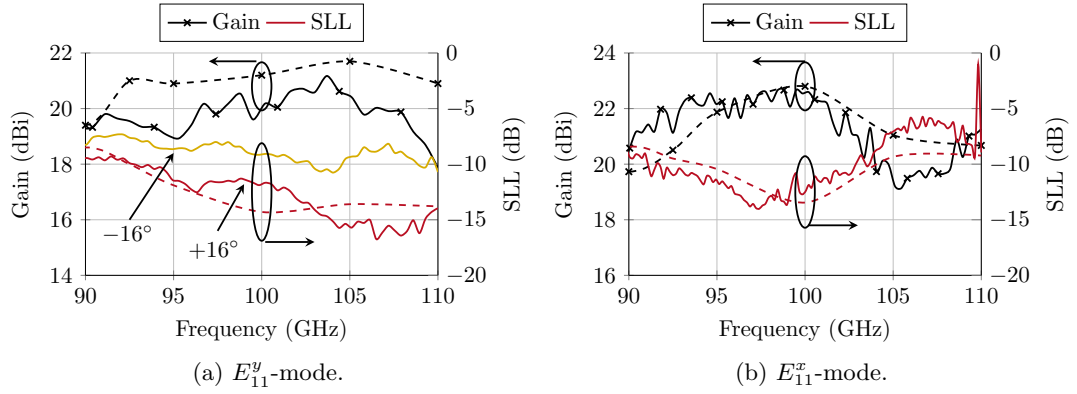


Figure 5.14: Simulated (dashed) versus measured (solid) course of gain and SLL (Azimuth) in W-band for both antennas. Imbalanced side lobes, indicated by their angle of occurrence, for the  $E_{11}^y$ -mode demonstrator in (a) shows its sensitivity to fabrication tolerances.

Table 5.1.: Comparison of different rod antenna arrays. Abbreviations: HWG - hollow waveguide, DWG - dielectric waveguide.

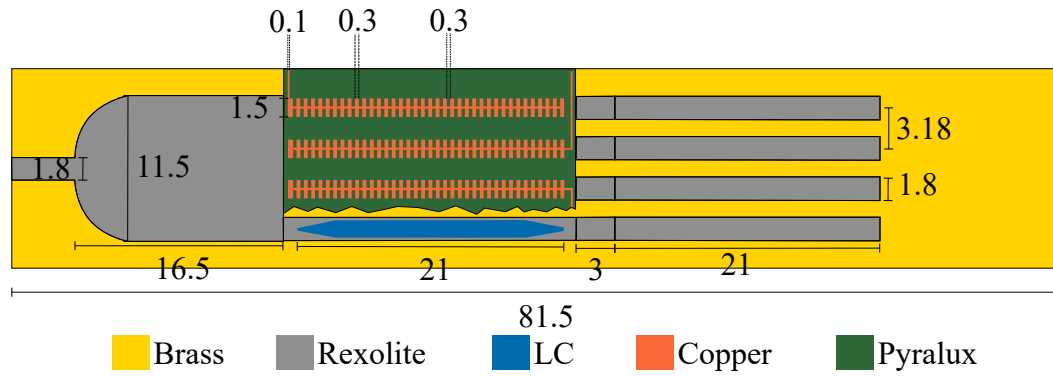
Topology	$f_0$ (GHz)	Size in $\lambda_0$ at $f_0$	# Elements	Power Division	Max. gain	$\epsilon_r$	Ref.
DIL	15	$3 \times 3$	4	Corporate	18	6	[PBA17]
DIL	35	$8.1 \times 3.5$	3	Serial	/	9	[Che+09]
HWG	70	$4.9 \times 0.5$	4	Corporate	20	5	[Kah+17]
HWG	100	$17 \times 2.6 \times 4$	16	Corporate	23.5	11	[Riv+16]
DWG	100	$5.5 \times 4$	4	MMI	17	2.53	[Ree+17c]
DWG	100	$8.8 \times 4.4 \times 4.4$	16	MMI	22	2.53	[Ree+18]
$E_{11}^y$ -DIL	100	$10 \times 4$	4	MMI	21	2.53	Sect. 5.1.2
$E_{11}^x$ -DIL	100	$10 \times 4$	4	MMI	23	2.53	Sect. 5.1.2
DWG	350	$13.4 \times 10$	40	Flare	20	11	[Wit+18]

efficiency ranges at these frequencies from 99% to 83% (simulated: 97% to 94%), when the slight frequency shift, visible in Fig. 5.14 (b), is taken into account.

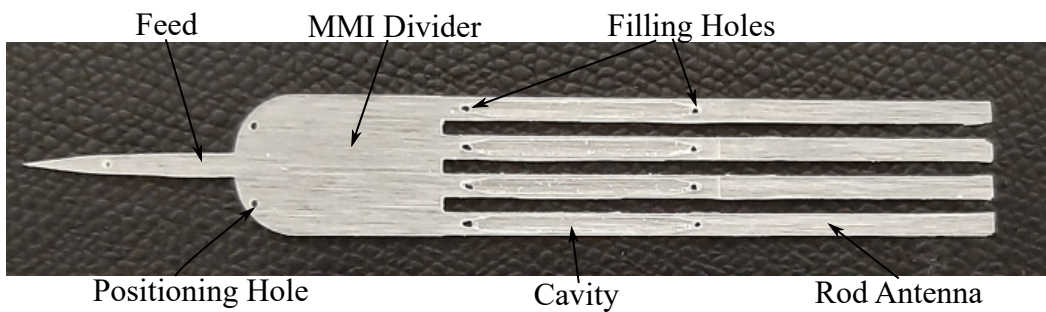
### 5.1.3. 1x4 Phased Array in $E_{11}^y$ -Mode for Beamsteering

With the investigation of phase shifters, power dividers, antenna elements and arrays, a phased array is realized by combining the corresponding components in this section. The  $E_{11}^y$ -mode is chosen for a phased array demonstrator, since integrated electrodes with good response time from Section 4.1.4 are available in this mode.

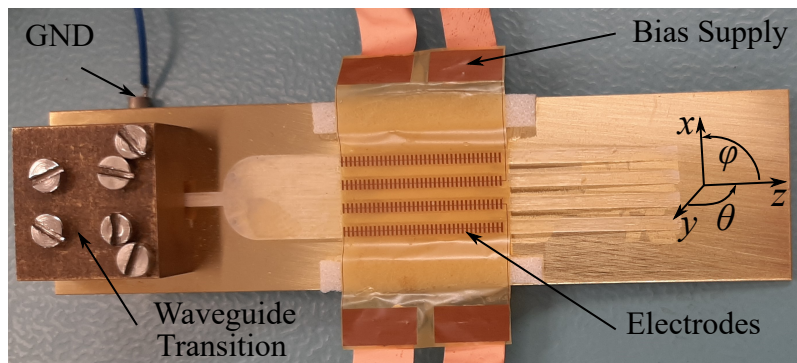




(a) Simulation Model (top view). The substrate above the bottom phase shifter is left out to show the LC cavity underneath. Dimensions are given in mm.



(b) Rexolite body.



(c) Array demonstrator.

Figure 5.15: (a) Phased array demonstrator schematic, (b) Rexolite body and (c) full assembly [Tes+22a] ©2022 IEEE.

The corresponding layout is illustrated in Fig. 5.15 (a), together with important dimensions from the previous sections and chapters. The Rexolite body of the phased array is milled in one piece, and the electrode structure for all four phase shifters is photolithographically processed on a Pyralux substrate. As with the phase shifter

## 5. Beamsteering Liquid Crystal Dielectric Image Line Antennas

from Section 4.1.4, the substrate is glued on top of the Rexolite structure. The phase shifters are individually filled with LC, and the filling holes are sealed with optical adhesive, before the structure is mounted on the ground plane. The demonstrator is shown in Fig. 5.15 (b) and (c). The magnitude of input reflection, for zero and full bias at the phase shifters, is given in Fig. 5.16. While good matching is obtained, the course of the measured  $|S_{11}|$  differs from simulations and of the obtained  $|S_{11}|$  for the array without phase shifters (Fig. 5.12 (b)). This discrepancy can be caused by reflections from the phase shifters with the electrode structure, which propagate through the MMI divider simultaneously and interfere at the input.

The obtained antenna patterns are shown in Fig. 5.17. In elevation, high agreement is obtained, but the main lobe presents more ripples in measurements than in simulations, which can be caused by the manual assembly of the electrode structure on top of the array. In azimuth, the bias voltages of the individual phase shifters need to be adjusted to counteract manufacturing tolerances, such that a  $0^\circ$  beam steering is obtained. These differences arise by different amounts of glue at the filling holes, and different glue layers underneath phase shifters and antennas. Hence, with no bias, a pre-steered pattern with non-desirable SLL is present.

At  $\varphi = 0^\circ$ , an SLL of  $-7.7$  dB and a gain of 18 dBi is obtained at 95 GHz. The HPBW is both  $11^\circ$  in azimuth and elevation plane, respectively. With the demonstrator, beam steering  $\pm 10^\circ$  can be achieved. With such a steered beam, the gain reduces to 17 dBi, and the SLL remains at around  $-7.5$  dB at 95 GHz. Simulations predict similar SLL, but a higher beam steering angle of  $12^\circ$ . At higher frequencies, i.e. at 100 GHz, the SLL rises to  $-5$  dB, and is not in line with simulations. The radiation of the top electrodes, discussed in Section 4.1.4, shows a simulated increase of radiated power from 100 GHz on, which can cause higher SLL. The voltage necessary for  $\varphi = 0^\circ$  and  $\varphi = \pm 10^\circ$  are given in Table 5.3. In principle, higher beam steering angles of up to  $\pm 25^\circ$  can be achieved if the phase shifters are longer, such as in [Ree+19b], and thus provide higher amounts of differential phase. With

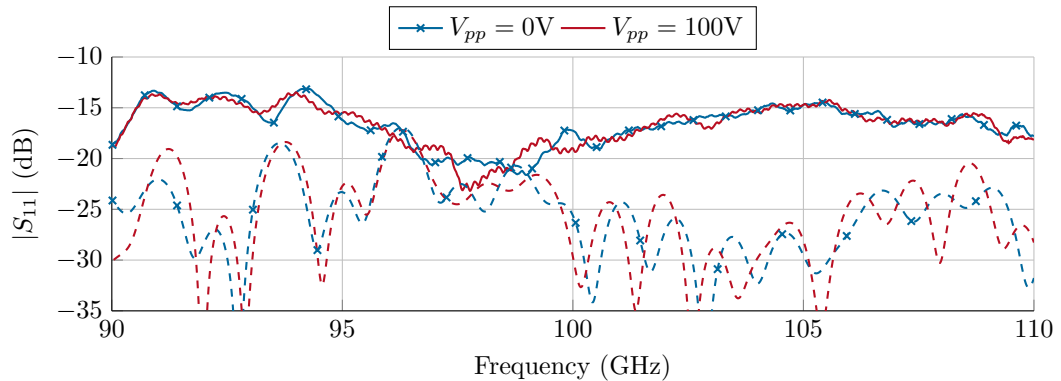


Figure 5.16: Measured (solid) and simulated (dashed)  $|S_{11}|$  of the phased array demonstrator with different  $V_{pp}$  at all phase shifters.

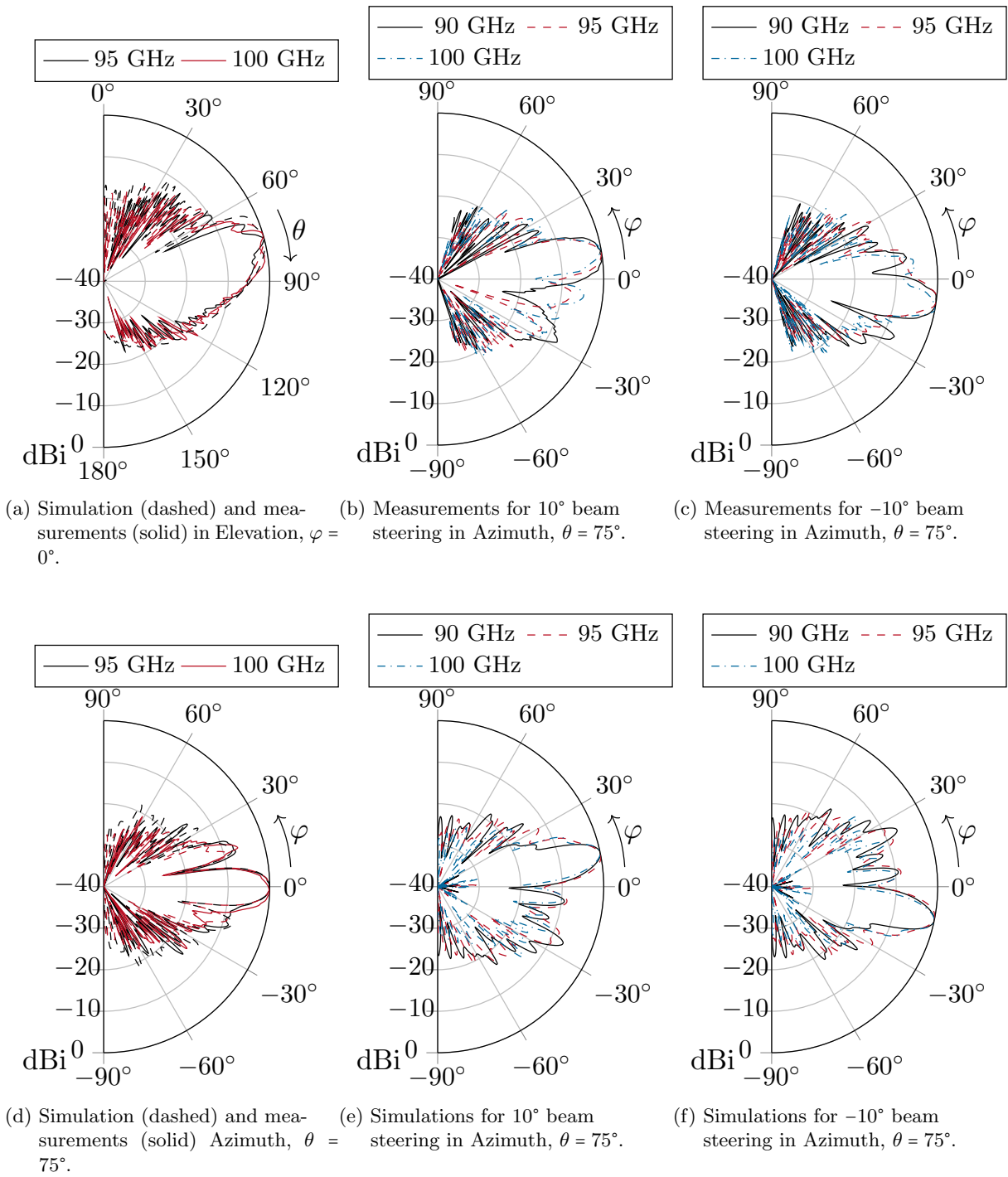


Figure 5.17: Simulated and measured far fields for the phased array demonstrator. (a), (d) - simulation and measurement with  $0^\circ$  beam steering, (b), (c) - measurements for  $\pm 10^\circ$  beam steering, and (e), (f) - corresponding simulations. Patterns are individually normalized for readability.

## 5. Beamsteering Liquid Crystal Dielectric Image Line Antennas

Table 5.2.: Comparison of different LC rod antenna phased arrays. Abbreviations: HWG - hollow waveguide, DWG - dielectric waveguide.

Topology	$f_0$ (GHz)	# Ele- ments	Gain (dBi)	SLL (dB)	$\eta$ (%)	$\varphi$ (°)	Ref.
HWG/DWG	90	4	9.1 to 11.5	-12 to -8	20-30	$\pm 25$	[Ree+19b]
DWG	90	4	13 to 14	-8	52-55	$\pm 10$	[Pol+20b]
DIL	95	4	17 to 18	-7.5	41-64	$\pm 10$	Sect. 5.1.3

Table 5.3.: Peak-to-peak voltages  $V_1$  to  $V_4$  at the phase shifters for the demonstrated beam steering angles.

$\varphi$	$V_1$	$V_2$	$V_3$	$V_4$
$-10^\circ$	12.5V	9V	55V	70V
$0^\circ$	0V	15V	25V	50V
$10^\circ$	0V	80V	2.5V	0V

the demonstrator at hand, the additional challenge to balance manufacturing tolerances decreases the achievable phase progression between the elements. Longer phase shifters result in an increased total length of the phased array. It is also possible to increase the height  $h$  of the DIL, which hosts the LC, slightly by  $\Delta h$ . By this, the total length of the array is not changed, but the response time will increase. The phase increase obtained by this technique is limited: an increase by  $\Delta h = 0.2 \cdot h$  of the given phase shifter of length  $l_{LC} = 21$  mm results in an additional  $\Delta\varphi = 50^\circ$ , but the switch-on response time is increased by a factor of 1.44 from 134 ms to 192 ms. A direct comparison to DWG phased arrays with MMI dividers is shown in Table 5.2. Higher gain with similar SLL is obtained, and the total measured efficiency from 90 GHz to 105 GHz is 65 % to 41 % (simulated: 63 % to 52 %), decreasing with frequency, is in a similar range as in [Pol+20b]. The presented demonstrator consists of less individual components, and has the clear advantage that neighboring electrodes do not affect each other. In [Ree+19b; Pol+20b], multiple voltages have to be adjusted if one central electrode changes its potential, which results in a complex interaction at each phase shifter. Hence, if only one phase shifter in these works needs to be adjusted, all others have to be adjusted as well.

## 5.2. Leaky Wave Antennas

A more simple way of biasing can be achieved by employing LWAs. LWAs are comparably easy to realize by including radiative structures in, on or next to a waveguide of arbitrary topology. Due to their simplicity, no complex feeding network is neces-

sary, and they are often of lower cost than a large phased array. They are of low profile and provide high directivity. The first LWA, a HWG with a long slot, was introduced by W.W. Hansen in the 1940s [Han46]. Since then, LWAs have been continuously researched and employed in practice. A comprehensive overview of LWAs is given in e.g. [JO07], but the most important aspects, necessary for the design of LC-LWAs and the interpretation of measurement results, are summarized on the following pages. The open structure of DILs, together with a reflective ground plane, makes them good candidates for LWAs, and several different approaches of creating LWAs in DIL topology have been tested [Ito77; Wu+12; PB17; PBA18]. In addition, LC has been included in LWAs in different topologies to steer the main beam at a fixed frequency. One of the earliest LC-LWAs is shown in [Dam+10; Dam11] which was followed by [Roi+14; Roi+15; Par15]. In these early works at frequencies from 7 GHz to 27 GHz, metamaterials are used, and maximum angular coverage from  $14^\circ$  to  $20^\circ$  are obtained when applying bias voltages of up to 120 V. However, these early demonstrators suffer from a non-mitigated open stop-band, which results in high reflection coefficients around the frequencies at broadside radiation. At frequencies below 30 GHz, good results for LC-LWAs are achieved by now [Ma+20; KN21], but due to their comparably low frequencies of operation, they are inherently narrowband. Even though there have been advances of LC-LWAs at higher frequencies, and good results have been demonstrated in simulations, they are not practically confirmed [Che+16; Fus+17; Foo19]. Especially higher mmW-frequencies are of particular interest for LWAs, due to higher achievable bandwidth for imaging, communication, or remote sensing applications.

As LWAs inherently scan their main beam with frequency, tuning with LC results in a shift of the whole sector covered by frequency scanning, as shown in Fig. 5.18. Hence, either a fixed frequency can be changed to radiate in different directions,

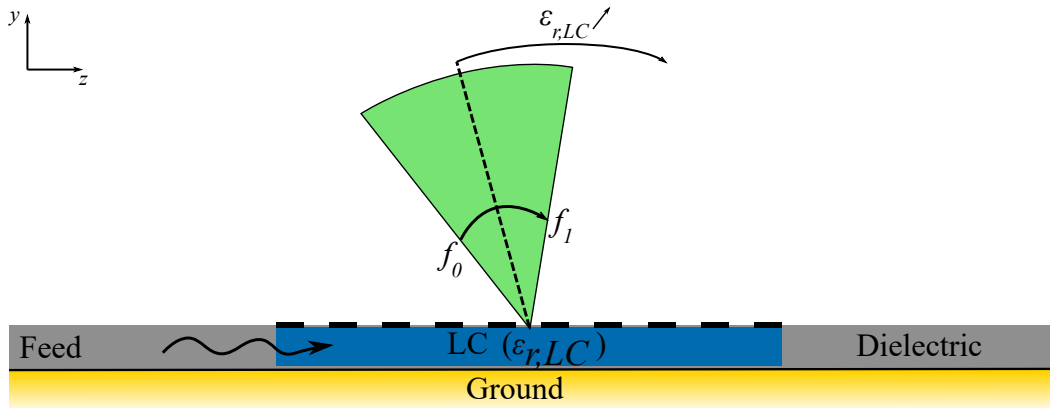


Figure 5.18: Schematic of an LC-LWA in DIL topology. The spatial coverage sector when changing the frequency of operation from  $f_0$  to  $f_1$  is steered by a change of the permittivity of the LC body below the radiators, indicated with black markings [Tes+22b] (CC BY 4.0).

## 5. Beamsteering Liquid Crystal Dielectric Image Line Antennas

or the whole utilized scanning sector is turned, which can add to diversity gain or extend the area of observation.

### 5.2.1. Operation Principle

The key characteristic of LWAs is that they are waveguide-based structures with a travelling wave which leaks power from the waveguide to free space. The earliest LWAs relied on a continuous perturbation of the waveguide, such as a slot along it. This simple type of perturbation only allows radiation in the direction of propagation, i.e. only towards endfire and with significant effort to broadside, but not to backfire [JO07]. In order to overcome this problem and enable full scanning from backfire to endfire, metamaterial-based approaches or periodic perturbations can be used [Dam+10; JO07]. In this dissertation, periodic structures are used as unit cells. Fig. 5.19 (a) shows a side view of a lossless DIL with an arbitrary imperfect (and hence partially leaking) boundary to free space at  $y = 0$ . This boundary can be created by e.g. periodic strips of width  $w$ , and periodicity  $p$  (Fig. 5.19 (b)). In Fig. 5.19 (a), "A" represents the source point, which is located at  $z \ll 0$ . The wave propagates in  $z$ -direction with the propagation wave number  $k_z$ /propagation constant  $\beta(\omega)$  (lossless case).  $k_{wg}$  is the guided wave number, and depends on the material inside the waveguide structure, hence  $k_{wg} = k_0$  if it is filled with air.  $k_c$  is the cutoff wave number and can be determined by the waveguide dimensions. Directly at the imperfect boundary to the upper medium (air), the propagation constant away from the DIL is

$$k_y = \sqrt{k_0^2 - \beta^2}. \quad (5.8)$$

In order to achieve  $k_y > 0$ ,  $\beta(\omega) < k_0$ , i.e. it has to be a fast wave, with a phase velocity greater than the speed of light. The wave travelling along the DIL has a

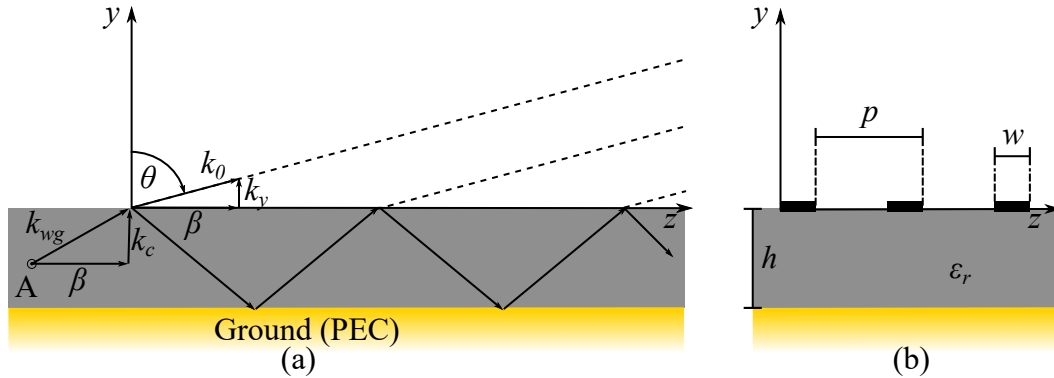


Figure 5.19: (a) Side view of an arbitrary two-dimensional lossless LWA, including the radiation principle. Dashed lines represent constant amplitudes. (b) an example of a periodical DIL-LWA with strip radiators of width  $w$ . Both structures are infinitely expanded in  $x$  direction.

complex wave number, even if all components are considered as lossless, since power is leaked and leaves the DIL ( $k_y > 0$ ). Hence,

$$k_z = \beta - j \cdot \alpha_{leak}, \quad (5.9)$$

where  $\beta$  is the phase constant, and  $\alpha_{leak}$  is the leakage constant. The phase constant, if the fast wave condition applies, determines the main beam elevation angle  $\theta$ , which changes with variation of  $\omega$ :

$$\theta(\omega) = \sin^{-1} \left[ \frac{\beta(\omega)}{k_0} \right]. \quad (5.10)$$

Hence, a change of frequency of operation or in the permittivity of the DIL medium results in a steer of the main beam. For periodic LWAs, see Fig. 5.19 (b), the Floquet-Bloch Theorem can be applied, which states that a time-harmonic ( $e^{j\omega t}$ ) electromagnetic field propagating along a periodic structure possesses the property  $E(x, z + p) = e^{jk_z p} E(x, z)$ , where  $p$  is the period of the structure/function. With the statement for a periodic function  $P(x, z) = P(x, z + p)$  we get

$$E(x, z) = e^{-jk_z z} P(x, z), \quad (5.11)$$

which means that the determination of the guided-wave field (Bloch mode) at any point on an infinite periodic structure can be obtained solely from the knowledge of the field distribution within a "unit cell" (UC), i.e. a single period  $p$ . Since all periodic functions can be expanded to Fourier series, i.e. by  $P(x, z) = \sum_{n=-\infty}^{\infty} a_n(x) e^{-jn(2\pi/p)z}$ , we obtain via Eqn. (5.11)

$$E(x, z) = e^{-jk_z z} \sum_{n=-\infty}^{\infty} a_n e^{-jn(2\pi/p)z} = \sum_{n=-\infty}^{\infty} a_n e^{-jk_{zn} z}, \quad (5.12)$$

with

$$k_{zn} = k_z + 2n\pi/p = \beta_n - j\alpha_{leak}, \quad \beta_n = \beta + n2\pi/p, \quad (5.13)$$

and  $a_n$  being the coefficient of the corresponding harmonics  $n = 0, \pm 1, \pm 2, \dots$ . As stated previously, the propagation constant  $\beta_n$  needs to fulfill the fast-wave condition in order to cause a leaky wave. The attenuation constant  $\alpha_{leak}$  is not changed with different  $n$ .

A very useful tool to analyze which spatial harmonic contributes in which way to leakage, is the Brillouin Diagram. In this dispersion diagram, UC investigations are used to predict bandwidth and scanning range of an LWA with an infinite number of UCs. Fig. 5.20 displays a Brillouin Diagram and highlights important zones in it. The  $n$ -th spatial harmonic only contributes to radiation if it is a fast-wave, i.e. lying in between the two dashed "air-lines" where  $|\beta| = k_0$ . The abscissa divides this region, where the positive side represents radiation in forward direction towards endfire, and the negative side backward radiation direction towards backfire; the abscissa itself represents broadside radiation. A typical course of three harmonics

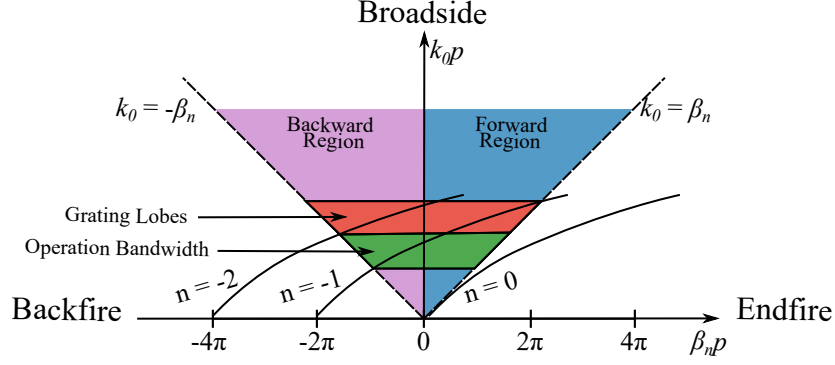


Figure 5.20: Representation of a typical Brillouin Diagram for a periodic LWA.

$\beta_0$ ,  $\beta_{-1}$  and  $\beta_{-2}$  is included in Fig. 5.20. It is undesirable if two spatial harmonics are in the fast-wave regime simultaneously, since they will both contribute to radiation to different angles  $\theta$ , and therefore a pattern with high grating lobes arises. Hence, the operational bandwidth of a particular spatial harmonic is not only limited by the fast-wave regime, but also by the frequency, when the next spatial harmonic becomes fast-wave. This is particularly important when tuning LC, i.e. changing the dispersion relations within the UCs. The different spatial harmonics  $\beta_n$  and the accompanied leakage constant  $\alpha_{leak}$  can be obtained by [Poz11; Lyu+16]

$$\beta_n p = \left| \text{Im} \left( \cosh^{-1} \left( \frac{1 - S_{11} S_{22} + S_{21} S_{12}}{2 S_{21}} \right) \right) \right| \quad (5.14)$$

$$\alpha p = \left| \text{Re} \left( \cosh^{-1} \left( \frac{1 - S_{11} S_{22} + S_{21} S_{12}}{2 S_{21}} \right) \right) \right|. \quad (5.15)$$

In the following section, focus on an  $E_{11}^y$ -mode LC-LWA is set. Results for an  $E_{11}^x$ -mode LC-LWA can be found in the appendix A.6.2.

### 5.2.2. Unit Cell and Antenna Design

Instead of treating the bias electrodes as an external means to bias LC, the aim in this section is to integrate the electrodes to the component, such that they contribute to the desired RF-performance, instead of disturbing it. An electrode which simultaneously provides good radiation characteristics has to satisfy several conditions:

- Radiation in fast-wave region, with good bandwidth and angular coverage
- Mitigation/elimination of periodic LWA issues, e.g. stop-band phenomena
- Supply of a large area above an LC cavity for efficient bias
- Geometries which can be biased, i.e. the UCs need to be electrically connected with no isolated entities.



It is often the case that some of these conditions contradict, e.g. when trying to suppress an open stop band with two nonidentical isolated radiation elements [PW07], only small areas on the DIL are covered, and the structures may not be connected to each other. Many radiator geometries such as strips and discs and various arrangements of them have been tested during this dissertation. Disc shapes do not satisfy the conditions listed above, even though they would be able to cover large areas of an LC cavity. When combining transversal and longitudinal strips/slots, good LWA characteristics can be obtained [PW07; Lyu+16], but these structures are not connected to each other, and can therefore not be used. The best results have been achieved with H-shaped UCs. They were first suggested by [PBA18], and can cover a sufficient area on top of a DIL. The longitudinal strips cancel reflected waves, while the thick, transversal strip contributes most to the radiation. In order to achieve almost full biasing of the LC cavity by the UC, the cavity is of slightly less width  $w_{LC} = 1.5 \text{ mm}$  than in the previous Section 4.1.1. Fig. 5.21 shows the model of both, a non-tunable Rexolite demonstrator for basic investigations, and its tunable extension to an LC-LWA. The H-shape of the UC does not differ between both demonstrators, but the LC-LWA is sealed with Pyralux foil on which the electrodes/radiators are etched on, similar to the phase shifters of Section 4.1.4 and Section 5.1.3. In order to bias the structure, a thin line connects all UCs for the LC-LWA. The corresponding dimensions of the optimized H-shape is given in Table 5.4, and the obtained phase and leakage constants are shown in Fig. 5.22, which highlights the contribution of the bias line to  $\alpha_{leak}$ . A positive side effect of the bias line is that it helps to eliminate residual effects of the mitigated open stop band, which is present with isolated UC, as visible e.g. at 92.5 GHz and  $\epsilon_{r,LC} = 2.46$  in Fig. 5.22 (b). However, the bias

Table 5.4.: Most important dimensions of the DIL-LWAs.

Parameter	$w$	$h$	$p$	$l_s$	$l_l$	$w_s$	$w_l$	$t$	$w_{conn}$	$w_{LC}$	$h_{LC}$
Value (mm)	1.8	0.9	2.3	0.7	1.5	1.5	0.3	0.009	0.075	1.25	0.8

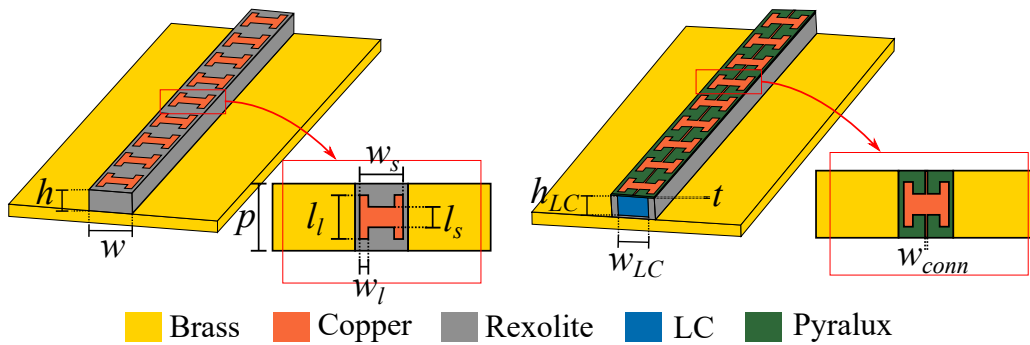


Figure 5.21: Antenna layouts with a detailed view on the UCs. Left: Rexolite-LWA with isolated UCs, right: LC-LWA with connected UCs on Pyralux foil, which seals the LC cavity [Tes+22b] (CC BY 4.0).

## 5. Beamsteering Liquid Crystal Dielectric Image Line Antennas

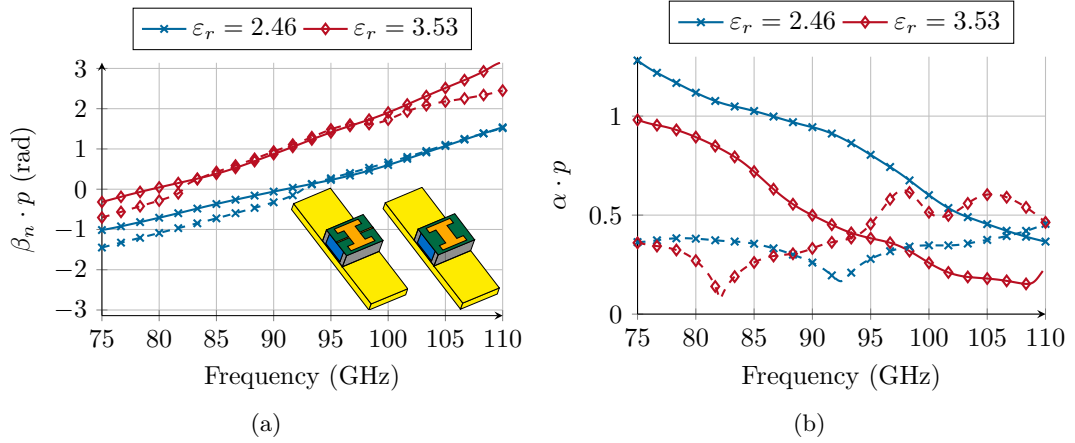


Figure 5.22: (a) Phase and (b) attenuation constants of isolated (dashed) and connected (solid) UCs, for highest and lowest LC permittivity. Representative pictures of both UCs are included in (a).

line increases leakage, especially at lower frequencies, which leads to more radiation at the first UCs. Therefore, a reduced gain can be expected when employing the bias line. Since an LC-LWA with isolated UCs can not be biased, the Rexolite-LWA is employed as a reference for result comparison, since its permittivity is highly similar to LC in perpendicular alignment ( $\epsilon_{r,LC} = 2.46$ ). Fig. 5.23 shows the corresponding Brillouin Diagrams for the UC-sets, which are practically verified in the following sections: 1) a Rexolite-based LWA without connection line between the UC (Fig. 5.23 (a)), and 2) an LC-based LWA with a connection line (Fig. 5.23 (b), (c)). Frequency scanning from 75 GHz to 105.3 GHz without grating lobes is predicted for Rexolite-LWA, with broadside radiation at 92.03 GHz. The LC-LWA shows very similar radiation characteristics with a frequency shift of approximately 1 GHz in perpendicular molecule alignment ( $\epsilon_{r,LC} = 2.46$ ) due to the high similarity in permittivity when compared to Rexolite ( $\epsilon_{r,Rex} = 2.53$ ). When tuning the LC to parallel alignment ( $\epsilon_{r,LC} = 3.53$ ), the scanning range is limited from 75 GHz to 97 GHz, due to the  $n = -2$  harmonic entering the fast-wave region, caused by the reduction of electrical length of one UC. This change shifts the harmonics to the right in the Brillouin Diagram, and affects their slope. Hence, broadside radiation is shifted by 11.07 GHz to 79.03 GHz, and grating lobes appear at lower frequencies. In order to assess general fabrication tolerances, the Rexolite-LWA is investigated, first.

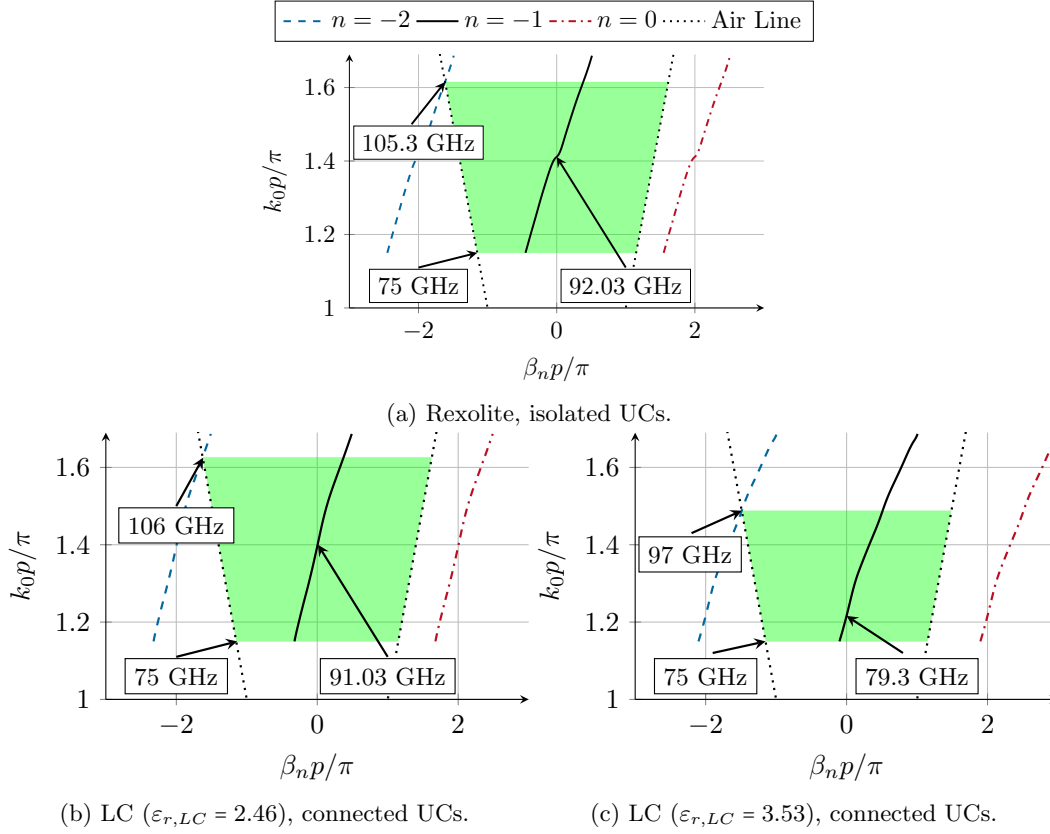


Figure 5.23: Brillouin Diagrams for the UC-setups shown in Fig. 5.21. The operation bandwidth without grating lobes is shaded in green. Lowest and highest frequency in W-band, as well as the broadside frequency are indicated with markers.

### 1) Frequency Scanning Solid Rexolite-LWA

The Rexolite-LWA is fabricated at the institute's clean room and laboratory facilities: a rectangular Rexolite block of  $30 \text{ mm} \times 90 \text{ mm}$  is sanded on one of its major surfaces, such that a smooth surface is obtained. The block is of height  $h = 0.9 \text{ mm}$  of the final DIL-LWA (c.f. Fig. 5.21). The smooth surface is metallized with a  $h_{gold} \approx 50 \text{ nm}$  thin gold layer with a Balzers BA510 evaporation system. The desired number  $N = 24$  of UCs are photolithographically structured on the block, which can host four rows of  $l_{LWA} = N \cdot p = 55.2 \text{ mm}$  long LWA structures. The LWA, together with tapered ends for feeding the DIL structure by the waveguide transition introduced in Section 3.3, is cut from the block by an LPKF ProtoMat S100 rapid prototype circuit board plotter. After cleaning, the LWA is mounted on its ground plane. Fig. 5.24 shows the structured substrate and the assembled demonstrator. In order to measure  $|S_{21}|$ , i.e. the residual power present after the wave propagates through the LWA, two waveguide transitions are connected to the demonstrator. For radiation pattern measure-

## 5. Beamsteering Liquid Crystal Dielectric Image Line Antennas

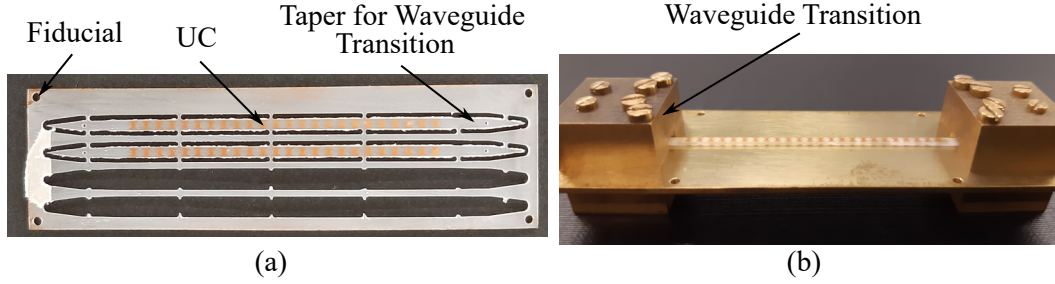


Figure 5.24: (a) Metallized Rexolite with partially removed LWA-structures, and (b) the fully assembled demonstrator [Tes+22b] (CC BY 4.0).

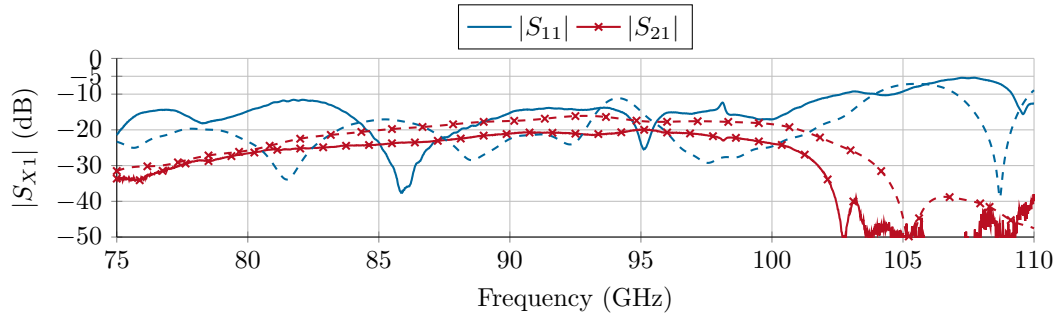


Figure 5.25: Simulated (dashed) and measured (solid) S-parameters.

ments, the second transition is replaced by absorbing material in order to reduce undesired reflections from the transition. The measurement setup for the Rexolite LWA and the upcoming LC-LWA can be found in Fig. A.7 in the appendix. The measured amplitude of transmission and reflection coefficients is shown in Fig. 5.25. For simulations, a finite model of the demonstrator shown in Fig. 5.24 (b) is used. The antenna is matched up to 103 GHz, and residual power drops at around 101 GHz, which is lower than both the full wave simulation of the finite structure and the Brillouin Diagram of the infinite structure predict. Fig. 5.26 shows the obtained radiation pattern at various frequencies. A typical fan shaped beam is obtained, where residual radiation to the forward region is caused by the waveguide transition. This radiation is visible at the patterns in Fig. 5.26 (a), (b) at  $\theta \approx 45^\circ$  to  $80^\circ$ . The frequency-dependent gain and SLL are shown in Fig. 5.26 (d), where, besides the slight frequency shift already visible in Fig. 5.25, high agreement is achieved. The slight difference is caused by a slightly higher  $h$  of the DIL. In Fig. A.8 and Fig. A.9 in the appendix, the influence of  $h$  on the S-parameters, gain and SLL is visualized. Due to the high agreement of simulation and measurement, the antenna provides a good basis for LC-integration. Fig. 5.26 (e) illustrates the scanning behavior in elevation plane as a heat map. The antenna scans with  $1.4^\circ \text{GHz}^{-1}$  from  $-30^\circ$  at 75 GHz through broadside to  $10^\circ$  at 102 GHz. Hence, a bandwidth of 0.714 GHz is available for every  $1^\circ$  of scanning angle. From 80 GHz to 100 GHz gain ranges between 16 dBi

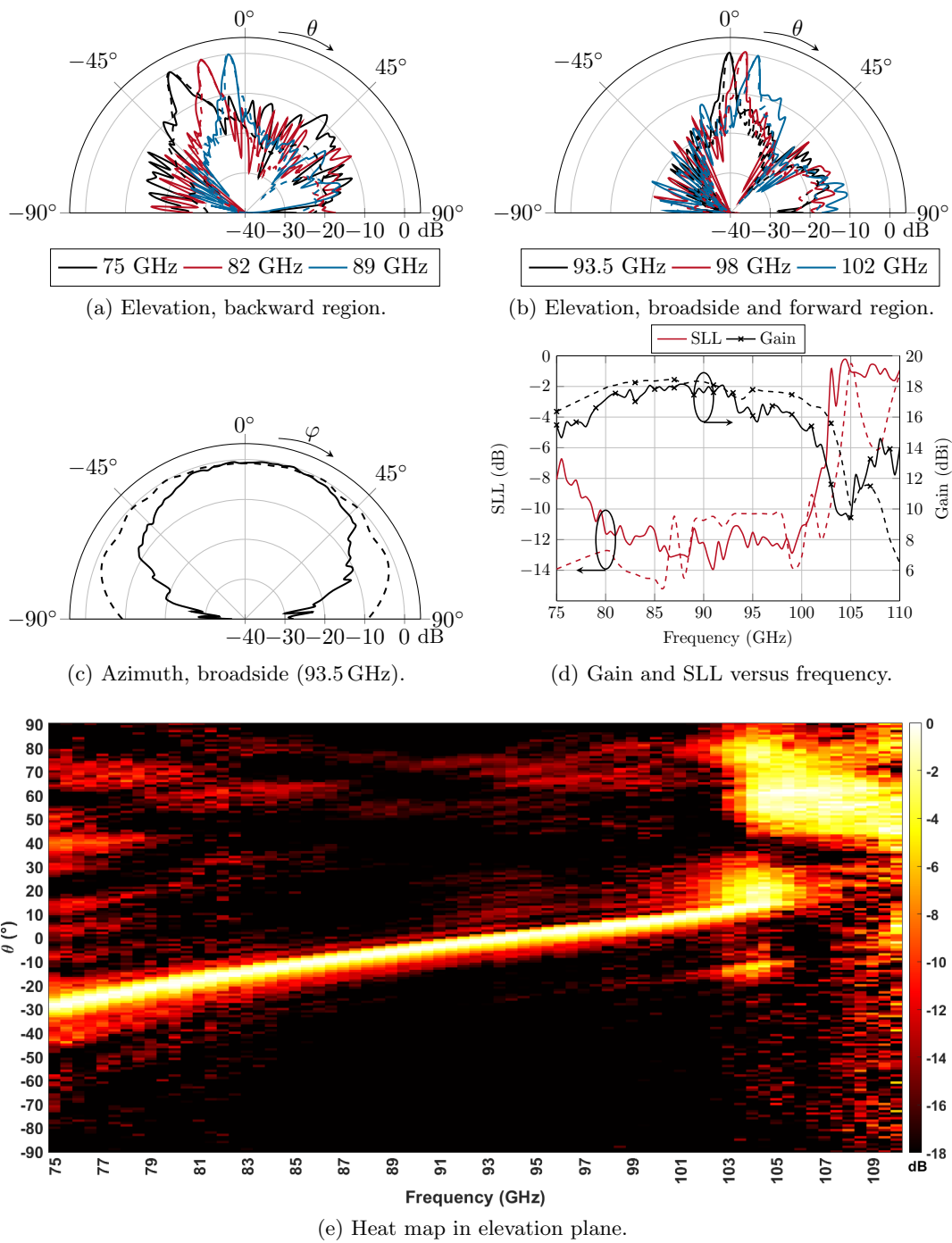


Figure 5.26: (a)-(c) Simulated (dashed) and measured (solid) normalized patterns, and (d) frequency dependent gain and SLL of the Rexolite-LWA. (e) Normalized measured scanning behavior as a heat map [Tes+22c] (CC BY 4.0).

## 5. Beamsteering Liquid Crystal Dielectric Image Line Antennas

and 18 dBi and the SLL is below  $-10$  dB. Cross-polarization is below  $-20$  dB and the measured antenna efficiency ranges from 69 % to 58 % (simulated 93 % to 87 %).

### 2) Rexolite-LWA with LC-Cavity for Steering of the Frequency Scanning Sector

On the basis of the results for the Rexolite-LWA, a direct comparison and assessment of the effects of LC-integration to the DIL-LWA can be conducted. The fabrication process of the LC-LWA is slightly different to the Rexolite-LWA, since the radiators have to be directly above a cavity in the DIL. Hence, the electrodes/radiator elements can not be metallized directly on a Rexolite structure. Instead, they are processed on a separate Pyralux foil, and are glued on Rexolite-DILs with a cavity, which are manufactured by CNC-milling. The Rexolite-DILs have two holes on the bottom of the cavity, and sealing and filling is similarly performed as with the phase shifters of the phased array in Section 5.1.3. Fig. 5.27 displays the assembly steps and the final demonstrator. The same number of  $N = 24$  UCs is used as with the Rexolite-

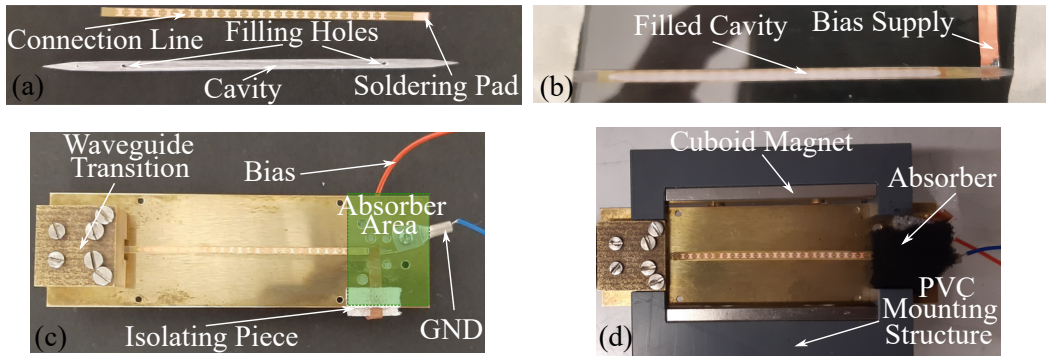


Figure 5.27: Assembly of the demonstrator. (a) Pyralux foil with electrode and bias structure, and Rexolite-DIL with cavity. (b) Filled LC-LWA, bottom view. (c) Assembly on ground plane with bias connections. (d) Final setup for measurements [Tes+22c] (CC BY 4.0).

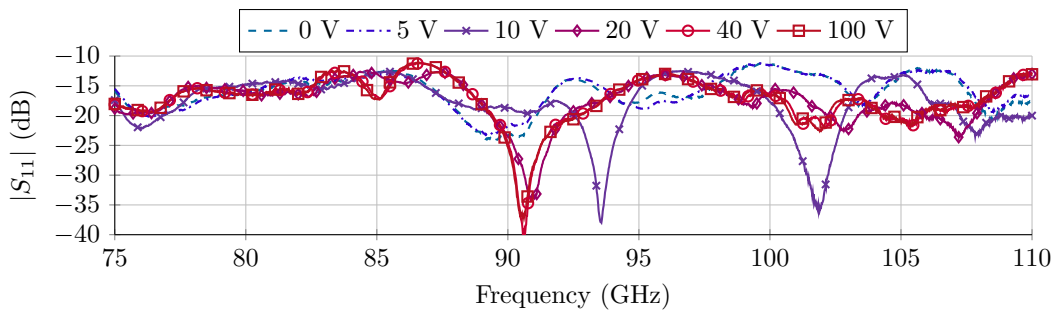


Figure 5.28:  $|S_{11}|$  for different bias voltages  $V_{pp}$ .

## 5.2. Leaky Wave Antennas

LWA, hence the antennas are of the same length  $l_{LWA} = 55.2$  mm. In order to utilize the anisotropy of the LC to the highest extent, two cuboid magnets, which provide a magnetic flux density of  $B = 70$  mT at the position of the LWA, are used for perpendicular LC alignment. Since the bias structure with soldering points and a clamp for ground connection are directly at the LWA's end, this area has to be shielded with absorber material. Otherwise, high reflections occur, which deteriorate

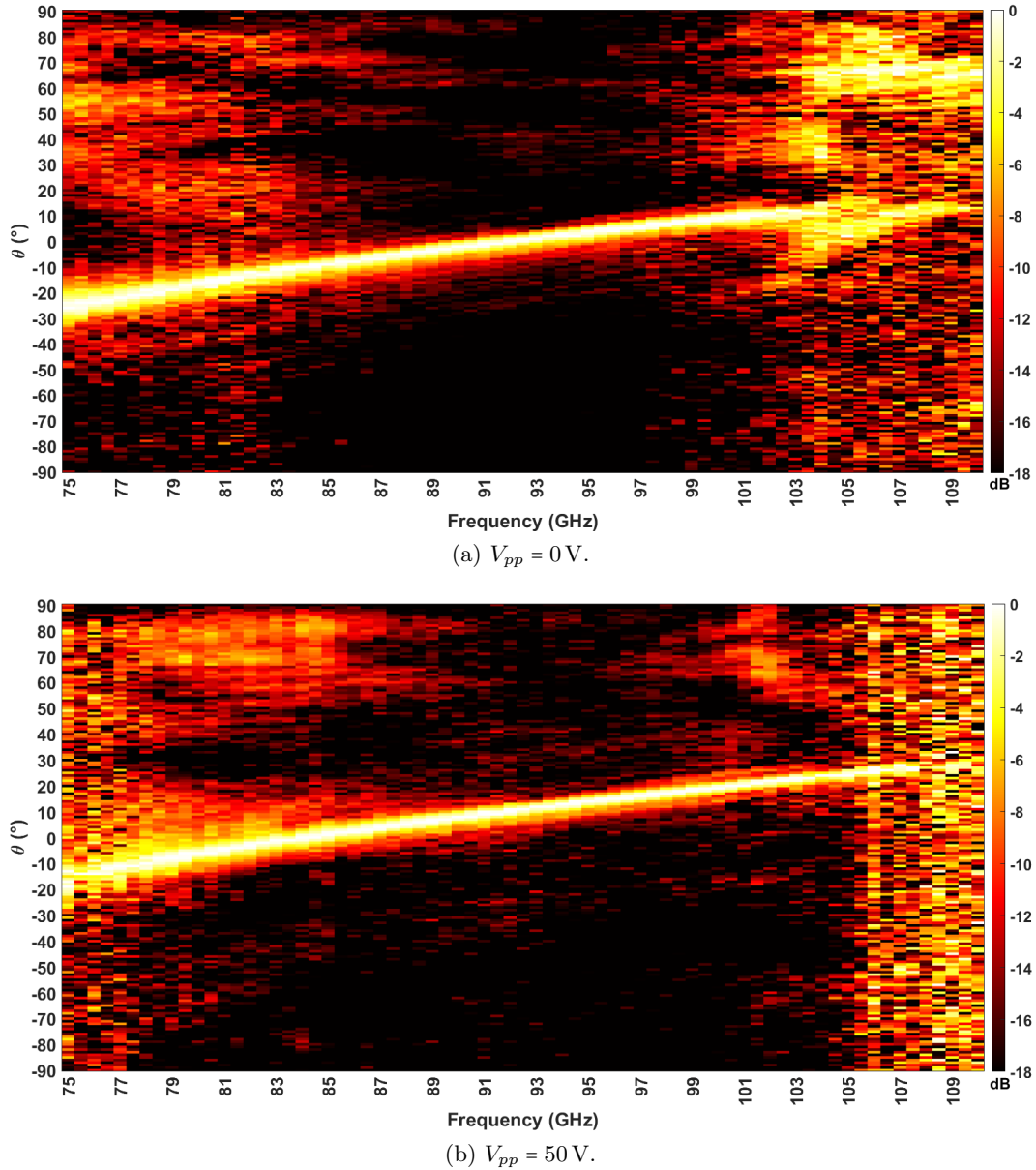


Figure 5.29: Heat maps of the measured beam steering behavior in elevation at W-band for different bias conditions [Tes+22b] (CC BY 4.0).

## 5. Beamsteering Liquid Crystal Dielectric Image Line Antennas

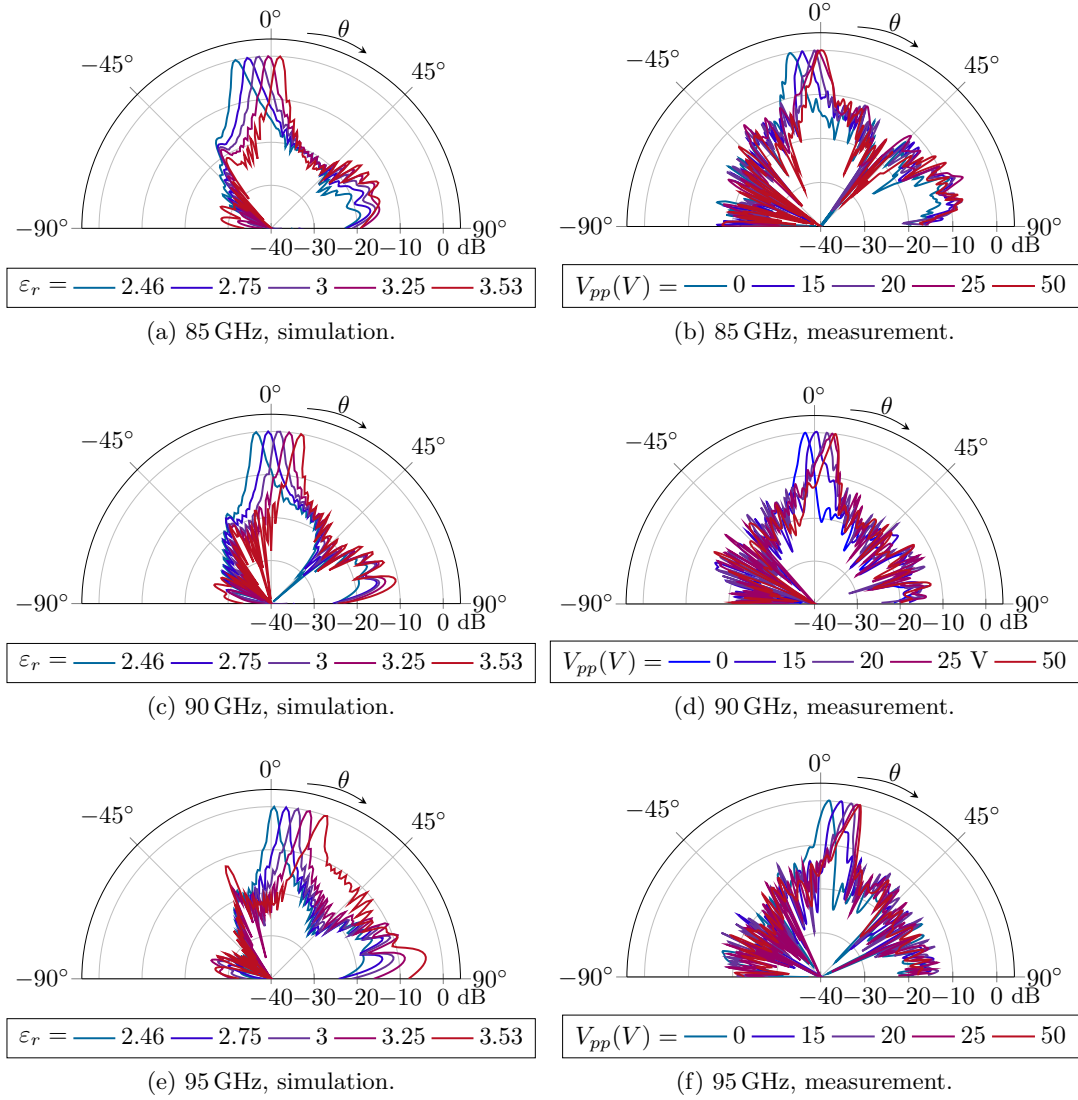


Figure 5.30: Simulated (left column) and measured (right column) patterns for beam steering at various frequencies and bias conditions (i.e. LC permittivities).

$|S_{11}|$  and the antenna pattern significantly. A 1 kHz bias voltage of peak-to-peak voltage  $V_{pp}$  is directly applied to the solder pad at the end of the LWA in order to bias the LC. Fig 5.28 displays the input reflection for different bias voltages. Regardless of bias voltage, matching with  $|S_{11}| < -10$  dB is maintained at all frequencies. Since the bias pad and the ground connection is present at the end of the LWA, no second waveguide transition can be connected to measure the residual power present at the end of the LWA. Due to the direct placement of the electrodes/radiators on the DIL, voltages of 50 V are sufficient for beam steering. Fig. 5.29 shows heat maps in



elevation plane for the unbiased and fully biased case. We observe a beam steering angle of  $\Delta\theta = 10^\circ$  at all frequencies.

The antenna efficiency ranges from 69% to 42%, decreasing with frequency (simulated: 85% to 55%). Utilizable SLLs are obtained from 85 GHz to 100 GHz. Detailed patterns in elevation for different bias conditions are shown in Fig. 5.30. The necessary bias for a desired beam steering angle  $\Delta\theta$  is plotted in Fig. 5.31 (a), and confirms saturation at 50 V. This is in line with the voltage characterization of the phase shifter of Section 4.1.4 (Fig. 4.20). When comparing simulation and measurement in Fig. 5.30, a difference in achievable  $\Delta\theta$  is noticeable. While simulations predict  $\Delta\theta = 15^\circ$  at all frequencies,  $\Delta\theta = 10^\circ$  is achieved in practice. The origins are the same as with the DIL phase shifters: fabrication tolerances and glue entering the cavity during sealing, non-optimal bias fields, and slightly reduced anisotropy of GT7-29001 at higher frequencies (c.f. Fig. 2.8). In fact, the practically achievable anisotropy, which can be estimated to be 73% of the theoretically available anisotropy, shown in Fig. 5.31 (b), extends the frequency range the antenna is usable in, and marks one of the most important trade-offs of this demonstrator: the more the tunable dielectric is changed to higher values, the lower the maximum usable frequency becomes due to grating lobes. This effect is shown at the simulated gain and SLL in Fig. 5.32 (a). The simulation predicts a maximum usable frequency of 95 GHz, if the highest LC permittivity of  $\varepsilon_{r,LC} = 3.53$  is assumed. In measurements, we see that this permittivity value is not reached, both due to bias conditions and reduced anisotropy of GT7-29001 at W-band frequencies. In fact, the simulated reduction in utilizable frequency range is not observable by the demonstrator, which presents operating frequencies of up to 100 GHz. In measurements, undesirable SLLs at frequencies from 75 GHz to 85 GHz are due to the waveguide transition and the high leakage constant of the connected UCs (see Fig. 5.22). From 85 GHz on, SLLs

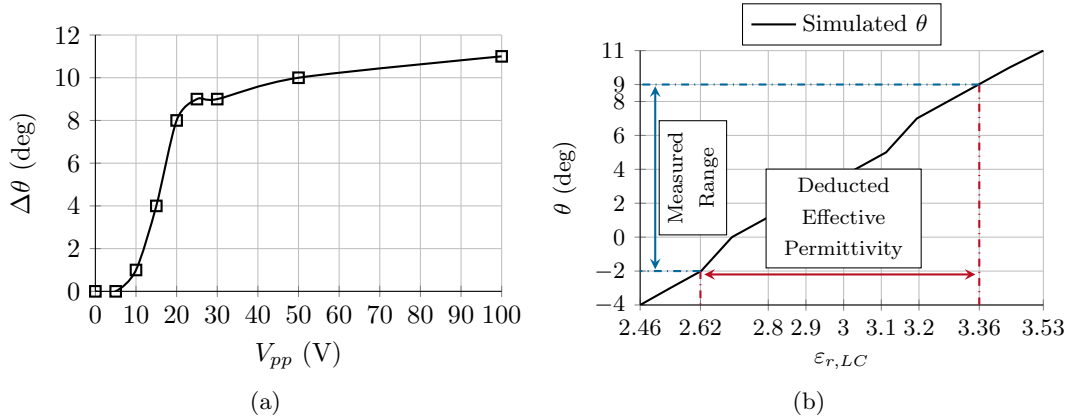


Figure 5.31: (a) Measured beam steering angle versus applied bias voltage, and (b) deduced uniform LC permittivity by mapping the measured beam steering angle to simulated values at different  $\varepsilon_{r,LC}$ . Both plots are at 90 GHz.

## 5. Beamsteering Liquid Crystal Dielectric Image Line Antennas

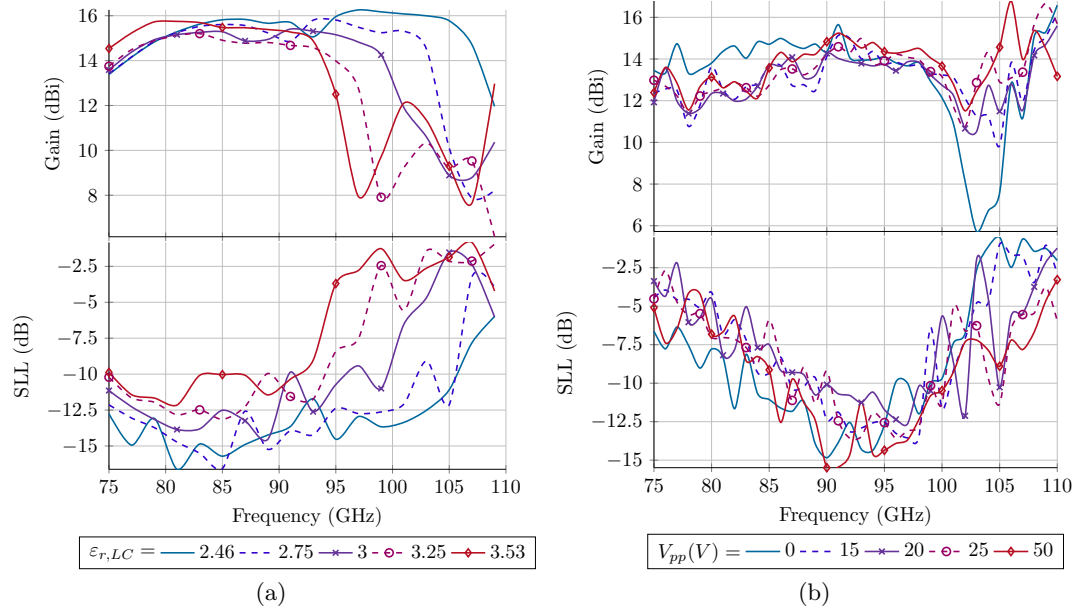


Figure 5.32: (a) Simulated and (b) measured gain and SLL at W-band.

are acceptable, with minor exceptions due to ripples in the main lobe. Good antenna patterns are still achievable at 100 GHz [Tes+22b]. The reduction in maximum frequency by tuning is not an issue, if narrowband operation or a lower frequency range, e.g. from 80 GHz to 90 GHz, is aimed for. If higher  $\Delta\theta$  is strived for, the width of the LC cavity should be increased. Simulations show that increasing the width from  $w_{LC} = 1.25$  mm (used for this demonstrator) to e.g.  $w_{LC} = 1.5$  mm increases  $\Delta\theta$  by  $2^\circ$ . Hence, a slight redesign of the DIL, to a wider general width and a wider cavity can be a suitable improvement. Adaptations in cross-section and UC shape allow a high degree of freedom for designing an LC-LWA for the desired frequency range, with the desired scanning capabilities, both with frequency and LC permittivity.

### Comparison of LC-LWAs

The presented LC-LWA demonstrator at around 90 GHz is up to now the only practically proven reconfigurable LC-LWA at this frequency range. By undergoing the full cycle of design, fabrication and microwave characterization, practical limitations and challenges have been identified, such as limited LC tunability and assembly of the demonstrator. The pure frequency scanning Rexolite demonstrator is a capable LWA which can scan thorough broadside without significant reduction in gain. In contrast to the LC-DIL phased array (Section 5.1.3), only one LC cavity has to be filled in the LC-based LWA, which eases fabrication tolerances, and only one voltage is directly linked to a beam steering angle. A translation to higher frequencies enables higher absolute bandwidths, less LC in the cavity, and less bias voltage to be applied. Even though there is no realized LC-LWA to compare to at around

100 GHz, Table 5.5 serves as an orientation to compare the proposed demonstrator to existing LC-LWAs at lower frequencies, or solely simulated approaches. Especially at higher frequencies, simulations can predict excellent behavior, but lack the assessment of practical limitations, e.g. by complex assembly and high sensitivity to tolerances. The very recent publications highlight the interest in LC beam steering LWAs, and a broad interest is present in conventional topologies such as microstrip lines at lower frequencies. The proposed demonstrator shows moderate scanning capabilities, which can be extended by LC-mixtures of higher anisotropy, adapted UC design, or a reshape of the underlying DIL cross-section. Due to the good material parameters of LC, and the easy scaling of the DIL topology to higher frequencies, an extension of the LC-LWA to those higher frequencies is possible. Overall, the rather simple layout of DIL LC-LWAs allow easy means of providing beam steering for a fixed frequency. This is a high advantage, since the antenna can be mounted on existing PCB layouts, as long as there is free space on the ground plane/top layer of the PCB. Hence, very cheap designs are possible, without multilayer approaches in order to include LC cavities, or special glass substrates.

## 5. Beamsteering Liquid Crystal Dielectric Image Line Antennas

Table 5.5.: Comparison of different LC-LWAs. If the topology is marked with an asterisk (\*), the results are only evaluated in simulations. Abbreviations: FPC - Fabry-Perot Cavity, GCPW - Grounded Coplanar Waveguide, MS - Microstrip Line, SIW - Substrate Integrated Waveguide, OSM - Open Stopband Mitigation.

Topology	$f$ (GHz)	# Elements	Scan ( $f$ )	Scan (LC)	Gain (dBi)	SLL (dB)	OSM	Ref.
MS	9.3 to 10.4	8	40°	25°	5.2 to 7.5	-5 to -11	n.a.	[SFW22]
SIW	10.1	43	n.a.	120°	8.5 to 12.5	-5 to -11	n.a.	[KN21]
MS	11.85 to 12.55	8	40°	22°	3.2 to 4.5	-5 to -6	no	[Ma+20]
MS	26 to 30	32	n.a.	14°	n.a.	<-10 at 26.7 GHz	no	[Roi+15]
MS*	25.85	5	n.a.	52°	9	<-10	no	[Tor+22]
GCPW*	37 to 44	40	80°	35°	$D = 18$	<-18	yes	[Fool19]
DIL	85 to 102	24	40°	10°	15	around -10	yes	Sect. 5.2.2
FPC*	560	-	n.a.	20° to 30°	$D = 15.5$	-5 to -10	yes	[Fus+17]

## 6. Towards Additively Manufactured Liquid Crystal Dielectric Image Line Components

Throughout the last chapters, manual assembly with the help of adhesives (sealing of filling holes, mounting on ground plane) contributed to varying performance of the proposed demonstrators. Hence, these chapters mark the limits of manual realization of the discussed components. If DIL (LC) components should be employed in practical applications, they need to be manufactured industrially. This enables a higher precision in fabrication through the automation of the manufacturing process, enabling even higher operating frequencies by miniaturizing the presented components. A promising manufacturing process is additive manufacturing (AM), which can provide sealed cavities in dielectric components, which do not need to be closed by an additional substrate as in the previous sections. There are many different general types of AM for polymers, such as Powder Bed Fusion, Material Extrusion (MEX), Material Jetting, or Vat Photopolymerization (VPP). AM has often been suggested as a suitable manufacturing technology for LC-DWGs, but many printable materials show poor mmW performance, due to high material loss [Jos18; Ree20]. In this dissertation, MEX and VPP have been tested for their suitability for LC-DIL components with different low-loss materials. Both technologies show specific advantages and disadvantages, which will be discussed in the next sections.

### 6.1. Material Extrusion for Low-Permittivity Components

In order to be able to transfer the concepts from the previous chapters directly, MEX for low permittivity components is investigated first. The results in this section have been obtained in cooperative work with the Lehrstuhl für Hochfrequenztechnik (LHFT) of the Friedrich-Alexander-Universität Erlangen-Nürnberg (FAU). For MEX, the raw material - either granulate or filament - is heated, such that special forms or layers can be deposited. A well-known MEX process is Fused Deposition Modeling. Since the granulate/filament needs to be heated to a viscous form before being deposited, only thermoplastics can be used for this process. In addition, their permittivity needs to be of similar values as the LC ( $\epsilon_r \approx 2$  to  $3$ ). Both, Zeonex RS420 and Creamelt COC, characterized in Section 3.2 and in [Cas+17], are suitable components. HDPE is not investigated, since it does not show stable printing properties [Dis+19]. Zeonex is a good candidate for DWGs, as shown in [Dis+19];

## 6. Towards Additively Manufactured Liquid Crystal Dielectric Image Line Components

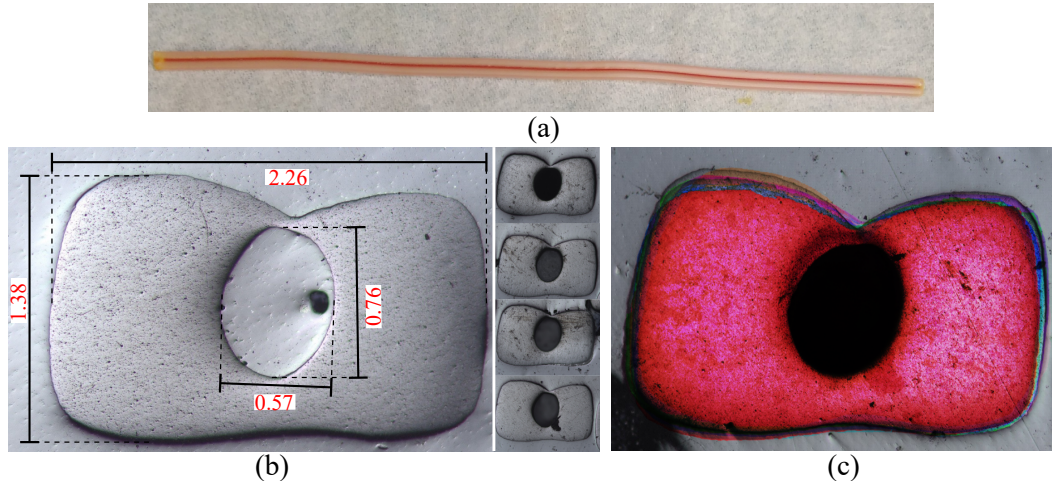


Figure 6.1: (a) Extruded DWG, filled with a colored LC and sealed at its end. (b) Multiple microsections along a 1 meter long extruded line, dimensions in millimeter. (c) Overlay of seven differently colored microsections to highlight deviation areas. Microsections from [Tes+21a] ©2021 IEEE and provided by the LHFT.

Dis20], where different cross-sections of the extrusion nozzle directly lead to DWGs of different cross-sections. Continuing with these results, first feasibility studies have been conducted in a fully dielectric layout without a ground plane [Tes+21a]. The extrusion nozzle is of rectangular cross-section and has a centered pin, which leads to a cavity in the extruded DWG, as no material is deposited at the pin's position. The cross-section of the rectangular nozzle is  $w \times h = 2.35 \text{ mm} \times 1.3 \text{ mm}$ , and the central pin has a diameter of  $D = 0.7 \text{ mm}$ . The DWG is filled with a syringe by pumping LC into one end of the line, until the LC exits at the opposite end of the DWG. Since the dielectric is a thermoplastic, the ends can be easily sealed, e.g. by a soldering iron or a hot blade. Fig. 6.1 shows an LC-DWG filled with a colored low-performance LC, various cross-sections of an extruded Zeonex DWG at different positions along a 1 m long printed line, and graphically illustrates the deviation of the cross-sections from each other. Slight differences with respect to the nozzle's dimensions are present, and deviations of the different microsections in the tens of millimeters are observed. Different lengths can be extruded such that the multi-line method from Section 3.1.2 can be applied to extract the attenuation coefficient  $\alpha$ . To be compatible to previous results, the waveguide transition from [DSV18b] is used. The measurement setup for electrical bias is shown in Fig. 6.2. In order to achieve a length difference which provides reliable results for  $\alpha$ ,  $\Delta l = 122 \text{ mm}$  is chosen, which requires the long electrode setup visible in Fig. 6.2. Due to the high electrode distance in the setup, a high voltage of  $V_{pp} = 500 \text{ V}$  is necessary to bias the LC-DWG. Fig. 6.3 (a) depicts the extracted attenuation coefficient  $\alpha$  by the technique discussed in Section 3.1.2. The filling of LC leads to a much higher  $\alpha$  than the empty

### 6.1. Material Extrusion for Low-Permittivity Components

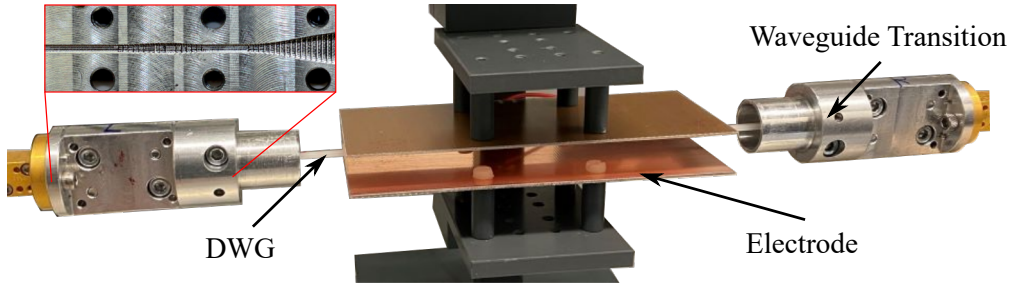


Figure 6.2: (b) Measurement setup for electrical bias. The inset picture shows the inside of the waveguide transition [Tes+21a] ©2021 IEEE .

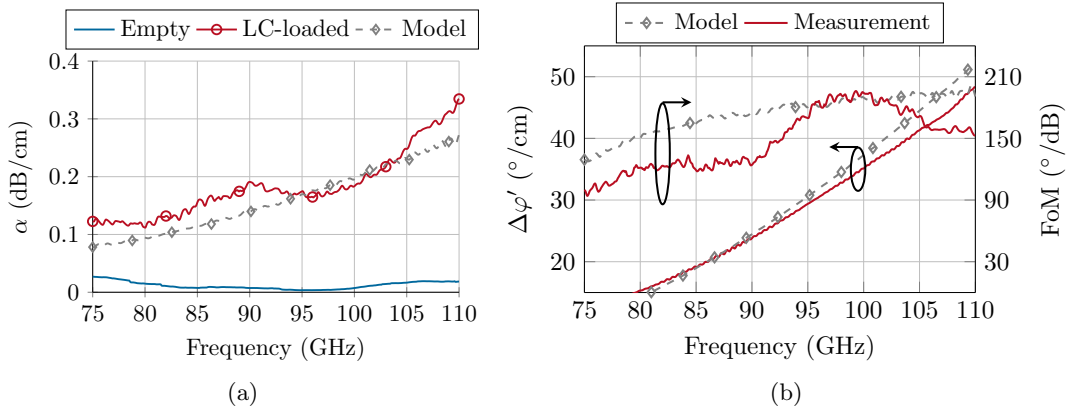


Figure 6.3: (a) Extracted attenuation coefficient  $\alpha$  for an empty and LC-filled (GT7-29001) DWG. The highest loss of each LC alignment state is summarized to the curve for the LC measurement. (b) Achieved differential phase shift per cm ( $\Delta\varphi'$ ) and obtained FoM using  $\alpha$  from (a).

waveguide investigated in [Dis+19]. The results of a simulation model, which takes the realized cross-section and elliptical hole (Fig. 6.1) into account, are included in the plot. The achievable phase shift and FoM is shown in Fig. 6.3 (b), where the phase shift is normalized to cm. A 7.2 cm long waveguide is necessary to achieve  $\Delta\varphi = 360^\circ$  at 110 GHz. Compared to the phase shifters introduced in Section 4.1.2 and Section 4.2, this is rather long, and is caused by the comparably low cavity size of the additively manufactured waveguide. For comparison, the area of the elliptical hole is  $0.34 \text{ mm}^2$ , while the rectangular area, e.g. of the  $E_{11}^y$ -mode LC-DIL phase shifter from Section 4.1.1, is  $1.28 \text{ mm}^2$ . If the cavity size can be increased while maintaining the same cross-section of the overall DWG, shorter waveguides with higher absolute phase shift can be realized, but at the expense of an increased  $\alpha$  [Tes+21a].

For DIL structures, a fabrication by partwise direct extrusion and partwise layer-based fabrication process can be employed. Unfortunately, Zeonex proved to have ad-

## 6. Towards Additively Manufactured Liquid Crystal Dielectric Image Line Components

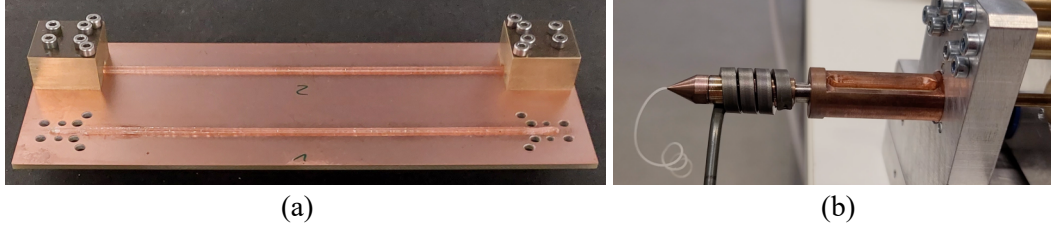


Figure 6.4: (a) First line structures directly printed on FR4 substrate. (b) Test of a heated nozzle head with 200  $\mu\text{m}$  opening diameter at the LHFT.

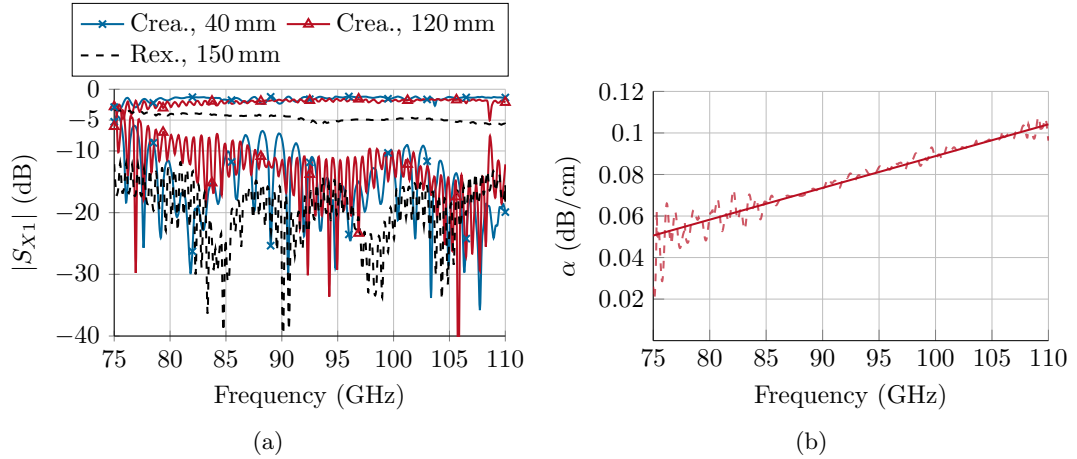


Figure 6.5: (a) S-parameters of different lines, including a reference measurement of Rexolite (mounted with adhesive, Section 3.1.2). (b) Simulated attenuation constant (raw - dashed, fit - solid) of the Creamelt lines.

hesion problems on metallic surfaces. Hence, the material was changed to Creamelt, which is of similar permittivity and loss tangent (c.f. Fig. 3.15 in Section 3.2). In addition, the fully metallic brass ground plane is switched to a copper-clad FR4 substrate, such that the heat during the fabrication process dissipates slower and the environment of a PCB is emulated. For manufacturing, the substrate is heated up to 90  $^{\circ}\text{C}$ , a temperature conventional electronics usually are able to withstand. In order to adhere properly on the copper cladding, a pre-treatment of the surface is necessary right before depositing the material. By the time of this dissertation, first tests of DILs without an LC cavity have been conducted. For layer-wise creation of a DIL with LC cavity, small feature sizes of down to 100  $\mu\text{m}$  are necessary for the  $E_{11}^y$ -mode phase shifter (Section 4.1.1). Thus, very small extrusion nozzles are necessary. For a nozzle diameter of 50  $\mu\text{m}$  very high pressure, equivalent to the weight force of about 2t needs to be applied to press the heated viscose dielectric through the nozzle head. The necessary modifications of the 3D-printers at the LHFT are still in progress. First results of line structures have been acquired, and are measured with the transitions introduced in Section 3.3, which are optimized for the slightly differ-



ent permittivity of Rexolite 1422. Fig. 6.4 shows the first test structures of Creamelt DILs directly printed on the top layer of copper-clad FR4. For these structures, a conventional extrusion nozzle with a diameter of 1.6 mm is used. Fig. 6.5 (a) shows the measured S-parameters of two printed lines compared to a manually assembled Rexolite line. Due to the optimization of the transition to Rexolite, better matching is achieved for this material. In addition, the big extrusion nozzle does not allow to precisely fabricate the necessary width in the waveguide transition and the taper. To ensure fitting of the transition on the DIL, slight mechanical post-treatment had to be applied to these line sections. Hence, matching of the Creamelt lines is in general worse than for Rexolite lines. Nonetheless, good first results are achieved, and show the potential of MEX for DIL components. Since printing space of the available printers is limited, Creamelt lines of maximum length  $l = 140$  mm can be realized. Therefore, a maximum line length difference  $\Delta l = 80$  mm is available for the multi-line based extraction of the attenuation coefficient  $\alpha$ . Due to different behavior of each individually modified line in the transition, and extremely low loss, unreliable data for  $\alpha$  of the printed line has been obtained so far. The accuracy of  $\alpha$  can be increased if higher  $\Delta l$  can be realized, and the loss starts to be dominated by the actual difference in line length, and not by the transitions [Dis20]. The latter is still present with the measurements of  $|S_{21}|$  of the Creamelt lines, as they show almost identical behavior. The little difference and good overall performance of  $|S_{21}|$  of the Creamelt lines is also due to the surface roughness of the copper cladding on the FR4 substrate, which is in the range of an RMS of only  $0.2 \mu\text{m}$  to  $0.3 \mu\text{m}$ . Good performance of  $\alpha$  can be estimated to range from  $0.06 \text{ dB cm}^{-1}$  to  $0.14 \text{ dB cm}^{-1}$  (from 75 GHz to 110 GHz), see Fig. 6.5 (b). These first promising results highlight the high potential in MEX for DIL components with possible LC-integration, and effort in the refinement of the fabrication process is steadily investigated by TU Darmstadt and FAU Erlangen-Nürnberg in the ongoing DFG proposal JA921/68-2.

## 6.2. Stereolithography for High-Permittivity Components

In order to increase component density, higher  $\varepsilon_r$  than 2 or 3 needs to be used for the DIL components. The main problem is that values of e.g.  $\varepsilon_r \approx 10$  are not suitable for LC-integration using the classic core-cladding approach with total internal reflection of dielectric waveguides. This problem can be circumvented if a different guiding structure is chosen. A possible approach is the slotted waveguide from the optical regime, first introduced in [Alm+04] and further investigated in [NMK06] and [Jah+18]. Crossovers with slotted DWGs can show high transmission efficiency, due to low radiation, crosstalk and reflection loss [Su+11]. For a slotted waveguide, a central air-slot is introduced into a dielectric of higher permittivity, e.g.  $\varepsilon_r \approx 10$ . If it is of rectangular cross-section, this waveguide type is referred to as the slot rectangular waveguide (SRW). In general, the inclusion of a slot can also be in horizontal direction, such as in the dielectric microstrip line [Zhu+18], or in the integrable Lay-

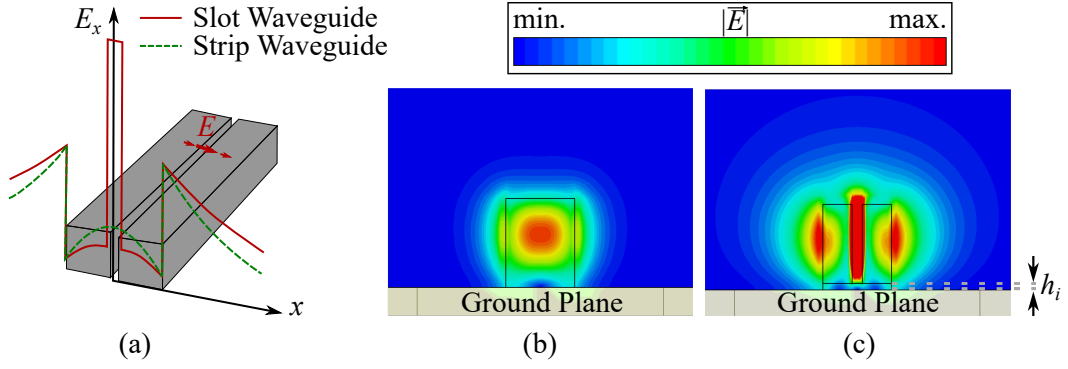


Figure 6.6: (a) Model of the SRW and the difference of its qualitative  $E$ -field profile in  $x$ -direction (solid) compared to a standard solid waveguide (dashed) [Jah+18]. (b) Simulated modal profile of the average electric field along the cross-section of a standard  $E_{11}^x$ -mode DIL and (c) an SRW. Both lines have  $\varepsilon_r = 10$ ,  $w \times h = 1 \text{ mm} \times 1.27 \text{ mm}$ , and the SRW has an additional insulation layer of  $\varepsilon_r = 2.53$  with  $h_i = 0.1 \text{ mm}$  and a slot width  $w_s = 150 \mu\text{m}$ . Both field views are at 92.5 GHz.

ered Ridge Dielectric Waveguide [PDK96]. The modal profile of a DIL-SRW and its field profile compared to a conventional  $E_{11}^x$ -mode DIL is shown in Fig. 6.6. Guidance of the EM wave in the low-permittivity slot is achieved by the sandwich structure of the SRW. Since the normal component of the dielectric displacement  $\vec{D}$  needs to be equal at the boundary of two materials, the corresponding normal component  $E_n$  of the  $E$ -field needs to satisfy the boundary condition

$$D_{n,1} = \varepsilon_0 \varepsilon_{r,1} \cdot E_{n,1} = \varepsilon_0 \varepsilon_{r,2} \cdot E_{n,2} = D_{n,2}, \quad (6.1)$$

with  $n = 1, 2$  representing medium 1 (dielectric of the waveguide) or medium 2 (slot, usually air). Hence, at the boundary, the  $E$ -field has a discontinuity, given by the ratio of  $E_{n,2}$  to  $E_{n,1}$

$$\frac{E_{n,2}}{E_{n,1}} = \frac{\varepsilon_{r,1}}{\varepsilon_{r,2}}. \quad (6.2)$$

Assuming  $\varepsilon_{r,2} = 1$  for air surroundings, the  $E_{n,2}$  is scaled by  $\varepsilon_{r,1} \cdot E_{n,1}$ . This is always the case, and is also true for the outer sides of the SRW where the field exponentially decays. In the slot, two of these discontinuities are close by and the field profiles overlap. As they add, they form a high field strength within the slot. An  $E_{11}^x$  modal profile is chosen in the following sections, since this mode shows low conductor loss and a vertical slot is easier to produce and to fill with LC afterwards. The ground plane serves as the mechanical anchor to hold the SRW in its place. This is an advantage over fully dielectric setups, since the continuous slot destabilizes the waveguide [NMK06]. First experiments in translating this concept to the mmW-regime, both with simulations and measurements, have been conducted with an air slot, which

## 6.2. Stereolithography for High-Permittivity Components

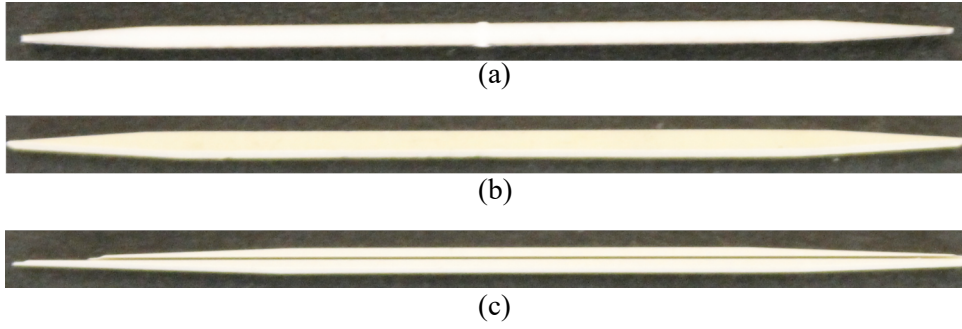


Figure 6.7: Fabricated high permittivity DILs in  $E_{11}^x$  mode. (a) Alumina DIL, (b) TMM10 DIL and (c) TMM10 SRW. Each rod has a tip-to-tip length of 48 mm and the same cross-section of  $w \times h = 1 \text{ mm} \times 1.27 \text{ mm}$ .

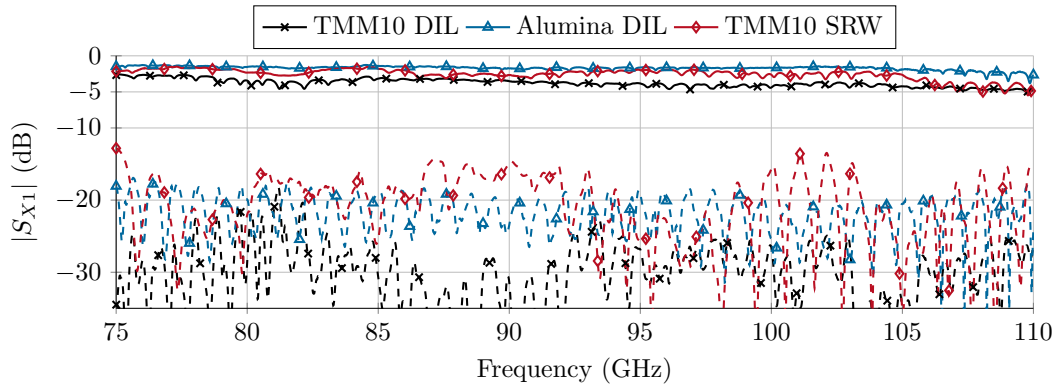


Figure 6.8: Measured  $|S_{11}|$  (dashed) and  $|S_{21}|$  (solid) of the lines shown in Fig. 6.7, including a hollow waveguide to DIL transition.

has to be filled with LC afterwards. The optimal slot width  $w_s$  can be determined with simulations: a slot which is too narrow contains only little power, and a very broad slot compromises the working principle of overlapping evanescent fields. Simulations show that an air slot inside a DIL of  $w \times h = 1 \text{ mm} \times 1.27 \text{ mm}$  should be between  $150 \mu\text{m}$  and  $200 \mu\text{m}$  to guide about 40% of the total power solely in the waveguide's slot. The dielectric material guides an additional 40% of power, while the remaining 20% propagate in the form of evanescent fields. These dimensions are optimized for an operation range of frequencies from 85 GHz to 103 GHz. Simulations show that by concentrating the  $E$ -field in an air slot of  $150 \mu\text{m}$ , the dielectric loss compared to a solid DIL decreases by 30%. In order to ease fabrication and assembly tolerances, and allow the propagation of the  $E_{11}^x$ -mode at lower frequencies, a  $100 \mu\text{m}$  thin isolation layer consisting of Rexolite 1422 is inserted between the SRW and the ground plane [Kno76; GWD82]. Fig. 6.7 shows three demonstrators for high permittivity DILs: two are regular  $E_{11}^x$ -mode DILs consisting of Rogers TMM10 ( $\epsilon_{r,TMM} = 9.2$ ,  $\tan \delta_{TMM} = 0.002$  [Coo]) and Alumina (99.6%,  $\epsilon_{r,Alu} = 9.4$ ,

## 6. Towards Additively Manufactured Liquid Crystal Dielectric Image Line Components

$\tan \delta_{Alu} = 0.0003$  [Raj+08]), respectively, and one is an SRW consisting of TMM10. Both materials are very hard, which makes processing by means of subtractive manufacturing a challenging task. The Alumina DIL is cut from Alumina sheets by a laser, and the TMM10 components are cut with a Disco DAD-341 dicing saw from TMM10 sheets. Hence, this approach comes with the limitation of processable sheet thickness. The most challenging problem is to create a slot, which is realized by a very thin saw blade of  $150 \mu\text{m}$  width, hence fulfilling the slot width exactly. However, no transition between a non-slotted DIL to the slotted part is possible with this fabrication approach, as the saw blade does not allow any tapered structure of the slot. As a result, the slot of the TMM10 SRW is continuous from one end to the other of the DIL, causing fragile taper tips (see Fig. 6.7), which can break and in turn degrade matching. Excitation of the structures is performed by an adapted waveguide transition of those from Section 3.3. These pre-study results are summarized in Fig. 6.8. The TMM10 DIL shows highest IL, even though it is the best-matched DIL of the three lines. Despite the damaged taper tips of the SRW, the slotted waveguide shows almost similar performance as the Alumina waveguide at frequencies where  $|S_{11}|$  is similar, even though the loss tangent of Alumina and TMM10 differs by a factor of 10. By concentrating the field in the slot, about 1 dB to 2 dB less IL than a solid TMM10 DIL is achieved. This technique can lead to high performance waveguides even if dielectrics of moderate  $\tan \delta$  are employed.

Nonetheless, conventional subtractive methods do not allow any transition from a slotted to a non-slotted part, and can not include taper structures for matching the slot-discontinuity to a solid waveguide. Alumina can be additively manufactured, e.g. by Stereolithography (SLA) and an additional sintering process. First non-reconfigurable mmW and sub-THz components have been successfully realized

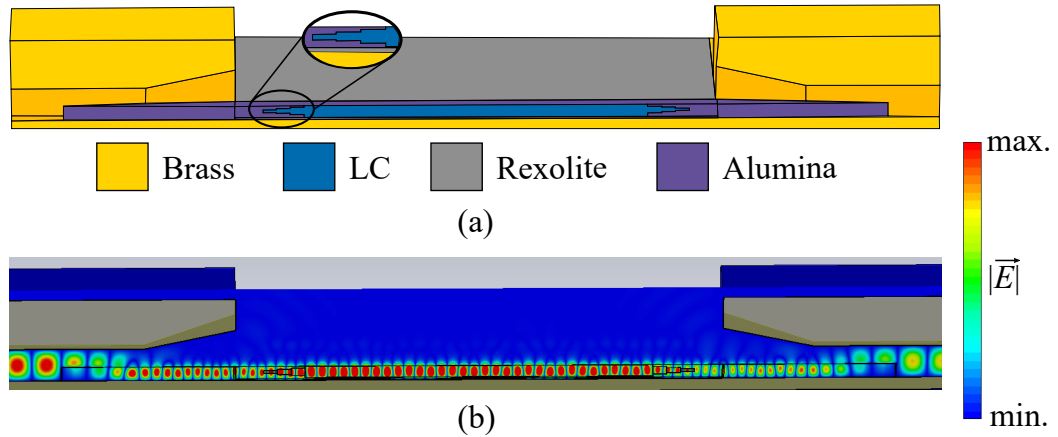


Figure 6.9: (a) Simulation model with a longitudinal cut along the SRW with an LC cavity, including two simplified waveguide transitions. (b) Instantaneous field view at 92.5 GHz.

## 6.2. Stereolithography for High-Permittivity Components

by additive manufacturing, e.g. in [Jim+19; Kad+22]. The Alumina components are manufactured at the Institute of Technology for Nanostructures of the University of Duisburg-Essen. With this technique, a viscose photopolymer ("slurry") is layer-wise selectively polymerized by a laser. After the polymerized component is finished, it is sintered. During this process, shrinkage of the component occurs, which has to be taken in account by upscaling of the physical size of the initially printed component. Fig. 6.9 shows a longitudinal cross-section of the simulation model of a first demonstrator for an additively manufacturable DIL LC-SRW phase shifter. In order to allow the undesired slurry to leave the slot, its upper side is open, but enclosed tapers are present at this demonstrator. Future refinement of the fabrication process can allow fully closed cavities. The whole LC cavity is  $l_{LC} = 20$  mm long, with two 3 mm long stepped tapers, shown in a magnified view in Fig. 6.9 (a). The taper steps are each 1 mm long and have heights of 0.2 mm, 0.4 mm and 0.6 mm, before the final slot height of 0.9 mm is reached. In order to address the permittivity difference between air and LC, the slot is  $w_s = 200$   $\mu\text{m}$  wide, i.e. 50  $\mu\text{m}$  wider than the air slot.

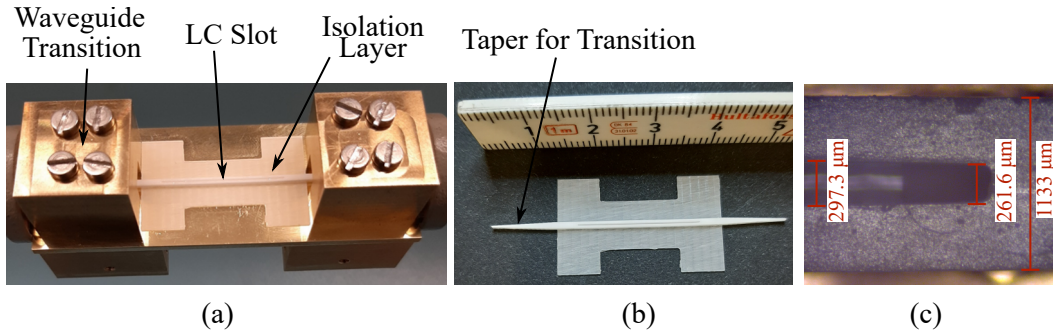


Figure 6.10: Fabricated components. (a) Measurement setup, (b) printed Alumina LC-SRW mounted on Rexolite isolation layer, and (c) microscopic picture of the beginning of the printed slot.

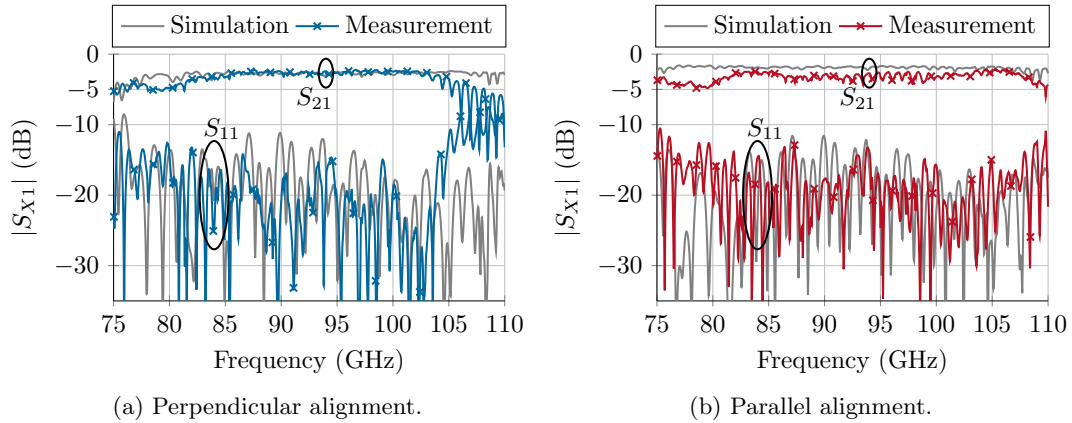


Figure 6.11: Measured S-parameters for different LC alignment states.

## 6. Towards Additively Manufactured Liquid Crystal Dielectric Image Line Components

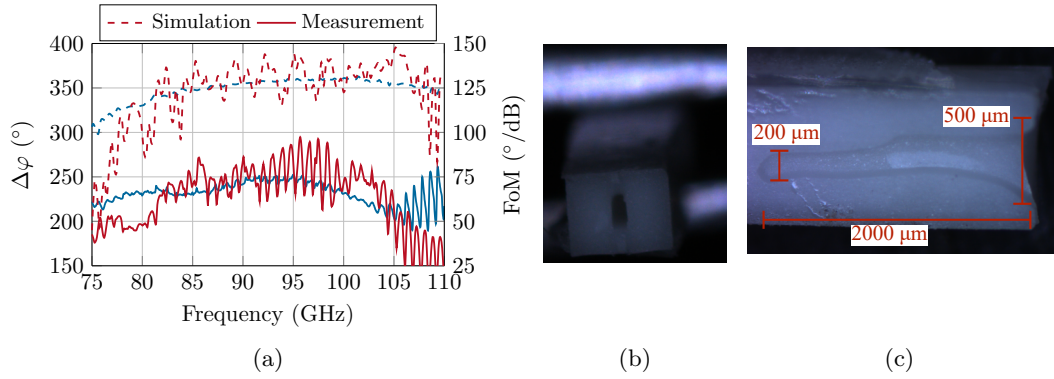


Figure 6.12: (a) Simulated (dashed) and measured (solid)  $\Delta\varphi$  (blue) and FoM (red). (b) Front view on the beginning of the internal taper. (c) Side view into the internal taper, cut open with a dicing saw.

Fig. 6.10 shows the fabricated components. The Rexolite isolation layer is milled such that it has a 100  $\mu\text{m}$  thick layer in the center, but 300  $\mu\text{m}$  thick sides for better mechanical stability and better handling when positioning the waveguide and the transitions. The SRW is glued into the channel of the isolation layer. After filling LC into the slot, the SRW is placed in an evacuation chamber for 30 minutes, to remove any air bubbles trapped in the taper tips and the structure is afterwards adhered to the ground plane. The measurement results for magnetic bias are displayed in Fig. 6.11 and Fig. 6.12 (a). Slight differences and ripples in parallel alignment are observed, which cause ripples in the extracted FoM. Nonetheless,  $|S_{21}| \approx -2.5 \text{ dB}$  is achieved, including the loss of the waveguide transitions. The FoM reaches a peak value of  $97^\circ \text{ dB}^{-1}$ , and will show more smooth and higher results, if manufacturing and assembly processes become more sophisticated. The results shown in Fig. 6.11 and Fig. 6.12 (a) are the best achievable results at the time of writing this dissertation. In the fabrication process, the slot width and deformed internal tapers are the main challenges to overcome (c.f. Fig. 6.10 (c) and Fig. 6.12 (c)), as they do not match the originally designed dimensions. Furthermore, manual mounting is still necessary, and slight misalignment affects more critically DILs with higher permittivity than low-permittivity DILs.

Even with these challenges, the demonstrator proves the innovative concept of combining high permittivity and LC for the first time. Electrodes similar to the setups in the previous chapters can be employed for an all-electric bias. With the advancement of reliable additive manufacturing of Alumina cavities, and an automated mounting procedure, LC-SRW components will be able to unfold their full potential for compact LC-DILs. Due to the inherent loss of the waveguide transitions in Fig. 6.11, the IL of the standalone component is lower, and hence, the FoM is higher.

### 6.3. Comparison and Discussion

Two different AM techniques have been tested for their feasibility of realizing LC-DIL structures. MEX has the advantage that it is a simple, cost-efficient technique, and materials with favorable micro- and millimeter-wave characteristics are available which match the general permittivity range of LC. Due to their low permittivity, the components introduced throughout this dissertation can be realized if the extrusion process is refined. The biggest challenge is the thin nozzle opening, which requires high pressure for extrusion of the viscose material, such that fine feature sizes can be realized. Good, direct adhesion on the ground plane could be achieved, which eliminates the use of glue. Hence, direct printing on an RF-PCB is possible and allows fast realization of conventional circuitry with innovative new dielectric (image line) components. Even without the inclusion of LC, inexpensive components, e.g. LWAs, can be produced by metallizing the extruded DIL by printing metallic ink with inkjet printers directly on the DIL component.

SLA offers the possibility to create LC-DIL components of higher permittivity. Since many high permittivity materials are hard to process mechanically, e.g. by milling, SLA proves to be a very good alternative for realizing Alumina components at mmW and beyond. Due to a novel combination technique of LC and high permittivity materials, smaller LC-components which are compatible to designs in silicon could be possible. The main challenge of these new components is the fabrication of enclosed cavities of small feature size. In the sintering process, which is time and energy intensive, deformations still need to be overcome. In addition, the demonstrator in this dissertation still requires manual mounting on a ground plane, which can introduce additional uncertainties. In fully dielectric setups, SLA could prove to be better suited for LC-integration, until more reliable assembly for high permittivity LC-DIL components is achieved. Alumina LC-DILs can provide higher integration density, since the components have smaller feature sizes and cross-sections, while they can provide higher Q-factors.

In light of the above, MEX can enable very cheap mmW components for fields of application where cost is a key factor, e.g. in the automotive industry. SLA is more expensive and is likely to be chosen for high quality components with high integration density.





## 7. Conclusion and Outlook

In order to satisfy the demand for increasing data rate and bandwidth in our rapidly digitizing society, innovative solutions for reconfigurable components at millimeter waves (mmW) are necessary. Conventional technology at higher mmW frequencies faces increased loss in waveguides and free-space, which has to be overcome. Reconfigurable components offer adaptation to the challenges linked to increasing frequency of operation. This work demonstrates the capabilities of novel, reconfigurable dielectric image line (DIL) components based on liquid crystal (LC). The W-band (75 GHz to 110 GHz) serves as the frequency range at which the concepts are developed and practically evaluated. It is shown that LC-DIL components combine advantages from fully dielectric waveguides with their low profile to form PCB-compatible mmW components with lower bias voltage requirements. A material study forms the basis of the investigation of the components, utilizing the Nicholson-Ross-Weir method. A flexible measurement setup is employed, such that different DIL components can be analyzed. The components are mounted on brass plates and different rectangular-waveguide-to-DIL transitions are connected to the respective demonstrators. Besides components in the fundamental  $E_{11}^y$ -mode, components are also investigated in the orthogonally polarized  $E_{11}^x$ -mode. The two necessary waveguide transitions are characterized in their contribution to loss in a full measurement setup, and the reduced sensitivity of the  $E_{11}^x$ -mode to surface roughness is practically verified. With basic knowledge of the transition's influence on measurements, the following key aspects have been investigated in this dissertation:

### 1. Performance analysis of LC-DIL phase shifters at W-band:

For the first time, DILs are combined with LC. Due to smaller cross-section in  $E_{11}^y$ -mode, less LC is necessary than compared to fully dielectric waveguides. It is pointed out that especially the parallel alignment of LC is crucial for the device performance: small deviations in alignment can lead to high fluctuations in the effective permittivity of the waveguide, which causes reduced phase shift. By characterizing the temperature-dependent change in performance of an  $E_{11}^y$  phase shifter, good linear behavior of the component in embedded environments is demonstrated. With the ground plane, active cooling can be included for LC-DIL components. The differences of  $E_{11}^x$ - and  $E_{11}^y$ -mode phase shifters in terms of electrode design, response time, and RF-performance is investigated and compared. By utilizing the DIL topology, the response times compared to LC-DWG phase shifters could be reduced by 47% to 65% to a range of 6 s to 9 s with a bias voltage of  $V_{pp} = 200$  V. By integrating the electrodes directly on the dielectric, the smallest possible switch-on time could

## 7. Conclusion and Outlook

be further decreased to 134 ms, which corresponds to a reduction by 99% and 97% compared to LC-DWG and the aforementioned LC-DIL phase shifters, respectively. The necessary voltage for the maximum phase shift compared to an LC-DWG could be reduced by 29%, from 70 V to 50 V. This approach is the only way of achieving comparably fast response time on voluminous dielectric LC-components, and the very recent publication of an LC-DWG [Hu+22] supports this conclusion. By comparing the demonstrators of this dissertation to various other LC mmW phase shifters, high performance LC-DILs, with FoMs of up to  $188^\circ \text{ dB}^{-1}$  can be achieved, while integration on PCB top layers can be ensured and allow for complex systems of different waveguide topologies.

### 2. Capabilities of beam steering LC-DIL antennas at W-band:

In order to address the high demand for mmW beam steering antennas, DIL antennas are tested for their capabilities of LC-based beam steering. A broadband and a narrowband approach are pursued: DIL rod antennas are analyzed first on their single element behavior before non-reconfigurable  $1 \times 4$  arrays, both in  $E_{11}^y$ - and  $E_{11}^x$ -mode, are presented. Multimode interference (MMI), is for the first time employed to achieve power division in the DIL topology. It is demonstrated that,  $E_{11}^x$ -MMI is possible without mode conversion to the fundamental  $E^y$ -mode. Differences in MMI divider design are discussed, and a suitable phase compensation technique, which does not interfere with the sensitive interaction of rod taper length and ground plane length, is introduced for both modes. The arrays are capable antennas with gain from 21 dBi to 23 dBi for  $E_{11}^y$ - and  $E_{11}^x$ -mode, respectively and do not radiate to broadside, but have a tilt angle due to the ground plane. This angle can be exploited in certain scenarios to cover specific areas, such as in assembly halls or for data exchange with a commercial airplane when it is in parking position. This is particularly useful at mmW, where multipath propagation leads to severe loss of power, and efficient illumination of the area of interest is necessary. In  $E^y$ -mode, phase shifters with integrated electrodes are combined with the array to form a phased array. Operating from 95 GHz to 105 GHz, it shows gain of 17 dBi to 18 dBi and a moderate scanning range of  $\pm 10^\circ$  with side-lobe levels of maximally  $-7.5$  dB. With longer phase shifters, higher scanning angles can be achieved.

A more narrowband approach is tested with leaky-wave antennas (LWAs). They can cover a whole spatial sector with frequency scanning. By adding LC, this sector can be steered, which corresponds to a spatial shift for each fixed-frequency beam. Hence, reconfigurable LWAs are often investigated at a fixed frequency. In contrast, in this dissertation, the beam steering capabilities of the LWAs are evaluated for a wide frequency range instead of only at one favorable frequency. Hence, the broadband behavior of the developed LC-DIL LWAs is not neglected. Both, a frequency scanning solid Rexolite DIL-LWA and an LC-DIL LWA, capable of changing its spatial coverage sector by applying a

bias voltage, are introduced. The frequency scanning Rexolite DIL-LWA is a capable antenna which does not require complex manufacturing techniques. For the LC-DIL LWA, metallic structures, directly placed on the DIL, are serving simultaneously as a radiation element and as an electrode. By this novel approach, comparable response times to milliseconds, as with the investigated phase shifters, are expected and no additional bias network is necessary. The gain of the non-reconfigurable layout of 18 dBi is reduced to 14 dBi when adding LC to the antenna in order to make it reconfigurable. The frequency scanning behavior from  $-30^\circ$  to  $10^\circ$  can be turned by  $10^\circ$  when applying bias to the LC in the antenna. The demonstrator shows good performance from 85 GHz to 100 GHz, and a bandwidth of 0.714 GHz is available for each  $1^\circ$  step. Radiation through broadside without severe degradation in matching or gain is possible. This type of antenna is best suited for steering applications in which simplicity instead of high-performance complexity is preferred, since only one voltage is directly related to the beam steering angle. The antenna is cheap and simple in its realization, and marks the first practically verified antenna of its type at frequencies around 100 GHz.

### 3. Novel printing technologies for tunable LC-based low- and high-permittivity DIL microwave components:

Due to encountered tolerances during the assembly of the various demonstrators discussed in this dissertation, additive manufacturing is investigated as an alternative fabrication technique of high potential, together with the Lehrstuhl für Hochfrequenztechnik of the Friedrich-Alexander University of Erlangen-Nürnberg. First, material extrusion (MEX) is investigated, with the initial concepts being tested in fully dielectric designs. The problems of adhering different materials to a ground plane are taken account for, and the first DILs printed on a copper-clad FR4 board are introduced. MEX for DILs proves to be a promising, unique way of achieving DIL components on PCBs with discrete components already mounted on them. While there are still challenges considering the feature size of the extrusion nozzles, this promising approach for low-permittivity DIL components is still investigated in the ongoing research project of Deutsche Forschungsgemeinschaft (DFG), project number JA 921/68-2. Even without LC-integration, proposed structures, e.g. the non-reconfigurable LWA, could be fast and very cost-efficiently realized.

In order to increase integration density and enable smaller components, the first approach to combine LC with materials of higher permittivity has been introduced in this dissertation. By inserting a narrow LC slot in the high permittivity material, it is ensured that the LC still affects the propagating wave significantly. After first tests with air slots, the necessity of additive manufacturing became clear. Stereolithography (SLA) enables 3D printed Alumina components of low feature size. With the Institute of Technology for Nanostructures of the University of Duisburg-Essen, a first demonstrator was realized. It is of low loss and achieves FoMs close to  $100^\circ \text{dB}^{-1}$ . Besides good

## 7. Conclusion and Outlook

performance, there are still fabrication challenges to overcome, since enclosed cavities tend to become obstructed with SLA. The combination technique of high-permittivity dielectrics and LC is not limited to the DIL topology.

In summary, this thesis demonstrated the capabilities of LC-DILs for integrated reconfigurable components and devices, which are backed up by measurements. Challenges in realization of the components have been revealed, and practical limitations are identified. While the components at the covered frequency range of 75 GHz to 110 GHz can be comparatively big in geometrical size, due to the permittivity of the DIL, increasing the frequency of operation leads to smaller components. With smaller components smaller LC cavities are achieved, and hence, faster response times and less bias voltage. The higher the frequency of operation, the more favorable the  $E_{11}^x$ -mode becomes, due to its robustness to surface roughness. Due to their intrinsic simplicity, the DIL components can become cost-efficient assets, which still have favorable mmW characteristics. Many of those components are necessary in sensor networks and access stations, or if vehicle-to-everything (V2X) communication, i.e. connections to infrastructure, other vehicles or else, is to be employed in a large scale.

### Outlook

Besides the elimination of manual fabrication issues by additive manufacturing, DIL components have to be able to support the demands of complex RF-frontends. Since dielectric waveguides can be a suitable interconnect to different PCBs or sensors, e.g. in a car [Dis20], integrated transitions from different waveguide topology to the DIL topology need to be established. This includes transitions to fully dielectric waveguides and planar metallic waveguides. With growing complexity of the RF-frontend itself, DILs have to be able to enable complex routing. While Chapter 3.1.2 introduced the capabilities of enabling lower curvature radii, crossovers are especially necessary for established RF-networks, e.g. the Butler matrix [But61]. First investigations on integrated transitions and crossovers show promising results:

- In order to address more compact excitation, the hollow waveguide transitions can still be refined to a more sophisticated and minimized layout, but planar metallic waveguide transitions should be focused on, such that no component of high profile remains (e.g. on a chip). Since many chips utilize differential lines, a transition with differential planar feeding should be aimed for. A possible solution can be a slotline-to-DIL transition, where the DIL needs to be of high permittivity and operated in  $E_{11}^x$ -mode. The concept of the transition is illustrated in Fig. 7.1 and Fig. 7.2. The slotline shares the main E-field component in  $x$ -direction with the  $E_{11}^x$ -mode DIL. Hence, placing a dielectric above the slot allows portions of the field guided by the slot to transition to the DIL above. The higher the permittivity of the DIL, the higher the portion of the E-field within the DIL. In order to transfer the power smoothly

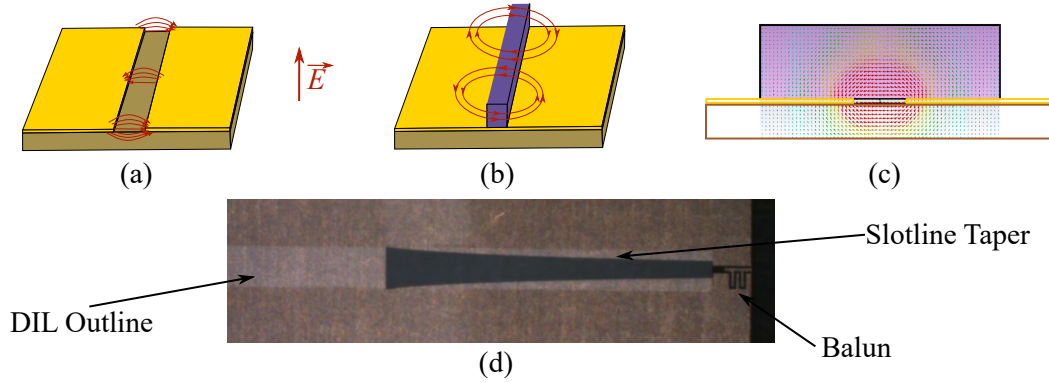


Figure 7.1: (a), (b) Representative E-field of a slotline and an  $E_{11}^x$ -mode DIL. (c) Simulated E-field distribution of a high permittivity DIL above a slotline. (d) Fabricated transition, including a Balun (CPW to slotline) and an exponential slotline taper. The DIL Outline is shown as a white shadow, produced by the camera system of the flip-chip machine, which was used to position and mount the DIL on the substrate.

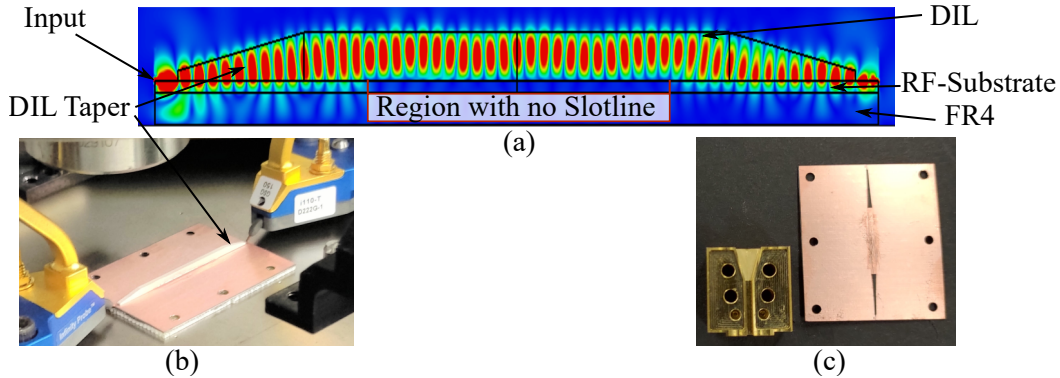


Figure 7.2: (a) Side view of the simulated instantaneous field view at 95 GHz inside a back-to-back setup of two transitions, with a pure DIL part without slotline at the center. (b) Practical measurement setup with a probing station. (c) Comparison of one hollow waveguide transition for the SRW (Section 6) and a back-to-back measurement setup of the planar transition.

from the slot to the DIL, the slotline is widened while the DIL is tapered in height. At the beginning of the transition, the DIL is of low height, which increases throughout the slotline taper. If a mode profile close to the  $E_{11}^x$ -mode is established in the DIL, a ground plane can be inserted to form a true DIL. Back-to-back setups have been tested both in simulations and measurements, utilizing TMM10. While results show that the concept is working, it still needs refinement, mainly due to assembly and adhesion issues.

## 7. Conclusion and Outlook

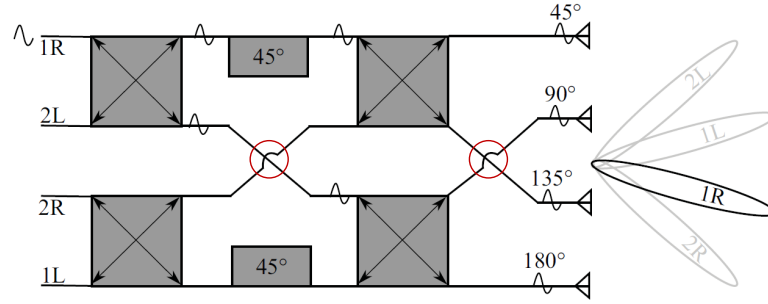


Figure 7.3: Schematic of a  $4 \times 4$  Butler matrix [Jos18]. Feeding at different ports results in different beam directions. The necessary crossovers are highlighted with red circles.

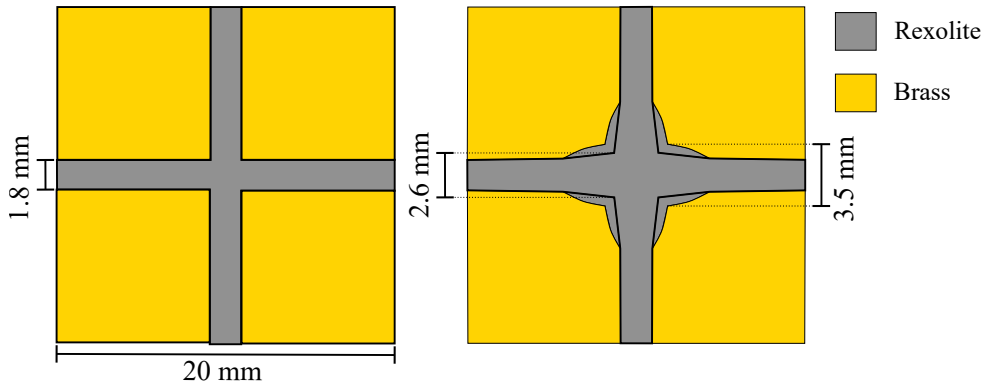
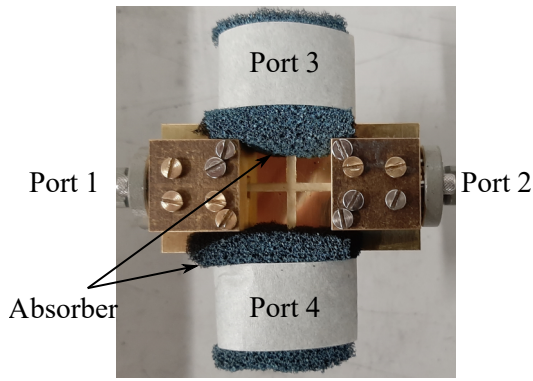
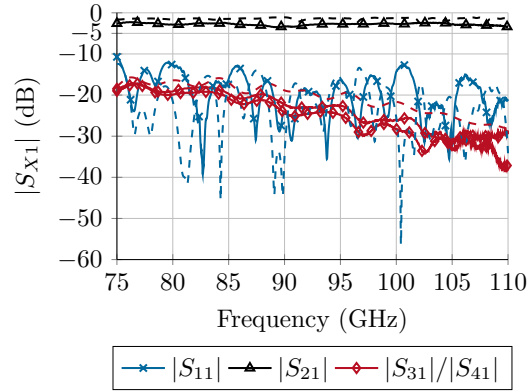


Figure 7.4: Top view on the layouts of the direct crossover (left) and expanded crossover (right) with same height  $h_{DIL} = 0.9$  mm. The elliptical expansions around the crossing are of height  $h_{exp} = 0.45$  mm.

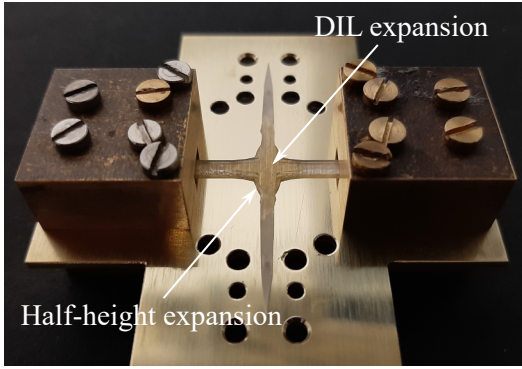
- Crossovers are key components for RF-frontends of growing complexity, e.g. for switched-beam antennas which rely on a Butler matrix [But61] as depicted in Fig. 7.3. Switched-beam antennas can be further improved by adding tunable phase shifters, which enable beam steering in between the fixed beam angles of the switching network [Jos18; Wan+22b]. In the optical range, crossovers of DWGs are extensively discussed in order to enable photonic integrated circuits [Wei+97; Fuk+04; Bog+07]. Those principles mixed with the behavior of DILs studied Chapter 3 can be translated to the mmW-frequency range in order to provide crossovers of low insertion loss and high isolation. By manipulating the cross-section of the DILs at their crossing, the performance of the crossover can be significantly increased. The layouts of two crossovers, one without modifications and one with elliptical extensions, are shown in Fig. 7.4. The modified crossover is tapered in its width at the crossing from 1.8 mm to 2.6 mm. In addition, following [Bog+07], a small elliptical expansion is introduced, with



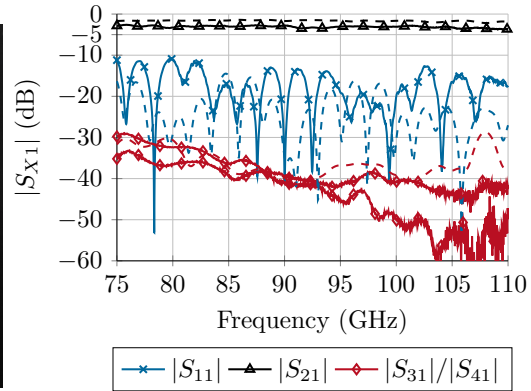
(a) Measurement setup of the unmodified crossover with absorbers.



(b) S-parameters of the unmodified crossover.



(c) Realized expanded crossover, shown without absorbers.



(d) S-parameters of the expanded crossover.

Figure 7.5: (a) Demonstrator of a direct crossing, (c) a modified crossing and corresponding obtained S-parameters (b), (d), respectively. Simulation results are dashed, measurements are solid. Since  $|S_{31}| = |S_{41}|$  in theory, only one dashed line represents the corresponding simulation.

a height  $h_{exp} = h_{DIL}/2 = 0.45$  mm around the crossing. This thin sublayer has a maximum width of 3.5 mm and the elliptical expansions have a major axis of  $l_{maj} = 10$  mm and a minor axis of  $l_{min} = 4$  mm. Fig. 7.5 shows the demonstrators of the unmodified and modified crossovers in  $E_{11}^y$ -mode, together with their corresponding S-parameters. For measurements, absorbers are used to shield unused ports and mitigate reflections from them. The modified crossing shows significant increase in isolation obtained by the slight redesign at the crossing of the waveguides. An improvement of the isolation by 10 dB to 17 dB is obtained.

The investigations in this dissertation, together with the steady advancement to

## *7. Conclusion and Outlook*

lower tolerances and feature sizes of additive manufacturing pave the way towards integrated, reconfigurable and complex DIL networks, which coexist with conventional circuitry on the same PCB at mmW and beyond.



## A. Appendix

### A.1. Relation of $S$ - and $T$ -Matrix

$$T = \begin{pmatrix} t_{11} & t_{12} \\ t_{21} & t_{22} \end{pmatrix} = \frac{1}{s_{21}} \begin{pmatrix} s_{12}s_{21} - s_{11}s_{22} & s_{11} \\ -s_{22} & 1 \end{pmatrix},$$
$$S = \begin{pmatrix} s_{11} & s_{12} \\ s_{21} & s_{22} \end{pmatrix} = \frac{1}{t_{22}} \begin{pmatrix} t_{12} & t_{11}t_{12} - t_{21}t_{12} \\ 1 & -t_{21} \end{pmatrix}.$$

### A.2. Extracted Permittivity and Permeability of an Empty Sample with the NRW Method

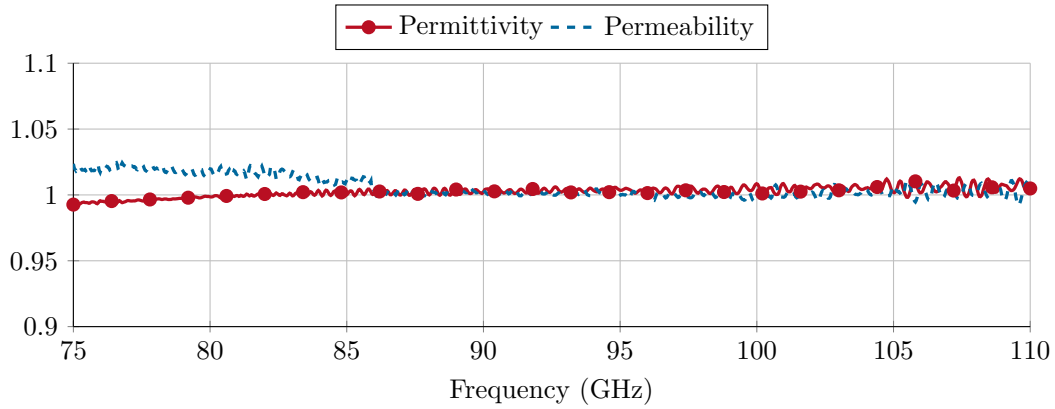


Figure A.1: Relative permittivity and permeability of an empty sample. The slight difference in permeability until 85 GHz can cause overestimated loss of the investigated samples. After 85 GHz, the difference in permittivity and permeability from 1 is less than 1%.

### A.3. Schematics of Waveguide Transitions

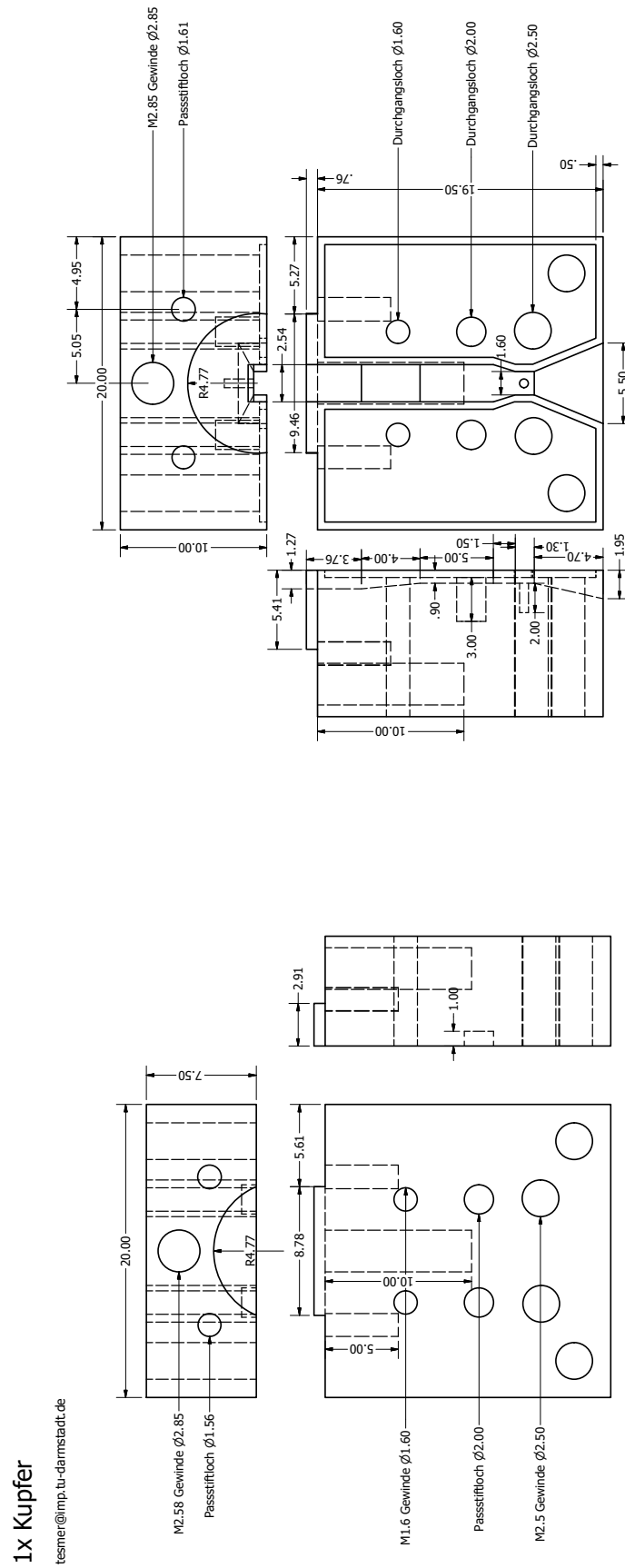


Figure A.2: Top and bottom part of the  $E_{11}^y$ -waveguide transition.

### A.3. Schematics of Waveguide Transitions

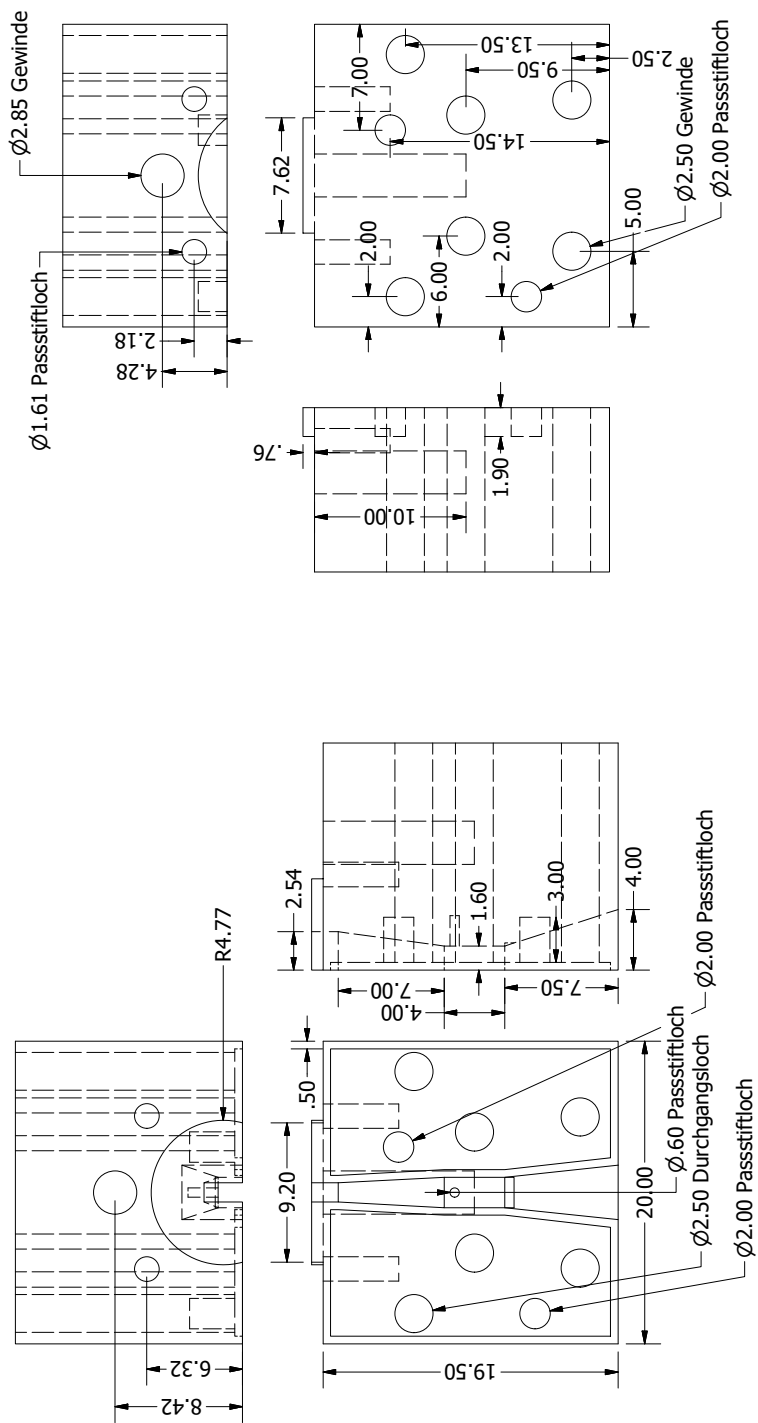


Figure A.3: Top and bottom part of the  $E_{11}^x$ -waveguide transition.

## A. Appendix

### A.4. Mode Conversion in the $E_{11}^x$ -Mode LC Phase Shifter

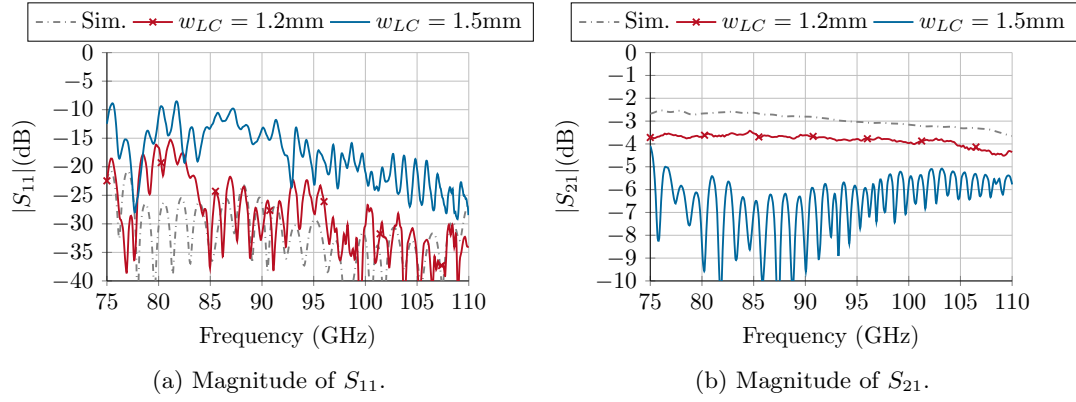


Figure A.4: Measured mode conversion due to a wide LC cavity. This effect is not predicted in simulations.

### A.5. Antenna Measurement Setups

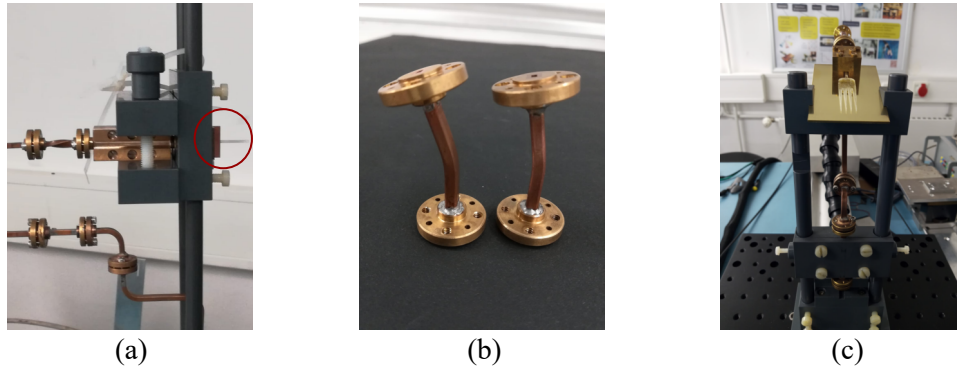


Figure A.5: Measurement setup for rod antennas. (a) measurement of endfire single rod antenna element in elevation plane, AUT marked in red. (b) tilted waveguide sections ( $15^\circ$  and  $18^\circ$  for  $E_{11}^y$ - and  $E_{11}^x$ -mode rod antenna elements, respectively) for measurements in azimuth plane. (c) measurement of rod array in azimuth,  $\theta$  maintained by tilted sections and PVC fixture for the ground plane.

## A.5. Antenna Measurement Setups



(a) DIL rod antennas. Left: as discussed in Section 5.1.1, right: with short ground.

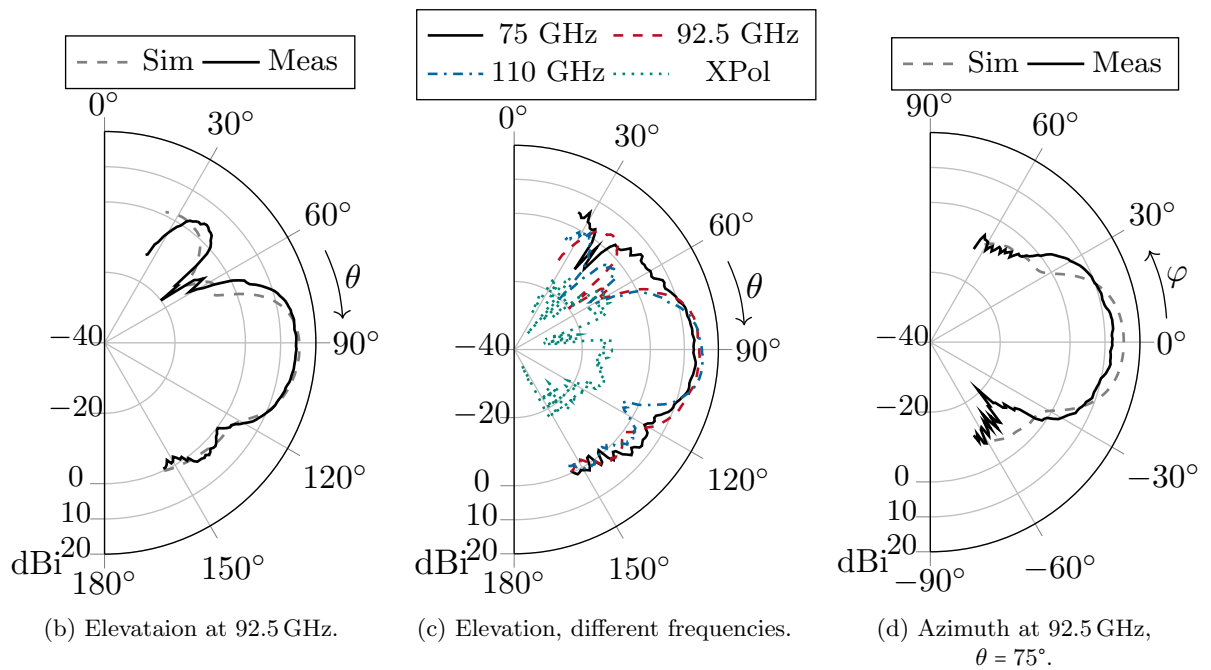


Figure A.6: Endfire-demonstrator and difference to DIL rod antenna with longer ground plane (a), and corresponding measurement results ((b) to (d)). Gain ranges from 12 dB to 14 dBi.

## A. Appendix

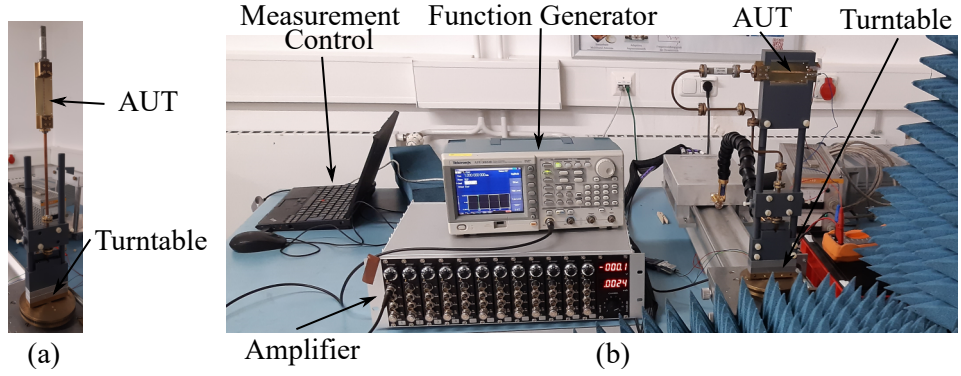


Figure A.7: Measurement setup for LWAs. (a) azimuth plane measurement of Rexolite-LWA, (b) elevation plane measurement of LC-LWA.

## A.6. Leaky Wave Antennas

### A.6.1. Frequency Scanning Rexolite LWA in $E_{11}^y$ -Mode

The following two plots show the sensitivity of the Rexolite LWA to slight variation in its height  $h$ . In practice, these variations can be caused by the glue layer. The plots confirm that a slightly higher  $h$  than anticipated in the simulations of the Rexolite LWA ( $h = 0.9$  mm). This can be observed especially in Fig. A.9, when comparing the frequency at which gain and SLL cross.

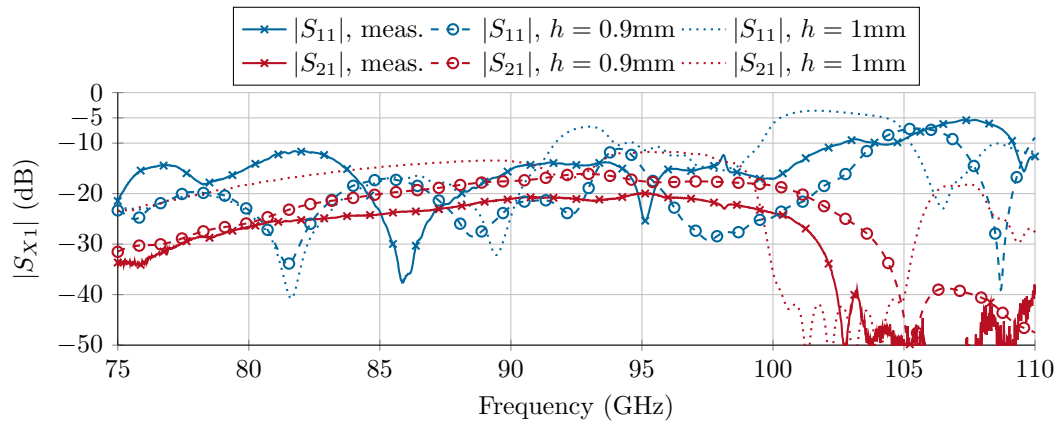


Figure A.8:  $|S_{11}|$  (blue) and  $|S_{21}|$  (red) of the Rexolite LWA. Measured results (solid) are compared to simulation results with different DIL height  $h$ .

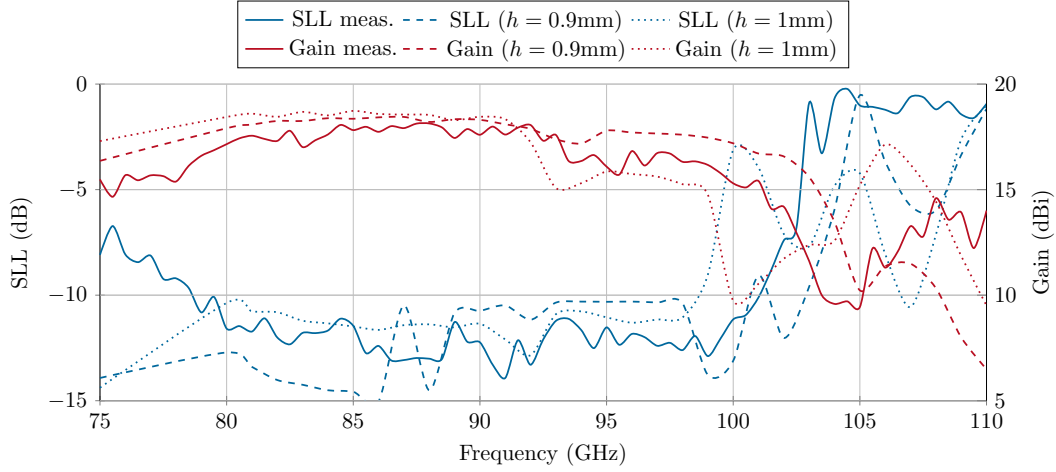


Figure A.9: SLL (blue) and gain (red) of the Rexolite LWA. Measured results (solid) are compared to simulation results with different DIL height  $h$ .

### A.6.2. LWA in $E_{11}^x$ -Mode

The consideration of electrodes and radiators can be extended from  $E_{11}^y$ -mode to  $E_{11}^x$ -mode. The obtained results are summarized in the following figures. Since the mode is different, the radiator is of different shape, as well. The  $E_{11}^x$ -mode appears to be less sensitive to a bias connection line. The unit cell (UC) layout and the demonstrator is shown in Fig. A.10, corresponding dimensions are given in Table A.1. Due to the width  $w_1$  of the unit cell, the LC cavity is less wide than in the  $E_{11}^y$ -mode LC-LWA. The same number of  $N = 24$  UCs as with the  $E_{11}^y$ -mode demonstrator is employed. The measured S-parameters are presented in Fig. A.11, both for a solid Rexolite

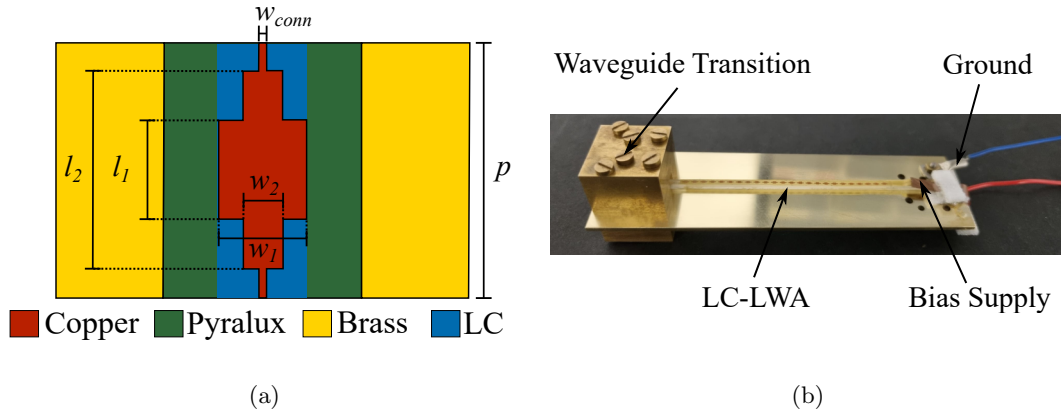


Figure A.10: (a) Unit cell layout, corresponding dimensions given in Table A.1, and (b) assembled demonstrator before mounting magnets to the sides of the ground plane.

## A. Appendix

Table A.1.: Most important dimensions of the  $E_{11}^x$  LC-LWA.

Parameter	$p$	$l_1$	$l_2$	$w_1$	$w_2$	$w_{conn}$	$w_{DIL}$	$h_{DIL}$
Value (mm)	2.6	1	2	0.875	0.4	0.075	2	1.8

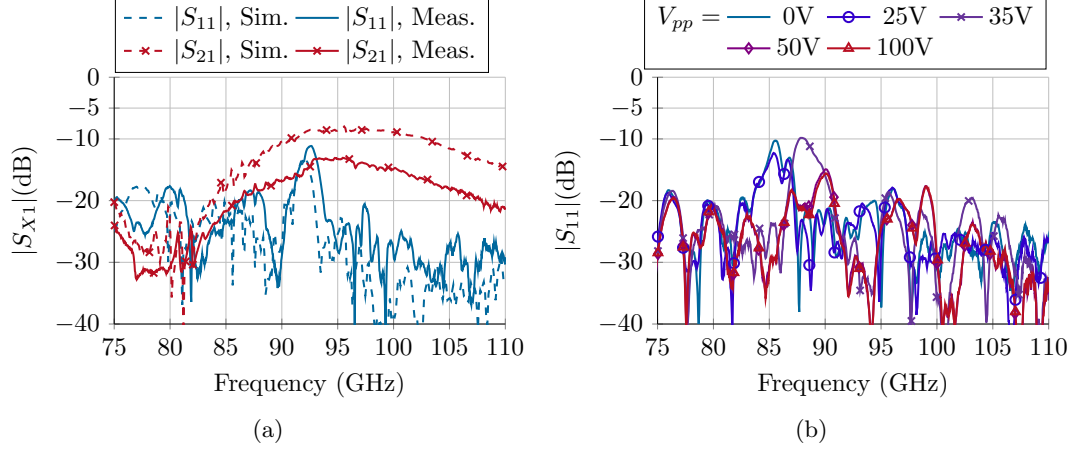


Figure A.11: Measured S-parameters of (a) the Rexolite demonstrator with simulation results and of (b) the LC-LWA demonstrator with different bias voltages applied.

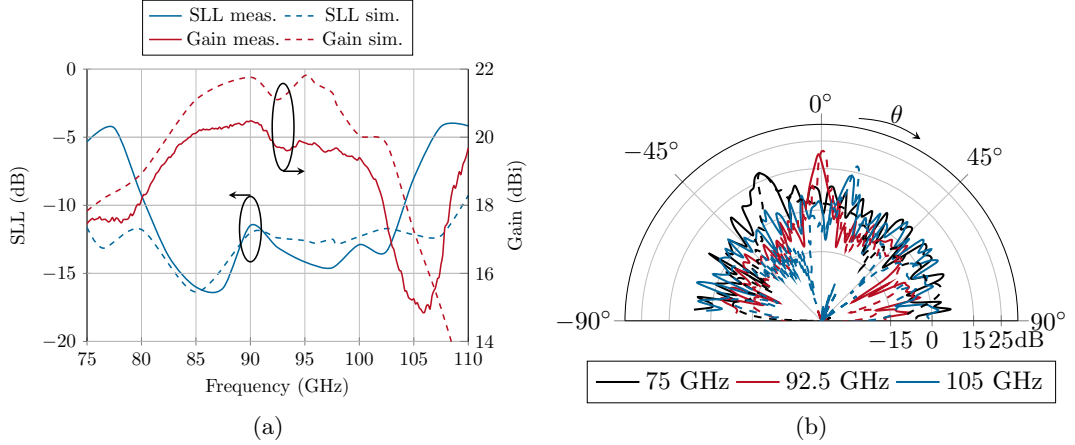


Figure A.12: (a) Gain and SLL the Rexolite demonstrator and (b) elevation pattern at selected frequencies.

LWA and the LC-LWA. As the  $E_{11}^x$ -mode is orthogonal to the  $E_{11}^y$ -mode, the static magnetic bias causes the LC to be in parallel alignment if no voltage is applied, and changes towards perpendicular alignment when the voltage is increased. Behavior of gain and SLL, as well as the pattern in elevation at selected frequencies of the Rexolite demonstrator are shown in Fig. A.12. The corresponding parameters for



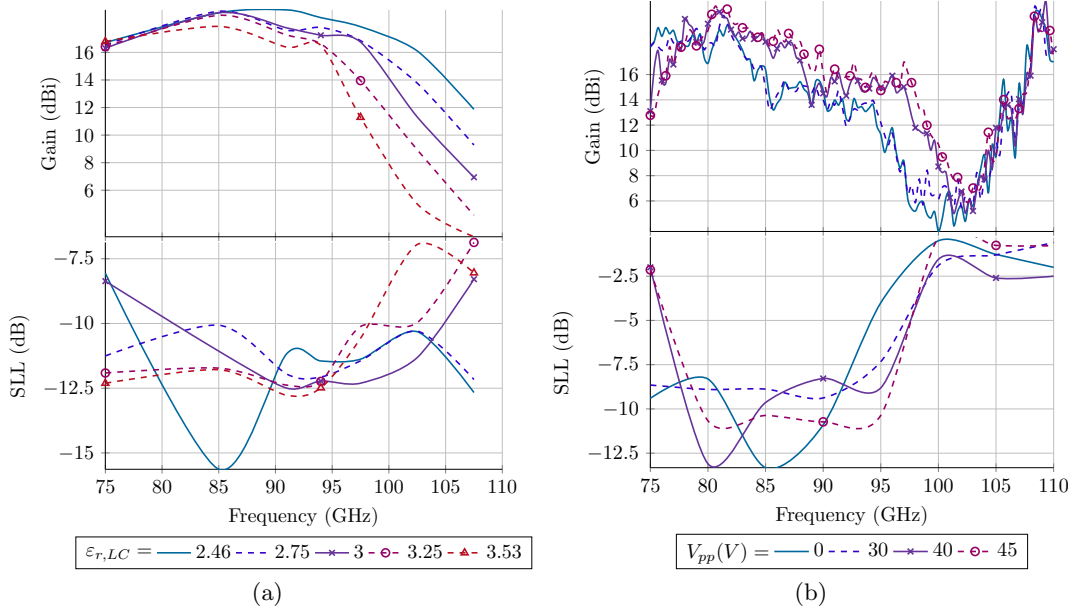


Figure A.13: (a) Simulated and (b) measured behavior of gain and SLL at different permittivity/bias voltages. Note different scaling of the SLL plots.

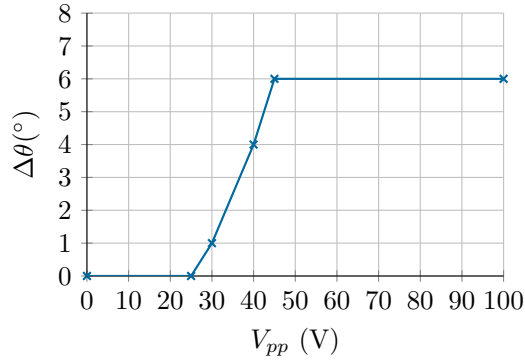


Figure A.14: Beam steering angle versus applied bias voltage.

the LC-LWA demonstrator are depicted in Fig. A.13. Cross polarization of the LC demonstrator is  $-12$  dB at broadside frequency of 94 GHz. The obtained elevation angles at different voltages are visualized in Fig. A.14. A higher bias voltage is necessary to align the LC molecules, due to the higher LC cavity height within the  $E_{11}^x$ -mode demonstrator. The LC-LWA faces higher variance in gain when tuning the LC, and lower beam steering angles are obtained.



## B. Acronyms

<b>AM</b>	Additive Manufacturing
<b>CNC</b>	Computer Numeric Control
<b>COC</b>	Cyclo Olefin Polymer
<b>CPW</b>	Coplanar Waveguide
<b>DIL</b>	Dielectric Image Line
<b>DWG</b>	Dielectric Waveguide
<b>EM</b>	Electro-Magnetic
<b>FoM</b>	Figure-of-Merit
<b>FPC</b>	Fabry-Perot Cavity
<b>GCPW</b>	Grounded Coplanar Waveguide
<b>GND</b>	Ground
<b>HWG</b>	Hollow Waveguide
<b>HDPE</b>	High-Density Polyethylene
<b>HPBW</b>	Half Power Beam Width
<b>IL</b>	Insertion Loss
<b>LC</b>	Liquid Crystal
<b>LWA</b>	Leaky Wave Antenna
<b>MEX</b>	Material Extrusion
<b>MMI</b>	Multimode Interference
<b>mmW</b>	Millimeter Wave
<b>MUT</b>	Material Under Test

## *B. Acronyms*

<b>MS</b>	Microstrip Transmission Line
<b>MS-NAM</b>	Microstrip Transmission Line with Nanowire Membrane
<b>M2M</b>	Machine-to-Machine
<b>NRD</b>	Non-Radiating Dielectric
<b>NRW</b>	Nicolson-Ross-Weir
<b>OSM</b>	Open Stopband Mitigation
<b>PCB</b>	Printed Circuit Board
<b>PEC</b>	Perfect Electric Conductor
<b>PPDW</b>	Parallel-Plate Dielectric Waveguide
<b>PPE</b>	Polyphenylene ether
<b>PTFE</b>	Polytetrafluoroethylene
<b>PVC</b>	Polyvinyl Chloride
<b>RF</b>	Radio Frequency
<b>RMS</b>	Root Mean Square
<b>RWG</b>	Rectangular Waveguide
<b>SIF</b>	Step Index Fibre
<b>SIW</b>	Substrate Integrated Waveguide
<b>SLA</b>	Stereolithography
<b>SLL</b>	Sidelobe Level
<b>SOLT</b>	Short-Open-Line-Thru
<b>SRW</b>	Slot Rectangular Waveguide
<b>sWL</b>	Sub-Wavelength Dielectric Line
<b>TRL</b>	Thru-Reflect-Line
<b>TE</b>	Transversal Electric
<b>TM</b>	Transversal Magnetic
<b>UC</b>	Unit Cell
<b>VNA</b>	Vector Network Analyzer
<b>VPP</b>	Vat Photopolymerization

# Bibliography

- [AH18] Zunnurain Ahmad and Jan Hesselbarth. “On-chip mounted millimeter-wave dielectric resonator antenna”. In: *2018 11th German Microwave Conference (GeMiC)*. IEEE, Mar. 2018. DOI: 10.23919/gemic.2018.8335049.
- [AKG09] A.S. Al-Zoubi, A.A. Kishk, and A.W. Glisson. “Aperture Coupled Rectangular Dielectric Resonator Antenna Array Fed by Dielectric Image Guide”. In: *IEEE Transactions on Antennas and Propagation* 57.8 (Aug. 2009), pp. 2252–2259. DOI: 10.1109/tap.2009.2024487.
- [Alm+04] Vilson R. Almeida, Qianfan Xu, Carlos A. Barrios, and Michal Lipson. “Guiding and confining light in void nanostructure”. In: *Optics Letters* 29.11 (June 2004), p. 1209. DOI: 10.1364/ol.29.001209.
- [Ata+13] Shaghik Atakaramians, Shahraam Afshar V., Tanya M. Monro, and Derek Abbott. “Terahertz dielectric waveguides”. In: *Advances in Optics and Photonics* 5.2 (June 2013), p. 169. DOI: 10.1364/aop.5.000169.
- [Atw85] H.A. Atwater. “Circuit Design of the Loaded-Line Phase Shifter”. In: *IEEE Transactions on Microwave Theory and Techniques* 33.7 (July 1985), pp. 626–634. DOI: 10.1109/tmtt.1985.1133038.
- [Bal05] Constantine A. Balanis. *Antenna Theory: Analysis and Design*. 3rd ed. John Wiley & Sons, 2005.
- [Bao+08] P Bao, T J Jackson, X Wang, and M J Lancaster. “Barium strontium titanate thin film varactors for room-temperature microwave device applications”. In: *Journal of Physics D: Applied Physics* 41.6 (Feb. 2008), p. 063001. DOI: 10.1088/0022-3727/41/6/063001.
- [BBM94] M. Bachmann, P. A. Besse, and H. Melchior. “General self-imaging properties in  $N \times N$  multimode interference couplers including phase relations”. In: *Applied Optics* 33.18 (Jan. 1994), p. 3905. DOI: 10.1364/ao.33.003905.
- [BKG16] Rajratan Basu, Daniel Kinnamon, and Alfred Garvey. “Graphene and liquid crystal mediated interactions”. In: *Liquid Crystals* 43.13-15 (June 2016), pp. 2375–2390. DOI: 10.1080/02678292.2016.1197429.
- [Bog+07] Wim Bogaerts, Pieter Dumon, Dries Van Thourhout, and Roel Baets. “Low-loss, low-cross-talk crossings for silicon-on-insulator nanophotonic waveguides”. In: *Optics Letters* 32.19 (Sept. 2007), p. 2801. DOI: 10.1364/ol.32.002801.

## Bibliography

- [BPM06] Daniel Bourreau, Alain Peden, and Sandrick Le Maguer. “A Quasi-Optical Free-Space Measurement Setup Without Time-Domain Gating for Material Characterization in the W-Band”. In: *IEEE Transactions on Instrumentation and Measurement* 55.6 (Dec. 2006), pp. 2022–2028. DOI: 10.1109/tim.2006.884283.
- [Bul+10] S. Bulja, D. Mirshekar-Syahkal, M. Yazdanpanahi, R. James, S. E. Day, and F. A. Fernández. “Liquid crystal based phase shifters in 60 GHz band”. In: *The 3rd European Wireless Technology Conference*. 2010, pp. 37–40.
- [But61] J. Butler. “Beam-forming matrix simplifies design of electronically scanned antennas”. In: *Electronic Design* 9 (1961), pp. 170–173.
- [Cas+17] Juan Castro, Eduardo A. Rojas-Nastrucci, Anthony Ross, Thomas M. Weller, and Jing Wang. “Fabrication, Modeling, and Application of Ceramic-Thermoplastic Composites for Fused Deposition Modeling of Microwave Components”. In: *IEEE Transactions on Microwave Theory and Techniques* 65.6 (June 2017), pp. 2073–2084. DOI: 10.1109/tmtt.2017.2655057.
- [CH97] Peter J. Collings and Michael Hird. *Introduction to Liquid Crystals Chemistry and Physics*. CRC Press, Sept. 1997. DOI: 10.1201/9781315272801.
- [Che+09] Huanyu Chen, Mohammad Neshat, Suren Gigoyan, Daryoosh Saeedkia, and Safieddin Safavi-Naeini. “A frequency agile beam steerable tapered dielectric image-line antenna array with novel feeding structure”. In: *2009 IEEE Radio and Wireless Symposium*. IEEE, Jan. 2009. DOI: 10.1109/rws.2009.4957306.
- [Che+16] Bang-Jun Che, Fan-Yi Meng, Yue-Long Lyu, and Qun Wu. “A Novel liquid crystal based leaky wave antenna”. In: *2016 IEEE MTT-S International Microwave Workshop Series on Advanced Materials and Processes for RF and THz Applications (IMWS-AMP)*. IEEE, July 2016. DOI: 10.1109/imws-amp.2016.7588324.
- [Coo] Rogers Cooperation. *TMM Thermoset Microwave Materials*. online. accessed: 02.12.2022. URL: <https://www.rogerscorp.com/advanced-electronics-solutions/tmm-laminates/tmm-10-laminates>.
- [Cos+17] Filippo Costa, Michele Borgese, Marco Degiorgi, and Agostino Monorchio. “Electromagnetic Characterisation of Materials by Using Transmission/Reflection (T/R) Devices”. In: *Electronics* 6.4 (Nov. 2017), p. 95. DOI: 10.3390/electronics6040095.

- [COT99] Linfeng Chen, C.K. Ong, and B.T.G. Tan. “Cavity perturbation technique for the measurement of permittivity tensor of uniaxially anisotropic dielectrics”. In: *IEEE Transactions on Instrumentation and Measurement* 48.6 (1999), pp. 1023–1030. DOI: 10.1109/19.816108.
- [DAH20] Utpal Dey, Souvik Agasti, and Jan Hesselbarth. “High-Gain Dielectric Endfire Antenna by Forward Scattering of Dielectric Spheres”. In: *IEEE Antennas and Wireless Propagation Letters* 19.12 (Dec. 2020), pp. 2310–2314. DOI: 10.1109/1awp.2020.3031015.
- [Dam+10] C. Damm, M. Maasch, R. Gonzalo, and R. Jakoby. “Tunable composite right/left-handed leaky wave antenna based on a rectangular waveguide using liquid crystals”. In: *2010 IEEE MTT-S International Microwave Symposium*. IEEE, May 2010. DOI: 10.1109/mwsym.2010.5518096.
- [Dam11] Christian Damm. *Artificial transmission line structures for tunable microwave components and microwave sensors*. en. Darmstadt, Techn. Univ., Diss., 2010. Aachen: Shaker, 2011. ISBN: 978-3-8440-0263-8. URL: <http://tubiblio.ulb.tu-darmstadt.de/55635/>.
- [DH11] Nemat Dolatsha and Jan Hesselbarth. “Propagation and excitation of the higher-order  $E_x^{11}$  mode in an insulated image guide”. In: *Microwave and Optical Technology Letters* 54.1 (Nov. 2011), pp. 179–181. DOI: 10.1002/mop.26450.
- [DH12] Nemat Dolatsha and Jan Hesselbarth. “Millimeter-Wave Chip-to-Chip Transmission Using an Insulated Image Guide Excited by an On-Chip Dipole Antenna at 90 GHz”. In: *IEEE Microwave and Wireless Components Letters* 22.5 (May 2012), pp. 266–268. DOI: 10.1109/lmwc.2012.2190273.
- [DH13] Nemat Dolatsha and Jan Hesselbarth. “Millimeter-Wave Antenna Array Fed by an Insulated Image Guide Operating in Higher-Order  $E_x^{11}$  Mode”. In: *IEEE Transactions on Antennas and Propagation* 61.6 (June 2013), pp. 3369–3373. DOI: 10.1109/tap.2013.2251598.
- [Dis+19] Felix Distler, Mark Sippel, Jan Schur, Gerald Gold, Klaus Helmreich, and Martin Vossiek. “Additively Manufactured Dielectric Waveguides for Advanced Concepts for Millimeter-Wave Interconnects”. In: *IEEE Transactions on Microwave Theory and Techniques* 67.11 (Nov. 2019), pp. 4298–4307. DOI: 10.1109/tmtt.2019.2939831.
- [Dis20] Felix Distler. “Innovative Leitungskonzepte für Dielektrische Wellenleiter im mmW-Frequenzbereich”. doctoralthesis. Friedrich-Alexander-Universität Erlangen-Nürnberg (FAU), 2020.

## Bibliography

- [DSV18a] Felix Distler, Jan Schur, and Martin Vossiek. “A Flexible Measurement System for Dielectric Waveguide Characterization at mmW Frequencies”. In: *2018 48th European Microwave Conference (EuMC)*. IEEE, Sept. 2018. DOI: 10.23919/eumc.2018.8541393.
- [DSV18b] Felix Distler, Jan Schur, and Martin Vossiek. “In-depth characterization of a dielectric waveguide for mmW transmission line applications”. In: *2018 IEEE 22nd Workshop on Signal and Power Integrity (SPI)*. IEEE, May 2018. DOI: 10.1109/sapiw.2018.8401671.
- [DuP] DuPont. *DuPont Pyralux AC Datasheet*. URL: <https://www.dupont.com/content/dam/dupont/amer/us/en/products/ei-transformation/documents/EI-10122-Pyralux-AC-Data-Sheet.pdf> (visited on 09/08/2022).
- [Fan+14] Weihai Fang, Peng Fei, Feng Nian, Yujie Yang, and Keming Feng. “A compact dielectric rod antenna array for wideband millimeter-wave applications”. In: *2014 44th European Microwave Conference*. IEEE, Oct. 2014. DOI: 10.1109/eumc.2014.6986767.
- [FB17] Yukang Feng and N. Scott Barker. “High performance 500–750 GHz RF MEMS switch”. In: *2017 IEEE MTT-S International Microwave Symposium (IMS)*. IEEE, June 2017. DOI: 10.1109/mwsym.2017.8058786.
- [FBJ12] Carsten Fritzsich, Saygin Bildik, and Rolf Jakoby. “Ka-band frequency tunable patch antenna”. In: *Proceedings of the 2012 IEEE International Symposium on Antennas and Propagation*. IEEE, July 2012. DOI: 10.1109/aps.2012.6348462.
- [Fer+22] Philippe Ferrari, Rolf Jakoby, Onur Hamza Karabey, Gustavo Rehder, and Holger Maune. *Reconfigurable Circuits and Technologies for Smart Millimeter-Wave Systems*. EuMA High Frequency Technologies Series. Cambridge University Press, 2022.
- [Fis13] Gerd Fischer. “4 Eigenwerte”. In: *Lineare Algebra*. Springer Fachmedien Wiesbaden, Nov. 2013, pp. 222–273. DOI: 10.1007/978-3-658-03945-5\_5.
- [Foo19] Senglee Foo. “Electronically steerable, low-sidelobe, CRLH-metamaterial leaky-wave antenna”. In: *2019 13th European Conference on Antennas and Propagation (EuCAP)*. 2019, pp. 1–4.
- [Fra58] F. C. Frank. “I. Liquid crystals. On the theory of liquid crystals”. In: *Discussions of the Faraday Society* 25 (1958), p. 19. DOI: 10.1039/df9582500019.



- [Fri+12] Carsten Fritzsche, Flavio Giacomozzi, Onur Hamza Karabey, Saygin Bildik, Sabrina Colpo, and Rolf Jakoby. “Advanced characterization of a W-band phase shifter based on liquid crystals and MEMS technology”. In: *International Journal of Microwave and Wireless Technologies* 4.3 (Apr. 2012), pp. 379–386. DOI: 10.1017/s1759078712000311.
- [Fuk+04] Tatsuhiko Fukazawa, Tomohisa Hirano, Fumiaki Ohno, and Toshihiko Baba. “Low Loss Intersection of Si Photonic Wire Waveguides”. In: *Japanese Journal of Applied Physics* 43.2 (Feb. 2004), pp. 646–647. DOI: 10.1143/jjap.43.646.
- [Fus+17] Walter Fuscaldo, Silvia Tofani, Dimitrios C. Zografopoulos, Paolo Baccarelli, Paolo Burghignoli, Romeo Beccherelli, and Alessandro Galli. “Tunable Fabry–Perot Cavity THz Antenna Based on Leaky-Wave Propagation in Nematic Liquid Crystals”. In: *IEEE Antennas and Wireless Propagation Letters* 16 (Apr. 2017), pp. 2046–2049. DOI: 10.1109/lawp.2017.2695324.
- [FW17] Carsten Fritzsche and Michael Wittek. “Recent developments in liquid crystals for microwave applications”. In: *2017 IEEE International Symposium on Antennas and Propagation & USNC/URSI National Radio Science Meeting*. IEEE, July 2017. DOI: 10.1109/apusncursinrsm.2017.8072651.
- [Gae+09] A. Gaebler, A. Moessinger, F. Goelden, A. Manabe, M. Goebel, R. Follmann, D. Koether, C. Modes, A. Kipka, M. Deckelmann, T. Rabe, B. Schulz, P. Kuchenbecker, A. Lapanik, S. Mueller, W. Haase, and R. Jakoby. “Liquid Crystal-Reconfigurable Antenna Concepts for Space Applications at Microwave and Millimeter Waves”. In: *International Journal of Antennas and Propagation* 2009 (2009), pp. 1–7. DOI: 10.1155/2009/876989.
- [Gae15] Alexander Gaebler. “Synthese steuerbarer Hochfrequenzschaltungen und Analyse Flüssigkristall-basierter Leitungsphasenschieber in Gruppenantennen für Satellitenanwendungen im Ka-Band”. de. PhD thesis. Darmstadt: Technische Universität, 2015. URL: <http://tuprints.ulb.tu-darmstadt.de/4691/>.
- [Ge+22] Jinqun Ge, Tengxing Wang, Yujia Peng, and Guoan Wang. “Electrically Tunable Microwave Technologies With Ferromagnetic Thin Film: Recent Advances in Design Techniques and Applications”. In: *IEEE Microwave Magazine* 23.11 (Nov. 2022), pp. 48–63. DOI: 10.1109/mmm.2022.3196415.
- [Goe+09] F. Goelden, A. Gaebler, M. Goebel, A. Manabe, S. Mueller, and R. Jakoby. “Tunable liquid crystal phase shifter for microwave frequencies”. In: *Electronics Letters* 45.13 (2009), p. 686. DOI: 10.1049/el.2009.1168.

## Bibliography

- [Goe69] J. E. Goell. “A Circular-Harmonic Computer Analysis of Rectangular Dielectric Waveguides”. In: *Bell System Technical Journal* 48.7 (Sept. 1969), pp. 2133–2160. DOI: 10.1002/j.1538-7305.1969.tb01168.x.
- [Göl10] Felix Gölden. “Liquid Crystal Based Microwave Components with Fast Response Times: Material, Technology, Power Handling Capability”. en. PhD thesis. Technische Universität Darmstadt, Fachgebiet Mikrowellentechnik, June 2010. URL: <http://tubiblio.ulb.tu-darmstadt.de/43281/>.
- [GW12] Nasser Ghassemi and Ke Wu. “Planar Dielectric Rod Antenna for Gigabyte Chip-to-Chip Communication”. In: *IEEE Transactions on Antennas and Propagation* 60.10 (Oct. 2012), pp. 4924–4928. DOI: 10.1109/tap.2012.2207359.
- [GWD82] R.V. Gelsthorpe, N. Williams, and N.M. Davey. “Dielectric waveguide; a low-cost technology for millimetre wave integrated circuits”. In: *Radio and Electronic Engineer* 52.11-12 (1982), p. 522. DOI: 10.1049/ree.1982.0076.
- [Han46] William. W. Hansen. *Radiating electromagnetic wave guide*. US Patent 2,402,622. June 1946.
- [Hei75] Jürgen F. Heitmann. “Dielektrische Bildleitungen zur Integration von Millimeterwellenschaltungen”. Aachen, Techn. Hochsch., Fak. f. Elektrotechnik, Diss., 1975. PhD thesis. 1975.
- [Hir+96] T.M. Hirvonen, P. Vainikainen, A. Lozowski, and A.V. Raisanen. “Measurement of dielectrics at 100 GHz with an open resonator connected to a network analyzer”. In: *IEEE Transactions on Instrumentation and Measurement* 45.4 (1996), pp. 780–786. DOI: 10.1109/19.516996.
- [Hof+03] A. Hofmann, E. Horster, J. Weinzierl, L.-P. Schmidt, and H. Brand. “Flexible low-loss dielectric waveguides for THz frequencies with transitions to metal waveguides”. In: *33rd European Microwave Conference Proceedings (IEEE Cat. No.03EX723C)*. IEEE, 2003. DOI: 10.1109/eumc.2003.177639.
- [Hu+22] Wei Hu, Di Jiang, Weiyi Zhang, Yuxin Liu, Kai Zhu, and Tiedi Zhang. “Design of a W-Band Dielectric Phase Shifter Based on Liquid Crystal”. In: *International Journal of Antennas and Propagation* 2022 (Nov. 2022). Ed. by Mauro Parise, pp. 1–6. DOI: 10.1155/2022/6486628.
- [IEE12] IEEE. *IEEE Standard for Information technology–Telecommunications and information exchange between systems–Local and metropolitan area networks–Specific requirements–Part 11: Wireless LAN Medium Access Control (MAC) and Physical Layer (PHY) Specifications*

- Amendment 3: Enhancements for Very High Throughput in the 60 GHz Band*. 2012. DOI: 10.1109/ieeestd.2012.6392842.
- [Isk+16] Ziyad Iskandar, Jose Lugo-Alvarez, Alfredo Bautista, Emmanuel Pistono, Florence Podevin, Vincent Puyal, Alexandre Siligaris, and Philippe Ferrari. “A 30–50 GHz reflection-type phase shifter based on slow-wave coupled lines in BiCMOS 55 nm technology”. In: *2016 46th European Microwave Conference (EuMC)*. IEEE, Oct. 2016. DOI: 10.1109/eumc.2016.7824618.
- [Ito76] T. Itoh. “Inverted Strip Dielectric Waveguide for Millimeter-Wave Integrated Circuits”. In: *IEEE Transactions on Microwave Theory and Techniques* 24.11 (Nov. 1976), pp. 821–827. DOI: 10.1109/tmtt.1976.1128967.
- [Ito77] T. Itoh. “Application of Gratings in a Dielectric Waveguide for Leaky-Wave Antennas and Band-Reject Filters (Short Papers)”. In: *IEEE Transactions on Microwave Theory and Techniques* 25.12 (Dec. 1977), pp. 1134–1138. DOI: 10.1109/tmtt.1977.1129287.
- [ITU15a] International Telecommunication Union (ITU). “Attenuation by atmospheric gases”. In: *ITU Recommendation p.676-11* (2015).
- [ITU15b] International Telecommunication Union (ITU). “IMT traffic estimates for the years 2020 to 2030”. In: *Report ITU-R M.2370-0* (2015).
- [Jah+18] Saman Jahani, Sangsik Kim, Jonathan Atkinson, Justin C. Wirth, Farid Kalhor, Abdullah Al Noman, Ward D. Newman, Prashant Shekhar, Kyunghun Han, Vien Van, Raymond G. DeCorby, Lukas Chrostowski, Minghao Qi, and Zubin Jacob. “Controlling evanescent waves using silicon photonic all-dielectric metamaterials for dense integration”. In: *Nature Communications* 9.1 (May 2018). DOI: 10.1038/s41467-018-04276-8.
- [JGW20] Rolf Jakoby, Alexander Gaebler, and Christian Weickhmann. “Microwave Liquid Crystal Enabling Technology for Electronically Steerable Antennas in SATCOM and 5G Millimeter-Wave Systems”. In: *Crystals* 10.6 (June 2020), p. 514. DOI: 10.3390/cryst10060514.
- [Jim+19] Alejandro Jimenez-Saez, Martin Schubler, Christopher Krause, Damian Pandel, Kamil Rezer, Gerd Vom Bogel, Niels Benson, and Rolf Jakoby. “3D Printed Alumina for Low-Loss Millimeter Wave Components”. In: *IEEE Access* 7 (2019), pp. 40719–40724. DOI: 10.1109/access.2019.2906034.
- [JLR12] Lukui Jin, R. M. Lee, and Ian Robertson. “Modelling of a double-sided dielectric resonator antenna array fed from dielectric insular image guide”. In: *2012 Loughborough Antennas & Propagation Conference (LAPC)*. IEEE, Nov. 2012. DOI: 10.1109/lapc.2012.6403074.

## Bibliography

- [JO07] David R. Jackson and Arthur Oliner. “Leaky-Wave Antennas”. In: ed. by Constantine A Balanis. *Modern Antenna Handbook*, Wiley Online Library, Nov. 2007. Chap. 7, pp. 325–367. DOI: <https://doi.org/10.1002/9780470294154.ch7>.
- [Jos+13] M. Jost, C. Weickhmann, S. Strunck, A. Gäbler, C. Fritzsich, O.H. Karabey, and R. Jakoby. “Liquid crystal based low-loss phase shifter for W-band frequencies”. In: *Electronics Letters* 49.23 (Nov. 2013), pp. 1460–1462. DOI: [10.1049/e1.2013.2830](https://doi.org/10.1049/e1.2013.2830).
- [Jos+15a] M. Jost, S. Strunck, A. Heunisch, A. Wiens, A. E. Prasetiadi, C. Weickhmann, B. Schulz, M. Quibeldey, O. H. Karabey, T. Rabe, R. Follmann, D. Koether, and R. Jakoby. “Continuously tuneable liquid crystal based stripline phase shifter realised in LTCC technology”. In: *2015 10th European Microwave Integrated Circuits Conference (EuMIC)*. IEEE, Sept. 2015. DOI: [10.1109/eumic.2015.7345156](https://doi.org/10.1109/eumic.2015.7345156).
- [Jos+15b] M. Jost, C. Weickhmann, T. Franke, A. E. Prasetiadi, W. Hu, M. Nickel, O. H. Karabey, and R. Jakoby. “Tuneable hollow waveguide devices for space applications based on liquid crystal”. In: *2015 SBMO/IEEE MTT-S International Microwave and Optoelectronics Conference (IMOC)*. IEEE, Nov. 2015. DOI: [10.1109/imoc.2015.7369046](https://doi.org/10.1109/imoc.2015.7369046).
- [Jos+17] M. Jost, R. Reese, M. Nickel, S. Schmidt, H. Maune, and R. Jakoby. “Interference based W-band single-pole double-throw with tuneable liquid crystal based waveguide phase shifters”. In: *2017 IEEE MTT-S International Microwave Symposium (IMS)*. IEEE, June 2017. DOI: [10.1109/mwsym.2017.8059003](https://doi.org/10.1109/mwsym.2017.8059003).
- [Jos+18] Matthias Jost, Roland Reese, Matthias Nickel, Holger Maune, and Rolf Jakoby. “Fully dielectric interference-based SPDT with liquid crystal phase shifters”. In: *IET Microwaves, Antennas & Propagation* 12.6 (May 2018), pp. 850–857. DOI: [10.1049/iet-map.2017.0695](https://doi.org/10.1049/iet-map.2017.0695).
- [Jos18] Matthias Jost. “Liquid crystal mixed beam-switching and beam-steering network in hybrid metallic and dielectric waveguide technology”. en. Dissertation, Technische Universität Darmstadt, 2018. PhD thesis. Aachen: TU Darmstadt, 2018. ISBN: 9783844060423. URL: <http://tubiblio.ulb.tu-darmstadt.de/106616/>.
- [Kad+22] Petr Kadera, Jesus Sanchez-Pastor, Hossein Eskandari, Tomas Tyc, Masoud Sakaki, Martin Schusler, Rolf Jakoby, Niels Benson, Alejandro Jimenez-Saez, and Jaroslav Lacik. “Wide-Angle Ceramic Retroreflective Luneburg Lens Based on Quasi-Conformal Transformation Optics for Mm-Wave Indoor Localization”. In: *IEEE Access* 10 (2022), pp. 41097–41111. DOI: [10.1109/access.2022.3166509](https://doi.org/10.1109/access.2022.3166509).

- [Kah+17] Henri Kahkonen, Vasilii Semkin, Juha Ala-Laurinaho, and Ville Viikari. “Dielectric-filled waveguide antenna array for millimeter-wave communications”. In: *2017 11th European Conference on Antennas and Propagation (EUCAP)*. IEEE, Mar. 2017. DOI: 10.23919/eucap.2017.7928294.
- [Kar14] Onur Hamza Karabey. “Electronic beam steering and polarization agile planar antennas in liquid crystal technology”. en. Zugl. Darmstadt, Techn. Univ., Diss., 2013. PhD thesis. Cham: TU Darmstadt, 2014. ISBN: 978-3-319-01423-4. URL: <http://tubiblio.ulb.tu-darmstadt.de/62416/>.
- [Kha+12] Subash Khanal, Tero Kiuru, Juha Mallat, Olli Luukkonen, and Antti V. Räsänen. “Measurement of Dielectric Properties at 75-325 GHz using a Vector Network Analyzer and Full Wave Simulator”. English. In: *Radioengineering* 21.2 (2012), pp. 551–556. ISSN: 1210-2512.
- [Kin52] D. D. King. “Dielectric Image Line”. In: *Journal of Applied Physics* 23.6 (June 1952), pp. 699–700. DOI: 10.1063/1.1702285.
- [KN21] Hyungcheol Kim and Sangwook Nam. “Performance Improvement of LC-based Beam Steering Leaky Wave Holographic Antenna using Decoupling Structure”. In: *IEEE Transactions on Antennas and Propagation* (2021), pp. 1–1. DOI: 10.1109/tap.2021.3118779.
- [Kno76] R.M. Knox. “Dielectric Waveguide Microwave Integrated Circuits—An Overview”. In: *IEEE Transactions on Microwave Theory and Techniques* 24.11 (Nov. 1976), pp. 806–814. DOI: 10.1109/tmtt.1976.1128965.
- [KS58] D.D. King and S.P. Schlesinger. “Dielectric Image Lines”. In: *IEEE Transactions on Microwave Theory and Techniques* 6.3 (July 1958), pp. 291–299. DOI: 10.1109/tmtt.1958.1124560.
- [KT70] RM Knox and PP Toullos. “Integrated circuits for the millimeter through optical frequency range”. In: *Proc. Symp. Submillimeter Waves*. Vol. 20. Brooklyn, NY. 1970, pp. 497–515.
- [Lam96] James W. Lamb. “Miscellaneous data on materials for millimetre and submillimetre optics”. In: *International Journal of Infrared and Millimeter Waves* 17.12 (Dec. 1996), pp. 1997–2034. DOI: 10.1007/bf02069487.
- [Lan+20] Trong Nghia Lang, Van Bao Bui, Yo Inoue, and Hiroshi Moritake. “Response Improvement of Liquid Crystal-Loaded NRD Waveguide Type Terahertz Variable Phase Shifter”. In: *Crystals* 10.4 (Apr. 2020), p. 307. DOI: 10.3390/cryst10040307.

## Bibliography

- [LD19] Feng Lin and Huizhong Deng. “Continuously Tunable True-Time-Delay Phase Shifter Based on Transmission Lines With Simultaneously Reconfigurable Impedance and Phase Constant”. In: *IEEE Transactions on Microwave Theory and Techniques* 67.12 (Dec. 2019), pp. 4714–4723. DOI: 10.1109/tmtt.2019.2944612.
- [LML93] K. C. Lim, J. D. Margerum, and A. M. Lackner. “Liquid crystal millimeter wave electronic phase shifter”. In: *Applied Physics Letters* 62.10 (Mar. 1993), pp. 1065–1067. DOI: 10.1063/1.108796.
- [LMT11] O. Luukkonen, S. I. Maslovski, and S. A. Tretyakov. “A Stepwise Nicolson–Ross–Weir-Based Material Parameter Extraction Method”. In: *IEEE Antennas and Wireless Propagation Letters* 10 (2011), pp. 1295–1298. DOI: 10.1109/lawp.2011.2175897.
- [Lyu+16] Yue-Long Lyu, Xiao-Xin Liu, Peng-Yuan Wang, Daniel Erni, Qun Wu, Cong Wang, Nam-Young Kim, and Fan-Yi Meng. “Leaky-Wave Antennas Based on Noncutoff Substrate Integrated Waveguide Supporting Beam Scanning From Backward to Forward”. In: *IEEE Transactions on Antennas and Propagation* 64.6 (June 2016), pp. 2155–2164. DOI: 10.1109/tap.2016.2550054.
- [Ma+20] Shuang Ma, Peng-Yuan Wang, Fan-Yi Meng, Jia-Hui Fu, and Qun Wu. “Electronically controlled beam steering leaky wave antenna in nematic liquid crystal technology”. In: *International Journal of RF and Microwave Computer-Aided Engineering* 30.6 (Feb. 2020). DOI: 10.1002/mmce.22188.
- [MA15] Rupendra Nath Mitra and Dharma P. Agrawal. “5G mobile technology: A survey”. In: *ICT Express* 1.3 (Dec. 2015), pp. 132–137. DOI: 10.1016/j.ictex.2016.01.003.
- [Mar69] E. A. J. Marcatili. “Dielectric Rectangular Waveguide and Directional Coupler for Integrated Optics”. In: *Bell System Technical Journal* 48.7 (Sept. 1969), pp. 2071–2102. DOI: 10.1002/j.1538-7305.1969.tb01166.x.
- [MIM75] W.V. McLevige, T. Itoh, and R. Mittra. “New Waveguide Structures for Millimeter-Wave and Optical Integrated Circuits”. In: *IEEE Transactions on Microwave Theory and Techniques* 23.10 (Oct. 1975), pp. 788–794. DOI: 10.1109/tmtt.1975.1128684.
- [MS60] Wilhelm Maier and Alfred Saupe. “Eine einfache molekular-statistische Theorie der nematischen kristallinflüssigen Phase. Teil II”. In: *Zeitschrift für Naturforschung A* 15.4 (1960), pp. 287–292. DOI: doi:10.1515/zna-1960-0401. URL: <https://doi.org/10.1515/zna-1960-0401>.

- [Mue+05] S. Mueller, C. Felber, P. Scheele, M. Wittek, C. Hock, and R. Jakoby. “Passive tunable liquid crystal finline phase shifter for millimeter waves”. In: *2005 European Microwave Conference*. IEEE, 2005. DOI: 10.1109/eumc.2005.1608852.
- [Mue+06] Stefan Mueller, Felix Goelden, Patrick Scheele, Michael Wittek, Christian Hock, and Rolf Jakoby. “Passive Phase Shifter for W-Band Applications using Liquid Crystals”. In: *2006 European Microwave Conference*. IEEE, Sept. 2006. DOI: 10.1109/eumc.2006.281317.
- [Mul+04] S. Muller, P. Scheele, C. Weil, M. Wittek, C. Hock, and R. Jakoby. “Tunable passive phase shifter for microwave applications using highly anisotropic liquid crystals”. In: *2004 IEEE MTT-S International Microwave Symposium Digest (IEEE Cat. No.04CH37535)*. IEEE, 2004. DOI: 10.1109/mwsym.2004.1339190.
- [New04] Robert E. Newnham. *Properties of Materials*. Oxford University Press, Nov. 2004. DOI: 10.1093/oso/9780198520757.001.0001.
- [NIH18] Toshiaki Nose, Ryota Ito, and Michinori Honma. “Potential of Liquid-Crystal Materials for Millimeter-Wave Application”. In: *Applied Sciences* 8.12 (Dec. 2018), p. 2544. DOI: 10.3390/app8122544.
- [NMK06] Michael Nagel, Astrid Marchewka, and Heinrich Kurz. “Low-index discontinuity terahertz waveguides”. In: *Optics Express* 14.21 (2006), p. 9944. DOI: 10.1364/oe.14.009944.
- [NR70] A. M. Nicolson and G. F. Ross. “Measurement of the Intrinsic Properties of Materials by Time-Domain Techniques”. In: *IEEE Transactions on Instrumentation and Measurement* 19.4 (Nov. 1970), pp. 377–382. DOI: 10.1109/tim.1970.4313932.
- [Ose33] C. W. Oseen. “The theory of liquid crystals”. In: *Transactions of the Faraday Society* 29.140 (1933), p. 883. DOI: 10.1039/TF9332900883.
- [Par15] Maria Roig Parras. “Tunable Metamaterial Leaky Wave Antenna based on Microwave Liquid Crystal Technology”. In: (2015). URL: <http://tuprints.ulb.tu-darmstadt.de/5136/>.
- [PB15] Chandra Shekhar Prasad and Animesh Bishwas. “Dual-beam dielectric image line tapered antenna in planar environment”. In: *2015 IEEE Applied Electromagnetics Conference (AEMC)*. IEEE, Dec. 2015. DOI: 10.1109/aemc.2015.7509199.
- [PB17] Chandra Shekhar Prasad and Animesh Biswas. “Dielectric Image Line-Based Leaky-Wave Antenna for Wide Range of Beam Scanning Through Broadside”. In: *IEEE Transactions on Antennas and Propagation* 65.8 (Aug. 2017), pp. 4311–4315. DOI: 10.1109/tap.2017.2714024.

## Bibliography

- [PBA17] Chandra Shekhar Prasad, Animesh Biswas, and M. Jaleel Akhtar. “A compact and broadband dielectric image line based antenna array in planar environment”. In: *Microwave and Optical Technology Letters* 60.1 (Dec. 2017), pp. 271–277. DOI: 10.1002/mop.30952.
- [PBA18] Chandra Shekhar Prasad, Animesh Biswas, and M. Jaleel Akhtar. “Leaky wave antenna for wide range of beam scanning through broadside in dielectric image line environment”. In: *Microwave and Optical Technology Letters* 60.7 (May 2018), pp. 1707–1713. DOI: 10.1002/mop.31224.
- [PDK96] G.E. Ponchak, N.I. Dib, and L.P.B. Katehi. “Design and analysis of transitions from rectangular waveguide to layered ridge dielectric waveguide”. In: *IEEE Transactions on Microwave Theory and Techniques* 44.7 (July 1996), pp. 1032–1040. DOI: 10.1109/22.508635.
- [Pol+19a] E. Polat, R. Reese, H. Tesmer, S. Schmidt, M. Spaeth, M. Nickel, C. Schuster, R. Jakoby, and H. Maune. “Characterization of Liquid Crystals Using a Temperature-Controlled 60 GHz Resonator”. In: *2019 IEEE MTT-S International Microwave Workshop Series on Advanced Materials and Processes for RF and THz Applications (IMWS-AMP)*. IEEE, July 2019. DOI: 10.1109/imws-amp.2019.8880077.
- [Pol+19b] Ersin Polat, Roland Reese, Matthias Jost, Matthias Nickel, Christian Schuster, Rolf Jakoby, and Holger Maune. “Liquid Crystal Phase Shifter Based on Nonradiative Dielectric Waveguide Topology at W-Band”. In: *2019 IEEE MTT-S International Microwave Symposium (IMS)*. IEEE, June 2019. DOI: 10.1109/mwsym.2019.8700759.
- [Pol+20a] Ersin Polat, Roland Reese, Henning Tesmer, Matthias Nickel, Rolf Jakoby, and Holger Maune. “Fully Dielectric Phased Array for Beamsteering Using Liquid Crystal Technology at W-Band”. In: *2020 14th European Conference on Antennas and Propagation (EuCAP)*. IEEE, Mar. 2020. DOI: 10.23919/eucap48036.2020.9135584.
- [Pol+20b] Ersin Polat, Henning Tesmer, Roland Reese, Matthias Nickel, Dongwei Wang, Peter Schumacher, Rolf Jakoby, and Holger Maune. “Reconfigurable Millimeter-Wave Components Based on Liquid Crystal Technology for Smart Applications”. In: *Crystals* 10.5 (Apr. 2020), p. 346. DOI: 10.3390/cryst10050346.
- [Pol23] Ersin Polat. “Grundlegende Untersuchungen von abstimmbaren Flüssigkristall-Filtern für Hochfrequenzanwendungen”. In: (2023).
- [Pou+10] J.P. Pousi, D.V. Lioubtchenko, S.N. Dudorov, and A.V. Raisanen. “High Permittivity Dielectric Rod Waveguide as an Antenna Array Element for Millimeter Waves”. In: *IEEE Transactions on Antennas and Propagation* 58.3 (Mar. 2010), pp. 714–719. DOI: 10.1109/tap.2009.2039314.



- [Poz11] David M. Pozar. *Microwave Engineering*. WILEY, Nov. 2011. 752 pp. ISBN: 0470631554. URL: [https://www.ebook.de/de/product/14948033/david\\_m\\_pozar\\_microwave\\_engineering.html](https://www.ebook.de/de/product/14948033/david_m_pozar_microwave_engineering.html).
- [Pra+15] A.E. Prasetiadi, O.H. Karabey, C. Weickhmann, T. Franke, W. Hu, M. Jost, M. Nickel, and R. Jakoby. “Continuously tunable substrate integrated waveguide bandpass filter in liquid crystal technology with magnetic biasing”. In: *Electronics Letters* 51.20 (Oct. 2015), pp. 1584–1585. DOI: 10.1049/e1.2015.2494.
- [PRB11] Adriano Luiz de Paula, Mirabel Cerqueira Rezende, and Joaquim Jose Barroso. “Modified Nicolson-Ross-Weir (NRW) method to retrieve the constitutive parameters of low-loss materials”. In: *2011 SBMO/IEEE MTT-S International Microwave and Optoelectronics Conference (IMOC 2011)*. IEEE, Oct. 2011. DOI: 10.1109/imoc.2011.6169293.
- [PW06a] A. Patrovsky and K. Wu. “94-GHz Planar Dielectric Rod Antenna With Substrate Integrated Image Guide (SIIG) Feeding”. In: *IEEE Antennas and Wireless Propagation Letters* 5 (2006), pp. 435–437. DOI: 10.1109/1awp.2006.885014.
- [PW06b] A. Patrovsky and Ke Wu. “Substrate integrated image guide (SIIG)-a planar dielectric waveguide technology for millimeter-wave applications”. In: *IEEE Transactions on Microwave Theory and Techniques* 54.6 (June 2006), pp. 2872–2879. DOI: 10.1109/tmtt.2006.875461.
- [PW07] Andreas Patrovsky and Ke Wu. “Substrate Integrated Image Guide Array Antenna for the Upper Millimeter-Wave Spectrum”. In: *IEEE Transactions on Antennas and Propagation* 55.11 (Nov. 2007), pp. 2994–3001. DOI: 10.1109/tap.2007.908558.
- [Qur+17] Aqeel A. Qureshi, David M. Klymyshyn, Matt Tayfeh, Waqas Mazhar, Martin Borner, and Jurgen Mohr. “Template-Based Dielectric Resonator Antenna Arrays for Millimeter-Wave Applications”. In: *IEEE Transactions on Antennas and Propagation* 65.9 (Sept. 2017), pp. 4576–4584. DOI: 10.1109/tap.2017.2724585.
- [Rah+21] Sofia Rahiminejad, Maria Alonso-delPino, Theodore Reck, Alex Peralta, Robert Lin, Cecile Jung-Kubiak, and Goutam Chattopadhyay. “A Low-Loss Silicon MEMS Phase Shifter Operating in the 550-GHz Band”. In: *IEEE Transactions on Terahertz Science and Technology* 11.5 (Sept. 2021), pp. 477–485. DOI: 10.1109/tthz.2021.3085123.
- [Raj+08] Khalid Z. Rajab, Mira Naftaly, Edmund H. Linfield, Juan C. Nino, Daniel Arenas, David Tanner, Raj Mittra, and Michael Lanagan. “Broadband Dielectric Characterization of Aluminum Oxide (Al<sub>2</sub>O<sub>3</sub>)”. In: *Journal of Microelectronics and Electronic Packaging* 5.1 (Jan. 2008), pp. 2–7. DOI: 10.4071/1551-4897-5.1.1.

## Bibliography

- [Rap+13] Theodore S. Rappaport, Shu Sun, Rimma Mayzus, Hang Zhao, Yaniv Azar, Kevin Wang, George N. Wong, Jocelyn K. Schulz, Mathew Samimi, and Felix Gutierrez. “Millimeter Wave Mobile Communications for 5G Cellular: It Will Work!” In: *IEEE Access* 1 (2013), pp. 335–349. DOI: 10.1109/access.2013.2260813.
- [RB00] G.M. Rebeiz and N.S. Barker. “Optimization of distributed MEMS transmission-line phase shifters-U-band and W-band designs”. In: *IEEE Transactions on Microwave Theory and Techniques* 48.11 (2000), pp. 1957–1966. DOI: 10.1109/22.883878.
- [Ree+17a] R. Reese, M. Jost, H. Maune, and R. Jakoby. “Design of a continuously tunable W-band phase shifter in dielectric waveguide topology”. In: *2017 IEEE MTT-S International Microwave Symposium (IMS)*. IEEE, June 2017. DOI: 10.1109/mwsym.2017.8058991.
- [Ree+17b] R. Reese, E. Polat, M. Jost, M. Nickel, R. Jakoby, and H. Maune. “Liquid crystal based phase shifter in a parallel-plate dielectric waveguide topology at V-band”. In: *2017 12th European Microwave Integrated Circuits Conference (EuMIC)*. IEEE, Oct. 2017. DOI: 10.23919/eumic.2017.8230731.
- [Ree+17c] Roland Reese, Matthias Jost, Matthias Nickel, Ersin Polat, Rolf Jakoby, and Holger Maune. “A Fully Dielectric Lightweight Antenna Array Using a Multimode Interference Power Divider at W-Band”. In: *IEEE Antennas and Wireless Propagation Letters* 16 (2017), pp. 3236–3239. DOI: 10.1109/lawp.2017.2771385.
- [Ree+18] Roland Reese, Henning Tesmer, Matthias Jost, Ersin Polat, Matthias Nickel, Rolf Jakoby, and Holger Maune. “A Compact Two-dimensional Power Divider for a Dielectric Rod Antenna Array Based on Multimode Interference”. In: *Journal of Infrared, Millimeter, and Terahertz Waves* 39.12 (Aug. 2018), pp. 1185–1202. DOI: 10.1007/s10762-018-0535-x.
- [Ree+19a] Roland Reese, Matthias Jost, Ersin Polat, Henning Tesmer, Jonathan Strobl, Christian Schuster, Matthias Nickel, Rolf Jakoby, and Holger Maune. “A Millimeter-Wave Beam-Steering Lens Antenna With Reconfigurable Aperture Using Liquid Crystal”. In: *IEEE Transactions on Antennas and Propagation* 67.8 (Aug. 2019), pp. 5313–5324. DOI: 10.1109/tap.2019.2918474.
- [Ree+19b] Roland Reese, Ersin Polat, Henning Tesmer, Jonathan Strobl, Christian Schuster, Matthias Nickel, Angel Blanco Granja, Rolf Jakoby, and Holger Maune. “Liquid Crystal Based Dielectric Waveguide Phase Shifters for Phased Arrays at W-Band”. In: *IEEE Access* 7 (2019), pp. 127032–127041. DOI: 10.1109/access.2019.2939648.

- [Ree20] Roland Reese. “Phasen- und aperturgesteuerte Antennen für Millimeterwellen mit integrierten Flüssigkristallsegmenten: Von metallischen zu voll-dielektrischen Strukturen”. In: (2020). DOI: 10.25534/TUPRINTS-00011597.
- [Ric07] Jürgen Richter. “Dielektrische Weitwinkellinsen und Speiseanordnungen für Focal Plane Array Antennen bildgebender Millimeterwellensysteme”. doctoralthesis. Friedrich-Alexander-Universität Erlangen-Nürnberg (FAU), 2007.
- [Riv+15] Alejandro Rivera-Lavado, Sascha Preu, Luis Enrique Garcia-Munoz, Andrey Generalov, Javier Montero-de-Paz, Gottfried Dohler, Dmitri Lioubtchenko, Mario Mendez-Aller, Stefan Malzer, Daniel Segovia-Vargas, and Antti V. Raisanen. “Array of Dielectric Rod Waveguide antennas for millimeter-wave power generation”. In: *2015 European Microwave Conference (EuMC)*. IEEE, Sept. 2015. DOI: 10.1109/eumc.2015.7345913.
- [Riv+16] Alejandro Rivera-Lavado, Luis-Enrique Garcia-Munoz, Andrey Generalov, Dmitri Lioubtchenko, Kerlos-Atia Abdalmalak, Sergio Llorente-Romano, Alejandro Garcia-Lamperez, Daniel Segovia-Vargas, and Antti V. Räsänen. “Design of a Dielectric Rod Waveguide Antenna Array for Millimeter Waves”. In: *Journal of Infrared, Millimeter, and Terahertz Waves* 38.1 (Sept. 2016), pp. 33–46. DOI: 10.1007/s10762-016-0310-9.
- [RJJ16] R. Reese, M. Jost, and R. Jakoby. “Evaluation of two W-band power dividers in a subwavelength dielectric fibre technology”. In: *Electronics Letters* 52.16 (Aug. 2016), pp. 1391–1393. DOI: 10.1049/el.2016.1092.
- [RL01] I. D. Robertson and S. Lucyszyn, eds. *RFIC and MMIC Design and Technology*. Institution of Engineering and Technology, Jan. 2001. DOI: 10.1049/pbcs013e.
- [Roi+14] Maria Roig, Matthias Maasch, Christian Damm, and Rolf Jakoby. “Dynamic beam steering properties of an electrically tuned liquid crystal based CRLH leaky wave antenna”. In: *2014 8th International Congress on Advanced Electromagnetic Materials in Microwaves and Optics*. IEEE, Aug. 2014. DOI: 10.1109/metamaterials.2014.6948665.
- [Roi+15] Maria Roig, Matthias Maasch, Christian Damm, and Rolf Jakoby. “Investigation and application of a liquid crystal loaded varactor in a voltage tunable CRLH leaky-wave antenna at Ka-band”. In: *International Journal of Microwave and Wireless Technologies* 7.3-4 (Mar. 2015), pp. 361–367. DOI: 10.1017/s1759078715000367.

## Bibliography

- [Rot+16] Edward J. Rothwell, Jonathan L. Frasch, Sean M. Ellison, Premjeet Chahal, and Raoul O. Ouedraogo. “ANALYSIS OF THE NICOLSON-ROSS-WEIR METHOD FOR CHARACTERIZING THE ELECTROMAGNETIC PROPERTIES OF ENGINEERED MATERIALS”. In: *Progress In Electromagnetics Research* 157 (2016), pp. 31–47. DOI: 10.2528/pier16071706.
- [SFW22] Odai Hassan Raheem Al Soad, Jiahui Fu, and Qun Wu. “A tunable X-shaped microstrip leaky wave antenna based on liquid crystal”. In: *International Journal of Communication Systems* 35.10 (Apr. 2022). DOI: 10.1002/dac.5175.
- [SI78] S. Shindo and T. Itanami. “Low-Loss Rectangular Dielectric Image Line for Millimeter-Wave Integrated Circuits”. In: *IEEE Transactions on Microwave Theory and Techniques* 26.10 (Oct. 1978), pp. 747–751. DOI: 10.1109/tmtt.1978.1129480.
- [SNS18] Seckin Sahin, Niru K. Nahar, and Kubilay Sertel. “Permittivity and Loss Characterization of SUEX Epoxy Films for mmW and THz Applications”. In: *IEEE Transactions on Terahertz Science and Technology* 8.4 (July 2018), pp. 397–402. DOI: 10.1109/tthz.2018.2840518.
- [Sol76] K. Solbach. “The Fabrication of Dielectric Image Lines Using Casting Resins and the Properties of the Lines in the Millimeter-Wave Range (Short Papers)”. In: *IEEE Transactions on Microwave Theory and Techniques* 24.11 (Nov. 1976), pp. 879–881. DOI: 10.1109/tmtt.1976.1128984.
- [Sol79a] K. Solbach. “The Measurement of the Radiation Losses in Dielectric Image Line Bends and the Calculation of a Minimum Acceptable Curvature Radius”. In: *IEEE Transactions on Microwave Theory and Techniques* 27.1 (Jan. 1979), pp. 51–53. DOI: 10.1109/tmtt.1979.1129557.
- [Sol79b] Klaus Solbach. “Untersuchung der dielektrischen Bildleitung zur Integration von Millimeterwellenschaltungen”. Duisburg, Gesamthochsch., Fachbereich 09 - Elektrotechnik, Diss., 1979. PhD thesis. 1979.
- [SP95] L.B. Soldano and E.C.M. Pennings. “Optical multi-mode interference devices based on self-imaging: principles and applications”. In: *Journal of Lightwave Technology* 13.4 (Apr. 1995), pp. 615–627. DOI: 10.1109/50.372474.
- [SRD90] M.A. Saed, S.M. Riad, and W.A. Davis. “Wideband dielectric characterization using a dielectric filled cavity adapted to the end of a transmission line”. In: *IEEE Transactions on Instrumentation and Measurement* 39.3 (June 1990), pp. 485–491. DOI: 10.1109/19.106277.

- [SRI81] Y. Shih, J. Rivers, and T. Itoh. “Directive Planar Excitation of an Image-Guide”. In: *MTT-S International Microwave Symposium Digest*. MTT005, 1981. DOI: 10.1109/mwsym.1981.1129801.
- [Ste04] Iain W. Stewart. *The Static and Dynamic Continuum Theory of Liquid Crystals*. CRC Press, Jan. 2004. DOI: 10.1201/9781315272580.
- [Su+11] Runzhou Su, Donghua Tang, Weiqiang Ding, Lixue Chen, and Zhongxiang Zhou. “Efficient transmission of crossing dielectric slot waveguides”. In: *Optics Express* 19.5 (Feb. 2011), p. 4756. DOI: 10.1364/oe.19.004756.
- [Sun+20] Shuang-Yuan Sun, Xuan Yu, Peng-Jun Wang, Chao-Fan Wan, Jun Yang, Zhi-Ping Yin, Guang-Sheng Deng, and Hong-Bo Lu. “Electronically Tunable Liquid-Crystal-based F-Band Phase Shifter”. In: *IEEE Access* (2020), pp. 1–1. DOI: 10.1109/access.2020.3017165.
- [SW78] K. Solbach and I. Wolff. “The Electromagnetic Fields and the Phase Constants of Dielectric Image Lines”. In: *IEEE Transactions on Microwave Theory and Techniques* 26.4 (Apr. 1978), pp. 266–274. DOI: 10.1109/tmtt.1978.1129363.
- [SW85] K. Solbach and I. Wolff. “Dielectric image line groove antennas for millimeter waves, Part II: Experimental verification”. In: *IEEE Transactions on Antennas and Propagation* 33.7 (July 1985), pp. 697–706. DOI: 10.1109/tap.1985.1143664.
- [Tak+05] Kohki Takatoh, Masanori Sakamoto, Ray Hasegawa, Mitsushiro Kodan, and Nobuyuki Itoh. *Alignment Technology and Applications of Liquid Crystal Devices*. CRC Press, July 2005. DOI: 10.1201/9780367800949.
- [Tak+09] Naoki Takayama, Kouta Matsushita, Shogo Ito, Ning Li, Keigo Bunsen, Kenichi Okada, and Akira Matsuzawa. “A multi-line de-embedding technique for mm-wave CMOS circuits”. In: *2009 Asia Pacific Microwave Conference*. IEEE, Dec. 2009. DOI: 10.1109/apmc.2009.5385333.
- [Tes+19a] Henning Tesmer, Roland Reese, Ersin Polat, Matthias Nickel, Rolf Jakoby, and Holger Maune. “Fully Dielectric Rod Antenna Arrays with Integrated Power Divider”. In: *Frequenz* 73.11-12 (Nov. 2019), pp. 367–377. DOI: 10.1515/freq-2019-0152.
- [Tes+19b] Henning Tesmer, Roland Reese, Ersin Polat, Matthias Nickel, Rolf Jakoby, and Holger Maune. “Liquid-Crystal-Based Fully Dielectric Lateral Wave Beam-Steering Antenna”. In: *IEEE Antennas and Wireless Propagation Letters* 18.12 (Dec. 2019), pp. 2577–2581. DOI: 10.1109/lawp.2019.2943722.

## Bibliography

- [Tes+20a] H. Tesmer, R. Reese, E. Polat, R. Jakoby, and H. Maune. “Dielectric Image Line Liquid Crystal Phase Shifter at W-Band”. In: *2020 German Microwave Conference (GeMiC)*. Mar. 2020, pp. 156–159.
- [Tes+20b] Henning Tesmer, Roland Reese, Ersin Polat, Rolf Jakoby, and Holger Maune. “Liquid Crystal Based Parallel-Polarized Dielectric Image Guide Phase Shifter at W-Band”. In: *2020 IEEE/MTT-S International Microwave Symposium (IMS)*. IEEE, Aug. 2020. DOI: 10.1109/ims30576.2020.9224005.
- [Tes+21a] Henning Tesmer, Gerald Gold, Felix Bachbauer, Ersin Polat, Mark Sippel, Rolf Jakoby, Martin Vossiek, and Holger Maune. “Feasibility of Additively Manufactured Tunable Liquid Crystal Loaded Dielectric Waveguides”. In: *IEEE Microwave and Wireless Components Letters* 31.8 (Aug. 2021), pp. 973–976. DOI: 10.1109/lmwc.2021.3082700.
- [Tes+21b] Henning Tesmer, Rani Razzouk, Ersin Polat, Dongwei Wang, Rolf Jakoby, and Holger Maune. “Temperature Characterization of Liquid Crystal Dielectric Image Line Phase Shifter for Millimeter-Wave Applications”. In: *Crystals* 11.1 (Jan. 2021), p. 63. DOI: 10.3390/cryst11010063.
- [Tes+22a] Henning Tesmer, Ersin Polat, Dongwei Wang, and Rolf Jakoby. “Fully-Integrated Dielectric Image Line Phased Array with Liquid Crystal Phase Shifters at W-Band”. In: *2022 52nd European Microwave Conference (EuMC)*. IEEE, Sept. 2022. DOI: 10.23919/eumc54642.2022.9924380.
- [Tes+22b] Henning Tesmer, Rani Razzouk, Ersin Polat, Dongwei Wang, and Rolf Jakoby. “Reconfigurable Liquid Crystal Dielectric Image Line Leaky Wave Antenna at W-Band”. In: *IEEE Journal of Microwaves* 2.3 (July 2022), pp. 480–489. DOI: 10.1109/jmw.2022.3175625.
- [Tes+22c] Henning Tesmer, Daniel Stumpf, Ersin Polat, Dongwei Wang, and Rolf Jakoby. “Dielectric Image Line Rod Antenna Array With Integrated Power Divider at W-Band”. In: *2022 16th European Conference on Antennas and Propagation (EuCAP)*. IEEE, Mar. 2022. DOI: 10.23919/eucap53622.2022.9769431.
- [TLC00] H. Tehrani, Ming-Yi Li, and Kai Chang. “Broadband microstrip to dielectric image line transitions”. In: *IEEE Microwave and Guided Wave Letters* 10.10 (2000), pp. 409–411. DOI: 10.1109/75.877228.
- [Tor+22] Elahehsadat Torabi, Danilo Erricolo, Pai-Yen Chen, Walter Fuscaldo, and Romeo Beccherelli. “Reconfigurable beam-steerable leaky-wave antenna loaded with metamaterial apertures using liquid crystal-based delay lines”. In: *Optics Express* 30.16 (July 2022), p. 28966. DOI: 10.1364/oe.464811.

- [Vol07] John L. Volakis. *Antenna Engineering Handbook*. Ed. by John L. Volakis. 4th ed. New York: McGraw-Hill Education, 2007. ISBN: 9780071475747.
- [Wan+22a] Dongwei Wang, Ersin Polat, Christian Schuster, Henning Tesmer, Gustavo P. Rehder, Ariana L. C. Serrano, Leonardo G. Gomes, Philippe Ferrari, Holger Maune, and Rolf Jakoby. “Fast and Miniaturized Phase Shifter With Excellent Figure of Merit Based on Liquid Crystal and Nanowire-Filled Membrane Technologies”. In: *IEEE Journal of Microwaves* 2.1 (Jan. 2022), pp. 174–184. DOI: 10.1109/jmw.2021.3131648.
- [Wan+22b] Dongwei Wang, Ersin Polat, Henning Tesmer, Holger Maune, and Rolf Jakoby. “Switched and Steered Beam End-Fire Antenna Array Fed by Wideband Via-Less Butler Matrix and Tunable Phase Shifters Based on Liquid Crystal Technology”. In: *IEEE Transactions on Antennas and Propagation* (2022), pp. 1–1. DOI: 10.1109/tap.2022.3142334.
- [Wei+13] Christian Weickhmann, Rolf Jakoby, Evan Constable, and R. A. Lewis. “Time-domain spectroscopy of novel nematic liquid crystals in the terahertz range”. In: *2013 38th International Conference on Infrared, Millimeter, and Terahertz Waves (IRMMW-THz)*. IEEE, Sept. 2013. DOI: 10.1109/irmmw-thz.2013.6665423.
- [Wei+97] Cailin Wei, F. Groen, M.K. Smit, I. Moerman, P. Van Daele, and R. Baets. “Integrated optical elliptic couplers: modeling, design, and applications”. In: *Journal of Lightwave Technology* 15.5 (May 1997), pp. 906–912. DOI: 10.1109/50.580835.
- [Wei17] Christian Weickhmann. “Liquid Crystals Towards Terahertz: Characterisation and Tunable Waveguide Phase Shifters for Millimetre-Wave and Terahertz Beamsteering Antennas”. en. PhD thesis. Darmstadt: Technische Universität Darmstadt, May 2017. URL: <http://tuprints.ulb.tu-darmstadt.de/6216/>.
- [Wei74] W.B. Weir. “Automatic measurement of complex dielectric constant and permeability at microwave frequencies”. In: *Proceedings of the IEEE* 62.1 (1974), pp. 33–36. DOI: 10.1109/proc.1974.9382.
- [WFS21] Michael Wittek, Carsten Fritzsche, and Dieter Schroth. “Employing Liquid Crystal-Based Smart Antennas for Satellite and Terrestrial Communication”. In: *Information Display* 37.1 (Jan. 2021), pp. 17–22. DOI: 10.1002/msid.1178.
- [Wil59] J.C. Wiltse. “Some Characteristics of Dielectric Image Lines at Millimeter Wavelengths”. In: *IEEE Transactions on Microwave Theory and Techniques* 7.1 (Jan. 1959), pp. 65–69. DOI: 10.1109/tmtt.1959.1124625.

## Bibliography

- [Wit+18] Withawat Withayachumnankul, Ryoumei Yamada, Masayuki Fujita, and Tadao Nagatsuma. “All-dielectric rod antenna array for terahertz communications”. In: *APL Photonics* 3.5 (May 2018), p. 051707. DOI: 10.1063/1.5023787.
- [Wit+20] Maxime De Wit, Simon Ooms, Bart Philippe, Yang Zhang, and Patrick Reynaert. “Polymer Microwave Fibers: A New Approach That Blends Wireline, Optical, and Wireless Communication”. In: *IEEE Microwave Magazine* 21.1 (Jan. 2020), pp. 51–66. DOI: 10.1109/mmm.2019.2945158.
- [WLJ02] C. Weil, G. Luessem, and R. Jakoby. “Tunable inverted-microstrip phase shifter device using nematic liquid crystals”. In: *2002 IEEE MTT-S International Microwave Symposium Digest (Cat. No.02CH37278)*. IEEE, 2002. DOI: 10.1109/mwsym.2002.1011632.
- [WRG77] N. Williams, A.W. Rudge, and S.E. Gibbs. “Millimetre-Wave Insular Guide Frequency Scanned Array”. In: *MTT-S International Microwave Symposium Digest*. MTT005, June 1977. DOI: 10.1109/mwsym.1977.1124514.
- [WS20] Ingo Wolff and Klaus Solbach. *Dielectric Image Lines*. Dr. Wolff, Aug. 2020. ISBN: 978-3-922697-42-8.
- [Wu+12] Ke Wu, Yu Jian Cheng, T. Djerafi, and Wei Hong. “Substrate-Integrated Millimeter-Wave and Terahertz Antenna Technology”. In: *Proceedings of the IEEE* 100.7 (July 2012), pp. 2219–2232. DOI: 10.1109/jproc.2012.2190252.
- [XCZ13] Quan Xue, Leung Chiu, and Hao-Tian Zhu. “A transition of microstrip line to dielectric microstrip line for millimeter wave circuits”. In: *2013 IEEE International Wireless Symposium (IWS)*. IEEE, Apr. 2013. DOI: 10.1109/ieee-iws.2013.6616811.
- [Xin+17] Jiang Xing, Li Quan, Li Xiaofeng, Liao Xin, and Wang Kun. “A 77ghz dielectric resonator antenna array using dielectric image insular guide”. In: *2017 Sixth Asia-Pacific Conference on Antennas and Propagation (APCAP)*. IEEE, Oct. 2017. DOI: 10.1109/apcap.2017.8420646.
- [YS08] C. Yeh and F. I. Shimabukuro. *The Essence of Dielectric Waveguides*. Springer US, 2008. DOI: 10.1007/978-0-387-49799-0.
- [Yu+19] Chengyong Yu, En Li, Zhiyong Zhang, Xiangru Wang, Chong Gao, Yafeng Li, Gaofeng Guo, and Hu Zheng. “Broadband complex permittivity measurements of nematic liquid crystals based on cavity perturbation method”. In: *Liquid Crystals* 47.1 (June 2019), pp. 89–98. DOI: 10.1080/02678292.2019.1630488.
- [YW06] Deng-Ke Yang and Shin-Tson Wu. *Fundamentals of Liquid Crystal Devices*. Wiley, Sept. 2006. DOI: 10.1002/9781118751992.



- [ZFB18] Dimitrios C. Zografopoulos, Antonio Ferraro, and Romeo Beccherelli. “Liquid-Crystal High-Frequency Microwave Technology: Materials and Characterization”. In: *Advanced Materials Technologies* (Dec. 2018), p. 1800447. DOI: 10.1002/admt.201800447.
- [Zhu+18] Haotian Zhu, Shu Mao, Quan Xue, and Ke Wu. “A Transition between Dielectric Microstrip Line and Substrate Integrated Waveguide for V-Band”. In: *2018 IEEE/MTT-S International Microwave Symposium - IMS*. IEEE, June 2018. DOI: 10.1109/mwsym.2018.8439380.
- [Zoc33] H. Zocher. “The effect of a magnetic field on the nematic state”. In: *Transactions of the Faraday Society* 29.140 (1933), p. 945. DOI: 10.1039/tf9332900945.



# Own Contributions

## First Author and Shared First Author

- [Pol+20b] Ersin Polat, Henning Tesmer, Roland Reese, Matthias Nickel, Dongwei Wang, Peter Schumacher, Rolf Jakoby, and Holger Maune. “Reconfigurable Millimeter-Wave Components Based on Liquid Crystal Technology for Smart Applications”. In: *Crystals* 10.5 (Apr. 2020), p. 346. DOI: 10.3390/cryst10050346.
- [Tes+19a] Henning Tesmer, Roland Reese, Ersin Polat, Matthias Nickel, Rolf Jakoby, and Holger Maune. “Fully Dielectric Rod Antenna Arrays with Integrated Power Divider”. In: *Frequenz* 73.11-12 (Nov. 2019), pp. 367–377. DOI: 10.1515/freq-2019-0152.
- [Tes+19b] Henning Tesmer, Roland Reese, Ersin Polat, Matthias Nickel, Rolf Jakoby, and Holger Maune. “Liquid-Crystal-Based Fully Dielectric Lateral Wave Beam-Steering Antenna”. In: *IEEE Antennas and Wireless Propagation Letters* 18.12 (Dec. 2019), pp. 2577–2581. DOI: 10.1109/lawp.2019.2943722.
- [Tes+20a] H. Tesmer, R. Reese, E. Polat, R. Jakoby, and H. Maune. “Dielectric Image Line Liquid Crystal Phase Shifter at W-Band”. In: *2020 German Microwave Conference (GeMiC)*. Mar. 2020, pp. 156–159.
- [Tes+20b] Henning Tesmer, Roland Reese, Ersin Polat, Rolf Jakoby, and Holger Maune. “Liquid Crystal Based Parallel-Polarized Dielectric Image Guide Phase Shifter at W-Band”. In: *2020 IEEE/MTT-S International Microwave Symposium (IMS)*. IEEE, Aug. 2020. DOI: 10.1109/ims30576.2020.9224005.
- [Tes+21a] Henning Tesmer, Gerald Gold, Felix Bachbauer, Ersin Polat, Mark Sippel, Rolf Jakoby, Martin Vossiek, and Holger Maune. “Feasibility of Additively Manufactured Tunable Liquid Crystal Loaded Dielectric Waveguides”. In: *IEEE Microwave and Wireless Components Letters* 31.8 (Aug. 2021), pp. 973–976. DOI: 10.1109/lmwc.2021.3082700.
- [Tes+21b] Henning Tesmer, Rani Razzouk, Ersin Polat, Dongwei Wang, Rolf Jakoby, and Holger Maune. “Temperature Characterization of Liquid Crystal Dielectric Image Line Phase Shifter for Millimeter-Wave Applications”. In: *Crystals* 11.1 (Jan. 2021), p. 63. DOI: 10.3390/cryst11010063.

- [Tes+22a] Henning Tesmer, Ersin Polat, Dongwei Wang, and Rolf Jakoby. “Fully-Integrated Dielectric Image Line Phased Array with Liquid Crystal Phase Shifters at W-Band”. In: *2022 52nd European Microwave Conference (EuMC)*. IEEE, Sept. 2022. DOI: 10.23919/eumc54642.2022.9924380.
- [Tes+22b] Henning Tesmer, Rani Razzouk, Ersin Polat, Dongwei Wang, and Rolf Jakoby. “Reconfigurable Liquid Crystal Dielectric Image Line Leaky Wave Antenna at W-Band”. In: *IEEE Journal of Microwaves 2.3* (July 2022), pp. 480–489. DOI: 10.1109/jmw.2022.3175625.
- [Tes+22c] Henning Tesmer, Daniel Stumpf, Ersin Polat, Dongwei Wang, and Rolf Jakoby. “Dielectric Image Line Rod Antenna Array With Integrated Power Divider at W-Band”. In: *2022 16th European Conference on Antennas and Propagation (EuCAP)*. IEEE, Mar. 2022. DOI: 10.23919/eucap53622.2022.9769431.

## Co-Author

- [Kam+22] Fynn Kamrath, Ersin Polat, Stipo Matic, Christian Schuster, Daniel Miek, Henning Tesmer, Patrick Boe, Dongwei Wang, Rolf Jakoby, Holger Maune, and Michael Hoft. “Bandwidth and Center Frequency Reconfigurable Waveguide Filter Based on Liquid Crystal Technology”. In: *IEEE Journal of Microwaves 2.1* (Jan. 2022), pp. 134–144. DOI: 10.1109/jmw.2021.3115244.
- [Nic+20] Matthias Nickel, Alejandro Jimenez-Saez, Prannoy Agrawal, Ahmed Gadallah, Andrea Malignaggi, Christian Schuster, Roland Reese, Henning Tesmer, Ersin Polat, Dongwei Wang, Peter Schumacher, Rolf Jakoby, Dietmar Kissinger, and Holger Maune. “Ridge Gap Waveguide Based Liquid Crystal Phase Shifter”. In: *IEEE Access 8* (2020), pp. 77833–77842. DOI: 10.1109/access.2020.2989547.
- [Pol+19a] E. Polat, R. Reese, H. Tesmer, S. Schmidt, M. Spaeth, M. Nickel, C. Schuster, R. Jakoby, and H. Maune. “Characterization of Liquid Crystals Using a Temperature-Controlled 60 GHz Resonator”. In: *2019 IEEE MTT-S International Microwave Workshop Series on Advanced Materials and Processes for RF and THz Applications (IMWS-AMP)*. IEEE, July 2019. DOI: 10.1109/imws-amp.2019.8880077.
- [Pol+20a] Ersin Polat, Roland Reese, Henning Tesmer, Matthias Nickel, Rolf Jakoby, and Holger Maune. “Fully Dielectric Phased Array for Beamsteering Using Liquid Crystal Technology at W-Band”. In: *2020 14th European Conference on Antennas and Propagation (EuCAP)*. IEEE, Mar. 2020. DOI: 10.23919/eucap48036.2020.9135584.

- [Pol+22] Ersin Polat, Fynn Kamrath, Stipo Matic, Henning Tesmer, Alejandro Jimenez-Saez, Dongwei Wang, Holger Maune, Michael Hoft, and Rolf Jakoby. “Novel Hybrid Electric/Magnetic Bias Concept for Tunable Liquid Crystal Based Filter”. In: *IEEE Journal of Microwaves* 2.3 (July 2022), pp. 490–495. DOI: 10.1109/jmw.2022.3180227.
- [Ree+18b] Roland Reese, Henning Tesmer, Matthias Jost, Ersin Polat, Matthias Nickel, Rolf Jakoby, and Holger Maune. “A Compact Two-dimensional Power Divider for a Dielectric Rod Antenna Array Based on Multimode Interference”. In: *Journal of Infrared, Millimeter, and Terahertz Waves* 39.12 (Aug. 2018), pp. 1185–1202. DOI: 10.1007/s10762-018-0535-x.
- [Ree+19a] Roland Reese, Matthias Jost, Ersin Polat, Henning Tesmer, Jonathan Strobl, Christian Schuster, Matthias Nickel, Rolf Jakoby, and Holger Maune. “A Millimeter-Wave Beam-Steering Lens Antenna With Reconfigurable Aperture Using Liquid Crystal”. In: *IEEE Transactions on Antennas and Propagation* 67.8 (Aug. 2019), pp. 5313–5324. DOI: 10.1109/tap.2019.2918474.
- [Ree+19b] Roland Reese, Ersin Polat, Henning Tesmer, Jonathan Strobl, Christian Schuster, Matthias Nickel, Angel Blanco Granja, Rolf Jakoby, and Holger Maune. “Liquid Crystal Based Dielectric Waveguide Phase Shifters for Phased Arrays at W-Band”. In: *IEEE Access* 7 (2019), pp. 127032–127041. DOI: 10.1109/access.2019.2939648.
- [Ree+19c] Roland Reese, Henning Tesmer, Ersin Polat, Matthias Jost, Matthias Nickel, Rolf Jakoby, and Holger Maune. “Fully Dielectric Rod Antenna Arrays with High Permittivity Materials”. In: *2019 12th German Microwave Conference (GeMiC)*. IEEE, Mar. 2019. DOI: 10.23919/gemic.2019.8698141.
- [Wan+21a] D. Wang, M. Nickel, P. Schumacher, E. Polat, H. Tesmer, R. Jakoby, and H. Maune. “A Planar Quasi Yagi-Uda Antenna Designed For Liquid Crystal Based End-Fire Phased Arrays”. In: *2021 IEEE Radio and Wireless Symposium (RWS)*. IEEE, Jan. 2021. DOI: 10.1109/rws50353.2021.9360363.
- [Wan+21b] D. Wang, E. Polat, H. Tesmer, and R. Jakoby. “Wideband evaluation of two types of slow-wave microstrip lines”. In: *Electronics Letters* 58.4 (Dec. 2021), pp. 156–158. DOI: 10.1049/e112.12389.
- [Wan+21c] Dongwei Wang, Ersin Polat, Henning Tesmer, Rolf Jakoby, and Holger Maune. “A Compact and Fast  $1 \times 4$  Continuously Steerable Endfire Phased-Array Antenna Based on Liquid Crystal”. In: *IEEE Antennas and Wireless Propagation Letters* 20.10 (Oct. 2021), pp. 1859–1862. DOI: 10.1109/lawp.2021.3096035.

- [Wan+22a] Dongwei Wang, Ersin Polat, Christian Schuster, Henning Tesmer, Gustavo P. Rehder, Ariana L. C. Serrano, Leonardo G. Gomes, Philippe Ferrari, Holger Maune, and Rolf Jakoby. “Fast and Miniaturized Phase Shifter With Excellent Figure of Merit Based on Liquid Crystal and Nanowire-Filled Membrane Technologies”. In: *IEEE Journal of Microwaves* 2.1 (Jan. 2022), pp. 174–184. DOI: 10.1109/jmw.2021.3131648.
- [Wan+22b] Dongwei Wang, Ersin Polat, Henning Tesmer, Rolf Jakoby, and Holger Maune. “Highly Miniaturized Continuously Tunable Phase Shifter Based on Liquid Crystal and Defected Ground Structures”. In: *IEEE Microwave and Wireless Components Letters* 32.6 (June 2022), pp. 519–522. DOI: 10.1109/lmwc.2022.3142410.
- [Wan+22c] Dongwei Wang, Ersin Polat, Henning Tesmer, Holger Maune, and Rolf Jakoby. “Switched and Steered Beam End-Fire Antenna Array Fed by Wideband Via-Less Butler Matrix and Tunable Phase Shifters Based on Liquid Crystal Technology”. In: *IEEE Transactions on Antennas and Propagation* (2022), pp. 1–1. DOI: 10.1109/tap.2022.3142334.

## Contribution to Books

- [Fer+22] Philippe Ferrari, Rolf Jakoby, Onur Hamza Karabey, Gustavo Rehder, and Holger Maune. *Reconfigurable Circuits and Technologies for Smart Millimeter-Wave Systems*. EuMA High Frequency Technologies Series. Cambridge University Press, 2022.

## Patents

1. Ersin Polat, Holger Maune, Henning Tesmer, and Rolf Jakoby. “Phasensteuerung von Flüssigkristallkomponenten”. Registration Number DE 102021132535.8 (2021).
2. Roland Reese, Matthias Nickel, Matthias Jost, Holger Maune, Rolf Jakoby, Henning Tesmer, and Ersin Polat. “Flüssigkristallgefüllte voll-dielektrische Gruppenantennenzur Strahlformung”. Patent Number: DE 102018119508.7 (2018).

## Awards

1. Best Student Paper Award (Co-author):  
R. Reese et al., ”Fully Dielectric Rod Antenna Arrays with High Permittivity Materials,” 2019 12th German Microwave Conference (GeMiC), 2019, pp. 13-16, doi: 10.23919/GEMIC.2019.8698141.

2. Best Paper Award (First Author):

H. Tesmer, R. Reese, E. Polat, R. Jakoby and H. Maune, "Dielectric Image Line Liquid Crystal Phase Shifter at W-Band," 2020 German Microwave Conference (GeMiC), 2020, pp. 156-159.

## Supervised Student Theses

- Robin Neuder: *Fundamental Analysis of Planar Dielectric Image Lines*, Bachelor Thesis, April 2019
- Daniel Stumpf: *Analysis of Dielectric Image Line Rod Antennas for Millimeter Wave Applications*, Bachelor Thesis, October 2020
- Fahd Tayanne: *Planar Transitions of Dielectric Image Lines to Metallic Transmission Lines at W-band*, Master Thesis, February 2021
- Rani Razzouk: *Dielectric Image Line Leaky Wave Antennas for Reconfigurable Millimeter-Wave Applications*, Master Thesis, August 2021
- Mohamed Kamkoum: *Parallel Polarized Dielectric Image Line Leaky Wave Antennas for Millimeter Wave Applications*, Bachelor Thesis, October 2022